

DISSERTATION - Doctoral Thesis

***A Theoretical Model For Optimal Propulsion of a
Compliant Wall in Interaction With a Channel Flow.
Application to The Prestrained-Membrane Pump***

ausgeführt zum Zwecke der Erlangung des akademischen Grades des
Doktors der technischen Wissenschaften (PhD)
unter der Leitung von

Ao.Univ.Prof. Dr. Herbert Steinrück
Institutsnummer E322
Institut für Strömungsmechanik und Wärmeübertragung

eingereicht an der Technischen Universität Wien

Fakultät für Maschinenwesen und Betriebswissenschaften

von

Dipl.-Ing. Markus Müllner
Matrikelnummer 9925690
2120 Wolkersdorf, Am Stiegl 5

Wien, im Januar 2015

Kurzfassung

In der vorliegenden Arbeit ist der Antriebsschub eines Schlagflügelgeräts diskutiert, das einen Körper antreibt. Schuberzeugung in äußerer Strömung und Pumpen von Fluid durch einen Kanal werden betrachtet. Sowohl vorgegebene Bewegung des Antriebs als auch Fluid-Struktur Interaktion für eine vorgespannte Membran werden betrachtet.

Der Schwerpunkt liegt auf der Optimierung des Vortriebswirkungsgrads der Bewegung in Form einer Pareto-Front für gegebenen Schub. Verschiedene Methoden werden verwendet um die Strömung zu beschreiben: Potentialtheorie wird verwendet mit Chebyshev-Polynomen und mit der Panel Methode. Die reibungsbehaftete Strömung wird numerisch gelöst mit einem selbstentwickelten Programm und mit einem kommerziellen Software-Paket.

Folgende neuartige Ergebnisse werden erhalten: Für einen mit kleinen Auslenkungen schlagenden Tragflügel in äußerer Strömung wird die optimale Bewegung analytisch bestimmt. Eine analytische Potentiallösung wird präsentiert für die Kanalströmung über eine auftriebserzeugende Oberfläche in allgemeiner Bewegung in der Nähe der Kanal-Mittelachse. Für die Flatterbewegung mithilfe einer vorgespannten Membran werden die Membranparameter in einem weiten Bereich variiert. Es stellt sich heraus dass der Antrieb mit einer flatternden Membran am effizientesten ist wenn die Membran die Bewegung einer stromabwärts wandernden Welle nachahmt. Für diese spezielle Bewegung wird für reibungsfreie und laminare Strömung gezeigt dass die Vorgabe von periodischen Bedingungen in Strömungsrichtung die Erzeugung einer Schubkraft verhindert.

Abstract

The present work discusses the propulsive output of a flapping device, used to propel a body. Both thrust production in external flow and pumping fluid in a channel are considered. Prescribed motions of the device as well as fluid-structure interaction for a prestrained membrane are considered.

The focus is on an optimization of the motion's propulsive efficiency as Pareto front for given thrust. Different methods are used to describe the flow: Potential theory is treated with Chebyshev polynomials and the panel method. Viscous flow is solved numerically with a self-developed code and a commercial software package.

The following novel results are obtained: For a foil flapping with small deflections in given external flow, the optimum motion is determined analytically. An analytical potential-flow solution is presented for the channel flow over a lifting surface in general motion in the vicinity of the channel's centerline. For the flapping device that uses a prestrained membrane, the membrane parameters are varied in a wide range. It turns out that the flapping-membrane device is most efficient when the membrane imitates the motion of a downstream travelling wave. For this specific motion, it is shown for both inviscid and laminar flow that enforcing periodic conditions in streamwise direction prohibits the generation of thrust.

Acknowledgements

First and foremost I would like to thank my thesis supervisor Prof. Herbert Steinrück for his scientific support, wise hints and endless patience. I also want to thank the second referee Prof. Philipp Gittler who immediately agreed to examine the work.

My success is due to the quiet support of my family. I sincerely thank my parents for always supporting the choices that I have made in my life. Thank you Thomas simply for being there whenever I needed advice. I will miss the time of disputes that were sometimes intense but always led to a common conclusion.

Furthermore I wish to express my gratitude to all my colleagues for fruitful scientific discussions at lunch and in the coffee breaks. Their company and support made studying a great time. In particular I want to thank Johannes Strecha for sharing the office with me (sorry that I always forgot to water the flowers), Dr. Georg Meyer for cracking jokes, Dr. Richard Jurisits for the excellent Turkish coffee, Ernst Hofmann and Dr. Thomas Loimer for talks about non-scientific topics, Dr. Christoph Buchner and Harald Neth for support and help with computer issues, and last but not least, the entire team at the institute.

List of Symbols

Roman letters

\tilde{A}	amplitude of travelling wave
A	pitching amplitude of flapping foil motion
(a_0, a_n)	Fourier coefficients of pressure difference across the body
A'_0	coefficient for leading-edge thrust
(a'_0, a''_0)	real- and imaginary part of a_0 , respectively
$a_c(1)$	auxiliary integral in linear system for trailing edge vorticity
\tilde{A}_{disk}	swept area in an actuator disk propeller model
\tilde{A}_h	cross section area of half-channel
A_λ	dimensionless wave steepness (with respect to the wavelength $\tilde{\lambda}$)
\tilde{A}_{LE}	max. deflection at the leading edge
A_{LE}	dimensionless max. deflection at the leading edge
A_{mn}	coefficient matrix in panel code for the lhs
$a_s(1)$	auxiliary integral in linear system for trailing edge vorticity
\tilde{A}_{TE}	max. deflection at the trailing edge
B	reference point of pitching for flapping foil motion
\tilde{B}	depth of channel
B_k	Bernoulli number
B_{mn}	coefficient matrix in panel code for the rhs
$\tilde{C}(\tilde{t})$	arbitrary time-dependent function
\tilde{c}	phase speed of downstream propagating wave
c	dimensionless phase speed of downstream propagating wave
$C(\sigma)$	Theodorsen function
c_{Tp}	propeller thrust coefficient
\tilde{D}_M	thickness of the membrane
\tilde{d}_h	hydraulic diameter of half-channel
D_0	frequency dependent auxiliary function
D_1	frequency dependent auxiliary function
E	dimensionless kinetic energy imparted to the wake per period
$\tilde{E}(\tilde{t})$	instantaneous power of kinetic energy imparted to the wake
$F(\sigma)$	real part of the Theodorsen function $C(\sigma)$
$F(z)$	complex velocity potential
$f(z)$	complex valued function

${}_1F_2$	generalized hypergeometric function
$f_c(1)$	auxiliary integral in linear system for trailing edge vorticity
F_d	dimensionless total force acting on the wavy wall
F_f	dimensionless viscous force acting on the wavy wall
F_p	dimensionless force due to pressure acting on the wavy wall
$f_s(1)$	auxiliary integral in linear system for trailing edge vorticity
g	auxiliary constant
$G(\sigma)$	imaginary part of the Theodorsen function $C(\sigma)$
\tilde{h}	semi channel width
H	plunging amplitude of flapping foil motion
$h(\zeta)$	analytic auxiliary function
i	imaginary unit
I_0	integral for influence coefficient in channel flow
I_1	integral for influence coefficient in channel flow
I_c	auxiliary integral in the panel code
\Im	imaginary part
I_s	auxiliary integral in the panel code
$J_n(k)$	Bessel function of the first kind
k	dimensionless wavenumber
K	frequency dependent auxiliary function
K_γ	coefficient for singularity of vorticity at the leading edge
$K(k)$	complete elliptic integral of the first kind
$K_0(i\sigma)$	modified Bessel function of the second kind
$K_1(i\sigma)$	modified Bessel function of the second kind
\tilde{L}	chord length/length of membrane
L	frequency dependent auxiliary function
$\tilde{L}(\tilde{t})$	instantaneous lift force
$\text{Li}_2(z)$	polylogarithm function of order two (dilogarithm)
m	index
\tilde{m}_{disk}	mass flux in an actuator disk propeller model
n	index
N	frequency dependent auxiliary function
\tilde{p}	fluid pressure
p	dimensionless fluid pressure
P	dimensionless time-averaged power, also: frequency dependent auxiliary function
$\tilde{P}(\tilde{t})$	instantaneous power
$P(t)$	dimensionless instantaneous power
$\Delta\tilde{p}$	pressure difference across the body
Δp_1	dimensionless pressure difference across the body in first order
\tilde{p}_L	fluid pressure on the lower side of the body surface
\tilde{p}_U	fluid pressure on the upper side of the body surface
Q	frequency dependent auxiliary function
R	frequency dependent auxiliary function

\Re	real part
Re_c	Reynolds number based on chord
Re_h	Reynolds number based on the hydraulic diameter \tilde{d}_h
Re_λ	Reynolds number based on the wavelength $\tilde{\lambda}$
$\tilde{r}^{(x)}$	radius of membrane curvature in x -direction
$\tilde{r}^{(z)}$	radius of membrane curvature in z -direction
S	frequency dependent auxiliary function
s	auxiliary coordinate
St	Strouhal number
\tilde{t}	time
t	dimensionless time
T	dimensionless time-averaged thrust
$\tilde{T}(\tilde{t})$	instantaneous thrust force
$T_n(x)$	Chebyshev polynomial of the first kind
T^{opt}	maximum attainable thrust by optimum motion
$\tilde{T}_p(\tilde{t})$	instantaneous thrust from surface pressure
T_p	dimensionless time-averaged thrust from pressure
$T_p(t)$	dimensionless instantaneous thrust from pressure
$\tilde{T}_s(\tilde{t})$	instantaneous thrust from nose suction
T_s	dimensionless time-averaged thrust from nose suction
$T_s(t)$	dimensionless instantaneous thrust from nose suction
(\tilde{u}, \tilde{v})	velocity components in horizontal and vertical direction, respectively
u	dimensionless velocity component in main flow direction
\tilde{U}	speed of oncoming flow
\tilde{U}_{disk}	flow velocity in the disk of an actuator disk propeller model
\tilde{U}_m	mean velocity in channel flow
$U_n(x)$	Chebyshev polynomial of the second kind
\tilde{U}_w	flow velocity in the wake of an actuator disk propeller model
\vec{v}	velocity vector
v	dimensionless velocity component in vertical direction
\tilde{w}	body deflection
$W(x_i)$	primitive integral of the deflection
$w(\zeta)$	complex valued velocity perturbation
w_1	dimensionless body deflection in first order
$w_{1,max}$	maximum value of the leading order deflection w_1
w_{Env}	envelope of flapping motion
(x, y)	dimensionless coordinate directions
$(\tilde{x}, \tilde{y}, \tilde{z})$	coordinate directions
x_A	streamwise position of the junction of flap and membrane
Δx_j	interval in the panel code
Δx_r	leading-edge region where the net portion of pressure thrust is generated
x_{LE}	dimensionless streamwise position of the leading edge
$x_{m,i}$	panel-midpoints

x_{TE}	dimensionless streamwise position of the trailing edge
z	complex coordinate

Greek letters

$\tilde{\alpha}_M$	coefficient in membrane equation for streamwise tension
α_M	dimensionless coefficient in membrane equation for streamwise tension
α_{max}	maximum total angle of attack
β	solution vector in panel code
(β_0, β_n)	Fourier coefficients of motion
$\tilde{\beta}_M$	coefficient in membrane equation for lateral tension
β_M	dimensionless coefficient in membrane equation for lateral tension
Γ	vortex strength
$\Gamma(t)$	circulation on the body
$\gamma(x, t)$	vorticity density
(γ_0, γ_n)	Fourier coefficients of spatial derivative of w_1
Γ_T	total circulation
Γ_w	single wake vortex
γ_w	vorticity density in the wake
ϵ	perturbation parameter
ζ	complex coordinate
η	propulsive efficiency
η_p	propeller efficiency
θ	auxiliary coordinate
$\tilde{\theta}$	auxiliary variable
$\tilde{\lambda}$	wavelength of body surface
λ	Lagrange multiplier
(λ_0, λ_n)	Fourier coefficients of lateral velocity perturbation
μ	Lagrange multiplier
μ_M	dimensionless coefficient for membrane inertia
$\tilde{\nu}$	kinematic viscosity of the fluid
ξ	horizontal coordinate component
$\Pi(\alpha^2, k)$	elliptic integral of the third kind
$\tilde{\rho}$	fluid density
$\tilde{\rho}_M$	density of the membrane
σ	reduced frequency based on semi-chord (compare to Ω)
$\tilde{\sigma}^{(x)}$	membrane tension in x -direction
$\tilde{\sigma}^{(z)}$	membrane tension in z -direction
τ	dimensionless time for periodic motion
φ	perturbation velocity potential
$\tilde{\Phi}$	velocity potential
χ	proportional feathering parameter
ψ	imaginary part of velocity potential
$\tilde{\omega}$	angular flapping frequency

Ω reduced frequency based on the chord (compare to σ)

Subscripts

c cosine component
 L lower side of body surface
 LE leading edge
 M membrane
 s sine component
 t partial derivative with respect to t
 TE trailing edge
 U upper side of body surface
 x partial derivative with respect to x
 y partial derivative with respect to y

Superscripts

(x) x -direction
 (z) z -direction

Overscripts

$-$ time average over one period
 \rightarrow physical vector
 \sim dimensional quantities

Contents

1	Introduction and Problem Formulation	1
1.1	Motivation	1
1.2	Biomimetic propulsion	1
1.2.1	Asymmetric excitation	2
1.2.2	Valveless pumping	2
1.2.3	Swimming of slender fish	3
1.3	Literature overview of discussed aspects	3
1.3.1	Flapping foil in optimal motion	4
1.3.2	Chordwise flexibility	5
1.3.3	Effect of channel walls	6
1.3.4	Drag reduction	7
1.3.5	Fluid-structure interaction	7
1.4	Organisation of work	7
1.5	Problem formulation and model description	8
1.5.1	Valveless membrane pump	8
1.5.2	Models and methods: overview	9
1.5.3	Potential theory for unsteady flow	9
1.5.4	Asymptotic approach for small deflections	10
1.5.5	Boundary conditions	10
1.5.6	Viscous flow	10
1.5.7	Membrane equation	11
1.5.8	Design- and operating parameters	11
1.5.9	Dimensionless formulation	12
1.5.10	Measurements by W. Zackl	14
2	2D-Potential Flow Theory	15
2.1	Unbounded domain	15
2.1.1	Pressure on the body	15
2.1.2	Vortex distribution	16
2.1.3	Kutta condition	16
2.1.4	Wake vortices	16
2.1.5	Singular integral equation	17
2.1.6	Time-harmonic motion	18

2.1.7	Representation by Chebyshev polynomials	19
2.1.8	Theodorsen function	21
2.1.9	Thrust, power and efficiency	21
2.2	Channel flow	23
2.2.1	Single vortex at the centerline and stack of vortices	24
2.2.2	Singular integral equation	25
2.2.3	Solution of the flow field	26
2.2.4	Circulation	30
2.2.5	Solution for time-harmonic motion	33
2.3	Panel method: Membrane in channel flow	35
2.3.1	Equations	36
2.3.2	Time-harmonic motion	36
2.3.3	Discretization	37
3	Propulsion	44
3.1	Flapping foil: potential flow in unbounded domain	44
3.1.1	Combined plunging and pitching motion	44
3.1.2	Forces for time-harmonic motion	45
3.1.3	Dimensionless time-averaged thrust and energy	46
3.1.4	Comparison of instantaneous forces to CFD results	46
3.1.5	Comparison of linear and nonlinear model at large deflections	47
3.1.6	Remarks to the limits of the potential flow model	49
3.2	Optimal foil motion	49
3.2.1	Optimization under constraints	50
3.2.2	Results	55
3.2.3	Propulsive performance for channel flow	60
3.3	Chordwise flexibility	62
3.3.1	Review of flexible foils	62
3.3.2	Travelling body wave of cosine shape	63
3.3.3	Comparison: Foil motion vs. travelling body wave	68
3.3.4	Propulsive efficiency for channel flow	68
3.4	Limit of large wave numbers	69
3.4.1	Body of finite length	69
3.4.2	Travelling pressure wave in the mid-chord limit	72
3.4.3	Periodic travelling wave as limit of the mid-chord problem	74
3.5	Viscous effects (periodic case)	77
3.5.1	Results in the literature	78
3.5.2	Discretization method	79
3.5.3	Results	80
3.5.4	Comparison to literature for different phase speeds	83

4	Fluid Structure Interaction	85
4.1	Membrane in unbounded flow	85
4.1.1	Forced oscillation of the leading-edge point	85
4.1.2	Formulation of the coupled problem	86
4.1.3	Boundary conditions	89
4.1.4	Solution procedure	90
4.1.5	Postprocessing	90
4.1.6	Results	90
4.2	Double channel membrane pump	99
4.2.1	Potential flow theory with the panel method	99
4.2.2	CFD results	99
4.2.3	Comparison of the CFD results to potential flow theory	105
5	Summary and Conclusions	108
5.1	Discussion of the inviscid model	108
5.2	Flapping foil motion, chordwise flexibility and TWS	108
5.3	FSI, TWS with prestrained membrane	109
5.4	The effect of channel width to chord ratio	109
5.5	Relation to viscous flow over TWS of infinite extension	110
A	Verification of The Panel Code	111
A.1	Steady channel flow	111
A.2	Flapping foil in unbounded domain	112
A.3	Travelling wavy surface in unbounded domain	113
A.4	Membrane without inertia in unbounded domain	113
B	Conversion to The Notation by Katz & Weihs For Large Deflection Motion	115
C	Optimal foil motion	117
C.1	Solution via Lagrange function	117
C.2	Direct approach with the elimination method	120
C.3	Limit $\sigma \rightarrow \infty$	124
C.4	Boundary optimum	125
D	Comparison of Common Discretization Schemes in Fluid Dynamics	128
D.1	FD-, FV- and FE-method	128
D.2	Incompressible versus compressible flow	129
D.3	Uniform versus nonuniform grid	129
D.4	Point versus cell average values	130
D.5	Staggered versus colocated grid	130
D.6	Physical versus computational space	130
D.7	PPM versus PPH	131
D.8	Reconstruction versus ansatz	131
D.9	Central versus upwind schemes	132

D.10	Explicit versus compact discretization method	132
D.11	Nonlinear terms	132
D.12	Boundary conditions	133
D.13	Avoiding a singular system	133
D.14	Solvers	134
D.15	Deconvolution	134
E	Verification of The Navier–Stokes Solver	135
E.1	Kovasznay flow	135
E.1.1	Analytical solution	135
E.1.2	Solution on non-uniform grid	136
E.2	Lid-driven cavity	138
E.2.1	Solution on uniform grid	138
E.2.2	Solution on non-uniform grid	140

Chapter 1

Introduction and Problem Formulation

1.1 Motivation

The present work is motivated from a novel valveless and bladeless pump invented by Wilhelm Zackl [120], the “Double Channel Membrane Pump“. This innovative concept of a pump has a simple design: A compliant membrane is placed on the centerline of a rigid channel. The membrane is clamped at the side walls to seal the upper against the lower half of the channel and prestrained in streamwise and lateral direction. Water or slurry may be used as working fluid. During operation of the pump, the membrane is excited at one end by periodic transverse motion. Thus, the membrane interacts in coupled manner with the fluid. In doing so, a mean flow evolves in the pump that is directed away from the excited end.

Zackl fabricated a see-through demonstration model that confirms operation conditions where the deflection of the membrane performs a travelling wave pattern in the downstream direction, as intended by the inventor ¹. In addition, Zackl has executed measurements for a pump of industrial scale and reported in detail the experimental results [120, 121].

In the present work, theoretical models for the pump are developed that take into account the most significant aspects regarding optimal design and operation parameters. The results may be used as a basis for future experiments and simulations.

1.2 Biomimetic propulsion

Due to its design and operational characteristics, the pump can be considered as bio-inspired propulsion system. Biomimetics is a broad field where the mechanics and dynamics of biological propulsion systems are examined. It includes the transport of fluid mass, momentum, and energy in both stationary and mobile systems. Applications include aquatic locomotion, conversion of fluid dynamic energy, and flow through compliant tubes.

¹U.S. Patent No. 7.101159 B2 9/2006, EP 1438514 B1, W. Zackl

When a technical invention is to be compared to existing biological systems, the foremost task is the understanding of the underlying working principle.

1.2.1 Asymmetric excitation

An examination of the start-up procedure of the pump may help to elucidate the working principle. In this regard, it is certainly of interest if the geometric asymmetry, evoked by the excitation of the membrane at one end, is crucial for the net flow through the pump. [110] showed for a plate in periodic plunging motion in an otherwise quiescent fluid, i. e. for a symmetric configuration, that symmetry breaking occurs when a certain stability limit – dependent on the ratio of plunging speed and fluid viscosity – is exceeded. Then, a thrust force is generated that leads to mean forward motion of the plate. From this result, it can be concluded that the geometrical asymmetry is not necessarily required to explain the pumping effect.

Nevertheless, the asymmetric configuration initiates the flow in a certain direction. In the present work, a "pitching plate pump" is considered where the mean flow evolves as result of the start-up phase. In the remaining part of the work, the discussion is restricted to problems with given mean flow and a time-periodic flow superimposed to it.

Valveless pumping can be achieved on the basis of several different propulsion principles. Pumping by downstream travelling waves, in particular, has analogy to two different propulsive mechanisms observed in nature: On one hand, the propulsion by downstream travelling waves is frequently observed in physiological systems; On the other hand, many aquatic animals propel themselves in form of rearward-propagating waves along their fins or body.

1.2.2 Valveless pumping

In living creatures, valveless transport in vessels is often realized by means of powered muscles that propagate a wave along the wall of a circular tube. This mechanism, called peristaltic pumping, can be found – for instance – in the esophageal and the gastrointestinal system. In such a system, usually the viscous forces in the fluid are dominant. The propulsion mechanism has a viscous origin and can be explained by lubrication theory [103]. Hose pumps are an example where the peristaltic principle is used in an industrial application. Micro-robotic self-propulsion or pumping in a highly viscous fluid by generating vibration-induced travelling waves on an elastic membrane is described in [88]. Valveless flow transport can also evolve from non-peristaltic contractions of the wall:

- In [1] a theory for a microfluidic pump is established that shows the occurrence of a net flow when there is a phase-lag between two actuation spots along the channel.
- A different principle, called impedance pumping, has been discovered by Gerhart Liebau in 1954. It makes use of different impedance coefficients (obtained by different geometrical and/or mechanical properties) of flexible tubes attached left and right to a compression point [31]. This principle is believed to support the heart in pumping the blood through the cardiac system. [59] proposed a model based on the Liebau effect to describe the circulation of blood in the early human foetus in spite of the lack of cardiac valves.

- Yet another principle is used in a valveless diffuser pump, first published in [100]. Here, different pressure loss coefficients in a nozzle and a diffuser enforce a mean flow.

Even though the listed propulsive principles are different to each other, they have in common that the achieved flow speed and Reynolds number are relatively low. The prestrained-membrane pump, however, operates at high Reynolds numbers [120], where the inertial forces in the fluid are dominant. In this regime, the propulsion by downstream travelling waves may be likened to the swimming of slender fish.

1.2.3 Swimming of slender fish

The propulsion of fish is classified in a well-established scheme of different modes, see the review article [89]. Undulatory propulsion is observed in both median and/or paired fin propulsion and in body and/or caudal fin movements. Non-pelagic rays generate thrust from backward undulatory waves along their pectoral fins [22]. [19] showed that ratfish pass waves rearward their pectorals that have uniform chordwise wave amplitude. The large pelagic dwellers, like vertebrates (fish, sharks) and cetaceans (whales and dolphins), propel themselves in form of lateral displacements propagating downstream along their surface that ends posterior in a large displacement flapping motion of a high caudal fin, or fluke, of crescent shape. This type of locomotion, called the thunniform mode (for its occurrence in the Scombridae) is interesting because the thrust-producing and drag generating parts are separated [54]. The main part of the propulsive thrust is produced by the streamlined, high aspect-ratio lunate tail. Sir James Lighthill [53] was the first to apply 2-dim potential flow theory of a flapping slender wing on lunate tail propulsion. Flapping wings produce both thrust and lift directly [114], but as the wave number is not large, the side forces do not cancel out. According to [89], "thunniform mode is the most efficient locomotion mode evolved in the aquatic environment".

It is well-known that flapping motions of large displacement are favourable in order to obtain practical thrust levels [37]. However, in the present study the amplitude of the propulsive mechanism is constraint due to the presence of channel walls and thus the small-amplitude linear model is employed. Optimal motion is studied as to obtain maximum propulsive efficiency for a given thrust. The Pareto curve is then used as "benchmark" to which the results from the coupled fluid-membrane model can be compared.

1.3 Literature overview of discussed aspects

With regard to the design and operation of the prestrained-membrane pump, the following five different aspects are discussed in the present work:

- I Propulsion by a flapping foil, optimum motion
- II Chordwise flexibility, prescribed travelling wave
- III Effect of channel walls
- IV Effect of fluid viscosity

V Fluid-structure interaction of membrane and flow

We refer to the review article on aerohydrodynamics of flapping-wing propulsors by Rozhdestvensky & Ryzhov [80] regarding the items I, II, and in part III (flying in ground effect).

1.3.1 Flapping foil in optimal motion

Flapping wing motion has been extensively studied in the literature. Comprehensive work has been done in the context of wing flutter in the 1930ies. A model for circulatory potential flow around a flapping foil in harmonic motion that takes into account the vortex wake, has been developed by Theodorsen [104]. A comprehensible physical interpretation of this model is given in [115]. The vortex wake significantly influences the lift force on the foil, even at a moderate flapping frequency.

Theodorsen’s model has been used by Garrick [26] to calculate the thrust developed by the airfoil, the power required to create the airfoil motion and the propulsive efficiency. Efficiency is the portion of power exerted that goes into providing thrust. While by the vortex street, energy is wasted into the wake, its presence is necessary if any thrust is to be produced at all.

The optimum propulsion of a two-dimensional flat plate wing in time-harmonic motion in parallel flow is discussed by [53] and [119] using Theodorsen’s linear model. Both authors come to the conclusion that the efficiency can be greatly improved when both plunging and pitching modes are admitted. Lighthill introduced the “proportional feathering parameter“ [54] that identifies the degree to which the foil pitch angle coincides with the slope of the trajectory the foil traces out as it propels through the fluid at rest. Competing tendencies of increasing efficiency and decreasing thrust exist as feathering is increased. [53] pointed out that the shape of the rounded leading-edge is of particular importance, since much of the thrust from wing theory is harvested from the fluid flow around the leading edge. In the comprehensive study [119], the optimum shape problem is stated such that the energy loss is minimized under the condition of a prescribed thrust coefficient (required to overcome viscous drag). One has to take into account, though, that with linear theory the thrust coefficient scales with the square of the flapping amplitude. As a result, the optimum shape problem for prescribed thrust predicts the amplitude to be infinite. This problem is circumvented in [119] by introducing the “proportional-loading parameter“, defined as the thrust coefficient divided by the square of the plunging amplitude. An equivalent approach is obtained when for prescribed mean thrust a constraint is put on the magnitude of the amplitude of the motion. We refer to [96] for a proof about the existence of the optimum solution for the simple case of a rigid profile in pure plunging motion.

At larger flapping amplitudes, the linear model ceases to be valid. Somewhat surprisingly, the model predicts the thrust force reasonably well for a foil flapping at large amplitude and low frequency. A comparison to large-amplitude potential flow theory [37] and to Navier–Stokes computations [108] shows that the agreement is good when the product of amplitude and frequency is roughly below a constant. Note that the product of amplitude and frequency is approximately equal to the Strouhal number. [107] emphasized that it is crucial to stay within a certain range of Strouhal numbers in order to obtain optimal thrust. Extensive literature exists regarding the thrust of a foil in pure plunging motion. Generally the thrust increases with the plunging amplitude. Stall occurs at a certain amplitude, but the thrust continues to grow with amplitude in the stalled regime, while the efficiency becomes very low.

Considerably less literature exists about maximizing the efficiency. In [7], both thrust and efficiency are reported for experiments of a foil in combined plunging and pitching motion. From that, it is clear that thrust and efficiency are competing trends, i. e. thrust is low at high efficiency. It would be certainly of interest, though, to determine a two-state optimum (or Pareto frontier) of thrust and efficiency. This idea has not achieved much attention in the literature, maybe on account of the large parameter space. A relevant study is [109], where a numerical optimization (at fixed reduced frequency) from Navier–Stokes results (computed in parallel) is pursued. In [78] experimental results (at fixed plunging amplitude) are plotted in the form of propulsive efficiency against the thrust coefficient. It can be concluded from these numerical and experimental results that the Pareto optimum is obtained when the ratio of flapping amplitude to chord is of order one, as it is observed in fish that swim in thunniform mode, see Sec. 1.2.3.

In the present work, Theodorsen’s linear model for small-amplitude motion is employed to find the optimal motion. In contrast to [119], the flapping amplitude in the course of motion over the period is constraint such that the optimum motion touches its boundary one time per period. To the author’s knowledge, an analytical relation between efficiency and thrust is given for the first time.

1.3.2 Chordwise flexibility

It has been proposed quite a long time ago that chordwise flexibility can enhance the propulsive efficiency. Wu [118] studied time-harmonic motion with arbitrary shape along the chord by making use of the approach outlined in [86], and provided a general formulation for time-averaged thrust, power and efficiency. In particular, progressive waves are studied and it is pointed out that it is advantageous from the viewpoint of efficiency to have the waves propagating downstream. A special case is the downstream propagating wave with uniform wave amplitude. This rather simple shape of a travelling wavy surface is examined in detail in the present work, with the aim to offer a reference for the prestrained-membrane solutions and to simplify the study on the effect of fluid viscosity. It is noted by Wu [118] that when the wave velocity becomes equal to the free-stream velocity, the wave form is frozen with respect to the fluid and travels along a sinusoidal path fixed in space. Thus, no circulation is created in this case for inviscid flow.

In Wu [119], the optimum shape of a flexible plate is analysed for the general case of infinite degrees of freedom. It turns out that the exact optimum shape is not unique since it can be determined only to a certain extent. Nevertheless, the efficiency can be further improved from the rigid-plate value. Later on, Sparenberg et. al. [96] noted that no optimum thrust producing swimming motion exists when only a constraint is put on the magnitude of the amplitude of the motion.

Katz & Weihs [38] employed unsteady potential flow theory to study the effect of flexibility on the aerodynamic characteristics of an airfoil that carries out a prescribed large-deflection motion at the leading edge and allows passive chordwise bending. Propulsive efficiency is improved when the airfoil is more flexible, but the loss in the thrust coefficient is considerable. Thus, the results appear to fall short to the premise of the optimum shape problem in [119] to maximize efficiency at a fixed thrust. Astonishingly, experimental evidence that chordwise flexibility is advantageous with regard to the efficiency-thrust Pareto optimum is given only recently in [78]. A comparison

of the measured results for a rigid and a flexible foil in combined pitching and plunging motion shows that efficiency improves by up to 36% with a small decrease in thrust.

Finally, the effect of finite span shall be mentioned. In [15], a small-amplitude travelling wave on a plate of finite span is considered. Unsteady three-dimensional potential flow is assumed and solved numerically. Remarkably, it is found that the undulatory motion can reduce three-dimensional effects in the flow and that the efficiency is only very weakly dependent on the aspect ratio at values of 0.5, 1, and 8.

1.3.3 Effect of channel walls

The flapping motion in a channel is similar to the flapping motion subject to the ground effect in the vicinity of one wall. The ground effect is an increase of the lift-to-drag ratio of a lifting system at small relative distances from the underlying ground. The method of images [36] is usually used to account for the boundary condition at the wall. Asymptotic theory can usually be employed when the dimensionless ground clearance is large, see [80]. Basically, there is no difference between a stationary and an oscillating foil with regard to the ground effect. However, in the latter case the flapping frequency appears as an additional parameter. In [34], the unsteady aerodynamic forces are addressed that act on an oscillating wing section in weak ground effect. A new asymptotic solution is obtained where the ratio of flapping frequency and inverse dimensionless distance is introduced as new independent parameter. [65] used URANS to study the unsteady motion of a downward cambered heaving airfoil in ground effect. In the stationary case, the flow stalls at a dimensionless clearance below 0.3. Nevertheless, the downforce further increases and reaches its maximum at a relative clearance of 0.17. For the heaving airfoil, however, at higher reduced frequencies inviscid effects overcome the large separation and the motion becomes stable as the behaviour of the flow is mainly inviscid.

The confined flow in the channel can be treated by a repeated application of the mirror reflections. Then, the complex potential of a source in midway of the channel walls can be given explicitly, cf. [36]. [29] used the Green's function for a point source at arbitrary position in the infinite channel and applied the fast multipole method that makes use of the fact that the velocity field induced by the point source decays exponentially along the length of the channel. As for the ground effect, wall correction formulae can be used to account for distant wind tunnel walls [36]. For a thin airfoil between wind tunnel walls, an integral equation occurs that can be solved approximately with the method of Keldysh & Lavrentiev [39] by expanding the kernel in a series of powers of the inverse dimensionless wall distance and invert the resulting integral expressions consecutively with Söhngen's inversion formula, see [36].

In the present work, we attempt to find a closed-form expression for the circulation caused by a slender body in inviscid flow being confined to a channel of arbitrary width. To the author's best knowledge, this solution has not been reported in the literature. A possible application can be the use as wall influence formula for measurements in wind tunnels or water tanks for oscillating bodies that operate in the field in unbounded freestream (like wind turbines), being more general than the usual correction formulae that account only for small perturbations from the walls. Within the theory of singular integral equations the result can be seen as a generalization of Söhngen's result to a more general kernel.

1.3.4 Drag reduction

The travelling wave-like wall deformation has been discussed in the context of drag reduction. [32] emphasized that applying travelling waves of wall deformation in the viscosity dominated regime (peristalsis) should be considered as pumping rather than drag reduction. In [32] drag reduction is considered as an action for a given pumping such that the total power is reduced to drive the same flux. A robotic swimmer/pump based on the downstream propagating wave mechanism operating at a low Reynolds number is studied in [88]. Barrett et. al. [9] presented experimental measurements of drag reduction for a fish-shaped robot in that it was demonstrated that the power required in the self-propulsive travelling wave motion is less than the power needed to tow the body straight and rigid at the same speed. Shen et. al. [91] used direct numerical simulation to study the turbulent flow over a smooth wavy wall undergoing transverse motion in the form of a streamwise travelling wave to gain physical insight to the understanding of fish-like swimming mechanisms in terms of drag reduction. Similarly, the propulsive performance of a fish-like travelling wavy wall was discussed by Lu & Yin [57] for the laminar case.

1.3.5 Fluid-structure interaction

The flow over a compliant membrane is a complex problem where the interaction between fluid and membrane determines the nature of the aerodynamic characteristics of the membrane. The investigation of this two-way coupled fluid-structure interaction presents a significant challenge to both experimental and numerical fluid dynamicists. The membrane is displaced and bended when a fluid load is applied. On the other hand, the membrane represents a kinematic boundary to the flow and as its shape changes, the flow around the membrane changes too, altering the forces on the membrane that again changes the displacements. As the inertial forces are dominant in the pump, the theoretical approach is based on the theory of inviscid incompressible flow around a slender profile [99].

The present problem has similarity to the flow over a flapping flag. [61] and [5] discussed the instability of a flapping flag clamped at the leading edge. The effect of the rigidity from a passively bending slender profile is discussed in the literature for a bending airfoil in large-amplitude prescribed leading edge motion [38], a flapping appendage with small-amplitude pitching motion at the leading edge [4], and heaving motion at the leading edge [60]. In all the cited studies the fluid is considered as incompressible and inviscid and the flow is solved with unsteady two-dimensional potential theory. In [98] the potential flow is employed in a CFD solver as part of a monolithic coupling strategy to obtain in every timestep a good prediction for the deformation of a membrane.

The membrane pump differs in two aspects to a flapping flag: The membrane is clamped at the sidewalls, resulting in a restoring force directed towards the undisturbed position. The effect from the channel walls needs to be considered.

1.4 Organisation of work

In the following chapters of this thesis, the above outlined aspects are discussed with regard to the modeling approach, the analytical and numerical implementation and the obtained results.

The subsequent section contains the formulation of the problem. It gives an overview of the used models and parameters and the dimensionless formulation of the problem. Chapter two starts with an introduction of the theory of unsteady potential flow over a flapping surface in oncoming flow. Based on that theory, afterwards the confining effect of channel walls on the bound circulation is discussed. Influence coefficients are given in closed form. Furthermore, a new panel method is delineated that accounts for the presence of the channel walls. The theory constituted in chapter two is applied in chapter three to find the optimum propulsive motion of a rigid flapping foil in oncoming flow. A novel relation between propulsive efficiency and thrust is given. The result is compared with a chordwise flexible flapping foil and with a single downstream propagating wave of uniform amplitude. The thrust generated by the downstream travelling wave is then discussed in the limit of large wave numbers at a fixed phase speed. The solution is compared to an infinitely extended wavy surface with periodic streamwise boundary conditions. For the periodic setting, fluid viscosity is taken into account. The results for pressure and velocity are compared to inviscid flow and turbulent flow. Furthermore, the dependence of the wall forces on the phase speed is discussed. The 4th chapter deals with the fluid structure interaction between the fluid and the membrane. Results for optimum design and operation are presented for an excited membrane in unbounded potential flow. The double channel membrane pump is studied at the end of the chapter. A comparison is given between inviscid flow in unbounded domain, potential flow in the channel using the panel code, and the channel flow solution obtained with a commercial CFD package. Summary and conclusions are given in chapter five.

1.5 Problem formulation and model description

1.5.1 Valveless membrane pump

We investigate the working principle of a novel valveless membrane pump that has been invented by Wilhelm Zackl ². Zackl has experimentally tested various designs of the pump. The results of his work are documented in [120]. There exist different variants of the valveless membrane pump. A sketch of a typical design is shown in Fig. 1.1.

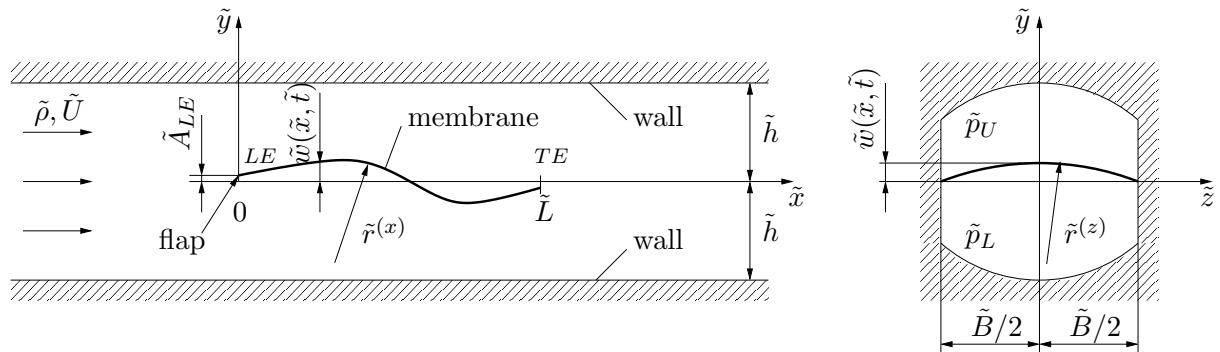


Figure 1.1: Sketch of the valveless membrane pump

²U.S. Patent No. 7.101159 B2 9/2006, EP 1438514 B1, W. Zackl

A membrane of flexible material is placed into a rigid channel or tube, dividing it into an upper and lower portion. Clamping at the sidewalls of the channel allows to prestretch the membrane in longitudinal and lateral direction. The channel of the pump is filled with a liquid working medium. The excitation of the membrane is achieved with a small, rigid flap, attached to the membrane's leading edge LE . In a different pump design, upstream the membrane (at the hinge of the flap), a rigid bridge wall is attached that divides the channel in a further section into an upper and lower portion. The unsteady motion of flap and membrane leads to a mean flow of the working medium (from left to right) with vortices leaving the membrane at the trailing edge TE .

1.5.2 Models and methods: overview

A fluid of constant density $\tilde{\rho}$ is assumed. The problem is considered in the \tilde{x} - \tilde{y} -plane as two-dimensional, Fig. 1.1. Time-harmonic solutions are discussed. Potential flow theory and small deflections are assumed throughout the work, except for Sec. 3.5 and Sec. 4.2 where the Navier–Stokes equations are solved to discuss the effect of viscosity. The speed of the oncoming flow is assumed as given Fig. 1.1, except for the case of a pitching plate pump in Sec. 4.2.2, where the size of the mean flow is part of the solution. From the viewpoint of the fluid, the propulsive body is considered as zero-thickness streamlined wing represented by its camber line. To describe the deflection of the body, either a prescribed motion or a model for the motion of the membrane, coupled to the fluid via the pressure difference across the membrane, are chosen. At first the flow in unbounded domain is considered. Then the effect from the channel walls is taken into account, see the sections 2.2, 2.3 and 4.2.

1.5.3 Potential theory for unsteady flow

If one assumes an ideal fluid (inviscid, constant density $\tilde{\rho}$) and the velocity vector field \vec{v} to be initially irrotational

$$\nabla \times \vec{v} = \vec{0} \quad (1.1)$$

one can introduce a velocity potential $\tilde{\Phi}$ such that

$$\vec{v} = \nabla \tilde{\Phi}. \quad (1.2)$$

Eqs. (1.1, 1.2) hold also for unsteady flow since for an ideal fluid the flow remains irrotational for all times. The conservation of mass states that

$$\tilde{u}_{\tilde{x}} + \tilde{v}_{\tilde{y}} = 0. \quad (1.3)$$

Here \tilde{u} and \tilde{v} denote the respective horizontal and vertical components of the velocity vector \vec{v} and the subscript denotes a partial derivative. From that, together with Eq. (1.2), follows the Laplace equation

$$\tilde{\Phi}_{\tilde{x}\tilde{x}} + \tilde{\Phi}_{\tilde{y}\tilde{y}} = 0. \quad (1.4)$$

The equation is the same as for steady flow as the time appears only as a parameter. The pressure can be determined from the unsteady Bernoulli equation

$$\tilde{\Phi}_{\tilde{t}} + \frac{\tilde{\Phi}_{\tilde{x}}^2}{2} + \frac{\tilde{\Phi}_{\tilde{y}}^2}{2} = -\tilde{p}/\tilde{\rho} + \tilde{C}(\tilde{t}) \quad (1.5)$$

where $\tilde{C}(\tilde{t})$ is an arbitrary function of time \tilde{t} determined from the boundary conditions. Eqs. (1.4), (1.5) are used for external flow and for the channel flow.

1.5.4 Asymptotic approach for small deflections

A parallel oncoming flow with uniform profile \tilde{U} is assumed, Fig. 1.1. The assumption of small deflections of the body

$$\tilde{w}(\tilde{x}, \tilde{t}) = \epsilon \tilde{w}_1(\tilde{x}, \tilde{t}) \quad (1.6)$$

with $\epsilon \ll 1$, where the index 1 denotes the first term in the expansion for small ϵ , allows the perturbation ansatz of small-disturbance flow

$$\tilde{\Phi}(\tilde{x}, \tilde{y}, \tilde{t}) = \tilde{U} \tilde{x} + \epsilon \tilde{U} \tilde{L} \varphi(\tilde{x}, \tilde{y}, \tilde{t}) + \dots \quad (1.7)$$

where the perturbation potential φ is scaled with the product of the oncoming flow speed and the chord for convenience.

1.5.5 Boundary conditions

Assuming that the body has negligible thickness, the kinematic boundary condition on the body surface $\tilde{y} = \tilde{w}(\tilde{x}, \tilde{t})$, $0 \leq \tilde{x} \leq \tilde{L}$ reads

$$\tilde{v}(\tilde{x}, \tilde{w}, \tilde{t}) = \tilde{w}_{\tilde{t}} + \tilde{u} \tilde{w}_{\tilde{x}} \quad (1.8)$$

where \tilde{w} is the deflection of the body from the channel axis. For small deflections Eq. (1.6), the linearized version

$$\tilde{v}_1(\tilde{x}, 0, \tilde{t}) = \tilde{w}_{1,\tilde{t}} + \tilde{U} \tilde{w}_{1,\tilde{x}} \quad (1.9)$$

can be used. The kinematic boundary conditions at the channel walls are

$$\tilde{v}(\tilde{x}, \pm \tilde{h}, \tilde{t}) = 0 \quad \text{for} \quad -\infty \leq \tilde{x} \leq +\infty. \quad (1.10)$$

We note that in Sec. 3.4.3, the assumption of small deflections is dismissed to discuss the effect of geometric nonlinearity. Then, Eq. (1.8) is used instead of Eq. (1.9).

1.5.6 Viscous flow

In Sec. 3.5, viscous flow over a wavy surface is discussed. The assumption of irrotational flow Eq. (1.1) is superseded by the stationary Navier–Stokes equations (cf. [21]) for a fluid with constant density $\tilde{\rho}$

$$(\tilde{u}^2)_{\tilde{x}} + (\tilde{u}\tilde{v})_{\tilde{y}} + \tilde{p}_{\tilde{x}}/\tilde{\rho} = \tilde{\nu} (\tilde{u}_{\tilde{x}\tilde{x}} + \tilde{u}_{\tilde{y}\tilde{y}}), \quad (1.11a)$$

$$(\tilde{u}\tilde{v})_{\tilde{x}} + (\tilde{v}^2)_{\tilde{y}} + \tilde{p}_{\tilde{y}}/\tilde{\rho} = \tilde{\nu} (\tilde{v}_{\tilde{x}\tilde{x}} + \tilde{v}_{\tilde{y}\tilde{y}}), \quad (1.11b)$$

that are used together with the conservation of mass Eq. (1.3). In Eq. (1.11) $\tilde{\nu}$ denotes the constant kinematic viscosity of the fluid. The no-slip boundary condition at the wavy wall

$$\tilde{u}(\tilde{x}, \tilde{w}, \tilde{t}) = 0 \quad (1.12)$$

is required in addition to Eq. (1.8).

1.5.7 Membrane equation

Using Newton's Law in \tilde{y} -direction gives the following equation for the prestretched membrane

$$-(\tilde{p}_U - \tilde{p}_L) = \frac{\tilde{\sigma}^{(x)}}{\tilde{r}^{(x)}} + \frac{\tilde{\sigma}^{(z)}}{\tilde{r}^{(z)}} + \tilde{D}_M \tilde{\rho}_M \frac{\partial^2 \tilde{w}}{\partial \tilde{t}^2}. \quad (1.13)$$

Here \tilde{p}_U and \tilde{p}_L are the pressure at the upper and lower surface of the membrane, respectively, see Fig. 1.1. $\tilde{\sigma}^{(x)}$ and $\tilde{\sigma}^{(z)}$ denote the membrane tension in main flow direction and lateral direction, respectively, and $\tilde{r}^{(x)}$ and $\tilde{r}^{(z)}$ denote the respective radii of membrane curvature. The last term in Eq. (1.13) accounts for membrane inertia. Internal bending moments are neglected. In the limit of small deflections, the membrane curvature in the \tilde{x} - \tilde{y} -plane (in the symmetry plane $\tilde{z}=0$) is approximately

$$\frac{1}{\tilde{r}^{(x)}} \approx -\frac{\partial^2 \tilde{w}}{\partial \tilde{x}^2}. \quad (1.14)$$

With the depth of the channel \tilde{B} , the curvature in lateral direction is (see Fig. 1.1, right)

$$\tilde{r}^{(z)^2} = \left(\frac{\tilde{B}}{2}\right)^2 + (\tilde{r}^{(z)} - \tilde{w})^2, \quad (1.15)$$

and for $\tilde{w} \ll \tilde{B}/2$ the curvature in the cross-section (\tilde{y} - \tilde{z} -plane) can be approximated by

$$\frac{1}{\tilde{r}^{(z)}} \approx \frac{8\tilde{w}}{\tilde{B}^2}. \quad (1.16)$$

With the pressure difference across the body expressed as $\Delta\tilde{p} = \tilde{p}_U - \tilde{p}_L$, Eq. (1.13) reads

$$\tilde{\alpha}_M \frac{\partial^2 \tilde{w}}{\partial \tilde{x}^2} - \tilde{\beta}_M \tilde{w} = \Delta\tilde{p} + \tilde{D}_M \tilde{\rho}_M \frac{\partial^2 \tilde{w}}{\partial \tilde{t}^2}, \quad (1.17)$$

with $\tilde{\alpha}_M = \tilde{\sigma}^{(x)}$, $\tilde{\beta}_M = 8\tilde{\sigma}^{(z)}/\tilde{B}^2$. The boundary conditions for the membrane equation are

$$\tilde{w}_{LE} = \tilde{A}_{LE} \sin(\tilde{\omega}\tilde{t}), \quad \left(\frac{\partial \tilde{w}}{\partial \tilde{x}}\right)_{TE} = 0, \quad (1.18)$$

where LE and TE denote the leading edge and trailing edge, respectively, and $\tilde{\omega}$ is the excitation angular frequency. Thus, a time-harmonic motion is expected to evolve and only time-harmonic solutions are considered.

1.5.8 Design- and operating parameters

Tab. 1.1 lists the range of parameters for the pump investigated by Zackl [120].

Parameter	Range of values	Units
Length of membrane \tilde{L}	0.20	m
Semi height of channel \tilde{h}	0.018	m
Depth of channel \tilde{B}	0.07	m
Hydraulic diameter of half-channel \tilde{d}_h	0.0211	m
Cross section area of half-channel \tilde{A}_h	8.056×10^{-4}	m ²
Density of fluid $\tilde{\rho}$	1000	kg/m ³
Kinematic viscosity of fluid $\tilde{\nu}$	1.15×10^{-6}	m ² /s
Membrane tension in main flow direction $\tilde{\sigma}^{(x)}$	1240-9000	N/m
Membrane tension in lateral direction $\tilde{\sigma}^{(z)}$	740-5000	N/m
Density of membrane $\tilde{\rho}_M$	1260	kg/m ³
Thickness of membrane \tilde{D}_M	0.002-0.004	m
Mean flow velocity \tilde{U}	0.5-4.2	m/s
Amplitude of excitation \tilde{A}_{LE}	0.018	m
Excitation angular frequency $\tilde{\omega}$	55-315	rad/s

Table 1.1: Range of operating parameters, selected from [120] (design B/B2)

Typical values for the membrane tension in flow direction and lateral direction for design B (cf. [121]) are $\tilde{\sigma}^{(x)} = 3120$ N/m and $\tilde{\sigma}^{(z)} = 1620$ N/m. In the design by Zackl the amplitude of excitation \tilde{A}_{LE} equals the semi height of the channel \tilde{h} . This is possible because in Zackl's design the channel is slightly wider at the LE .

1.5.9 Dimensionless formulation

Dimensionless numbers

The problem of an oscillating section in a channel has four fundamental length scales from which three independent dimensionless ratios can be constructed. One is the ratio ϵ of the transversal displacement to the chord, the other is the ratio h of the semi-channel width to the chord, and the third is the distance the fluid travels during one oscillation period of the body, expressed by the reduced frequency.

It is very important to emphasize that different dimensionless formulations are used in each section, depending on the individual problem. Before these differences are discussed, the scaling used consistently throughout the work shall be outlined:

The oncoming flow speed is used as reference speed \tilde{U} and for the reference pressure $\tilde{\rho}\tilde{U}^2$

$$u = \frac{\tilde{u}}{\tilde{U}}, \quad v = \frac{\tilde{v}}{\tilde{U}}, \quad p = \frac{\tilde{p}}{\tilde{\rho}\tilde{U}^2}.$$

The membrane parameters for streamwise strain, lateral strain and inertia in Eq. (1.13) are

given in dimensionless form as

$$\alpha_M = \frac{2\tilde{\sigma}^{(x)}}{\tilde{\rho}\tilde{U}^2\tilde{L}}, \quad \beta_M = \frac{4\tilde{\sigma}^{(z)}\tilde{L}}{\tilde{B}^2\tilde{\rho}\tilde{U}^2}, \quad \mu_M = \frac{1}{2} \frac{\tilde{\rho}_M}{\tilde{\rho}} \left(\frac{\tilde{\omega}\tilde{L}}{\tilde{U}} \right)^2 \frac{\tilde{D}_M}{\tilde{L}}. \quad (1.19)$$

The CFD results in Sec. 4.2.2 are presented in dimensional form. Regarding the dimensionless formulations, the following three differences occur with respect to the reference length scale and the reference time scale:

- I Time-periodic motion of a body of finite length in unbounded domain. The semi-chord $\tilde{L}/2$ is used as reference length and the inverse of the angular frequency $\tilde{\omega}$ to scale time. The dimensionless coordinates, time, and reduced frequency are then

$$x = \frac{\tilde{x}}{\tilde{L}/2}, \quad y = \frac{\tilde{y}}{\tilde{L}/2}, \quad \tau = \tilde{\omega}\tilde{t}, \quad \sigma = \frac{\tilde{\omega}\tilde{L}}{2\tilde{U}}. \quad (1.20)$$

This scaling is used in the sections 3.1, 3.3, 3.4, and 4.1. In particular for the downstream travelling wave of prescribed shape in the sections 3.3 and 3.4, the downstream propagating phase speed \tilde{c} is used in the dimensionless phase speed and wavenumber as

$$c = \frac{\tilde{c}}{\tilde{U}}, \quad k = \frac{\tilde{\omega}\tilde{L}}{2\tilde{c}}. \quad (1.21)$$

- II General or time-periodic motion of a body of finite length in a channel. The chord \tilde{L} is used as reference length, and either \tilde{L}/\tilde{U} (general) or $1/\tilde{\omega}$ (time-periodic) is used as timescale. The Reynolds number is built with the hydraulic diameter \tilde{d}_h . The dimensionless coordinates, channel width, times, reduced frequency and Reynolds number are

$$x = \frac{\tilde{x}}{\tilde{L}}, \quad y = \frac{\tilde{y}}{\tilde{L}}, \quad h = \frac{\tilde{h}}{\tilde{L}}, \quad t = \frac{\tilde{t}\tilde{U}}{\tilde{L}}, \quad \tau = \tilde{\omega}\tilde{t}, \quad \Omega = \frac{\tilde{\omega}\tilde{L}}{\tilde{U}}, \quad \text{Re}_h = \frac{\tilde{U}\tilde{d}_h}{\tilde{\nu}}. \quad (1.22)$$

This scaling is used in the sections 2.2 and 2.3.

- III Time-periodic motion of a travelling wave of prescribed shape with amplitude \tilde{A} and infinite streamwise extension. The wavelength $\tilde{\lambda}$ is used as reference length. The dimensionless coordinates, wave steepness, phase speed, and Reynolds number are

$$x = \frac{\tilde{x}}{\tilde{\lambda}}, \quad y = \frac{\tilde{y}}{\tilde{\lambda}}, \quad A_\lambda = \frac{\tilde{A}}{\tilde{\lambda}}, \quad c = \frac{\tilde{c}}{\tilde{U}}, \quad \text{Re}_\lambda = \frac{\tilde{U}\tilde{\lambda}}{\tilde{\nu}}. \quad (1.23)$$

This scaling is used in Sec. 3.4.3 and Sec. 3.5.

In Sec. 2.1, the representation by Chebyshev polynomials I as well as the representation by vortices II are outlined. With the given scaling, e. g. from Eq. (1.20), the equations for the motion with small deflections Eq. (1.6), the boundary conditions Eqs. (1.9, 1.10) and the membrane equation Eq. (1.13), respectively, are formulated dimensionless as:

Motion

$$w(x, t) = \epsilon w_1(x, t). \quad (1.24)$$

Boundary conditions

$$v_1(x, 0, t) = w_{1,t} + w_{1,x} \quad \text{for } x_{LE} \leq x \leq x_{TE}, \quad (1.25)$$

$$v_1(x, \pm h, t) = 0 \quad \text{for } -\infty \leq x \leq +\infty. \quad (1.26)$$

Membrane equation

$$-\mu_M w_{1,\tau\tau} + \alpha_M w_{1,xx} - \beta_M w_1 = \Delta p_1 \quad \text{for } x_{LE} \leq x \leq x_{TE}. \quad (1.27)$$

1.5.10 Measurements by W. Zackl

The best results that have been achieved in the experiments (cf. [120]) in terms of flow velocity, hydraulic power and pressure gain are shown in Tab. 1.2.

Outcome	$\tilde{\omega}$ in rad/s	\tilde{U} in m/s	Pressure gain in Pa	Re_h
max. flow velocity	188	0.5	8600	77000
max. hydraulic power	251	2.4	30000	43000
max. pressure gain	314	4.2	57000	8500

Table 1.2: Results from the experiments in [120] (design B/B2).

The Reynolds number is calculated from Eq. (1.22) using the data given in Tab. 1.1. For the case of max. hydraulic power in Tab. 1.2 the following values for the dimensionless parameters reduced frequency Eq. (1.20), leading-edge amplitude, and membrane parameters Eq. (1.19) are obtained

$$\sigma \approx 10.7, \quad \tilde{A}_{LE}/\tilde{L} \approx 0.09, \quad \alpha_M \approx 5.7, \quad \beta_M \approx 48, \quad \mu_M \approx 4.3.$$

Chapter 2

2D-Potential Flow Theory

2.1 Unbounded domain

The unsteady potential flow theory has been used in the past to study the unsteady motion of a thin airfoil [36], fluid-structure interaction problems in aeroelasticity [11], as well as swimming of slender fish Sec. 1.2.3, and the flapping flag problem Sec. 1.3.5. Theodorsen [104] was the first to present a complete mathematical description to the problem of wing flutter by employing unsteady potential flow theory. He used a sheet of 2-dim. sources and sinks to describe the non-circulatory part of the flow in an unbounded domain [11]. We note that the method is somewhat different to the approach used by Schwarz [86] who applied a distribution of vortices along the body and the wake, see [11]. In Theodorsen's model, the wake of shed counter-vortices continually moves away from the airfoil at free-stream velocity.

Sections 2.1.1–2.1.6 present the mathematical approach used by Schwarz [86]. However, when a flexible structure is involved, it is more convenient to use a formulation in mapped coordinates represented by Chebyshev polynomials. This method has been pursued by Küssner [45] and will be outlined in Sec. 2.1.7 following the notation by Wu [118].

2.1.1 Pressure on the body

Assuming small deflections as defined in Sec. 1.5.4, Eq. (1.5) can be linearized and the dimensionless perturbation pressure at the body can be expressed as

$$p_1 = -(\varphi_t + \varphi_x), \quad (2.1)$$

where φ denotes the perturbation potential from Eq. (1.7). For a given motion, φ needs to be chosen such that the boundary condition Eq. (1.25) is fulfilled. In unbounded domain, two methods are common. These methods are the distribution of vortices (introduced originally by L. Prandtl in spanwise direction) and the Chebyshev expansion.

2.1.2 Vortex distribution

A single vortex of strength Γ placed on the horizontal axis (at $y = 0$) generates the complex flow potential

$$F(z) = -i \frac{\Gamma}{2\pi} \ln[z - \xi] \quad (2.2)$$

(cf. [36], Eq. (6.17)). Following Schwarz [86], a chordwise distribution of vortices $d\Gamma(\xi, t) = \gamma(\xi, t)d\xi$ is applied at the undisturbed position of the body, Fig. 2.1. A relation between the derivative of the potential on the upper and lower side of the body surface, respectively, and the distribution of vortices can be obtained with the help of the Sokhotski–Plemelj theorem (cf. [68], p. 42)

$$\varphi_x(x, 0^\pm, t) = \mp \frac{\gamma(x, t)}{2}. \quad (2.3)$$

The pressure difference across the body can then be derived from Eq. (2.1)

$$\Delta p_1(x, t) = \left(\int_0^x \gamma_t(\xi, t) d\xi + \gamma(x, t) \right). \quad (2.4)$$

2.1.3 Kutta condition

We require the Kutta condition at the trailing edge $x = 1$

$$\Delta p_{TE} = 0. \quad (2.5)$$

The condition of vanishing pressure across the trailing edge is a generalization of the classical Kutta condition for the steady case. The limits of validity of the unsteady Kutta condition are discussed, for instance in Katz & Plotkin [36], Sec. 13.11. A discussion of the limits of the model for a flapping foil is given later in Sec. 3.1.6. The circulation about the body is obtained by integration of the vorticity along the chord as

$$\Gamma(t) = \int_0^1 \gamma(x, t) dx. \quad (2.6)$$

Eq. (2.5) then reads with Eq. (2.4)

$$\Gamma_t(t) + \gamma(1, t) = 0 \quad (2.7)$$

Thus, the vorticity shed from the trailing edge has a strength equal and opposite to the temporal change of the bound circulation.

2.1.4 Wake vortices

In contrast to the steady case, in the unsteady case the vortex strength at the trailing edge $\gamma(1, t)$ cannot vanish. A comprehensible physical explanation of the mechanism of production of wake vortices is given by Von Kármán & Sears [115]. When a starting airplane produces body circulation in order to create a lifting force, it leaves behind a counter-rotating circulation at the runway, Fig. 2.1 left. If the motion of the body is smooth in time, a small starting vortex will

emerge from the trailing edge at any instant. The evolving sequence of discrete starting vortices may then be smeared and the distribution of vortices on the body can thus be extended into the wake, Fig. 2.1 right.

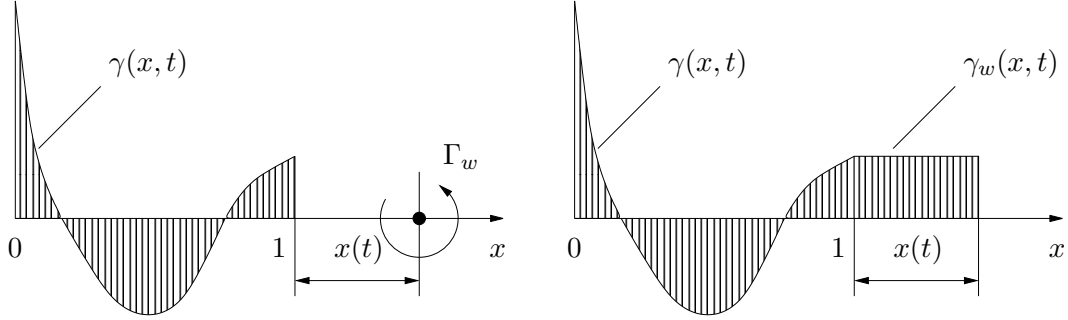


Figure 2.1: Vortex shedding from the trailing edge: left: starting vortex; right: continuous description for smooth motion.

The unsteady Kutta condition is related to the principle of conservation of total circulation. Applying Kelvin's theorem $D\Gamma_T/Dt = 0$ (cf. [36]) to the total circulation $\Gamma_T = \Gamma + \Gamma_w$, one obtains

$$\frac{d}{dt} \left(\int_0^1 \gamma(x, t) dx + \frac{d\Gamma_w}{dx} x(t) \right) = 0 \quad (2.8)$$

or with the continuous distribution of wake vortices $\frac{d\Gamma_w}{dx} = \gamma_w(1, t)$ and Eq. (2.6)

$$\Gamma_t(t) + \gamma_w(1, t) \frac{dx(t)}{dt} = 0. \quad (2.9)$$

A comparison to Eq. (2.7) shows that the condition of vanishing pressure across the trailing edge corresponds to $dx(t)/dt = U = 1$ at the trailing edge and a continuous continuation of the vortex distribution $\gamma(1, t) = \gamma_w(1, t)$. As a consequence, we assume that in the wake the fluid moves at approximately the free-stream speed and prescribe the transport of vortices in the wake (omitting the subscript w in the notation) according to

$$\gamma(x, t) = \gamma(1, t - (x - 1)) \quad \text{for } x \geq 1. \quad (2.10)$$

We note that a generalization of the vortex method to channel flow is presented in Sec. 2.2.

2.1.5 Singular integral equation

The derivatives of the potential are related to the distribution of vortices by

$$\varphi_x(x, 0^\pm, t) = \mp \frac{\gamma(x, t)}{2}, \quad (2.3 \text{ revisited})$$

$$\varphi_y(x, 0^\pm, t) = v_1(x, 0, t) = \frac{1}{2\pi} \left(\int_0^1 \frac{\gamma(\xi, t)}{x - \xi} d\xi + \int_1^\infty \frac{\gamma(\xi, t)}{x - \xi} d\xi \right). \quad (2.11)$$

Here f indicates that the Cauchy principal value has to be taken. This set of equations plays an important role in aerodynamics, see for instance Bisplinghoff et. al. [11]. The explicit dependence on the time t is omitted in the following notation. Eq. (2.11) is a singular integral equation with a Cauchy kernel (cf. [68]) that we want to solve together with the kinematic boundary condition Eq. (1.25) at the body $0 \leq x \leq 1$. The task is to invert Eq. (2.11) such that the distribution of vortices on the body $\gamma(x)$ can be expressed explicitly for a given $v_1(x, 0)$. This approach has been pursued by Schwarz [86] and it is outlined in detail in [11]. In the procedure the following steps are applied: From Eq. (2.10), the distribution of vorticity in the wake is given by the strength of the vorticity at the trailing edge. Schwarz assumes the strength of the wake vorticity as interim given and applies an inversion formula found by Söhngen [95] to Eq. (2.11). From the inversion, a free time-dependent function, physically related to the strength of circulation around the body, is determined such that the vorticity at the trailing edge is constraint. Then, the inversion yields

$$\gamma(x) = \frac{1}{\pi} \sqrt{\frac{1-x}{x}} \left(2 \int_0^1 \sqrt{\frac{\xi}{1-\xi}} \frac{v_1(\xi, 0)}{\xi-x} d\xi + \int_1^\infty \sqrt{\frac{\xi}{\xi-1}} \frac{\gamma(\xi)}{\xi-x} d\xi \right). \quad (2.12)$$

The inversion of the Cauchy integral for the most general case (over the union of smooth arcs) is given in [68]. The circulation about the body, Eq. (2.6), is obtained by exchanging the order of integration

$$\Gamma = 2 \int_0^1 v_1(\xi, 0) \sqrt{\frac{\xi}{1-\xi}} d\xi + \int_1^\infty \gamma(\xi) \left(\sqrt{\frac{\xi}{\xi-1}} - 1 \right) d\xi. \quad (2.13)$$

This result is already given in [115]. The wake model Eq. (2.10) is now inserted into Eq. (2.13). Note that at this stage the circulation still depends on the vorticity at the trailing edge. The circulation is fixed by applying the Kutta condition Eq. (2.7). From that $\gamma(1, t)$ can be determined.

2.1.6 Time-harmonic motion

By employing the scaling II from Eq. (1.22) and assuming time-harmonic motion, we introduce the reduced frequency (introduced first by Birnbaum)

$$\Omega = \frac{\tilde{\omega} \tilde{L}}{\tilde{U}} \quad (2.14)$$

and a new time scale $\tau = \Omega t$. Then, Eqs. (1.25, 2.7, 2.10) are recast to

$$v_1(x, 0, \tau) = \Omega w_{1,\tau} + w_{1,x}, \quad (2.15)$$

$$\int_0^1 \gamma_\tau(\xi, \tau) d\xi + \frac{1}{\Omega} \gamma(1, \tau) = 0, \quad (2.16)$$

$$\gamma(x, \tau) = \gamma(1, \tau - \Omega(x-1)). \quad (2.17)$$

The equations in this time scaling are used in Sec. 2.2.5 and Sec. 2.3.

2.1.7 Representation by Chebyshev polynomials

So far, a distribution of vortices has been used to describe the potential flow. However, a second approach, the representation by Chebyshev polynomials, is more suitable to describe chordwise flexibility. Unfortunately, this approach cannot be extended easily to channel flows. It makes use of an expansion proposed by Prandtl in his famous lifting-line theory for the load in spanwise direction. Here, however, the expansion is used in streamwise direction. For a time-harmonic motion with small deflections, Eq. (1.24) can be written as

$$w(x, \tau) = \epsilon \Re[w_1 \exp(i\tau)] , \quad (2.18)$$

where \Re denotes the real part and i is the imaginary unit. It is convenient to define the motion in terms of Fourier cosine series. Following [45] and [118], we apply the Glauert mapping $x = \cos \theta$ and write

$$w_1 = \frac{\beta_0}{2} + \sum_{n=1}^{\infty} \beta_n \cos(n\theta) \quad (2.19)$$

in terms of the Fourier coefficients

$$\beta_n = \frac{2}{\pi} \int_0^{\pi} w_1 \cos(n\theta) d\theta . \quad (2.20)$$

Note that with the mapping to θ the body ranges from $x = -1$ to $x = 1$. It is thus convenient to use the semi-chord as reference length, see Eq. (1.20). Aiming at ϵ in Eq. (2.18) to express the ratio of maximum deflection to the chord, we require the motion to have a maximum deflection in the course of one period of $w_{1,max} = 2$. By making use of the Prandtl acceleration potential for the flow field (cf. [118] for details), one obtains for the pressure difference across the body the expression

$$\Delta p_1(\theta, \tau) = -\Re \left[\left(a_0 \tan \frac{\theta}{2} + 2 \sum_{n=1}^{\infty} a_n \sin(n\theta) \right) \exp(i\tau) \right] , \quad (2.21)$$

which satisfies already the generalized Kutta condition Eq. (2.5) at $\theta = 0$. The coefficient a_0 determines the strength of the singularity of the pressure difference at the leading edge $\theta = \pi$. It is important at this stage to establish the general relation between the parameters of motion (the Fourier coefficients of the deflection, β_n) and the parameters of the pressure (the Fourier coefficients a_n). At first, from Eq. (2.19), the derivative of w_1 with respect to x is expanded in a cosine series (cf. [118]) as

$$\frac{\partial w_1}{\partial x} = \frac{\gamma_0}{2} + \sum_{n=1}^{\infty} \gamma_n \cos(n\theta) . \quad (2.22)$$

By making use of well-known relations for trigonometric functions (cf. [2], 4.3.31), one obtains the relation

$$\gamma_{n-1} - \gamma_{n+1} = 2n\beta_n \quad (2.23)$$

and by induction

$$\gamma_{2n} = 2 \sum_{m=n}^{\infty} (2m+1)\beta_{2m+1}, \quad (2.24)$$

$$\gamma_{2n+1} = 2 \sum_{m=n}^{\infty} (2m+2)\beta_{2m+2}. \quad (2.25)$$

for $n = 0, 1, 2, \dots$. Then, the lateral velocity perturbation

$$v_1 = -\Re \left[\left(\frac{\lambda_0}{2} + \sum_{n=1}^{\infty} \lambda_n \cos(n\theta) \right) \exp(i\tau) \right] \quad (2.26)$$

satisfies the kinematic boundary condition Eq. (1.25) when the relation

$$\lambda_n = -(\gamma_n + i\sigma\beta_n) \quad (2.27)$$

for $n = 0, 1, 2, \dots$ holds. Here σ denotes the reduced frequency from the dimensionless set in Eq. (1.20). In addition, we differentiate Eq. (2.1) with respect to y and obtain the linearized momentum equation in lateral direction at the body surface

$$-p_{1,y} = v_{1,t} + v_{1,x}. \quad (2.28)$$

Then, Eq. (2.28) together with Eq. (2.26) and Cauchy–Riemann equations for potential flow (cf. [45]) lead to the following relations between the Fourier coefficients of the motion and the pressure [118]

$$a_0 = (\lambda_0 + \lambda_1) C(\sigma) - \lambda_1, \quad (2.29)$$

$$a_n = \lambda_n + \frac{i\sigma}{2n} (\lambda_{n-1} - \lambda_{n+1}) \quad (2.30)$$

for $n = 1, 2, \dots$. In Eq. (2.29), Here $C(\sigma)$ denotes the Theodorsen function that is described in the Sec. 2.1.8. With Eqs. (2.23, 2.27), one can write Eq. (2.30) as

$$a_n = -\gamma_n - i2\sigma\beta_n - \frac{\sigma^2}{2n} (\beta_{n+1} - \beta_{n-1}) \quad (2.31)$$

for $n = 0, 1, 2, \dots$. The Fourier terms $\cos(n\theta)$ and $\sin(n\theta)$ in w_1 and Δp_1 , respectively, can be transformed back to the x -coordinate $x = \cos \theta$ by making use of definitions of the Chebyshev polynomials of the first kind $T_n(x)$ and second kind $U_n(x)$ ([2], 22.3.15 and 22.3.16),

$$T_n(x) = \cos(n\theta), \quad \sqrt{1-x^2} U_{n-1}(x) = \sin(n\theta), \quad (2.32)$$

with the sum-representation

$$T_n(x) = \sum_{k=0}^{\lfloor \frac{n}{2} \rfloor} \frac{n!}{(2k)!(n-2k)!} x^{n-2k} (x^2-1)^k,$$

$$U_{n-1}(x) = \sum_{k=0}^{\lfloor \frac{n}{2} \rfloor} \frac{n!}{(2k+1)!(n-2k-1)!} x^{n-2k-1} (x^2-1)^k.$$

2.1.8 Theodorsen function

The Theodorsen function [104] is given by

$$C(\sigma) = \frac{K_1(i\sigma)}{K_0(i\sigma) + K_1(i\sigma)} = F(\sigma) + iG(\sigma). \quad (2.33)$$

It is solely a function of the reduced frequency σ and can be expressed by the modified Bessel functions of the second kind K_0 and K_1 , respectively. Fig. 2.2 shows plots of $C(\sigma)$.

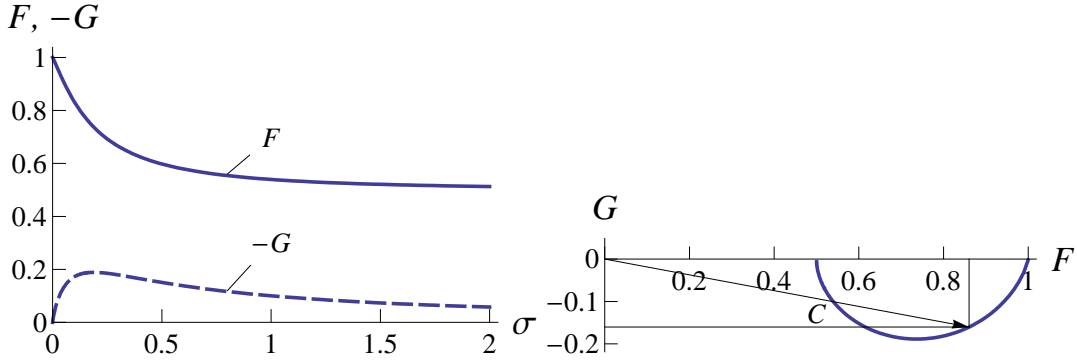


Figure 2.2: Theodorsen function. Left: Real- and imaginary part. Right: Complex polar plot.

Similar plots are given in the work by Garrick [26] and in classical textbooks [11], [36]. The Theodorsen function is a transfer function relating sinusoidal inputs of reduced frequency σ to their aerodynamic response. The instantaneous values of the lift force per unit span that acts on the body is given from the difference of the surface pressure on the upper and lower side as

$$\tilde{L}(\tilde{t}) = \int_{\tilde{x}_{LE}}^{\tilde{x}_{TE}} \Delta\tilde{p}(\tilde{x}, \tilde{t}) d\tilde{x}. \quad (2.34)$$

Regarding the lift force caused by the circulatory portion of the flow, $C(\sigma)$ accounts for the change in magnitude and phase with changes in reduced frequency σ . Physically speaking, the difference of $C(\sigma)$ from the value one is a consequence of the wake vortices. When σ is small, the so-called quasi steady-state assumption may be used, which neglects the influence of the wake vortices on the flow in that $C(\sigma)$ is replaced with the value one. In that case, the circulatory portion of the lift force depends only on the instantaneous value of the circulation at the body.

2.1.9 Thrust, power and efficiency

The definitions made in this section for thrust, power and efficiency are used below to study propulsion for a prescribed motion in Ch. 3 and for fluid structure interaction in Ch. 4. The thrust force per unit span acting on the body surface in negative x-direction is given by

$$\tilde{T}(\tilde{t}) = \tilde{T}_p(\tilde{t}) + \tilde{T}_s(\tilde{t}) \quad (2.35)$$

with the thrust per unit span from the difference of the surface pressure on the upper and lower side

$$\tilde{T}_p(\tilde{t}) = - \int_{\tilde{x}_{LE}}^{\tilde{x}_{TE}} \Delta\tilde{p}(\tilde{x}, \tilde{t}) \frac{\partial\tilde{w}}{\partial\tilde{x}} d\tilde{x} \quad (2.36)$$

and the contribution from nose suction

$$\tilde{T}_s(\tilde{t}) = \epsilon^2 \frac{1}{2} \pi \tilde{\rho} \tilde{U}^2 \frac{\tilde{L}}{2} A_0'^2, \quad (2.37)$$

where A_0' is given by (cf. [118])

$$A_0' = a_0' \cos \tau - a_0'' \sin \tau. \quad (2.38)$$

Here a_0' and a_0'' denote the real- and imaginary part of

$$a_0 = a_0' + i a_0'' \quad (2.39)$$

that is given by Eq. (2.29). The suction force $\tilde{T}_s(\tilde{t})$ acts on the leading edge and is due to the inverse square-root singularity of the pressure difference at the leading edge, cf. Eq. (2.21). $\tilde{T}_s(\tilde{t})$ is obtained in the limit of the contours' radius of curvature tending to zero. An introductory example for the need of inclusion of leading-edge suction is given in [36], Sec. 5.4. The power required to drive the body is given by

$$\tilde{P}(\tilde{t}) = \int_{\tilde{x}_{LE}}^{\tilde{x}_{TE}} \Delta\tilde{p}(\tilde{x}, \tilde{t}) \frac{\partial\tilde{w}}{\partial\tilde{t}} d\tilde{x}. \quad (2.40)$$

From the principle of conservation of energy, the kinetic energy imparted to the fluid [118] is determined from the power input minus the time rate of work done by the thrust

$$\tilde{E}(\tilde{t}) = \tilde{P}(\tilde{t}) - \tilde{T}(\tilde{t}) \tilde{U}. \quad (2.41)$$

In dimensionless form, using $\epsilon^2 \frac{\pi}{4} \tilde{\rho} \tilde{U}^2 \tilde{L} / 2$ as scale for the forces, we obtain

$$T_p(t) = -\frac{4}{\pi} \int_{x_{LE}}^{x_{TE}} \Delta p_1 \frac{\partial w_1}{\partial x} dx, \quad (2.42)$$

$$T_s(t) = 2 A_0'^2, \quad (2.43)$$

$$P(t) = \frac{4}{\pi} \int_{x_{LE}}^{x_{TE}} \Delta p_1 \frac{\partial w_1}{\partial t} dx. \quad (2.44)$$

The time-averaged values are defined as ¹

$$T_s = \overline{T_s(t)}, \quad T_p = \overline{T_p(t)}, \quad T = T_p + T_s, \quad P = \overline{P(t)}, \quad E = P - T. \quad (2.45)$$

¹The instantaneous values are indicated as functions of time t , while the symbols without the overbar denote time-average values

The overbar denotes the time average over one flapping period. Since A'_0 in Eq. (2.38) is a time-harmonic signal, the time-average value of the leading-edge thrust becomes

$$T_s = 2 \overline{A_0'^2} = a_0'^2 + a_0''^2. \quad (2.46)$$

The hydrodynamic propulsive efficiency for producing average useful thrust is given as (denoting $U = 1$ to identify the numerator as power)

$$\eta = \frac{TU}{P} = \frac{1}{1 + E/T}. \quad (2.47)$$

2.2 Channel flow

In this section a novel analytical solution of the unsteady potential flow over a surface oscillating about the centerline of a channel is presented. The results for the velocity field, vorticity distribution and circulation on the surface are given.

Potential flow in a channel has been examined in the literature. Greengard [29] determines the Green's function of a single potential source at arbitrary position in a channel of infinite extension. The method of images (cf. [36], Sec. 6.8) is repeatedly employed to fulfill the kinematic boundary condition at the channel walls. It is emphasized that the velocity field induced by the point source decays exponentially along the length of the channel. In the present problem we assume the flapping surface to lie in the vicinity of the channel's centerline.

As in unbounded domain (see Sec. 2.1.5 for details), jump conditions across the flapping surface and wake are to be fulfilled. Following Schwarz [86], a distribution of vortices can be used to describe the problem. The unsteady Kutta condition is used to constrain the vorticity at the trailing edge. Altogether, the approach gives rise to a singular integral equation. However, in contrast to the problem in unbounded domain, the integral kernel is not of Cauchy type and thus Söhngen's inversion formula cannot be applied.

For large channel width with respect to the chord, Keldysh & Lavrentiev [39] presented an asymptotic approach (cf. [36], Sec. 7.5) that expands the kernel in terms of powers of the inverse channel width and applies Söhngen inversion to the resultant Cauchy-type integral equations term by term in consecutive order.

The aim in the present work is, however, to obtain a solution in closed form. An inversion formula in a channel of any width has been given by the present author [67] for a somewhat different physical problem that is stationary and comprises a wake of prescribed constant strength (cf. [85]). Complex function theory together with the repeated method of images has been used to obtain the velocity field and, in using a representation by distributed vortices, a generalized version of Söhngen's formula. The present problem of a flapping surface is slightly more involved as the strength of vorticity in the wake is not known a priori. Schwarz overcame this difficulty by starting the inversion of the integral equation with the assumption of interim given strength of wake vorticity (see Sec. 2.1.5). In the present work, we pursue a more direct approach. As in [67], complex function theory with an appropriate auxiliary function is employed to obtain the velocity field in the entire domain of the channel in closed form directly from the motion of the body. The solution is then evaluated at the channel centerline to determine the distribution of vorticity along the body surface. The size of bound circulation is fixed by the Kutta condition.

A possible application of the results are wall correction formulae for measurements in wind tunnels or water basins, where the measured lift and thrust forces on unsteadily moving surfaces are to be corrected to imitate the original operation in freestream (as for wind turbines, etc.).

We note that the flow problem in the channel has a similarity to the flapping propulsion close to a wall. According to the review article by Rozhdestvensky [80] “it is not possible to obtain a closed-form solution of the corresponding integral equation in linear formulation for a foil oscillating in inviscid flow at finite distance from an interface”. It is well known that the lift force on the foil increases when the gap width becomes small (ground effect, cf. [36]). If the channel width becomes too small, the assumptions of irrotational flow may no longer be valid and viscous effects may become significant.

Interesting results have been obtained by Molina et. al. [65] by using URANS for a downwards cambered heaving airfoil in ground effect. For the non-oscillating steady case, they reported maximum downforce at a gap to chord ratio of 0.17 that is 71 percent greater than in freestream. At ride height lower than that, force reduction caused by stall has been observed. For the heaving foil, however, Molina et. al. [65] reported that at high flapping frequencies the force reduction region in extreme ground effect disappears and the aerodynamic performance of the airfoil, dominated by added mass effects, behaves like in inviscid flow.

We start with the description of a single potential vortex in the channel to demonstrate how the channel wall boundary changes the kernel in the integral equation. Then, the novel inversion method is presented.

2.2.1 Single vortex at the centerline and stack of vortices

In order to obtain a basic solution that fulfills the kinematic boundary conditions at the upper and lower wall Eq. (1.26), we use the procedure of iterative imaging of a single vortex for unbounded flow (cf. [36], Sec. 6.8). The complex potential $F(z) = \varphi + i\psi$ with $z = x + iy$ is introduced. In case of an infinite domain, the well-known fundamental solution for the potential of a single vortex of strength Γ placed at $z = \xi$ is given by Eq. (2.2). Fig. 2.3 shows a sketch of a single vortex on the centerline of a channel.

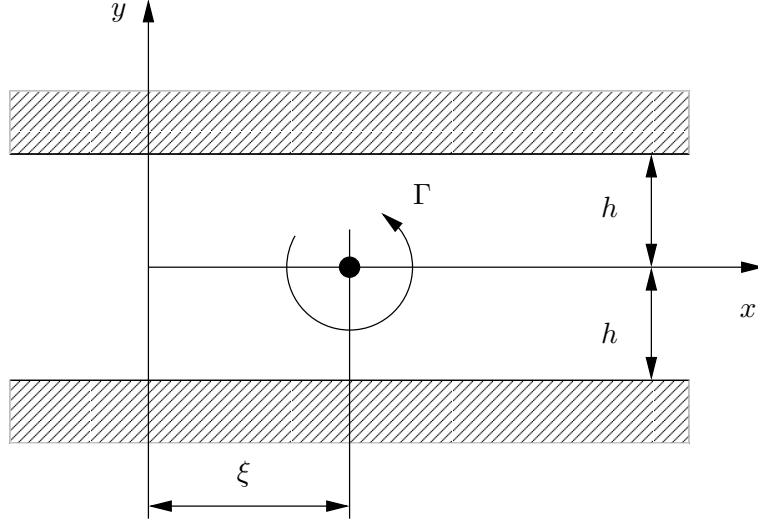


Figure 2.3: Single vortex of strength Γ at the centerline of a channel of semi-width h .

To satisfy the boundary conditions at the channel walls $y = \pm h$ the method of images is applied. Then, for an infinite stack of clockwise vortices at $y = 0, \pm 4h, \pm 8h \dots$ and counterclockwise vortices at $y = \pm 2h, \pm 6h \dots$, the complex potential is

$$F(z) = -i \frac{\Gamma}{2\pi} (\ln[z - \xi] - \ln[z - (\xi + i2h)] - \ln[z - (\xi - i2h)] + \ln[z - (\xi - i4h)] + \ln[z - (\xi + i4h)] - \ln[z - (\xi + i6h)] - \ln[z - (\xi - i6h)] + \dots). \quad (2.48)$$

By adding and subtracting terms and skipping constants $\ln[(2h)^2], \ln[(4h)^2], \dots$ we obtain

$$F(z) = -i \frac{\Gamma}{2\pi} \left(\ln[z - \xi] - \ln \prod_{n=1}^{\infty} \left[1 + \left(\frac{z - \xi}{2nh} \right)^2 \right] + \ln \left[\prod_{n=1}^{\infty} \left[1 + \left(\frac{z - \xi}{4nh} \right)^2 \right] \right]^2 \right). \quad (2.49)$$

Making use of $\prod_{n=1}^{\infty} \left[1 + \frac{x^2}{n^2} \right] = \frac{1}{\pi x} \sinh(\pi x)$ from [2], 4.5.68, and by omitting constants, the result for the complex potential of the vortex stack becomes

$$F(z) = -i \frac{\Gamma}{2\pi} \ln \frac{\sinh^2\left(\pi \frac{z - \xi}{4h}\right)}{\sinh\left(\pi \frac{z - \xi}{2h}\right)} = -i \frac{\Gamma}{2\pi} \ln \left| \tanh \left(\pi \frac{z - \xi}{4h} \right) \right| \quad (2.50)$$

(compare to [36], Eq. (6.89)). With $F(z) = \varphi + i\psi$, the real part is

$$\varphi = \frac{\Gamma}{2\pi} \arctan \frac{\sin\left(\pi \frac{y}{2h}\right)}{\sinh\left(\pi \frac{x - \xi}{2h}\right)}. \quad (2.51)$$

2.2.2 Singular integral equation

We apply a distribution of vortex stacks Eq. (2.50) $d\Gamma(\xi, t) = \gamma(\xi, t)d\xi$ on the x -axis (at $w = 0$) along the body and in the wake. Similarly to the problem in unbounded domain in Sec. 2.1.5,

we obtain for the derivatives of the potential from Eq. (2.51)

$$\varphi_x(x, 0^\pm, t) = \lim_{y \rightarrow 0^\pm} \frac{1}{2h} \int_0^\infty \gamma(\xi, t) \frac{\cosh \frac{\pi(x-\xi)}{2h} \sin \frac{\pi y}{2h}}{\cos \frac{\pi y}{h} - \cosh \frac{\pi(x-\xi)}{h}} d\xi = \mp \frac{\gamma(x, t)}{2}, \quad (2.52)$$

$$\varphi_y(x, 0^\pm, t) = \frac{1}{4h} \int_0^\infty \frac{\gamma(\xi, t)}{\sinh \frac{\pi(x-\xi)}{2h}} d\xi, \quad (2.53)$$

with

$$\varphi_x(x, 0^+) = [u_1(x, 0^+) - 1] = -[u_1(x, 0^-) - 1] = -\frac{\gamma(x)}{2}, \quad (2.54)$$

$$\varphi_y(x, 0^\pm) = v_1(x, 0) \quad (2.55)$$

(with the dependence on time t being omitted in the notation). Note that the distribution of vortex stacks fulfills the kinematic boundary condition at the channel walls Eq. (1.26). In addition, the distribution of vortex strength on the centerline shall fulfill the kinematic boundary condition at the body Eq. (1.25). This requires to solve the singular integral equation Eq. (2.53). The inversion formula for the unbounded domain, as outlined in Sec. 2.1.5, can not be applied to the channel flow problem.

If the channel width is large (compared to the chord), the presence of the channel walls can be taken into account as higher order effect. According to [36], Keldysh & Lavrentiev [39] performed a series expansion of the kernel function in Eq. (2.53) in powers of $1/h$. To this end, the representation

$$\frac{1}{\sinh \xi} = \frac{1}{\xi} - \sum_{k=1}^{\infty} \frac{2(2^{2k-1} - 1)}{(2k)!} B_{2k} \xi^{2k-1}$$

can be used ([2], 4.5.65), where B_k is the Bernoulli number. Note that the first term on the rhs equals the kernel in unbounded domain. The resultant Cauchy-type integral equations for each term can then be solved consecutively by Söhngen's inversion formula (cf. [36], Sec. 7.5).

In contrast to that approach, we attempt to solve the channel flow analytically and pursue an approach that considers the flow field in the entire domain.

2.2.3 Solution of the flow field

Following the ideas from [8] as delineated in [84], we start with Cauchy's integral formula

$$f(z) = \frac{1}{2\pi i} \oint \frac{f(\zeta)}{\zeta - z} d\zeta \quad (2.56)$$

with $z = x + iy$, $\zeta = \xi + i\eta$ and set for the analytic function

$$f(\zeta) = w(\zeta)h(\zeta), \quad (2.57)$$

in where

$$w(\zeta) = [u(\zeta) - 1] - iv(\zeta) \quad (2.58)$$

is the complex valued velocity perturbation, and $h(\zeta)$ is an analytic auxiliary function which will be specified below. In the notation of the respective velocity components u and v we have

dropped the index 1 that indicates perturbation. The method of images is used to satisfy the boundary condition at the channel walls Eq. (1.10). In doing so, the body and the wake region are successively mirrored about the channel walls that are each a distance h apart from the centerline, so that one obtains a successive sequence of (virtual) channels, see Fig. 2.4. On each of the bodies and wake regions, the tangential component of the velocity is – in general – discontinuous. Therefore the path of integration for the integral in Eq. (2.56) has to be cut and passed around the bodies and wakes, as indicated in Fig. 2.4.

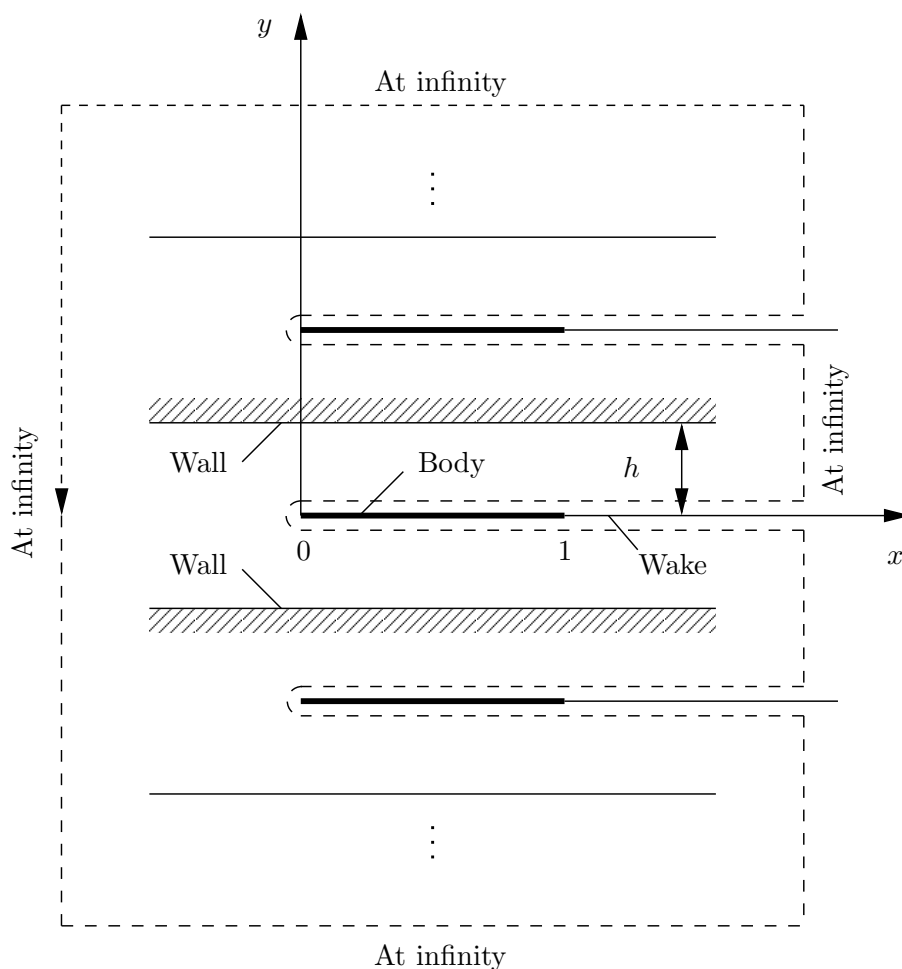


Figure 2.4: Successively mirrored body and wake in the channel of semi-width h . Path of integration to derive the potential-flow solution (dashed line).

If one presumes $h(\zeta)$ to be bounded at $\zeta \rightarrow \infty$, the path of integration at infinity does not

contribute to the integral in Eq. (2.56), and it follows from Eqs. (2.56–2.58) that

$$w(z) = \frac{1}{2\pi ih(z)} \int_0^\infty \left(\frac{f(\xi, 0^+) - f(\xi, 0^-)}{\xi - z} + \frac{f(\xi, 2h^+) - f(\xi, 2h^-)}{(\xi + i2h) - z} + \frac{f(\xi, -2h^+) - f(\xi, -2h^-)}{(\xi - i2h) - z} + \frac{f(\xi, 4h^+) - f(\xi, 4h^-)}{(\xi + i4h) - z} + \frac{f(\xi, -4h^+) - f(\xi, -4h^-)}{(\xi - i4h) - z} + \dots \right) d\xi. \quad (2.59)$$

The velocity perturbation along the body and the wake in each of the virtual channels can be expressed by the velocity perturbation in the physical channel

$$v(\xi, 2nh) = (-1)^n v(\xi, 0) \quad \text{for } -\infty < \xi < +\infty, \quad (2.60)$$

$$u(\xi, 2nh^\pm) - 1 = (-1)^n [u(\xi, 0^\pm) - 1] \quad \text{for } \xi \geq 0, \quad (2.61)$$

for $n = -N, \dots, -1, 0, 1, \dots, N$. The alternating sign $(-1)^n$ and an infinite number of virtual channels $N \rightarrow \infty$ are necessary to satisfy the boundary conditions at the walls, Eq. (1.10). We require

$$h(\xi, 2nh^-) = -h(\xi, 2nh^+) \quad \text{for } 0 \leq \xi \leq 1, \quad (2.62)$$

$$h(\xi, 2nh^-) = h(\xi, 2nh^+) \quad \text{for } \xi > 1, \quad (2.63)$$

to achieve that the jump discontinuity $f(\xi, 2nh^+) - f(\xi, 2nh^-)$ on the bodies $0 \leq \xi \leq 1$ no longer depends on the a priori unknown tangential velocity and that $f(\xi, 2nh^+) - f(\xi, 2nh^-)$ in the wake regions $\xi > 1$ no longer depends on the vertical velocity perturbation, respectively. Thus, inserting Eqs. (2.60) to (2.63) into Eq. (2.57) gives

$$f(\xi, 2nh^+) - f(\xi, 2nh^-) = -2iv(\xi, 0)h(\xi, 2nh^+) \quad \text{for } 0 \leq \xi \leq 1, \quad (2.64)$$

$$f(\xi, 2nh^+) - f(\xi, 2nh^-) = 2[u(\xi, 0^+) - 1](-1)^n h(\xi, 2nh^+) \quad \text{for } \xi > 1. \quad (2.65)$$

Hence, Eq. (2.59) may be written as

$$w(z) = \frac{1}{2\pi ih(z)} \left\{ -2i \int_0^1 v(\xi, 0) \left(\frac{h(\xi, 0^+)}{\xi - z} - \frac{h(\xi, 2h^+)}{\xi + i2h - z} - \frac{h(\xi, -2h^+)}{\xi - i2h - z} + \frac{h(\xi, 4h^+)}{\xi + i4h - z} + \frac{h(\xi, -4h^+)}{\xi - i4h - z} \mp \dots \right) d\xi + 2 \int_1^\infty [u(\xi, 0^+) - 1] \left(\frac{h(\xi, 0^+)}{\xi - z} - \frac{h(\xi, 2h^+)}{\xi + i2h - z} - \frac{h(\xi, -2h^+)}{\xi - i2h - z} \pm \dots \right) d\xi \right\}. \quad (2.66)$$

We require that the entire flow field in each of the virtual channels is in principle the same as in the physical channel, except that it is turned upside down in every other channel. Thus

$$h(\xi, 2nh^+) = h(\xi, 0^+). \quad (2.67)$$

As a consequence, $h(\xi, 0^+)$ can be factored out of the bracket in Eq. (2.66). For an infinite number of virtual channels, the remaining expression inside the bracket can then be simplified

according to

$$\begin{aligned} & \frac{1}{\xi - z} + \sum_{n=1}^{\infty} (-1)^n \left(\frac{1}{\xi + i2nh - z} + \frac{1}{\xi - i2nh - z} \right) = \\ & \frac{1}{\xi - z} + 2(\xi - z) \sum_{n=1}^{\infty} \frac{(-1)^n}{(2nh)^2 + (\xi - z)^2} = \frac{\pi}{2h} \frac{1}{\sinh \left[\frac{\pi}{2h} (\xi - z) \right]}, \end{aligned} \quad (2.68)$$

where $\operatorname{csch} z = \frac{1}{z} + 2z \sum_{k=1}^{\infty} \frac{(-1)^k}{\pi^2 k^2 + z^2}$ from [117] has been used for the last simplification. With Eq. (2.67) and Eq. (2.68) we obtain

$$\begin{aligned} w(z) = \frac{1}{2\pi i h(z)} & \left\{ -2i \int_0^1 v(\xi, 0) h(\xi, 0^+) \frac{\pi}{2h} \frac{1}{\sinh \left[\frac{\pi}{2h} (\xi - z) \right]} d\xi + \right. \\ & \left. 2 \int_1^{\infty} [u(\xi, 0^+) - 1] h(\xi, 0^+) \frac{\pi}{2h} \frac{1}{\sinh \left[\frac{\pi}{2h} (\xi - z) \right]} d\xi \right\}. \end{aligned} \quad (2.69)$$

An analytic auxiliary function that fulfills all the required conditions Eqs. (2.62, 2.63, 2.67) is

$$\begin{aligned} h(\zeta) = \zeta^{1/2} (1 - \zeta)^{-1/2} (\zeta + i2h)^{1/2} [1 - (\zeta + i2h)]^{-1/2} (\zeta - i2h)^{1/2} [1 - (\zeta - i2h)]^{-1/2} \dots = \\ \sqrt{\frac{\zeta \prod_{n=1}^{\infty} \left[1 + \left(\frac{\zeta}{2nh} \right)^2 \right]}{1 - \zeta \prod_{n=1}^{\infty} \left[1 + \left(\frac{1-\zeta}{2nh} \right)^2 \right]}} = \sqrt{\frac{\sinh \left(\frac{\pi}{2h} \zeta \right)}{\sinh \left[\frac{\pi}{2h} (1 - \zeta) \right]}}, \end{aligned} \quad (2.70)$$

where $\sinh z = z \prod_{k=1}^{\infty} \left[1 + \frac{z^2}{\pi^2 k^2} \right]$ from [2], 4.5.68 has been used for the last simplification. Hence, inserting Eq. (2.70) and Eq. (2.58) into Eq. (2.69) gives the result for the components of the complex velocity perturbation

$$\begin{aligned} [u(z) - 1] - iv(z) = \frac{1}{2h} \sqrt{\frac{\sinh \left[\frac{\pi}{2h} (1 - z) \right]}{\sinh \left(\frac{\pi}{2h} z \right)}} & \left\{ - \int_0^1 v(\xi, 0) \sqrt{\frac{\sinh \left(\frac{\pi}{2h} \xi \right)}{\sinh \left[\frac{\pi}{2h} (1 - \xi) \right] \sinh \left[\frac{\pi}{2h} (\xi - z) \right]}} d\xi + \right. \\ & \left. \int_1^{\infty} [u(\xi, 0^+) - 1] \sqrt{\frac{\sinh \left(\frac{\pi}{2h} \xi \right)}{\sinh \left[\frac{\pi}{2h} (\xi - 1) \right] \sinh \left[\frac{\pi}{2h} (\xi - z) \right]}} d\xi \right\}, \end{aligned} \quad (2.71)$$

where from Eq. (2.70)

$$h(\zeta) = \sqrt{\frac{\sinh \left(\frac{\pi}{2h} \zeta \right)}{-\sinh \left[\frac{\pi}{2h} (\zeta - 1) \right]}} = \pm i \sqrt{\frac{\sinh \left(\frac{\pi}{2h} \zeta \right)}{\sinh \left[\frac{\pi}{2h} (\zeta - 1) \right]}} \quad \text{for } \operatorname{Im}[\zeta] \geq 0 \quad \text{and} \quad \operatorname{Im}[\zeta] > 1 \quad (2.72)$$

has been used for the second integral. With $z = x + iy$ and $y \rightarrow 0$ one immediately obtains the velocity perturbation in the plane of the body. Taking the real part of Eq. (2.71) gives the

distribution of the tangential velocity perturbation. With Eq. (2.54) one obtains at the body

$$\gamma(x) = \frac{1}{h} \sqrt{\frac{\sinh \left[\frac{\pi}{2h}(1-x) \right]}{\sinh \left(\frac{\pi}{2h}x \right)}} \left\{ \int_0^1 v(\xi, 0) \sqrt{\frac{\sinh \left(\frac{\pi}{2h}\xi \right)}{\sinh \left[\frac{\pi}{2h}(1-\xi) \right]} \frac{d\xi}{\sinh \left[\frac{\pi}{2h}(\xi-x) \right]}} + \int_1^\infty \frac{\gamma(\xi)}{2} \sqrt{\frac{\sinh \left(\frac{\pi}{2h}\xi \right)}{\sinh \left[\frac{\pi}{2h}(\xi-1) \right]} \frac{d\xi}{\sinh \left[\frac{\pi}{2h}(\xi-x) \right]}} \right\} \quad \text{for } 0 \leq x \leq 1, \quad (2.73)$$

where \int denotes the Cauchy principal value. We thus have obtained an inversion formula to Eq. (2.53), cf. [67, 99]. In the limit $h \rightarrow \infty$ one obtains the solution in unbounded domain Eq. (2.12).

2.2.4 Circulation

With the definition of the circulation around the body Eq. (2.6) we find by integration of Eq. (2.73)

$$\Gamma(t) = \frac{1}{h} \int_0^1 \left(\sqrt{\frac{\sinh \left[\frac{\pi}{2h}(1-x) \right]}{\sinh \left(\frac{\pi}{2h}x \right)}} \int_0^1 v(\xi, 0, t) \sqrt{\frac{\sinh \left(\frac{\pi}{2h}\xi \right)}{\sinh \left[\frac{\pi}{2h}(1-\xi) \right]} \frac{d\xi}{\sinh \left[\frac{\pi}{2h}(\xi-x) \right]}} \right) dx + \frac{1}{2h} \int_0^1 \left(\sqrt{\frac{\sinh \left[\frac{\pi}{2h}(1-x) \right]}{\sinh \left(\frac{\pi}{2h}x \right)}} \int_1^\infty \gamma(\xi, t) \sqrt{\frac{\sinh \left(\frac{\pi}{2h}\xi \right)}{\sinh \left[\frac{\pi}{2h}(\xi-1) \right]} \frac{d\xi}{\sinh \left[\frac{\pi}{2h}(\xi-x) \right]}} \right) dx \quad (2.74)$$

and with exchanged order of integration we obtain

$$\Gamma(t) = 2 \int_0^1 v(\xi, 0, t) \sqrt{\frac{\sinh \left(\frac{\pi}{2h}\xi \right)}{\sinh \left[\frac{\pi}{2h}(1-\xi) \right]}} I_0 d\xi + \int_1^\infty \gamma(\xi, t) \sqrt{\frac{\sinh \left(\frac{\pi}{2h}\xi \right)}{\sinh \left[\frac{\pi}{2h}(\xi-1) \right]}} (I_0 - I_1) d\xi, \quad (2.75)$$

with the integrals

$$I_0 = \frac{1}{2h} \int_0^1 \sqrt{\frac{\sinh \left[\frac{\pi}{2h}(1-x) \right]}{\sinh \left(\frac{\pi}{2h}x \right)}} \frac{dx}{\sinh \left[\frac{\pi}{2h}(\xi-x) \right]}, \quad (2.76a)$$

$$I_1 = I_0 - \frac{1}{2h} \int_0^1 \sqrt{\frac{\sinh \left[\frac{\pi}{2h}(1-x) \right]}{\sinh \left(\frac{\pi}{2h}x \right)}} \frac{dx}{\sinh \left[\frac{\pi}{2h}(\xi-x) \right]} \quad (\xi \geq 1). \quad (2.76b)$$

In order to solve I_0 we perform a substitution for the variable $y = \frac{\pi}{b}(x - \frac{1}{2})$ and for the parameter $\eta = \frac{\pi}{b}(\xi - \frac{1}{2})$, and subsequent to that the substitution $s = \sinh^2 y$. From this expression, the primitive integral is solved with the help of the software package *Mathematica*. By evaluation of the primitive integral in bounds, observing the principal value, and by making use of well-known transformations for elliptic integrals (cf. [2, 74]), we obtain for the integral in Eq. (2.76a)

$$I_0 = \frac{2k}{\pi} \frac{\sqrt{1-\alpha^2}}{\alpha} \left[K(k) - \left(1 - \frac{\alpha}{k}\right) \Pi(\alpha^2, k) \right], \quad (2.77)$$

where K and Π are the complete elliptic integral of the first kind and the elliptic integral of the third kind, respectively, and the parameters

$$\alpha = \tanh[\pi(\xi - 1/2)/(2h)], \quad k = \tanh[\pi/(4h)]$$

incorporate the dependence on the semi-channel width h . It is important to emphasize that we denote the so-called modulus k in the parameter list of the elliptic integrals (following [74], Ch. 19), instead of the historically older form where the parameter $m = k^2$ is denoted (the form used in [2], and by *Mathematica*). With I_0 known, we determine the integral I_1 from Eq. (2.76b) and find (using again [74])

$$I_1 = \sqrt{\frac{\sinh\left[\frac{\pi}{2h}(\xi - 1)\right]}{\sinh\left(\frac{\pi}{2h}\xi\right)}}. \quad (2.78)$$

With Eq. (2.78) the expression for the circulation Eq. (2.75) simplifies to (note that $\Im m[I_1] = I_1/i$)

$$\Gamma(t) = 2i \int_0^1 v(\xi, 0, t) \frac{I_0}{I_1} d\xi + \int_1^\infty \gamma(\xi, t) \left(\frac{I_0}{I_1} - 1 \right) d\xi, \quad (2.79)$$

where I_0 and I_1 are given by Eqs. (2.77, 2.78). Finally we have obtained a rather simple representation of the instationary circulation around a zero-thickness body moving in the vicinity of the centerline of an infinitely long channel. Note that in Eq. (2.79) only the ratio of the integrals I_0/I_1 appears. In the following the expansions for both large and small channel width are discussed.

Expansion for large channel width

In the limit of large channel width $h \rightarrow \infty$ one obtains from an expansion of Eqs. (2.77, 2.78)

$$\begin{aligned} \lim_{h \rightarrow \infty} I_0 &= 1 + \frac{\pi^2}{64h^2}(3 - 4\xi) + \dots, \\ \lim_{h \rightarrow \infty} I_1 &= \sqrt{\frac{\xi - 1}{\xi}} \left(1 + \frac{\pi^2}{48h^2}(1 - 2\xi) + \dots \right) \end{aligned}$$

and thus from Eq. (2.79)

$$\begin{aligned} \lim_{h \rightarrow \infty} \Gamma(t) &= 2 \int_0^1 v(\xi, 0, t) \sqrt{\frac{\xi}{1 - \xi}} \left(1 + \pi^2 \frac{5 - 4\xi}{192h^2} + \dots \right) d\xi + \\ &\int_1^\infty \left[\sqrt{\frac{\xi}{\xi - 1}} \left(1 + \pi^2 \frac{5 - 4\xi}{192h^2} + \dots \right) - 1 \right] \gamma(\xi, t) d\xi. \end{aligned} \quad (2.80)$$

The leading terms resemble the result in unbounded domain Eq. (2.13). The perturbation term that accounts for the presence of the channel walls is of order h^{-2} , in accordance with the corresponding stationary example outlined in [36], Sec. 7.5 (where the perturbation method by Keldysh & Lavrentiev [39] has been used). One may observe that the perturbation caused by distant channel walls is one order less than the perturbation of order h^{-1} caused by the weak ground effect (cf. [36]).

Expansion for small channel width

In the limit of small channel width $h \rightarrow 0$ follows

$$I_1 \sim \exp\left(-\frac{\pi\xi}{4h}\right) \sqrt{2 \sinh \frac{\pi(\xi-1)}{2h}},$$

$$I_0 \sim \begin{cases} \frac{\xi}{h} \exp \frac{\pi(1-2\xi)}{4h} & (0 \leq \xi \leq 1) \\ I_1 + \frac{1}{h} \exp \frac{\pi(1-2\xi)}{4h} & (\xi > 1) \end{cases}$$

and thus from Eq. (2.79)

$$\Gamma(t) \sim \frac{2}{h} \int_0^1 v(\xi, 0, t) \frac{\xi}{\sqrt{1 - \exp \frac{\pi(\xi-1)}{h}}} d\xi + \frac{1}{h} \int_1^\infty \frac{1}{\sqrt{\exp \frac{\pi(\xi-1)}{h} - 1}} \gamma(\xi, t) d\xi. \quad (2.81)$$

Regarding the size of the terms in orders of h , we have $v = \mathcal{O}(1)$ and thus the size of the body integral can be estimated using the transformation $s = \pm\pi\frac{1-\xi}{h}$ for $\xi \leq 1$

$$\frac{2}{h} \int_0^1 \frac{\xi}{\sqrt{1 - \exp \frac{\pi(\xi-1)}{h}}} d\xi = \frac{2}{\pi} \int_0^{\frac{\pi}{h}} \frac{1 - \frac{h}{\pi}s}{\sqrt{1 - \exp(-s)}} ds \sim \frac{1}{h} + \frac{4}{\pi} \ln 2 + \left(\frac{4}{\pi^2} \ln^2 2 - \frac{1}{3}\right) h + \dots$$

From the wake model Eq. (2.10) follows that $|\gamma(\xi, t)| \leq |\gamma(1, t)|$ for $\xi > 1$. Thus, an upper bound for the wake integral in Eq. (2.81) reads

$$\frac{1}{h} \int_1^\infty \frac{1}{\sqrt{\exp \frac{\pi(\xi-1)}{h} - 1}} d\xi = \frac{1}{\pi} \int_0^\infty \frac{ds}{\sqrt{\exp(s) - 1}} = 1.$$

As a consequence of the Kutta condition Eq. (2.7) $\gamma(1, t) \sim \Gamma(t)$. Then Eq. (2.81) gives

$$\Gamma(t) \sim \mathcal{O}(h^{-1}) \quad \text{for } h \rightarrow 0. \quad (2.82)$$

Hence, the forces on the body grow beyond bounds as the channel width is decreased. Certainly, the applicability of two-dim. potential flow theory is limited when the channel width becomes very small. The underlying assumptions that the viscous layers that form along the body and the walls can be treated as a higher order effect and that the flow follows the contour of the body, a condition required to produce high forces, may no longer be valid. Regarding both limitations, interesting numerical results have been given by Molina et. al. [65] for a heaving foil in extreme ground effect. Their results indicate that at high flapping frequencies, added mass effects overcome large separation and viscous effects do not play a role in the aerodynamic performance.

Fig. 2.5 plots the influence coefficients in Eq. (2.79) that describe to which amount the distribution of the streamwise vertical velocity component v and the wake vorticity γ , respectively, contribute to the body circulation.

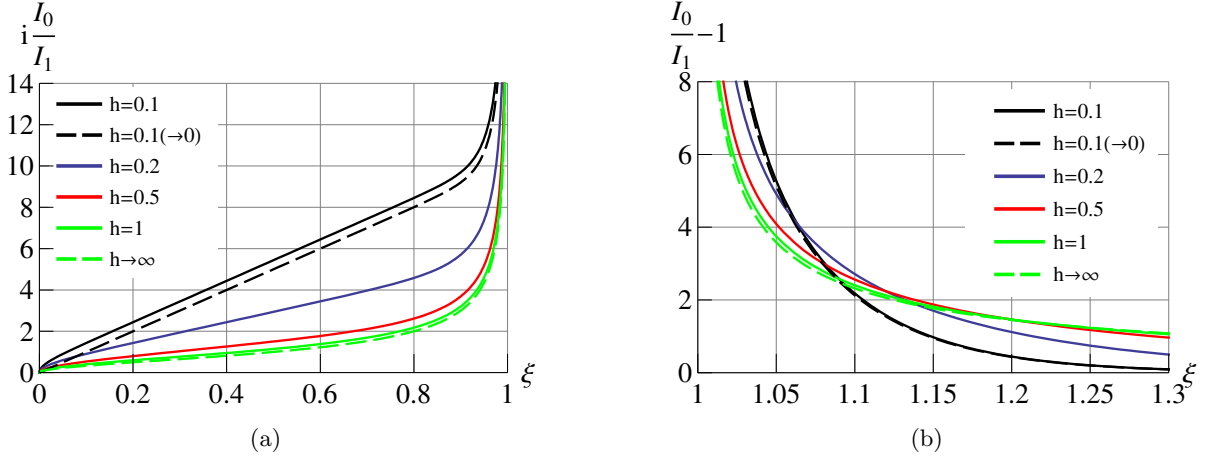


Figure 2.5: Influence coefficients for the circulation around the body in Eq. (2.79) for different semi-channel width h : (a) coefficient for vertical velocity on the body; (b) coefficient for vorticity in the wake. ($\rightarrow 0$) indicates the use of the leading term of the expansion for small h .

The influence coefficient on the body $i I_0/I_1$ increases monotonically along ξ , while the influence coefficient in the wake $(I_0/I_1) - 1$ decreases. Both coefficients are singular at the trailing edge $\xi = 1$, illustrating that the size of the circulation is strongly affected by the behaviour at this point. As $i I_0/I_1$ grows beyond bounds in the limit $h \rightarrow 0$, the asymptotic solution for small h is compared to the exact solution at a finite value of $h = 0.1$. A comparison of the wake coefficients $(I_0/I_1) - 1$ for large channel width and small channel width shows the transition from an algebraic decay Eq. (2.80) to an exponential decay Eq. (2.81). Consequently, the wake coefficient for smaller/larger h is larger/smaller near the trailing edge $\xi = 1$ and decays stronger/weaker far downstream from the body $\xi \rightarrow \infty$.

2.2.5 Solution for time-harmonic motion

With the result for the circulation, it is straightforward to determine the strength of vorticity at the trailing edge from the Kutta condition. Using the scaling II Eq. (1.22) for time-harmonic motions and taking the derivative of Eq. (2.79) yields for Eq. (2.16)

$$2i \int_0^1 v_\tau(\xi, 0, \tau) \frac{I_0}{I_1} d\xi + \int_1^\infty \left(\frac{I_0}{I_1} - 1 \right) \gamma_\tau(\xi, \tau) d\xi + \frac{1}{\Omega} \gamma(1, \tau) = 0, \quad (2.83)$$

where Ω is the dimensionless frequency given in Eq. (2.14). With the ansatz

$$w_1(\xi, \tau) = w_c(\xi) \cos \tau + w_s(\xi) \sin \tau, \quad (2.84a)$$

$$\gamma(\xi, \tau) = \gamma_c(\xi) \cos \tau + \gamma_s(\xi) \sin \tau \quad (2.84b)$$

the vorticity distribution in the wake, Eq. (2.17), is given by $\gamma(\xi, \tau) = \gamma_c(1) \cos(\tau - \Omega(\xi - 1)) + \gamma_s(1) \sin(\tau - \Omega(\xi - 1))$. Inserting Eq. (2.84) into Eq. (2.83) we obtain

$$2i \int_0^1 \left(-\frac{d}{d\xi} w_c(\xi) \sin \tau + \frac{d}{d\xi} w_s(\xi) \cos \tau - \Omega (w_c(\xi) \cos \tau + w_s(\xi) \sin \tau) \right) \frac{I_0}{I_1} d\xi - \int_1^\infty \left(\frac{I_0}{I_1} - 1 \right) \sin(\tau - \Omega(\xi - 1)) d\xi \gamma_c(1) + \int_1^\infty \left(\frac{I_0}{I_1} - 1 \right) \cos(\tau - \Omega(\xi - 1)) d\xi \gamma_s(1) + \frac{1}{\Omega} (\gamma_c(1) \cos \tau + \gamma_s(1) \sin \tau) = 0. \quad (2.85)$$

Comparing coefficients of $\cos \tau$ and $\sin \tau$ yields two linear equations for the unknowns $\gamma_c(1)$ and $\gamma_s(1)$:

$$\begin{aligned} \frac{\pi}{\Omega} \gamma_s(1) + f_c(1) - a_c(1) \gamma_c(1) - a_s(1) \gamma_s(1) &= 0, \\ -\frac{\pi}{\Omega} \gamma_c(1) + f_s(1) + a_s(1) \gamma_c(1) - a_c(1) \gamma_s(1) &= 0, \end{aligned} \quad (2.86)$$

with the abbreviations

$$\begin{aligned} a_c(1) &= \pi \int_1^\infty \cos(\Omega(\xi - 1)) \left(\frac{I_0}{I_1} - 1 \right) d\xi, \\ a_s(1) &= -\pi \int_1^\infty \sin(\Omega(\xi - 1)) \left(\frac{I_0}{I_1} - 1 \right) d\xi, \\ f_c(1) &= -2\pi i \int_0^1 \left(\Omega w_s(\xi) + \frac{d}{d\xi} w_{1,c}(\xi) \right) \frac{I_0}{I_1} d\xi, \\ f_s(1) &= -2\pi i \int_0^1 \left(-\Omega w_c(\xi) + \frac{d}{d\xi} w_{1,s}(\xi) \right) \frac{I_0}{I_1} d\xi. \end{aligned} \quad (2.87)$$

I_0 and I_1 are given in Eq. (2.77) and Eq. (2.78), respectively.

Heaving motion

A simple time-harmonic heaving motion $w_1 = \cos \tau$ ($0 \leq \xi \leq 1$) is considered ($w_c = 1$, $w_s = 0$) in order to study the effect of the channel width h and heaving frequency Ω on the vortex strength distribution at the trailing edge $\xi = 1$. The results are obtained from Eq. (2.86) and are shown in Fig. 2.6.

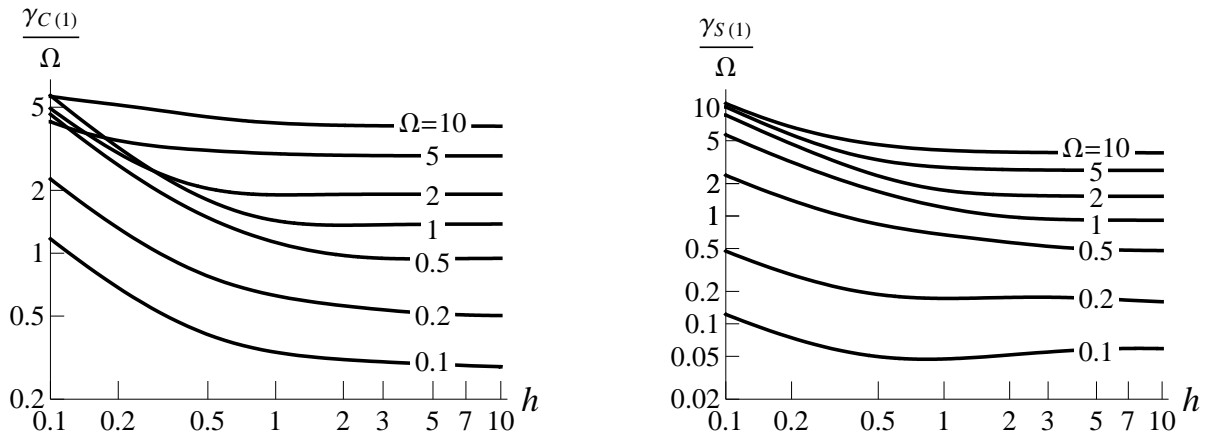


Figure 2.6: Heaving motion $w_1 = \cos \tau$: Vorticity at the trailing edge, normalized with the dimensionless heaving frequency $\Omega = \tilde{\omega}\tilde{L}/\tilde{U}$, as a function of the dimensionless semi-channel width $h = \tilde{h}/\tilde{L}$ for different values of Ω . Left: cosine component; Right: sine component.

In Fig. 2.6 the trailing edge vorticity is normalized with the frequency Ω . The size of the vortex strength at the trailing edge generally increases with increasing frequency. At low frequency, $\gamma_S(1)$ is significantly smaller than $\gamma_C(1)$ as a consequence of the prescribed cosine motion (quasi-steady response). At high frequencies $\gamma_S(1)$ and $\gamma_C(1)$ are of the same size. The solutions are practically independent of h at very large values of the half-channel width $h \approx 10$. The increase of vorticity with decreasing channel width demonstrates the “wall-effect”. A double logarithmic plot is used to examine if the solution obeys the h^{-1} behaviour at small values of h according to Eq. (2.82). This seems to be the case as the curves resemble lines of constant slope when the channel width is small ($h < 0.2$). The increase of the vortex strength due to the channel effect starts at smaller/larger values of h when the heaving frequency is higher/lower. The slope of the $\gamma_C(1)$ curve at very low values of h seems to be independent of the frequency when the frequency is below $\Omega \approx 1$, but the slope decreases at higher frequencies. Furthermore, it is interesting to note that the vorticity $\gamma_S(1)$ does not necessarily increase monotonically with a decreasing channel width. For the low heaving frequencies ($\Omega \leq 0.2$) a minimum of $\gamma_S(1)$ occurs at intermediate values of h .

When a fluid structure interaction problem is considered, the benefit of the analytical approach is somewhat limited as the deflection w_1 (that is required in Eq. (2.86) to determine the trailing-edge values) is not known in advance. Aiming at coupling the flow solution to the motion of a membrane (Sec. 1.5), a panel method is presented that solves the singular integral equation in Sec. 2.2.2 and the membrane equation simultaneously.

2.3 Panel method: Membrane in channel flow

In this section a panel method is developed for the unsteady channel flow over a membrane. In the panel method, singularity elements are distributed along the boundary surface (cf. [36]), which is a logical extension of the analytical method presented in Sec. 2.2. We construct panel

elements for the channel flow based on the singular integral equation Eq. (2.53) and a piecewise linear distribution of the vorticity strength.

2.3.1 Equations

The equations from above for the unsteady channel flow over a membrane are summarized. Scaling II is used in the panel code, see Sec. 1.5.9. Assuming a time-periodic motion and inserting the kinematic condition Eq. (2.15) and the transport of wake vorticity Eq. (2.17) into the integral equation for channel flow Eq. (2.53) yields

$$\frac{\pi}{2h} \int_0^1 \frac{\gamma(\xi, \tau)}{\sinh \left[\frac{\pi}{2h}(x - \xi) \right]} d\xi + \frac{\pi}{2h} \int_1^\infty \frac{\gamma(1, \tau - \Omega(\xi - 1))}{\sinh \left[\frac{\pi}{2h}(x - \xi) \right]} d\xi = 2\pi(\Omega w_{1,\tau}(x, \tau) + w_{1,x}(x, \tau)) \quad (2.88)$$

for $0 \leq x \leq 1$. The model for the vorticity in the wake reduces the size of the problem in that the distribution of vorticity needs to be solved only on the body. The Kutta condition Eq. (2.16)

$$\int_0^1 \gamma_\tau(\xi, \tau) d\xi + \frac{1}{\Omega} \gamma(1, \tau) = 0 \quad (2.89)$$

completes the description of the flow model. The body motion is split into two parts where either the deflection is given explicitly or the membrane equation Eq. (1.27) holds:

$$w_1(x, \tau) \text{ prescribed} \quad \text{for } 0 \leq x \leq x_A, \quad (2.90a)$$

$$\begin{aligned} -2\mu_M w_{1,\tau\tau}(x, \tau) + \frac{\alpha_M}{2} w_{1,xx}(x, \tau) - 2\beta_M w_1(x, \tau) = \\ \Omega \int_0^x \gamma_\tau(\xi, \tau) d\xi + \gamma(x, \tau) \quad \text{for } x_A < x \leq 1. \end{aligned} \quad (2.90b)$$

The trailing-edge condition in Eq. (1.18) reads

$$w_{1,x}(1, \tau) = 0. \quad (2.91)$$

2.3.2 Time-harmonic motion

With the ansatz for time-harmonic motion

$$w_1(x, \tau) = w_c(x) \cos \tau + w_s(x) \sin \tau, \quad (2.84a \text{ revisited})$$

$$\gamma(x, \tau) = \gamma_c(x) \cos \tau + \gamma_s(x) \sin \tau \quad (2.84b \text{ revisited})$$

follows for Eq. (2.88) the system of the respective sine and cosine components

$$\begin{aligned} \frac{\pi}{2h} \int_0^1 \underbrace{\frac{\gamma_c(\xi)}{\sinh \left[\frac{\pi}{2h}(x - \xi) \right]} d\xi}_{I_e(x)} - [I_c \cos(\Omega(1 - x)) + I_s \sin(\Omega(1 - x))] \frac{\pi}{2h\Omega} \gamma_c(1) + \\ [I_s \cos(\Omega(1 - x)) - I_c \sin(\Omega(1 - x))] \frac{\pi}{2h\Omega} \gamma_s(1) = 2\pi \left(\Omega w_s(x) + \frac{d}{dx} w_c(x) \right), \end{aligned} \quad (2.92a)$$

$$\frac{\pi}{2h} \int_0^1 \frac{\gamma_s(\xi)}{\sinh\left[\frac{\pi}{2h}(x-\xi)\right]} d\xi - [I_s \cos(\Omega(1-x)) - I_c \sin(\Omega(1-x))] \frac{\pi}{2h\Omega} \gamma_c(1) - [I_c \cos(\Omega(1-x)) + I_s \sin(\Omega(1-x))] \frac{\pi}{2h\Omega} \gamma_s(1) = 2\pi \left(-\Omega w_c(x) + \frac{d}{dx} w_s(x) \right), \quad (2.92b)$$

with the abbreviations

$$I_c = \int_{\Omega(1-x)}^{\infty} \frac{\cos \eta d\eta}{\sinh\left(\frac{\pi}{2h\Omega}\eta\right)}, \quad I_s = \int_{\Omega(1-x)}^{\infty} \frac{\sin \eta d\eta}{\sinh\left(\frac{\pi}{2h\Omega}\eta\right)}, \quad \eta = \tilde{\omega} \frac{\xi - x}{\tilde{U}}.$$

$I_e(x)$ in Eq. (2.92a) is introduced for later use. The other equations are decomposed likewise. The Kutta condition

$$\int_0^1 \gamma_s(\xi) d\xi + \frac{1}{\Omega} \gamma_c(1) = 0, \quad (2.93a)$$

$$\int_0^1 \gamma_c(\xi) d\xi - \frac{1}{\Omega} \gamma_s(1) = 0, \quad (2.93b)$$

the membrane equation (grouping inertia and lateral strain)

$$\Omega \int_0^x \gamma_s(\xi) d\xi + \gamma_c(x) = \frac{\alpha_M}{2} \frac{d^2}{dx^2} w_c(x) - 2(\beta_M - \mu_M) w_c(x), \quad (2.94a)$$

$$-\Omega \int_0^x \gamma_c(\xi) d\xi + \gamma_s(x) = \frac{\alpha_M}{2} \frac{d^2}{dx^2} w_s(x) - 2(\beta_M - \mu_M) w_s(x), \quad (2.94b)$$

and finally the condition for the deflection at the trailing edge

$$\frac{d}{dx} w_c(1) = 0, \quad (2.95a)$$

$$\frac{d}{dx} w_s(1) = 0. \quad (2.95b)$$

2.3.3 Discretization

Piecewise linear distribution of vorticity

We want to solve the equations of the time-periodic problem numerically. To this end, the body surface is divided into panels. A panel resides on the interval $[x_j, x_{j+1}]$. Nonuniformity in the length of the panels $\Delta x_j = x_{j+1} - x_j$ is allowed for in the composition of the discretization. On each panel, the distribution of vorticity is assumed to have a given shape. In a first attempt, a constant strength distribution has been employed on each panel (cf. [36], Sec. 10.2.3 for unbounded domain). The discretization works fine if the motion of the body is prescribed everywhere. However, when fluid structure interaction is considered (i. e. the deflection is part of the solution), odd-even decoupling occurs in the numerical solution. For that reason, on each of the n -panels, a linear interpolation function (cf. [36], Sec. 10.3.3) is used to discretize the vortex distribution

$$\left. \begin{aligned} \gamma_c(\xi) &= \frac{x_{j+1}-\xi}{\Delta x_j} \gamma_{c,j} + \frac{\xi-x_j}{\Delta x_j} \gamma_{c,j+1} \\ \gamma_s(\xi) &= \frac{x_{j+1}-\xi}{\Delta x_j} \gamma_{s,j} + \frac{\xi-x_j}{\Delta x_j} \gamma_{s,j+1} \end{aligned} \right\} \text{ on } x_j \leq \xi \leq x_{j+1}, \text{ for } j = 0, \dots, n-1. \quad (2.96)$$

The piecewise linear distribution, as shown in Fig. 2.7, is uniquely described by its values at the nodes

$$\left. \begin{array}{l} \gamma_{c,j} \\ \gamma_{s,j} \end{array} \right\} \quad j = 0, \dots, n. \quad (2.97)$$

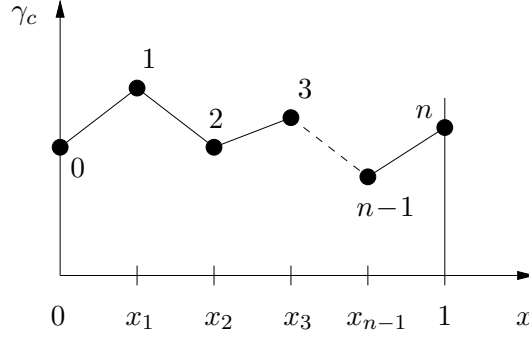


Figure 2.7: The chordwise distribution of vorticity (shown here for γ_c) is assumed to be linear on each panel; panel nodes are shown as \bullet .

The approach is of second order accuracy with respect to the spacing Δx . The following distribution for the position of the panel nodes is used

$$x_j = \left(\frac{j}{n}\right)^2 \left(3 - \frac{2j}{n}\right) \quad \text{for } j = 0, \dots, n. \quad (2.98)$$

This distribution permits a better resolution at the *LE* and *TE*, see the example in Appendix A.1.

Circulation

From the discretization in Eq. (2.96), the circulation from the *LE* up to the panel node $x = x_i$ is obtained by employing the trapezoidal rule

$$\int_0^{x_i} \gamma(\xi) d\xi = \frac{1}{2} \sum_{j=0}^{i-1} (\gamma_j + \gamma_{j+1}) \Delta x_j. \quad (2.99)$$

The discretized Kutta condition Eq. (2.93) thus reads

$$\sum_{j=0}^{n-1} (\gamma_{s,j} + \gamma_{s,j+1}) \Delta x_j + \frac{1}{\Omega} \gamma_{c,n} = 0, \quad (2.100a)$$

$$\sum_{j=0}^{n-1} (\gamma_{c,j} + \gamma_{c,j+1}) \Delta x_j - \frac{1}{\Omega} \gamma_{s,n} = 0. \quad (2.100b)$$

Deflection

From the n panels, a number of m panels are chosen to be membrane panels, see Fig. 2.8.

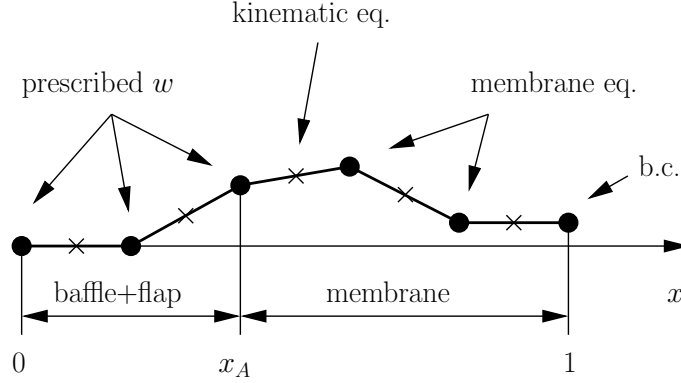


Figure 2.8: Details of the discretization (schematic, no. of panels $n = 5$, $m = 3$): Part with prescribed motion from $0 \leq x \leq x_A$, part with membrane from $x_A < x \leq 1$; panel nodes \bullet and panel midpoints \times ;

The kinematic boundary condition is evaluated at the panel-midpoints

$$x_{m,i} = \frac{x_i + x_{i+1}}{2}. \quad (2.101)$$

On the part with prescribed motion ($0 \leq x \leq x_A$), the deflection given in Eq. (2.90a) is assigned directly to the right-hand side of Eq. (2.92)

$$w_s(x_{m,i}), \quad w_c(x_{m,i}), \quad \frac{d}{dx}w_s(x_{m,i}), \quad \frac{d}{dx}w_c(x_{m,i}). \quad (2.102)$$

On the membrane ($x_A < x \leq 1$) the unknown deflections are positioned in the nodes of the panels, denoted as $w_i = w(x_i)$ for $i = 0, \dots, m - 1$. For the kinematic condition, the midpoint values are linearly interpolated as

$$w(x_{m,i}) = \frac{w_i + w_{i+1}}{2}, \quad \frac{d}{dx}w(x_{m,i}) = \frac{w_{i+1} - w_i}{\Delta x_i}. \quad (2.103)$$

The interpolation is second order accurate with respect to Δx . The membrane equation Eq. (2.94) is evaluated at the panel nodes. The second derivative is discretized to second order accuracy

$$\frac{d^2}{dx^2}w(x_i) = \frac{2}{\Delta x_i(\Delta x_i + \Delta x_{i-1})\Delta x_{i-1}} \begin{bmatrix} \Delta x_i \\ -(\Delta x_i + \Delta x_{i-1}) \\ \Delta x_{i-1} \end{bmatrix}^T \begin{bmatrix} w_{i-1} \\ w_i \\ w_{i+1} \end{bmatrix}. \quad (2.104)$$

The integrals in Eq. (2.94) are discretized as in Eq. (2.99). For the boundary condition at the trailing edge Eq. (2.95) we obtain

$$w_{c,m-1} - w_{c,m-2} = 0, \quad w_{s,m-1} - w_{s,m-2} = 0. \quad (2.105)$$

Elements of the system matrix

The collocation point of each panel is placed on its midpoint given in Eq. (2.101), see Fig. 2.8. Then, from inserting the linear vortex distribution Eq. (2.96) into Eq. (2.92a), we obtain for $I_e(x_{m,i})$ the expression

$$\sum_{j=0}^{n-1} \left(\gamma_{c,j} \frac{1}{\Delta x_j} \int_{x_j}^{x_{j+1}} \frac{x_{j+1} - \xi}{\sinh \left[\frac{\pi}{2h} (x_{m,i} - \xi) \right]} d\xi + \gamma_{c,j+1} \frac{1}{\Delta x_j} \int_{x_j}^{x_{j+1}} \frac{\xi - x_j}{\sinh \left[\frac{\pi}{2h} (x_{m,i} - \xi) \right]} d\xi \right) \quad (2.106)$$

for $i = 0, \dots, n-1$. As the wall effect is taken into account, the panel weights (integrals) differ from those in classical textbooks [36]. The integrals need to be evaluated so as to fill up the system matrix. When the midpoint $x_{m,i}$ lies on the panel $i = j$, the Cauchy principal value has to be taken for the integrals. To circumvent quadrature, we make use of the principal function

$$-\frac{\pi^2}{h} \int \frac{b - \xi}{\sinh \left[\frac{\pi}{2h} \left(\frac{a+b}{2} - \xi \right) \right]} d\xi = 2h \left(\text{Li}_2(z^2) - 4 \text{Li}_2(z) \right) + \pi(a+b-2\xi) \left[\ln(1-z) - \ln(1+z) \right] - \pi(a-b) \ln \tanh \left[\frac{\pi}{8h} (a+b-2\xi) \right] \quad (2.107)$$

with

$$z = \exp \left[-\frac{\pi}{4h} (a+b-2\xi) \right].$$

$\text{Li}_2(z)$ denotes the polylogarithm function. Evaluation in bounds yields the required expressions

$$\begin{aligned} \frac{\pi}{2h} \frac{1}{\Delta x_j} \int_{x_j}^{x_{j+1}} \frac{x_{j+1} - \xi}{\sinh \left[\frac{\pi}{2h} (x_{m,i} - \xi) \right]} d\xi = \\ \frac{h}{\pi \Delta x_j} \left\{ \pi^2 \delta_{ij} + \text{sgn}[x_{j+1} - x_{m,i}] \sum_{k=1}^{\infty} \frac{e^{-\frac{\pi}{h} |x_{j+1} - x_{m,i}|k} - 4e^{-\frac{\pi}{2h} |x_{j+1} - x_{m,i}|k}}{k^2} - \right. \\ \left. \text{sgn}[x_j - x_{m,i}] \sum_{k=1}^{\infty} \frac{e^{-\frac{\pi}{h} |x_j - x_{m,i}|k} - 4e^{-\frac{\pi}{2h} |x_j - x_{m,i}|k}}{k^2} \right\} + \ln \left| \tanh \frac{\pi (x_j - x_{m,i})}{4h} \right|, \quad (2.108) \end{aligned}$$

$$\begin{aligned} \frac{\pi}{2h} \frac{1}{\Delta x_j} \int_{x_j}^{x_{j+1}} \frac{\xi - x_j}{\sinh \left[\frac{\pi}{2h} (x_{m,i} - \xi) \right]} d\xi = \\ -\frac{h}{\pi \Delta x_j} \left\{ \pi^2 \delta_{ij} + \text{sgn}[x_{j+1} - x_{m,i}] \sum_{k=1}^{\infty} \frac{e^{-\frac{\pi}{h} |x_{j+1} - x_{m,i}|k} - 4e^{-\frac{\pi}{2h} |x_{j+1} - x_{m,i}|k}}{k^2} - \right. \\ \left. \text{sgn}[x_j - x_{m,i}] \sum_{k=1}^{\infty} \frac{e^{-\frac{\pi}{h} |x_j - x_{m,i}|k} - 4e^{-\frac{\pi}{2h} |x_j - x_{m,i}|k}}{k^2} \right\} - \ln \left| \tanh \frac{\pi (x_{j+1} - x_{m,i})}{4h} \right|, \quad (2.109) \end{aligned}$$

where δ_{ij} is Kronecker-Delta and sgn is the sign function. Again, for $i = j$ the principal value is to be understood for the integral. The advantage of the representation of matrix entries by infinite sums is their rapid convergence. For typical cases it suffices to truncate the sums at $k \approx 25$ to attain accuracy errors below 1 percent.

In the limit of large channel width we obtain from the expansion for $h \rightarrow \infty$

$$\lim_{h \rightarrow \infty} \frac{\pi}{2h} \frac{1}{\Delta x_j} \int_{x_j}^{x_{j+1}} \frac{x_{j+1} - \xi}{\sinh \left[\frac{\pi}{2h} (x_{m,i} - \xi) \right]} d\xi = 1 + \frac{x_{m,i} - x_{j+1}}{\Delta x_j} \ln \left| \frac{x_{m,i} - x_{j+1}}{x_{m,i} - x_j} \right| + \frac{\Delta x_j (2x_j + x_{j+1} - 3x_{m,i})}{144} \left(\frac{\pi}{h} \right)^2 + \dots, \quad (2.110)$$

$$\lim_{h \rightarrow \infty} \frac{\pi}{2h} \frac{1}{\Delta x_j} \int_{x_j}^{x_{j+1}} \frac{\xi - x_j}{\sinh \left[\frac{\pi}{2h} (x_{m,i} - \xi) \right]} d\xi = -1 + \frac{x_j - x_{m,i}}{\Delta x_j} \ln \left| \frac{x_{m,i} - x_{j+1}}{x_{m,i} - x_j} \right| + \frac{\Delta x_j (x_j + 2x_{j+1} - 3x_{m,i})}{144} \left(\frac{\pi}{h} \right)^2 + \dots, \quad (2.111)$$

(implying the case $i = j$). The leading terms agree with the result in unbounded domain (cf. [36], Eq. (10.76)), while the correction term is of order $\mathcal{O}(h^{-2})$ as expected from the analytical result. The above formulae for large h will be used in unbounded domain (without the h -correction) to compare the results of the panel code to the method that uses an expansion into Chebyshev polynomials in Sec. 4.1. With the elements of the system matrix given, the system of equations can be set up.

System of equations

Fig. 2.9 shows the linear system (matrix, solution vector, and rhs) and depicts a typical fill-in pattern of the system matrix and the rhs.

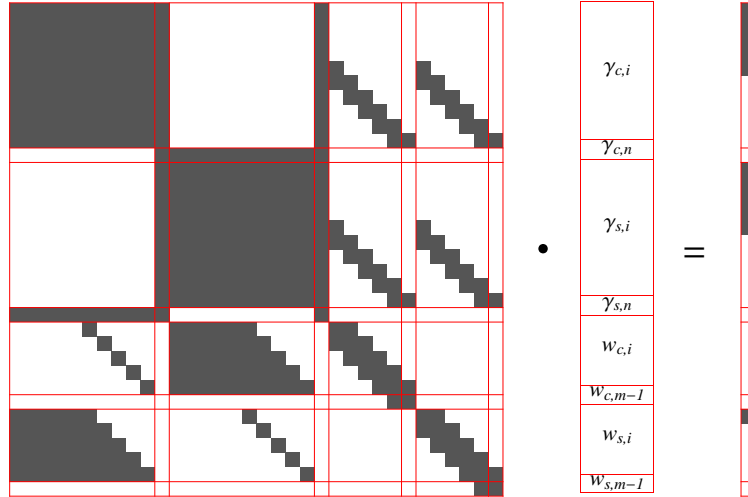


Figure 2.9: Structure of the matrix and the right hand side in the system of equations (schematic, no. of panels $n = 10$, $m = 6$): Elements with non-zero entries (fill-in) are shown as \blacksquare ; Equations are arranged in the order of Eqs. (2.92a), (2.93a), (2.92b), (2.93b), (2.94a), (2.95a), (2.94b), (2.95b); The elements of the solution vector are $\{\gamma_{c,i} | \gamma_{c,n} | \gamma_{s,i} | \gamma_{s,n} | w_{c,i} | w_{c,m-1} | w_{s,i} | w_{s,m-1}\}$ for $i = 0, \dots, n - 1$;

Postprocessing

In order to evaluate the thrust force from surface pressure Eq. (2.42), we need the first derivative of the deflection in the nodes. To obtain the first derivative with second order accuracy, three cases are distinguished

$$\frac{dw(x_i)}{dx} = \begin{cases} -\frac{(2\Delta x_0 + \Delta x_1) w_0}{\Delta x_0(\Delta x_0 + \Delta x_1)} + \frac{(\Delta x_0 + \Delta x_1) w_1}{\Delta x_0 \Delta x_1} - \frac{\Delta x_0 w_2}{\Delta x_1(\Delta x_0 + \Delta x_1)} & (i = 0) \\ -\frac{\Delta x_{i+1} w_{i-1}}{\Delta x_i(\Delta x_i + \Delta x_{i+1})} + \frac{(\Delta x_{i+1} - \Delta x_i) w_i}{\Delta x_i \Delta x_{i+1}} + \frac{\Delta x_i w_{i+1}}{\Delta x_{i+1}(\Delta x_i + \Delta x_{i+1})} & (i = 1, \dots, n-1) \\ 0 & (i = n) \end{cases}$$

The last line is introduced to comply with the boundary condition Eq. (2.95). To accurately evaluate the power, we introduce the primitive integral of the deflection. Applying the trapezoidal rule as in Eq. (2.99), we obtain

$$W(x_i) = \int_0^{x_i} w(\xi) d\xi = \frac{1}{2} \sum_{j=0}^{i-1} (w_j + w_{j+1}) \Delta x_j.$$

To determine the suction force at the leading edge, the well-known asymptotic behaviour

$$\gamma(0) = \lim_{x \rightarrow 0} \frac{K_\gamma}{\sqrt{x}}$$

is used, see for instance Eq. (2.73). Since a linear distribution of γ is employed in the panel code (see Fig. 2.7), the panel adjacent to the leading edge (the first panel) is not capable to reproduce the behaviour at the singularity. Hence, the second panel (in streamwise direction) is used to determine K_γ . Provided that the second panel is in close proximity to the leading edge such that the asymptotic expression holds, one obtains

$$\int_{x_1}^{x_2} \gamma(x) dx \approx \int_{x_1}^{x_2} \frac{K_\gamma}{\sqrt{x}} dx = 2K_\gamma (\sqrt{x_2} - \sqrt{x_1}).$$

On the other hand, the integral value can be expressed via the vorticity in the nodes 1 and 2 given as result of the panel code. With the linear interpolation Eq. (2.96), we have

$$\int_{x_1}^{x_2} \gamma(x) dx \approx \frac{\gamma_1 + \gamma_2}{2} \Delta x_1.$$

Equating then yields an approximation for the leading-edge coefficient

$$K_\gamma \approx \frac{\gamma_1 + \gamma_2}{4} \left(\sqrt{\Delta x_0} + \sqrt{\Delta x_0 + \Delta x_1} \right).$$

The coefficients for thrust from pressure and power are given as in Eqs. (2.42, 2.44)

$$T_p(t) = -\frac{8}{\pi} \int_0^1 \Delta p_1(x, t) w_{1,x}(x, t) dx,$$

$$P(t) = \frac{8}{\pi} \int_0^1 \Delta p_1(x, t) w_{1,t}(x, t) dx .$$

(the difference by a factor of two arises from the different scaling of the reference length, Sec. 1.5.9). The time-averaged values (see Eq. (2.45)) for the leading-edge thrust, thrust from surface pressure and power, respectively, can be expressed as (cf. [66], Eqs. (4.24), (4.20), (4.21))

$$T_s = K_{\gamma,c}^2 + K_{\gamma,s}^2 , \quad (2.112)$$

$$T_p = -\frac{8}{\pi} \left(\frac{1}{2} \int_0^1 \frac{d}{dx} w_s(x) \gamma_s(x) dx - \frac{\gamma_s(1)}{2} w_s(1) + \frac{\Omega}{2} \int_0^1 w_s(x) \gamma_c(x) dx + \right. \\ \left. \frac{1}{2} \int_0^1 \frac{d}{dx} w_c(x) \gamma_c(x) dx - \frac{\gamma_c(1)}{2} w_c(1) - \frac{\Omega}{2} \int_0^1 w_c(x) \gamma_s(x) dx \right) \quad (2.113)$$

and

$$P = \frac{4\Omega}{\pi} \left(-\gamma_c(1) W_s(1) + \int_0^1 w_s(x) \gamma_c(x) dx - \Omega \int_0^1 W_s(x) \gamma_s(x) dx \right) - \\ \frac{4\Omega}{\pi} \left(-\gamma_s(1) W_c(1) + \int_0^1 w_c(x) \gamma_s(x) dx + \Omega \int_0^1 W_c(x) \gamma_c(x) dx \right) . \quad (2.114)$$

The panel code has been applied to several test examples, see Appendix A. Results for a prescribed motion in a channel (flapping foil and travelling wavy surface) are given in Ch. 3. A comparison to CFD results for a coupled problem is shown in Ch. 4.

Chapter 3

Propulsion

3.1 Flapping foil: potential flow in unbounded domain

3.1.1 Combined plunging and pitching motion

We use the classical model by Theodorsen [104] for a rigid two-dimensional flat plate wing in unsteady potential flow described in Sec. 2.1. The solution for the thrust force is given by Garrick [26]. The model has been used by Lighthill [53] to study lunate tail propulsion of fast swimming fish. The model is based on the following assumptions:

- 2-dim potential flow with freestream velocity \tilde{U} , density $\tilde{\rho}$,
- slender body of length \tilde{L} with rounded LE and sharp TE ,
- small deflections ($\epsilon \ll 1$),
- time-harmonic motion.

The instantaneous forces of the linear model are compared to a CFD result for a flapping foil with a NACA 0012 profile. The limits of the model assumptions with respect to the size of the amplitude, applicability of the Kutta condition, the dynamic stall limit are discussed in Sec. 3.1.6. In the time-harmonic motion Eq. (2.18), the complex valued amplitude function w_1 for combined plunging and pitching motion is given as

$$w_1 = H - iA(x - B), \quad (3.1)$$

where H , A , and B are the plunging amplitude, pitching angle amplitude, and reference point for the pitching motion, respectively. A sketch of the situation is given in Fig. 3.1.

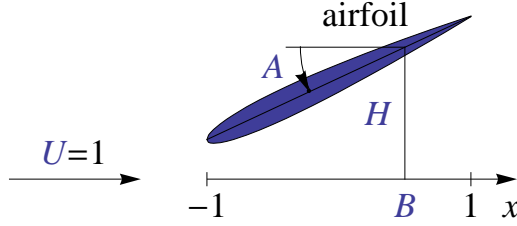


Figure 3.1: Nomenclature for flapping airfoil: plunging amplitude H , max. pitching angle A , reference point for pitching B .

The phase angle between plunging and pitching motion is chosen as 90° . As pointed out by Lighthill [54], a change in the phase difference can be achieved by giving H an imaginary part. This is simply equal to a change in the position B . The size of H and A can be chosen arbitrarily as the linear model allows to absorb a different scaling in the small parameter ϵ . However, we choose the parameters of motion such that ϵ represents the maximum excursion of the foil with respect to the chord. Thus, as in Sec. 2.1.7, we require $w_{1,max} = 2$.

Lighthill [54] related the pitching and plunging amplitudes to each other by the so-called feathering parameter, defined as

$$\chi = \frac{A}{H\sigma}. \quad (3.2)$$

The feathering parameter identifies the degree to which the foil pitch angle coincides with the slope of the path that the pitch axis traces out as the foil moves from right to left in the fluid at rest. When $\chi = 0$, the foil performs pure plunging motion. When $\chi = 1$, the pitch angle follows exactly the slope of the foil and, when $B = 1/2$, there is no thrust. Lighthill called this case “perfect feathering”. We note that it is important to set the phase angle to 90° to make χ a meaningful quantity.

Lighthill [54] proposed that the pitching-axis should fall in the range $1/2 \leq B \leq 1$ (near by or at the trailing edge) and feathering should be within the range $0.6 \leq \chi \leq 0.8$ in order to obtain optimum flapping motion of the foil. The proposed values serve as a guidance for the problem of optimal propulsion below and are used afterwards for comparison.

3.1.2 Forces for time-harmonic motion

The representation by Chebyshev polynomials outlined in Sec. 2.1.7 is used to obtain the expressions for the forces. For the flapping motion the sums in Eq. (2.19) and in the pressure difference Eq. (2.21) are finite. The instantaneous value of the lift force is then obtained from Eq. (2.34)

$$\tilde{L}(\tilde{t}) = \epsilon \Re \left[\pi \tilde{\rho} \tilde{U}^2 \frac{\tilde{L}}{2} (a_0 + a_1) \exp(i\tilde{\omega}\tilde{t}) \right], \quad (3.3)$$

(the lift force is denoted as time-dependent function $\tilde{L}(\tilde{t})$ to distinguish it from the chord \tilde{L}) with the coefficients in Eqs. (2.29, 2.30) given as

$$a_0 = A\sigma + A(2B - 1)\sigma F - 2(A - H\sigma)G + i[2(A - H\sigma)F + A(2B - 1)\sigma G],$$

$$a_1 = \sigma(-2A + H\sigma) + iAB\sigma^2,$$

where F and G are defined in Eq. (2.33). The nose suction force Eq. (2.37) is then

$$\begin{aligned} \tilde{T}_s(\tilde{t}) = \epsilon^2 \frac{1}{2} \pi \tilde{\rho} \tilde{U}^2 \frac{\tilde{L}}{2} \{ [A\sigma + A(2B - 1)\sigma F - 2(A - H\sigma)G] \cos(\tilde{\omega}\tilde{t}) - \\ [2(A - H\sigma)F + A(2B - 1)\sigma G] \sin(\tilde{\omega}\tilde{t}) \}^2, \end{aligned}$$

and the thrust force from the surface pressure Eq. (2.36)

$$\begin{aligned} \tilde{T}_p(\tilde{t}) = \epsilon^2 \frac{1}{2} \pi \tilde{\rho} \tilde{U}^2 \frac{\tilde{L}}{2} 2A \sin(\tilde{\omega}\tilde{t}) \{ [-\sigma(A - H\sigma) + A(2B - 1)\sigma F - 2(A - H\sigma)G] \cos(\tilde{\omega}\tilde{t}) - \\ [AB\sigma^2 + 2(A - H\sigma)F + A(2B - 1)\sigma G] \sin(\tilde{\omega}\tilde{t}) \}. \end{aligned}$$

The total thrust from Eq. (2.35) is then

$$\begin{aligned} \frac{\tilde{T}(\tilde{t})}{\epsilon^2 \frac{1}{2} \pi \tilde{\rho} \tilde{U}^2 \frac{\tilde{L}}{2}} = [A\sigma - A(1 - 2B)\sigma F - 2(A - H\sigma)G]^2 \cos^2(\tilde{\omega}\tilde{t}) + \\ \left\{ -2[A - 2(A - H\sigma)F + A(1 - 2B)\sigma G] [A(1 - 2B)\sigma F + 2(A - H\sigma)G] + \right. \\ \left. 2A\sigma [-(A - H\sigma)(1 + 2F) + A(1 - 2B)\sigma G] \right\} \cos(\tilde{\omega}\tilde{t}) \sin(\tilde{\omega}\tilde{t}) + \\ \left\{ [2(A - H\sigma)F - A(1 - 2B)\sigma G - A]^2 - A^2(1 + 2B\sigma^2) \right\} \sin^2(\tilde{\omega}\tilde{t}). \end{aligned} \quad (3.4)$$

3.1.3 Dimensionless time-averaged thrust and energy

Time-averaged values over one period of the energy E imparted to the fluid and the thrust T acting on the body as given in Eq. (2.45) are

$$E = [4A^2 - 8AH\sigma + (A^2(1 - 2B)^2 + 4H^2)\sigma^2] (F - F^2 - G^2), \quad (3.5)$$

$$\begin{aligned} T = A^2(1 - 2B)\sigma^2 - (4A^2 - 4AH\sigma + 2A^2(1 - 2B)\sigma^2) F + \\ (-2A^2(1 + 2B)\sigma + 4AH\sigma^2) G + \\ [4A^2 - 8AH\sigma + (A^2(1 - 2B)^2 + 4H^2)\sigma^2] (F^2 + G^2). \end{aligned} \quad (3.6)$$

From E and T the propulsive efficiency can be calculated with Eq. (2.47). In the cases of “perfect feathering” motion, $\chi = 1$ and $B = 1/2$, there is no vorticity shed into the wake (non-circulatory flow) and consequently $E = T = 0$. However, there are non-zero instantaneous thrust and lift forces due to the added mass effect (cf. [11], Sec. 5.2).

3.1.4 Comparison of instantaneous forces to CFD results

A flapping NACA 0012 profile in free stream is investigated with the commercial software Fluent[®] 6.3.26 in order to compare the result to linear theory. It is of particular interest to what extent the linear model can predict the instantaneous forces acting on a slender foil.

In the CFD model, a moving mesh procedure is used to guarantee a boundary-fitted grid at the foil. For the fluid the incompressible Euler equations are solved. The time-stepping is continued until the flow solution is periodic in time. The following motion parameters are chosen:

$$\epsilon = 0.1, \quad H = 1.789, \quad A = 0.447, \quad B = 1, \quad \sigma = 0.314.$$

The maximum excursion is reached at the leading edge. H and A are chosen such that $w_{1,max} = 2$. Following Lighthill's recommendation for the position of the pitch axis and the size of the feathering parameter (Sec. 3.1.1), the axis is placed at the trailing edge $B = 1$ and feathering in Eq. (3.2) amounts to $\chi = 0.796$. The values given to the flapping amplitude ϵ and the reduced frequency σ are relatively small. The results for the instantaneous lift $\tilde{L}(\tilde{t})$ and thrust $\tilde{T}(\tilde{t})$ from the linear model and the CFD simulation are shown in Fig. 3.2.

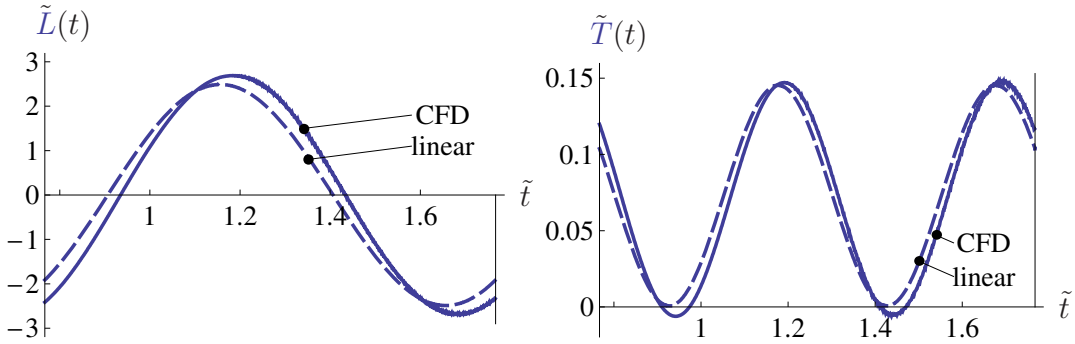


Figure 3.2: Instantaneous forces on a flapping NACA 0012 foil as a function of time. Comparison of the linear model to a CFD simulation. Left: Lift force; Right: Thrust force.

Lift and thrust of the linear model are given by Eq. (3.3) and Eq. (3.4), respectively. The analytical and numerical results are in good agreement and it can be concluded that the linear model predicts the forces (including nose-suction) quite well. It is interesting that a relatively high grid resolution (200 cells along the chord, nonuniform spacing) is necessary to obtain the thrust force accurately. This makes the CFD method costly and inappropriate for finding optimal motions.

3.1.5 Comparison of linear and nonlinear model at large deflections

The linear model has several limitations. First and foremost, the linear model is confined to motions with small deflections that are focused in the present work. Nevertheless, it is of interest to check if reasonable results can be obtained at values of the expansion variable being not too small. In doing so, the linear model is compared to an advanced potential flow model proposed by Katz & Weihs [38] using potential flow theory that accounts for the nonlinear effect due to large foil deflections and the free motion of the vortex wake. The thin foil moves along the curved path of large amplitude in such a way that the disturbance in the flow and pressure field caused by the foil's motion remains small. [38] continuously varied the plunging amplitude \tilde{H} at the leading edge and superimposed a pitching motion defined by a pitch axis at the leading edge $B = -1$ and 90° phase shift, with a pitching amplitude chosen such that the *effective* angle

of attack remains at a small value of 5° (a case where flow separation is unlikely to occur in reality). Three different flapping frequencies are considered. The conversion to the notation in the mentioned paper is given in Appendix B. It suffices to replicate Eq. (B.1) to provide the parameters

$$\sigma = \left\{ \frac{\pi}{40}, \frac{2\pi}{40}, \frac{3\pi}{40} \right\}, \quad H = 2 \frac{\tilde{H}}{\tilde{L}}, \quad A = 2\sigma \frac{\tilde{H}}{\tilde{L}} - 5^\circ, \quad B = -1. \quad (3.7)$$

that are to be plugged into Eqs. (3.5), (3.6), (2.47). The obtained propulsive efficiency η and the thrust coefficient given by $c_T = \frac{\pi}{4} T^1$ are plotted in Fig. 3.3.

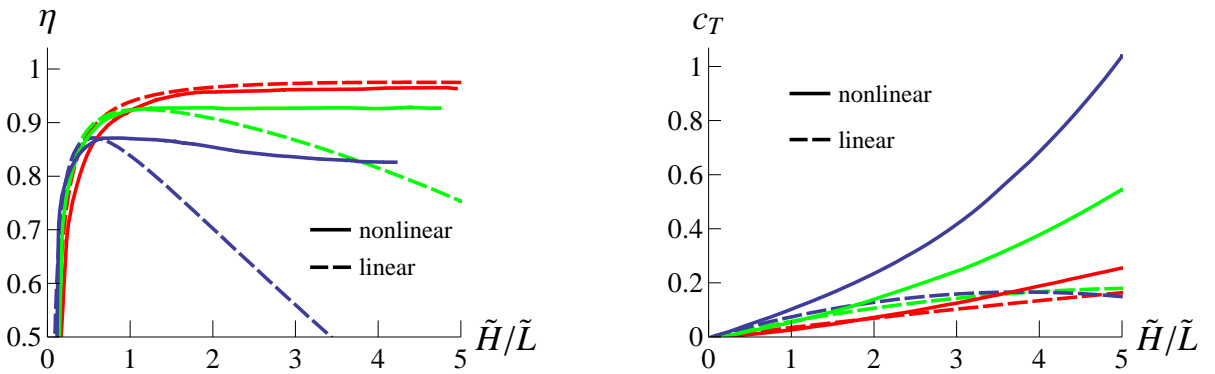


Figure 3.3: Comparison of linear and nonlinear potential model of a plunging and pitching plate in large amplitude motion. Left: propulsive efficiency; Right: thrust coefficient; (red, green, blue) have $\sigma = \left\{ \frac{\pi}{40}, \frac{2\pi}{40}, \frac{3\pi}{40} \right\}$, respectively. Nonlinear solutions reproduced from [38].

The curves for efficiency and thrust agree well even for $\tilde{H}/\tilde{L} = 5$ as long as the flapping frequency σ is small, while at higher σ the agreement is good as long as \tilde{H}/\tilde{L} is below ≈ 1 . This result is surprising as the linear model does not account for large deflections and wake dynamics. It can be concluded from Fig. 3.3 that the agreement between linear and nonlinear potential flow theory is good when the product of frequency σ and maximal excursion ϵ does not exceed a certain limit, say $\epsilon\sigma \approx 0.24$. The product is approximately equivalent to the Strouhal number defined by the ratio of streamwise and lateral distance of the vortex centers in the wake $St \approx 2\epsilon\sigma/\pi$. Triantafyllou et. al. [107] emphasized the importance of the Strouhal number for the dynamics in the wake. In agreement to the present comparison, Streitlien & Triantafyllou [102] concluded from a comparison of a simulation for two-dimensional ideal flow, a Kármán vortex street model, and linear theory that the linear model predicts thrust well for all but the highest Strouhal numbers.

For the present example by Katz & Weihs, the linear theory significantly underestimates the achievable thrust coefficient c_T as \tilde{H}/\tilde{L} increases. At first glance, the trend of c_T with \tilde{H}/\tilde{L} seems to contradict the inherent feature of the linear model that the thrust coefficient scales with the square of the amplitude. However, in the present case the ratio of pitching to plunging motion changes with the amplitude Eq. (3.7). As the effective angle of attack is held constant,

¹ c_T is the thrust coefficient as defined in Katz & Weihs [38]

the feathering parameter given in Eq. (3.2) increases with \tilde{H}/\tilde{L} , with the consequence that the thrust coefficient c_T degrades. The present comparison is restricted to motions that comply with the assumptions required by potential flow theory. We discuss the limits of the potential flow model in the next subsection.

3.1.6 Remarks to the limits of the potential flow model

It has been shown in the previous subsection that the linear model by Theodorsen can be applied to motions with larger deflections when the product of deflection and frequency is kept below a certain threshold. The inviscid model relies on the validity of the unsteady Kutta condition and on the assumption of attached flow. The limits of the model assumptions have been investigated quite well in the literature for pure plunging motion. Results from panel codes, CFD simulations and experiments have been compared.

The applicability of the unsteady Kutta condition is discussed in [36], Sec. 13.11. Although measurements show that the streamlines do not leave parallel to the trailing edge at $\sigma > 0.6$, the pressure and lift distributions are not significantly affected even at higher frequencies. [37] studied the vortex rollup of the wake behind a heaving airfoil and found good agreement between experiment and an unsteady panel code for the case $\epsilon = 0.019$, $\sigma = 8.5789$ ($\epsilon\sigma = 0.163$). As the shape of the wake is associated to the airfoil's circulation that is fixed by the trailing edge condition, the unsteady Kutta condition can still be used to calculate the lift. In agreement to that, Navier–Stokes computations by [108] for an airfoil in pure plunging oscillation predict attached flow at exactly the same value ($\epsilon\sigma = 0.16$) and the onset of dynamic stall when $\epsilon\sigma = 0.175$ is exceeded. Only light flow separation occurs at $\epsilon\sigma = 0.24$. Surprisingly, Jones et. al. [35] reported for an airfoil plunging at small deflection $\epsilon = 0.04$ and high frequency $\sigma = 7.5$ that the velocity profile in the wake derived from a panel code agrees well with experiments (despite the high value $\epsilon\sigma = 0.30$), while at $\epsilon\sigma \geq 0.41$ they observe a non-symmetric vortex wake in the experiment (called dual-mode) that cannot be predicted with the panel code.

From the viewpoint of optimum motion, pure plunging is of minor significance because the efficiency decreases rapidly when the frequency is increased so as to generate useful thrust. In this regard, combined plunging and pitching motion is of more interest. When plunging and pitching are combined appropriately such that the effective angle of attack is kept low, flow separation may be suppressed at the levels of $\epsilon\sigma$ where separation is present in pure plunging motion.

We conclude that we expect the linear model to apply for large deflection plunging motions at correspondent low frequency $\epsilon\sigma \leq 0.24$, small angle pitching motions at all frequencies, and appropriate combinations of both.

3.2 Optimal foil motion

In this section the optimum propulsive motion for a flapping foil is discussed on the basis of the linear model. Linear theory is based on the assumptions of small foil deflections, but can be reasonably applied at large foil excursion when the frequency is low, see the discussion in Sec. 3.1.6.

We attempt to find the optimum motion in terms of a Pareto front (cf. [97]) of maximum propulsive efficiency for a given thrust. Most optimizations focus on finding motions that maximize the thrust coefficient. The thrust coefficient generally increases with the flapping amplitude and can be raised further with increasing amplitude even when massive flow separation occurs. However, the propulsive efficiency in the stalled regime is very low. On the other hand, when only the efficiency is optimized, the resulting thrust becomes impractically small ([109], case 3).

The experimental results by Anderson et. al. [7] for combined plunging and pitching motion clearly show that thrust and efficiency are competing trends. An optimization that includes both thrust and efficiency has been undertaken by Tuncer & Kaya [109]. They conducted a numerical optimization (at fixed reduced frequency $\sigma = 0.5$) of Navier–Stokes results for a flapping airfoil at a Reynolds number based on chord of $\text{Re}_c = 10^4$ and obtained a maximum propulsive efficiency of $\eta = 0.675$ at a plunging amplitude based on the chord of $H = 0.83$. The results show that the two-state optimization yields an optimal dimensionless flapping amplitude less than 1. The maximum efficiency from the simulation is significantly lower than the measured value $\eta = 0.87$ by [7] for $H = 0.75$ at $\text{Re}_c = 4 \times 10^4$. The discrepancy may have its cause in the fixed frequency or in higher viscous drag due to lower Reynolds number. Apart from that, the exceptionally high efficiency reported in [7] has not been confirmed in later experiments by the same group: [78] and [79] reported for a flapping foil under equivalent conditions as in [7] a maximum measured propulsive efficiency of $\eta \approx 0.667$ and $\eta = 0.715$, respectively.

In [78] the experimental results are plotted in the form of propulsive efficiency against the thrust coefficient. As can be seen from the equation of the efficiency Eq. (2.47), the problem of finding motions with maximum efficiency for given thrust can be equivalently stated as done by Wu [119] such that the energy loss is minimized under the side condition of prescribed thrust. [119] introducing the so-called “proportional-loading parameter“ defined as the thrust coefficient divided by the square of the plunging amplitude. However, under these conditions no limit is given to the pitching amplitude and the resulting thrust coefficient depends on the initially unknown plunging amplitude.

In the present optimization, the thrust coefficient is directly prescribed and the flapping amplitude is constraint along the entire chord:

$$|w_1(x, t)| \leq w_{1,max} \quad \text{for} \quad -1 \leq x \leq 1.$$

3.2.1 Optimization under constraints

We want to optimize the efficiency η as a function of the motion variables A , B , H , and σ under the side conditions of given thrust ($T \geq 0$) and restricted amplitude of motion $w_{1,max}$. We start with the optimization using the Lagrange multiplier method. Once the Lagrange optimization problem is stated the procedure is straightforward. However, the expressions quickly become quite longish. Thus, thereafter a more direct approach is presented that leads to the same results, but allows to give the expressions in a somewhat compacter form. An expansion of the results at large flapping frequency then motivates the search for a boundary optimum.

Lagrange multiplier method

The optimization with a Lagrange function under constraints is a well-known procedure, cf. [41] for an introduction. In the present optimization we minimize the energy E in Eq. (3.5) under two side conditions. Then the Lagrange function reads

$$h = E + \mu g_1 + \lambda g_2, \quad (3.8)$$

where μ and λ are the Lagrange multipliers and the side conditions are

$$g_1 = T(A, B, H, \sigma) - \underbrace{T}_{\text{given}} = 0, \quad (3.9)$$

$$g_2 = H^2 + A^2(1 + B)^2 - \underbrace{w_{1,max}^2}_{\text{given}} = 0. \quad (3.10)$$

The first side condition prescribes the thrust T and the second condition limits the amplitude of motion to $w_{1,max}$. Note that as a consequence of considering Eq. (2.47) at a given thrust T , requiring a minimum of E is equivalent to finding a maximum of η . The second condition Eq. (3.10) is stated such that the maximum amplitude $w_{1,max}$ is reached at the leading edge. We remark that for a rigid foil it suffices to fix the amplitude either at the LE or at the TE in order to restrict the amplitude along the entire chord. However, following the recommendation for optimum motion by Lighthill [54], the pivot point for pitching should be placed close to the trailing edge. When the pitching axis is in the downstream half of the chord $B \geq 0$, the foil's maximum deflection occurs at the LE . The present results have been checked against the case where the amplitude is constraint at the TE and prove to be superior. From Eq. (3.8) the optimum motion is obtained as solution of

$$\frac{\partial h}{\partial A} = 0, \quad \frac{\partial h}{\partial B} = 0, \quad \frac{\partial h}{\partial H} = 0, \quad \frac{\partial h}{\partial \sigma} = 0, \quad g_2 = 0, \quad g_1 = 0, \quad (3.11)$$

which have to be solved for the optimization variables A, B, H, σ and the Lagrange multipliers μ and λ . The explicit form of the equations is given in Appendix C.1. A difficulty that appears in finding a solution is that E and T in Eq. (3.8) and Eq. (3.9), respectively, depend nonlinearly on σ , as Eq. (3.5) and Eq. (3.6) contain F and G that are related to Bessel functions of the parameter σ . In the attempt of finding a solution, this problem is circumvented by using T as an unknown instead of σ , which is now assumed as given. Then, the analysis leads to an algebraic equation of order 6 for the pitching motion reference point B , Fig. 3.1. This straightforward, but tedious procedure is outlined in Appendix C.1. Still, the expression for B is too prolate to write it down. Fortunately, the same result can be obtained by using a more direct approach that turns out to be easier. The equality of the result for B to that from Eq. (3.11) has been checked with *Mathematica* by a symbolic comparison. The idea and the results of the direct approach are given in the following.

Elimination method

The solution procedure is simplified by employing the so-called elimination method, cf. [41]. Details of the calculation are given in Appendix C.2. First, we write the expression for energy

Eq. (3.5) and the respective side conditions Eqs. (3.9, 3.10) in explicit form as

$$E = E(A, B, H, \sigma), \quad (3.12)$$

$$T = T(A, B, H, \sigma), \quad (3.13)$$

$$w_{1,max} = w_{1,max}(A, B, H). \quad (3.14)$$

Then, in the elimination step, the conditions Eqs. (3.13, 3.14) are used together with Eq. (3.12) to eliminate the optimization variables H and A . One obtains a given function f of the form (Appendix C.2, Eq. (C.30))

$$f(B, \sigma, E; T, w_{1,max}) = 0 \quad (3.15)$$

that we interpret as an implicit expression for the energy E , where the side conditions are incorporated and represented by the given parameters T and $w_{1,max}$. The optimization that yields a minimum of E (equal to a maximum of η) is then stated as

$$\frac{\partial f}{\partial B} = 0, \quad \frac{\partial f}{\partial \sigma} = 0. \quad (3.16)$$

As in the Lagrange multiplier method, we write $T = T(\sigma)$ and express all solutions as functions of σ instead of T . The following closed-form results are obtained (see Appendix C.2)

$$T(\sigma; w_{1,max}) = -\frac{L}{K} \left[1 - \left(\frac{Q}{Q'} \left(\frac{K'}{K} - \frac{L'}{L} \right) \right)^2 \right], \quad (3.17)$$

$$E(\sigma; w_{1,max}) = 4 \left[\frac{\sqrt{L/(KQ)'}}{(1/Q)'} \right]^2, \quad (3.18)$$

where the prime indicates a derivative with respect to σ , and the σ -dependent functions are

$$K = 2G\sigma + 3\sigma^2 - 2F(2 + 3\sigma^2) + (F^2 + G^2)(4 + 9\sigma^2), \quad (3.19)$$

$$L = w_{1,max}^2 4\sigma^2 \left[\sigma^2/4 + F + \sigma G - (1 + \sigma^2)(F - F^2 - G^2) \right], \quad (3.20)$$

$$Q = \frac{(4 + 9\sigma^2)(F - F^2 - G^2)}{K}. \quad (3.21)$$

F and G are given in Eq. (2.33). Energy E and thrust T are related by

$$E = \frac{Q}{K} \left(\sqrt{L + KT} - \sqrt{L} \right)^2. \quad (3.22)$$

The location of the pitching axis B can be expressed via the auxiliary variables

$$S = w_{1,max}^2 4\sigma^2 - E(\sigma; w_{1,max}) / (F - F^2 - G^2), \quad (3.23)$$

$$R = w_{1,max}^2 4\sigma^2 (F^2 + G^2) - T(\sigma; w_{1,max}) + \left(\frac{F}{2} + \sigma \frac{G}{2} - F^2 - G^2 \right) S, \quad (3.24)$$

$$D_0 = \left(2 + \frac{7}{2}\sigma^2\right) F - \sigma^2 \left(1 - \frac{3}{2}\sigma G\right), \quad (3.25)$$

$$D_1 = 2\sigma^2(1 + F) + 2(2 + 3\sigma^2)\sigma G, \quad (3.26)$$

$$N = R^2(4 + 9\sigma^2)(4\sigma)^2 - 24\sigma^2 RSD_1 + S^2 D_1^2, \quad (3.27)$$

$$P = R^2(4 + 9\sigma^2)8\sigma^2 - 24\sigma^2 RSD_0 - RD_1[(w_{1,max}8\sigma)^2 - 2S(4 - 3\sigma^2)] + 2S^2 D_0 D_1 \quad (3.28)$$

as

$$B = B(\sigma; w_{1,max}) = -\frac{P}{2N}. \quad (3.29)$$

B is only a function of σ , as E and T can be eliminated by inserting Eqs. (3.17, 3.18) into Eqs. (3.23, (3.24)). From the result for B , the pitching amplitude A , plunging amplitude H , and the feathering parameter χ , respectively, can be determined. The pitching amplitude (Appendix C.2, Eq. (C.29)) reads

$$A = A(\sigma; w_{1,max}) = \sqrt{\frac{R}{D_0 + D_1 B}} \quad (3.30)$$

with R , D_0 , D_1 , and B from Eqs. (3.24–3.26, 3.29). The plunging amplitude follows from Eq. (3.10)

$$H = H(\sigma; w_{1,max}) = \sqrt{w_{1,max}^2 - A^2(1 + B)^2}$$

and the feathering parameter χ from Eq. (3.2). The efficiency is obtained by inserting Eqs. (3.17, 3.18) into Eq. (2.47). The results are equal to those obtained with the Lagrange multiplier method and are shown in Sec. 3.2.2.

Thrust-free solution

From Eq. (3.22) it is evident that $E = 0$ at $T = 0$. Then, from Eq. (3.18)

$$\left(\frac{L}{KQ}\right)' = 0$$

which gives with Eq. (3.21)

$$\frac{(4 + 9\sigma^2)'}{4 + 9\sigma^2} + \frac{(F - F^2 - G^2)'}{F - F^2 - G^2} = \frac{L'}{L}$$

with L from Eq. (3.20). The solution for $w_{1,max} = 2$ is

$$\sigma = 1.16882, \quad B = 1/2, \quad H = 0.990898, \quad A = 1.158182, \quad T_s = -T_p = (A\sigma)^2 = 1.8325, \quad (3.31)$$

with T_s from Eq. (2.46). It is interesting that the curve of optimum motions passes through the thrust-free point $T = 0$ at a reduced frequency σ that is *not* small compared to one, as one would expect from intuition in order to reduce the energy spent into the wake. In the contrary, σ is of order one. Since $B = 1/2$ and $T = 0$, Eq. (3.6) enforces $A = H\sigma$. Thus, the feathering parameter χ in Eq. (3.2) is exactly one.

Limit of large reduced frequency

The results for optimal motion from above are considered in the limit of large reduced frequency σ . The details of the calculation are given in Appendix C.3. Setting $w_{1,max} = 2$, an expansion of Eqs. (3.17, 3.18) with respect to $\sigma \gg 1$ yields

$$T = \frac{21229}{12996} - \frac{438544535}{35557056 \sigma^2} + \dots ,$$

$$E = \frac{5041}{12996} - \frac{168306281}{35557056 \sigma^2} + \dots .$$

From this result, one can see that the optimization limits the attainable thrust to $T^{opt} = \frac{21229}{12996}$. The propulsive efficiency Eq. (2.47) is

$$\eta = \frac{1}{1 + E/T} = \frac{299}{370} + \frac{2370511}{3285600 \sigma^2} + \dots$$

The solution of Eq. (3.29) is

$$B = \frac{1}{2} + \frac{3053}{34656 \sigma^2} + \dots \quad (3.32)$$

and from that

$$A = \frac{4}{3} - \frac{55835}{77976 \sigma^2} + \dots \quad (3.33)$$

$$H = \frac{223}{114 \sigma} + \dots \quad (3.34)$$

The feathering parameter Eq. (3.2) reads

$$\chi = \frac{152}{223} + \frac{10244006}{8503659 \sigma^2} + \dots \quad (3.35)$$

Based on the present optimization, no optimum solution exists when the required thrust T is above the threshold T^{opt} . This result is surprising because the setup of the optimization appears reasonable. On the other hand, irrespective of the optimization problem, an expansion of Eq. (3.6) at large reduced frequencies σ – with A , H , and B kept constant – shows that $T \sim \sigma^2$, i. e. the thrust T exceeds T^{opt} when σ is sufficiently large. Consequently, a boundary optimum must exist at a very high flapping frequency.

The boundary optimum

The solution of the above optimization problem reaches a finite thrust $T = T^{opt}$ as $\sigma \rightarrow \infty$. Nonetheless, Eq. (3.6) admits motions such that $T \rightarrow \infty$ in the limit $\sigma \rightarrow \infty$. Thus, in the present case we attempt to find optima in the limit of infinite frequency that fulfill the requirements of $T > T^{opt}$ and max. amplitude $w_{1,max}$. Although an expansion at infinite frequency is problematic, following the discussion in Sec. 3.1.6, the results may still be applicable to large frequency motions ($\sigma \approx 8$) at small deflection ($\epsilon \approx 0.03$). The above optimization problem is

altered such that we seek a minimum of the energy E as function of A , B , H at *given* frequency $\sigma \rightarrow \infty$. The approach allows to find a closed-form expression that relates the maximum attainable efficiency η to the thrust T . The Lagrange function h is adopted from Eq. (3.8) as

$$h = \lim_{\sigma \rightarrow \infty} E + \mu \left[\lim_{\sigma \rightarrow \infty} T(A, B, H, \sigma) - T \right] + \lambda \left[H^2 + A^2(1 + B)^2 - w_{1,max}^2 \right], \quad (3.36)$$

with the Lagrange multipliers μ and λ . Since σ is given (as infinite), the condition $\partial h / \partial \sigma = 0$ in Eq. (3.11) is dropped. Then

$$\frac{\partial h}{\partial A} = 0, \quad \frac{\partial h}{\partial B} = 0, \quad \frac{\partial h}{\partial H} = 0, \quad g_2 = 0, \quad \lim_{\sigma \rightarrow \infty} g_1 = 0, \quad (3.37)$$

with g_1 and g_2 as in Eq. (3.9) and Eq. (3.10), respectively. These are 5 equations for the 5 unknowns A , B , H , μ and λ . For simplicity, we take $w_{1,max} = 2$. Details of the solution procedure are provided in Appendix C.4. The solution to Eq. (3.37) is

$$\begin{aligned} B &= \frac{1}{2} + \frac{3(-3 - T + 3\sqrt{1+T})}{8} \frac{1}{\sigma^2} + \dots \\ A &= \frac{4}{3} - \frac{-44 - 9T + 60\sqrt{1+T}}{54} \frac{1}{\sigma^2} + \dots \\ H &= \frac{1 + 3\sqrt{1+T}}{3} \frac{1}{\sigma} + \dots \end{aligned}$$

Note that at $T = T^{opt}$ the results match Eqs. (3.32)–(3.34). From Eq. (3.5)

$$E = \left(\sqrt{1+T} - 1 \right)^2 + \dots$$

and with Eq. (2.47) follows a relation between the efficiency and the thrust

$$\eta = \frac{1}{2} + \frac{1}{2\sqrt{1+T}} + \dots \quad (3.38)$$

3.2.2 Results

The results for optimal propulsive motion from the previous sections for the amplitude constraint at $w_{1,max} = 2$ are displayed in the Figs. 3.4, 3.5 and 3.6.

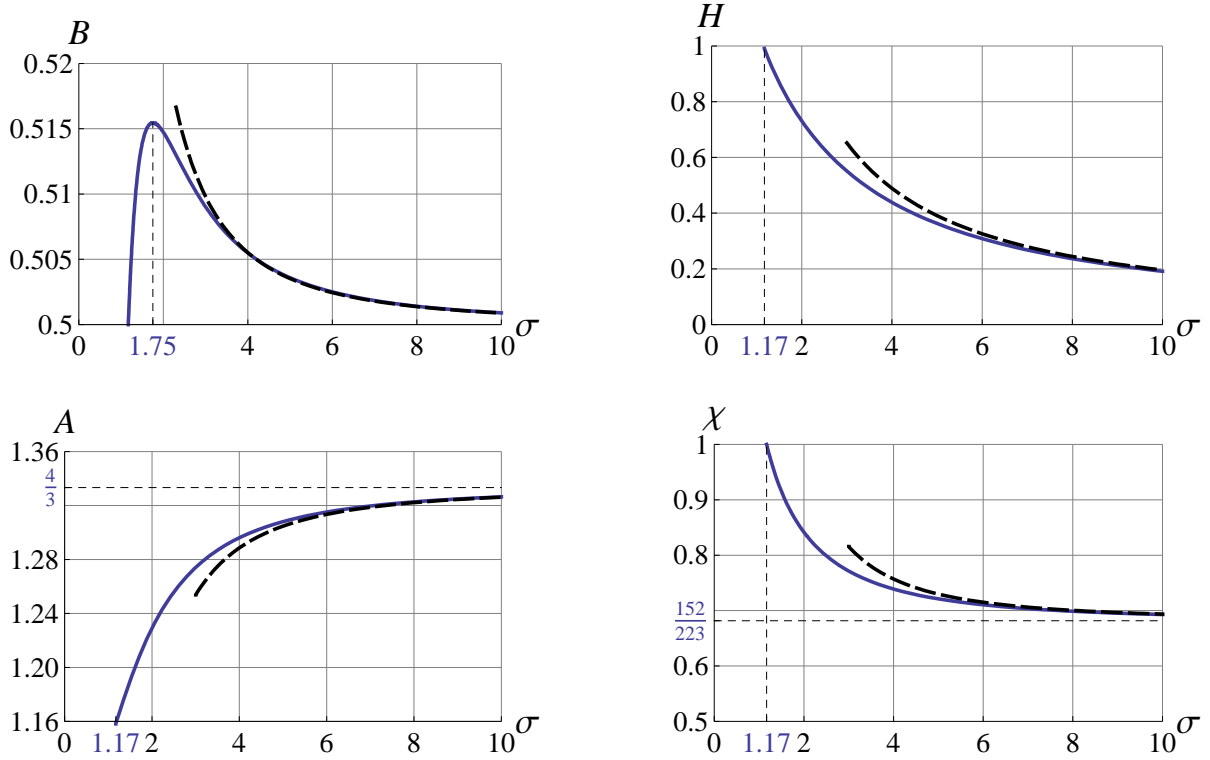


Figure 3.4: Result for optimal foil motion over the reduced frequency σ ; left top: pivot point B , right top: plunging amplitude H , left bottom: pitching amplitude A , right bottom: feathering parameter χ ; Blue lines: Optimal motion in the range $T < T^{opt}$; Black, dashed lines: Asymptotic lines for $\sigma \rightarrow \infty$ by Eqs. (3.32)–(3.35).

The location of the pitching axis falls in the range $1/2 \leq B \leq 1$ proposed by Lighthill [54]. However, Lighthill suggested to position the axis closer to the trailing edge, while the present results indicate that the axis should be placed a small distance downstream of the 3/4 chord point ($x = 0.5$). At a flapping frequency of $\sigma \approx 1.17$, the thrust force vanishes and the foil moves through the fluid in a “perfect feathered” mode. The values for this motion are given in Eq. (3.31). The farthestmost downstream position of B is reached at $\sigma \approx 1.75$. At higher frequencies, the axis streamwise distance to the 3/4 chord point degrades with rising σ . With increasing frequency σ , the plunging amplitude H decays while the pitching amplitude A increases. Eqs. (3.33) and (3.34) show for $\sigma \rightarrow \infty$ that the pitching amplitude reaches the constant value $A = 4/3$ while H asymptotically decays to zero with the inverse of σ . The feathering parameter arrives at $\chi = 1$ in the thrust-free case (see Sec. 3.1.1) and falls in the upper zone of the range $0.6 \leq \chi \leq 0.8$ proposed in [54], with the limiting value $\chi \approx 0.68$ at $\sigma \rightarrow \infty$.

Fig. 3.5 depicts the relation of flapping frequency to thrust and energy, respectively, in optimum motion.

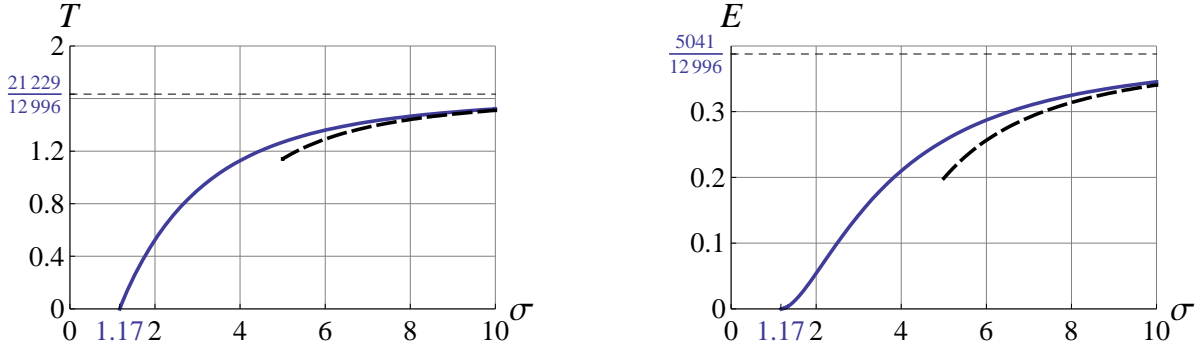


Figure 3.5: Result for optimal foil motion over the reduced frequency σ ; left: Thrust T right: energy per period that is imparted to the wake E ; Black, dashed lines: Asymptotic lines for $\sigma \rightarrow \infty$.

Both thrust and energy vanish at the frequency $\sigma \approx 1.17$. Thus optimal motion for low thrust occurs at a finite flapping frequency. With the Lagrange optimization, thrust and energy reach the constant value of $T \approx 1.63$ and $E \approx 0.39$ for $\sigma \rightarrow \infty$. When the thrust level is above the value of $T^{opt} = 21229/12996$, a closed-form relation between the efficiency η and the thrust T can be given, see Fig. 3.6.

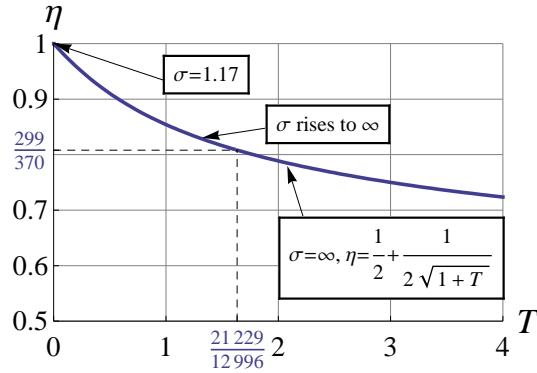


Figure 3.6: η - T -Pareto of optimal foil motion.

Thus, the η - T envelope has two branches. It follows immediately from Eq. (3.38) that $\eta \rightarrow 1/2$ at $T \rightarrow \infty$. Although the closed-form relation between efficiency and thrust is only valid for $T > T^{opt}$, it still gives a good approximation in the interval $T = [0, T^{opt}]$ and exactly passes through the point $\eta = 1$ at $T = 0$. To the author's knowledge this simple relation for flapping foils is given here for the first time.

Although parts of the η - T envelope are derived from the unrealistic assumption of infinite frequency, the curve can be utilized as ideal efficiency for optimum flapping wing propulsion that can be compared to ideal curves of other means of propulsion like jet drive or screw propeller, see Sec. 3.3.1.

Remarks on optimal foil motion

The obtained optimal foil motion encounters some limitations:

- The leading edge suction force T_s has a large contribution to the total thrust and the thrust from the surface pressure T_p counteracts T_s . The leading-edge suction can induce flow separation at the nose of the foil. A tolerance should be determined if a certain thrust level is reliable. However, such a limit depends on the specific shape of the surface and cannot be obtained in the framework of potential flow theory.
- Due to the high frequencies high lateral forces may occur. There are two possibilities to circumvent this problem:
 - Flapping foil with vanishing lift force (discussed in what follows),
 - Travelling body wave with counteracting lateral forces (fish-like motion, see Sec. 3.3.2).

Foil motion with vanishing lift force

It is of interest if there exist motions with vanishing lift force that produce a thrust. Following [115], the lift force on a flapping foil can be decomposed into three parts: $\tilde{L}_1(\tilde{t})$ denotes the lift from the added mass being a part of the non-circulatory part of the flow; The circulatory part of the lift is represented by the Theodorsen function $C(\sigma)$ and can be split into $\tilde{L}_0(\tilde{t})$ (that is interlinked to the circulation on the body Γ) and $\tilde{L}_2(\tilde{t})$ (containing the explicit dependence on wake vorticity).

With non-circulatory time-periodic flow, neither thrust nor power can be generated in the time average, see Sec. 3.1.3. However, the *instantaneous* thrust and lift force are generally non-zero due to the added mass effect (cf [11], Sec. 5.2). With circulatory flow, in general $T \neq 0$, $P \neq 0$. It is of interest to have a look at motions with $T > 0$ and $P > 0$, but $\tilde{L}(\tilde{t}) = 0$ for all \tilde{t} . The solution for the flapping foil with vanishing lateral force (zero lift) at all instants in time is obtained from Eq. (3.3) by setting $a_0 + a_1 = 0$. Then:

$$H = 2 \left[1 + \left(\frac{\sigma^3 + 5\sigma^2 G + 6\sigma (F^2 + G^2)}{\sigma^2 F + 4F^2 + (\sigma + 2G)^2} \right)^2 \right]^{-\frac{1}{2}}$$

$$B = \frac{2F^2 + G(\sigma + 2G)}{4F^2 + (\sigma + 2G)^2}$$

$$A = \frac{2\sigma (4F^2 + (\sigma + 2G)^2)}{\sqrt{(\sigma^2 F + 4F^2 + (\sigma + 2G)^2)^2 + \sigma^2 (6F^2 + (\sigma + 2G)(\sigma + 3G))^2}}$$

$$E = \frac{16\sigma^6 (F - F^2 - G^2)}{\sigma^2 (1 + \sigma^2 + 2F) + (4 + 9\sigma^2) (F^2 + G^2) + 2\sigma (2 + 3\sigma^2) G}$$

$$T = \frac{4\sigma^4 (\sigma^2 (1 - 2F) + (4 + \sigma^2) (F^2 + G^2) + 4\sigma G)}{\sigma^2 (1 + \sigma^2 + 2F) + (4 + 9\sigma^2) (F^2 + G^2) + 2\sigma (2 + 3\sigma^2) G}$$

$$\eta = 1 - \frac{\sigma^2 (F - F^2 - G^2)}{4F^2 - \sigma^2 F + (\sigma + 2G)^2}$$

The relation between the efficiency and the thrust is shown in Fig. 3.7 and compared to the optimum propulsion in Fig. 3.6.

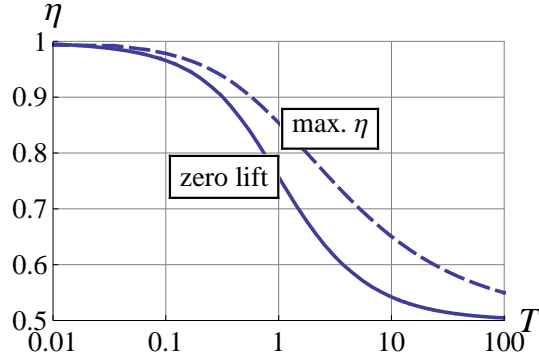


Figure 3.7: Comparison of zero lift with optimal foil motion

Comparison to propeller efficiency

The maximum efficiency of the flapping foil shall be compared to propeller efficiency by using the well-known Rankine–Froude “actuator disk” theory. The ideal propeller efficiency is related to the velocities by

$$\eta_p = \frac{2}{1 + \frac{\tilde{U}_w}{\tilde{U}}}$$

where \tilde{U} and \tilde{U}_w are the velocities in the oncoming flow and wake, respectively. The mass flux in the actuator disk is $\tilde{m}_{disk} = \tilde{\rho} \tilde{A}_{disk} \tilde{U}_{disk}$, with $\tilde{U}_{disk} = \frac{\tilde{U}_w + \tilde{U}}{2}$. The propeller thrust is

$$\tilde{T}_p = \tilde{m}_{disk} (\tilde{U}_w - \tilde{U}).$$

The thrust coefficient defined for the propeller c_{Tp} uses the swept area \tilde{A}_{disk} as reference. Then (cf. [13], Ch. 9)

$$\eta_p = \frac{2}{1 + \sqrt{1 + c_{Tp}}}. \quad (3.39)$$

The relation to the thrust coefficient with respect to the wetted surface $c_{Tp} = c_T / (2\epsilon)$ gives

$$\eta_p = \frac{2}{1 + \sqrt{1 + \frac{c_T}{2\epsilon}}}.$$

It may be of interest under what condition which means of propulsion gives higher efficiency. Equality of flapping foil efficiency Eq. (3.38) and propeller efficiency $\eta = \eta_p$ is obtained (for ϵ being not too large) at

$$c_T^{eq} = 16\epsilon - 6\sqrt{\pi}\epsilon^{3/2} + \dots$$

with $\eta \lesssim \eta_p$ for $c_T \lesssim c_T^{eq}$. The thrust coefficient c_T reached by flapping motion is usually lower than c_T^{eq} and thus the ideal propeller excels the efficiency of the flapping foil. A comparison for larger deflection ϵ is shown in Fig. 3.10.

3.2.3 Propulsive performance for channel flow

In this section the panel code is employed to study the effect of the presence of channel walls for the flapping foil motion. Solutions for the dependence of the trailing edge vorticity on the channel width have been discussed for pure heaving motion in Sec. 2.2.5. In this section, the effect of the channel width on the propulsive performance is discussed. A foil in combined plunging- and pitching motion is considered and the channel width is varied in a large range to study the effect from the presence of the channel walls. The flapping parameters are given as follows:

$$H = 1.9343, \quad A = 0.338824, \quad B = 0.50054, \quad \sigma = 1, \quad h = 0.5, \dots, 10.$$

The parameters are equal to those for unbounded domain in the test case Appendix A.2. The cosine and sine components of the strength of vorticity at the trailing edge are shown in Fig. 3.8.

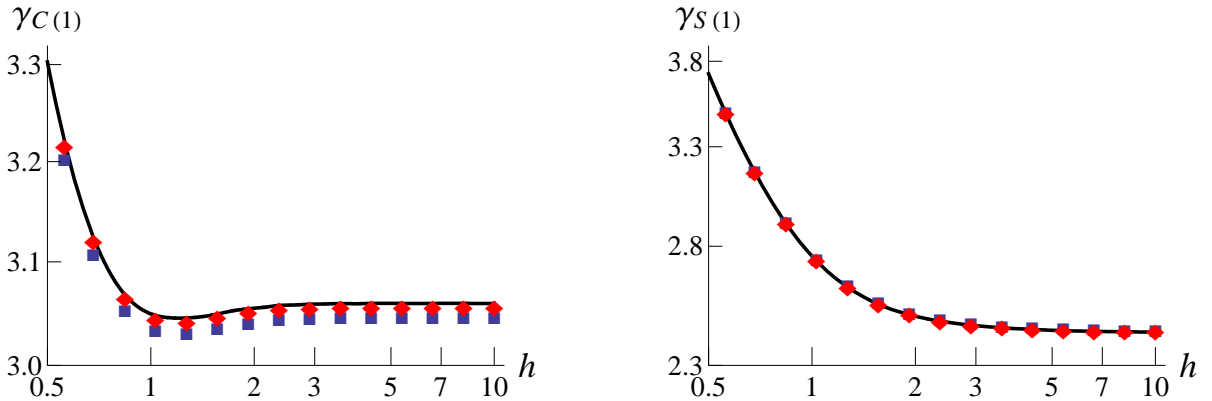


Figure 3.8: Flapping foil: vorticity at the trailing edge as function of the semi-channel width h ; Blue points \blacksquare : panel-code with 15 panels, Red points \blacklozenge : panel-code with 30 panels; black line: result from analytical approach.

The analytical results are obtained from the system Eq. (2.86). A double logarithmic plot is used. The result from the analytical approach and from the panel code with 15 and 30 panels are in good agreement to each other. The size of the vorticity at the trailing edge increases with decreasing channel width. However, the vorticity $\gamma_C(1)$ does not vary monotonically with the channel width and has a minimum at the semi-channel width of order one. This effect is produced with both the analytical approach and the panel code. At the lowest considered value of $h = 0.5$ (being not small compared to one), the increase in vorticity is not as strong as predicted by the asymptotic estimate for $h \rightarrow 0$. The results from the postprocessing of the panel code for the forces, power, and efficiency are shown in Fig. 3.9.

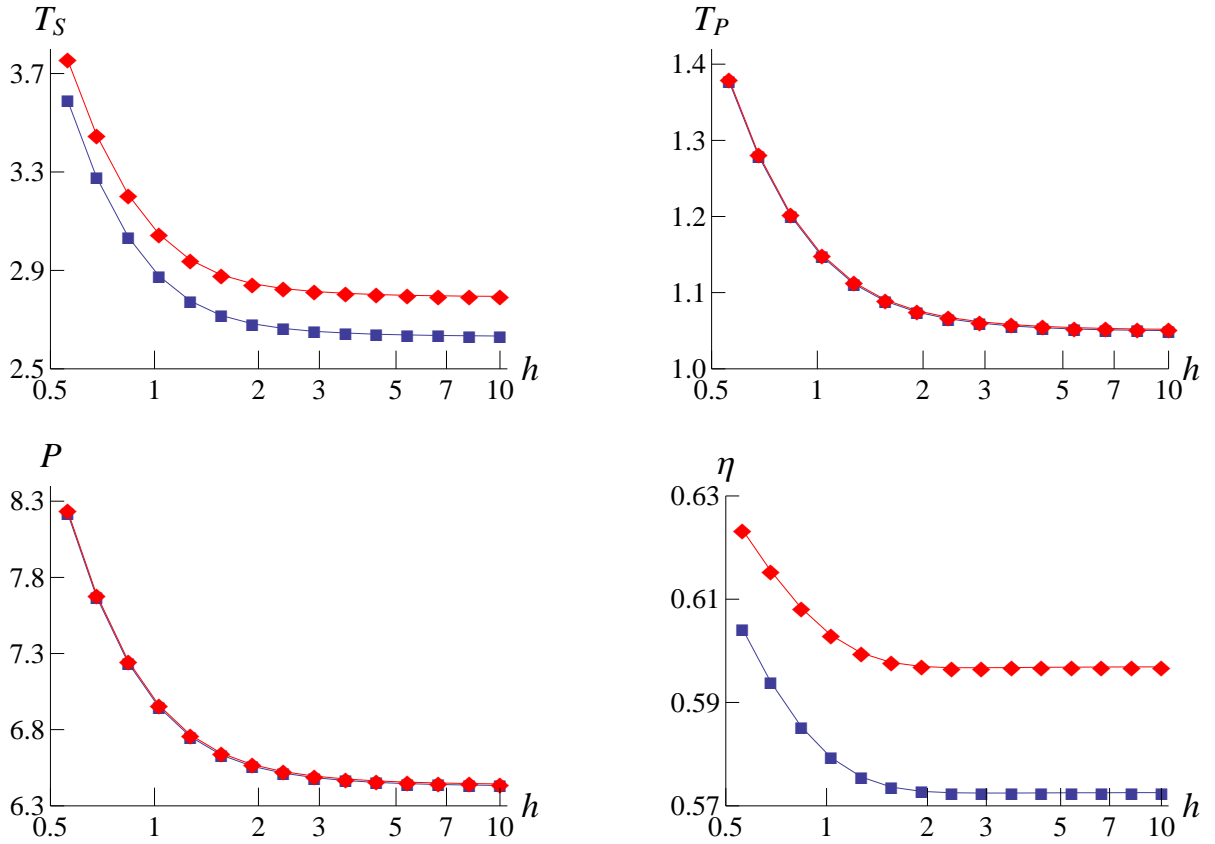


Figure 3.9: Flapping foil: Results for different semi-channel width h ; Blue points \blacksquare : panel-code with 15 panels, Red points \blacklozenge : panel-code with 30 panels; leading-edge suction force T_s , Pressure thrust T_p , power P , efficiency η .

The minimum at intermediate channel width that is observed in the trailing-edge vorticity is not present in the forces. The results for the leading-edge force with 15 panels and 30 panels, respectively, are still off by about 5 percent, while the difference for power P and pressure thrust T_p is already as low as 0.2 percent.

At large semi-channel width h , the solution for unbounded domain in Appendix A.2 is approached. From Tab. A.1, the exact result for the efficiency is $\eta = 0.623$ at infinite h . The difference in η from the panel-code results is predominantly caused by the inaccurate prediction of the leading-edge suction T_s . Thrust and power increase significantly when the channel width is reduced, while the increase in efficiency is not so pronounced.

3.3 Chordwise flexibility

3.3.1 Review of flexible foils

Swimming by downstream propagating waves has been identified by Wu [118] to be advantageous with respect to propulsive efficiency. Undulatory propulsion is used by many species of fish, see Sec. 1.2.3 for details. In comparison to a rigid foil, chordwise flexibility is required to perform such motions. Katz & Weihs [38] performed simulations of an airfoil in prescribed leading edge motion and showed that passive chordwise bending can enhance the propulsive efficiency. However, the gain in efficiency is accompanied by a considerable reduction in the generated thrust. From their results, one may draw the conclusion that chordwise flexibility is disadvantageous in terms of the efficiency-thrust trade-off as it is discussed for rigid-foil flapping in Sec. 3.1. However, recently experimental evidence has been given by Prempraneerach et. al. [78] that chordwise flexibility is advantageous also with respect to the efficiency-thrust optimum. Their results for rigid foil and flexible foil in combined pitching and plunging motion are compared in Fig. 3.10.

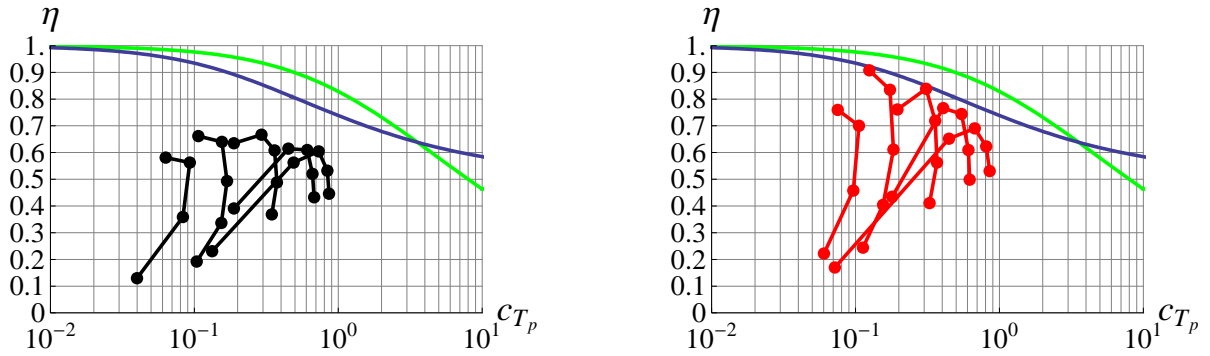


Figure 3.10: Performance measurements of a rigid and a *flexible* foil (reproduced from [78], Fig. 16, explanation in the text); left: rigid foil; right: flexible foil; Blue curve: Present model of optimum *rigid* foil motion (see above); Green curve: optimum propeller efficiency.

The measurements in [78] have been performed on a NACA 0014 foil at a heave to chord ratio of $\epsilon = 0.75$ and at a Reynolds number based on chord of $Re_c = 4 \times 10^4$. In the figures, the experimental results are sorted by Strouhal number of $St = 0.15, 0.2, 0.3, 0.4, 0.45$ (results from left to right) and on each curve, the maximum total angle of attack is varied $\alpha_{max} = 10^\circ, 15^\circ, 20^\circ, 25^\circ, 30^\circ$. At low Strouhal number, η degrades with increasing α_{max} (no data point is shown for $St = 0.15$, $\alpha_{max} = 30^\circ$).

The maximum efficiency for the rigid foil is $\eta \approx 0.667$. With the flexible foil, the efficiency improves up to 91% with only a small decrease in thrust. The distinction between a rigid and a flexible foil may explain the discrepancy to the maximum efficiency of $\eta = 0.87$ reported by Anderson et. al. [7] for measurements under practically the same conditions.

The green line in Fig. 3.10 shows the ideal propeller efficiency Eq. (3.39) plotted also in the original figure by [78]. For comparison, the Pareto for the *rigid* flapping foil from Fig. 3.6 is added

to the plot as blue line. It must be stressed that the linear model does not cope with the effects of nonlinear deflection, wake dynamics, flow separation and finite Reynolds number (viscous drag) and is presumably quite inaccurate under the conditions given in Fig. 3.10. However, it is interesting to observe that the experimental results for the rigid foil stay below the Pareto curve, while the points for the flexible foil coincide with the Pareto for the rigid foil. At the measured level of thrust, the ideal screw propeller seems to be slightly superior to an ideal flapping foil propulsor.

It is evident from the results by Prempraneerach et. al. that chordwise flexibility can be advantageous. This is certainly true also at small deflections. A device that resembles a downstream propagating wave (a travelling wavy surface) can be expected to be even more efficient than a flexible foil. The solutions for a travelling wave with uniform wave amplitude are discussed in the following section.

3.3.2 Travelling body wave of cosine shape

In this section, the progressive wave solution as studied by Wu [118] is outlined. The representation by Chebyshev polynomials described in Sec. 2.1.7 allows closed-form solutions. The thrust from the surface pressure is studied in detail and is compared below to the travelling wavy surface at large wave number and with infinite streamwise extension in Sec. 3.4. The expressions for kinetic energy, thrust, power, and efficiency are provided in a simple form. We consider an undulating cosine wave with w_1 defined as in Eq. (2.18) as

$$w_1 = 2e^{-ikx}, \quad (3.40)$$

where k denotes the dimensionless wavenumber defined in Eq. (1.21). We apply the Jacobi–Anger expansion (cf. [2], 9.1.44)

$$e^{-ikx} = e^{-ik \cos \theta} = J_0(k) + 2 \sum_{n=1}^{\infty} (-i)^n J_n(k) \cos(n\theta) \quad (-1 \leq x \leq 1), \quad (3.41)$$

where $J_n(k)$ is the Bessel function of the first kind. The coefficients β_n and γ_n of the cosine expansion of w_1 and $\partial w_1 / \partial x$ defined in Eq. (2.19) and Eq. (2.22) can be expressed as ([2], 9.1.21)

$$\beta_n = \frac{4}{\pi} \int_0^\pi e^{-ik \cos \theta} \cos(n\theta) d\theta = 4i^{-n} J_n(k) \quad \text{for } n = 0, 1, 2, \dots \quad (3.42)$$

and with [118], Eq. (68)

$$\gamma_n = 4i^{-(n+1)} k J_n(k) \quad \text{for } n = 0, 1, 2, \dots \quad (3.43)$$

The Fourier coefficients a_n for the pressure difference in Eq. (2.21) are then given by Eqs. (2.29), (2.30) as

$$a_0 = 4(\sigma - k) [J_0(G - iF) - J_1(F - 1 + iG)], \quad (3.44)$$

$$a_n = 4 \frac{(\sigma - k)^2}{k} i(-i)^n J_n(k). \quad (3.45)$$

Regarding the higher order modes in Eq. (2.21), a different formulation is obtained by making use of the integral definition (cf. [2], 9.1.21)

$$J_n(k) = \frac{i^{-n}}{\pi} \int_0^\pi e^{ik \cos \tilde{\theta}} \cos(n\tilde{\theta}) d\tilde{\theta}$$

Inserting $J_n(k)$ into a_n gives

$$\begin{aligned} \sum_{n=1}^{\infty} a_n \sin(n\theta) &= 4 \frac{(\sigma - k)^2}{k} i \sum_{n=1}^{\infty} (-i)^n \frac{(-i)^n}{\pi} \int_0^\pi e^{ik \cos \tilde{\theta}} \cos(n\tilde{\theta}) d\tilde{\theta} \sin(n\theta) = \\ &= 4 \frac{(\sigma - k)^2}{k} i \frac{1}{\pi} \int_0^\pi e^{ik \cos \tilde{\theta}} \sum_{n=1}^{\infty} (-1)^n \cos(n\tilde{\theta}) \sin(n\theta) d\tilde{\theta}, \end{aligned}$$

where integration and summation have been interchanged. Using well-known transformations to exponential expressions ([2], 4.3.33 and 4.3.1) and the sum formula for geometric series, we find

$$\begin{aligned} \sum_{n=1}^{\infty} (-1)^n \cos(n\tilde{\theta}) \sin(n\theta) &= \sum_{n=1}^{\infty} (-1)^n \frac{\sin[n(\tilde{\theta} + \theta)] - \sin[n(\tilde{\theta} - \theta)]}{2} = \\ \frac{i}{4} \left(\frac{1}{1 + e^{i(\tilde{\theta} - \theta)}} - \frac{1}{1 + e^{-i(\tilde{\theta} - \theta)}} - \frac{1}{1 + e^{i(\tilde{\theta} + \theta)}} + \frac{1}{1 + e^{-i(\tilde{\theta} + \theta)}} \right) &= -\frac{\sin \theta}{2(\cos \tilde{\theta} + \cos \theta)} \end{aligned}$$

and thus, we obtain

$$\sum_{n=1}^{\infty} a_n \sin(n\theta) = -4 \frac{(\sigma - k)^2}{k} i \frac{\sin \theta}{2\pi} \int_0^\pi \frac{e^{ik \cos \tilde{\theta}}}{\cos \tilde{\theta} + \cos \theta} d\tilde{\theta},$$

where the principal value has to be taken. Then, with $\xi = \cos \tilde{\theta}$, $d\xi/d\tilde{\theta} = -\sqrt{1 - \xi^2}$, Eq. (2.21) transforms the pressure into

$$\Delta p_1(x, \tau) = -\Re \left\{ \left[a_0 \frac{\sqrt{1 - x^2}}{1 + x} - 4 \frac{2(\sigma - k)^2}{k} i \frac{\sqrt{1 - x^2}}{2\pi} \int_{-1}^1 \frac{e^{ik\xi}}{\sqrt{1 - \xi^2} \xi + x} \frac{d\xi}{\xi + x} \right] e^{i\tau} \right\}. \quad (3.46)$$

Thrust from pressure

The contribution of the surface pressure to the thrust force shall be discussed here in detail. Eq. (2.42) is used to calculate the pressure thrust. The deflection can be expressed as a function of x from the prescribed motion Eq. (3.40), the Jacobi–Anger expansion Eq. (3.41), and the definition of the Chebyshev polynomials Eq. (2.32) as

$$w_1 = \Re \left[\left(\frac{\beta_0}{2} + \sum_{n=1}^{\infty} \beta_n T_n(x) \right) e^{i\tau} \right].$$

Thus

$$\frac{\partial w_1}{\partial x} = \sum_{n=1}^{\infty} \Re[\beta_n] n U_{n-1}(x) \cos \tau - \sum_{n=1}^{\infty} \Im[\beta_n] n U_{n-1}(x) \sin \tau.$$

On the other hand, we can use the definition

$$\frac{\partial w_1}{\partial x} = w_{x,c} \cos \tau + w_{x,s} \sin \tau.$$

When we compare both expressions and insert the Fourier coefficients β_n from Eq. (3.42), we obtain

$$w_{x,c} = 4 \sum_{n=1}^{\infty} J_n(k) \cos \frac{n\pi}{2} n U_{n-1}(x), \quad w_{x,s} = 4 \sum_{n=1}^{\infty} J_n(k) \sin \frac{n\pi}{2} n U_{n-1}(x). \quad (3.47)$$

The difference pressure from Eq. (2.21) becomes with Eq. (2.32) and a_n from Eq. (3.45)

$$\Delta p_1 = -\Re \left\{ \left[a_0 \frac{\sqrt{1-x^2}}{1+x} + 8 \frac{(\sigma-k)^2}{k} \underbrace{i \sum_{m=1}^{\infty} (-i)^m J_m(k) \sqrt{1-x^2} U_{m-1}(x)}_{S.T.} \right] e^{i\tau} \right\}. \quad (3.48)$$

Then, by comparison to the definition

$$\Delta p = \Delta p_c \cos \tau + \Delta p_s \sin \tau$$

one obtains the cosine- and sine component of the difference pressure

$$\begin{aligned} \Delta p_c &= -\sqrt{1-x^2} \left[\frac{a'_0}{1+x} + 8 \frac{(\sigma-k)^2}{k} \sum_{m=1}^{\infty} \sin \frac{m\pi}{2} J_m(k) U_{m-1}(x) \right], \\ \Delta p_s &= \sqrt{1-x^2} \left[\frac{a''_0}{1+x} + 8 \frac{(\sigma-k)^2}{k} \sum_{m=1}^{\infty} \cos \frac{m\pi}{2} J_m(k) U_{m-1}(x) \right], \end{aligned}$$

where a'_0 and a''_0 are defined by Eq. (2.39) and can be divide out from Eq. (3.44) as

$$a'_0 = 4(\sigma-k) [GJ_0(k) - (F-1)J_1(k)], \quad a''_0 = -4(\sigma-k) [FJ_0(k) + GJ_1(k)]. \quad (3.49)$$

The thrust force $T_p(t)$ due to surface pressure can be calculated from Eq. (2.42). Since both $\partial w_1/\partial x$ and Δp_1 are harmonic, the time-averaged pressure thrust T_p in Eq. (2.45) can be expressed as

$$T_p = -\frac{4}{2\pi} \int_{-1}^1 (\Delta p_c w_{x,c} + \Delta p_s w_{x,s}) dx. \quad (3.50)$$

A significant simplification can be attained if each of the sums in T_p is expanded. In $\Delta p_c w_{x,c}$, for instance, the product of the term in $w_{x,c}$ with index n with the term in Δp_c with index m gives an expression

$$\sin \frac{n\pi}{2} \cos \frac{m\pi}{2} U_{n-1}(x) U_{m-1}(x).$$

Performing the integration in Eq. (3.50) and making use of well-known orthogonality relations of Chebyshev polynomial of second kind and trigonometric function, respectively, one obtains

$$\underbrace{\sin \frac{n\pi}{2} \cos \frac{m\pi}{2}}_{0 \text{ if } n=m} \underbrace{\int_{-1}^1 \sqrt{1-x^2} U_{n-1}(x) U_{m-1}(x) dx}_{0 \text{ if } n \neq m} = 0.$$

Thus, only the *low order* term in the pressure (with factor a_0) contributes to thrust from pressure

$$T_p = \frac{2}{\pi} \int_{-1}^1 \frac{\sqrt{1-x^2}}{1+x} (a_0' w_{x,c} - a_0'' w_{x,s}) dx. \quad (3.51)$$

Before T_p is further simplified we want to emphasize that although the sum term $S.T.$ in Eq. (3.48) does not contribute to T_p , it may contribute significantly to the pressure. We anticipate a result in Sec. 3.4.2, where the pressure at mid-chord is considered in the limit of high wave numbers $k \rightarrow \infty$ and it turns out that the sum term $S.T.$ in Eq. (3.48) becomes dominant over the a_0 -term. The sums in Eq. (3.47) can be determined simply by virtue of the undulating cosine wave motion Eq. (3.40) as

$$w_{x,c} = -2k \sin(kx), \quad w_{x,s} = 2k \cos(kx). \quad (3.52)$$

Then, the integrals in Eq. (3.51) are readily identified as Bessel functions of the first kind (cf. [2]) and thus

$$T_p = 4k [a_0' J_1(k) - a_0'' J_0(k)], \quad (3.53)$$

or when Eq. (3.49) is inserted

$$T_p = 16k(\sigma - k) (J_0^2 F - J_1^2 F + J_1^2 + 2J_0 J_1 G). \quad (3.54)$$

Results

The dimensionless time-averaged quantities defined as in Sec. 2.1.9 are (cf. [118])

$$E = 16 (J_0^2 + J_1^2) (\sigma - k)^2 (F - F^2 - G^2), \quad (3.55)$$

$$T = 16\sigma(\sigma - k) ((J_0^2 - J_1^2) F + J_1^2 + 2J_0 J_1 G) - E, \quad (3.56)$$

$$P = \frac{\sigma}{k} T_p, \quad (3.57)$$

$$\eta = 1 - \frac{(J_0^2 + J_1^2) (F - F^2 - G^2) (1 - \frac{k}{\sigma})}{(J_0^2 - J_1^2) F + J_1^2 + 2J_0 J_1 G}. \quad (3.58)$$

Note that for the prescribed travelling wavy surface of uniform amplitude holds $\partial w_1 / \partial t = -c \partial w_1 / \partial x$, where $c = \sigma / k$ is the dimensionless phase speed defined in Eq. (1.21). Then, it follows immediately from Eqs. (2.42, 2.44) that $P(t) = c T_p(t)$ and as a consequence of that follows Eq. (3.57). T_p is given in Eq. (3.54). The results for different values of k and σ are shown in Fig. 3.11.

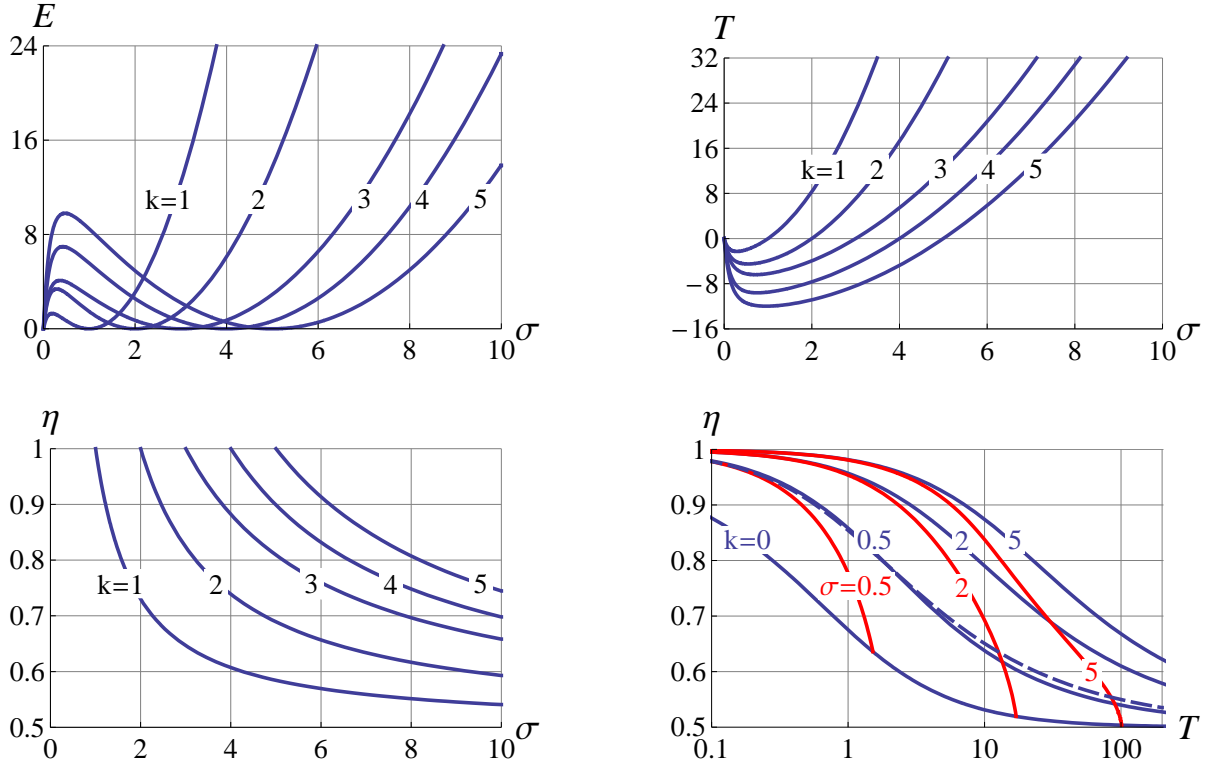


Figure 3.11: Results for travelling wavy surface: Energy imparted to the wake per period, E , thrust force T , propulsive efficiency η , and η vs. T ; Blue lines: const. dimensionless wavenumber k , red lines: const. dimensionless frequency σ , dashed line: best rigid foil (for comparison).

Note that every point in η - T has a unique representation by σ and k . An important solution is $E = T = 0$, $\eta = 1$ for $\sigma = k$ ($c = 1$). Thrust is generated $T > 0$ only when $\sigma > k$ ($c > 1$). Note that the efficiency tends to $\eta = 1$ when σ and k are increased. It can be assumed that the potential flow model is no longer applicable when the frequency and/or wave number exceed certain limits. However, the potential flow model may still be applicable for high frequencies (up to $\sigma \approx 8$) when the deflection is very small, see the discussion in Sec. 3.1.6. The case of large frequency and wave number (with the phase speed c of order one) and infinite streamwise extension are examined in Sec. 3.4. A limitation to the assumptions of potential flow theory may be given from the occurrence of flow separation on the travelling wave due to high waviness of the surface. However, the result for viscous flow in Sec. 3.5 shows that separation does not occur in case of a downstream travelling wave.

For the travelling wave with zero wave number $k = 0$, one obtains from Eqs. (3.56, 3.58)

$$T = 16 \sigma^2 (F^2 + G^2) ,$$

$$\eta = (F^2 + G^2) / F .$$

This special case $k = 0$ is equals to the solution of a foil in pure plunging motion. The result has been obtained first by Garrick [26].

3.3.3 Comparison: Foil motion vs. travelling body wave

One may compare the results for a rigid foil in optimum flapping motion from Sec. 3.2.2 to the travelling wave solution. In the right bottom plot in Fig. 3.11, the optimum foil motion is shown as dashed line. The optimum motion of a rigid flapping foil is approximately as efficient as the travelling wavy surface with $k \approx 0.5$. Although the rigid foil does not offer chordwise curvature, by its combined plunging and pitching motion it resembles features of a downstream travelling wave.

3.3.4 Propulsive efficiency for channel flow

In this section, the effect of channel width on the propulsive efficiency for the travelling wavy surface is examined with the help of the panel code. The forced motion travelling wavy surface from Appendix A.3 for $\sigma = 5$, $k = 3$ with 15 panels is considered in the channel. The effect of the channel width on the results for the travelling wavy surface is discussed. The results are given in Figs. 3.12, 3.13.

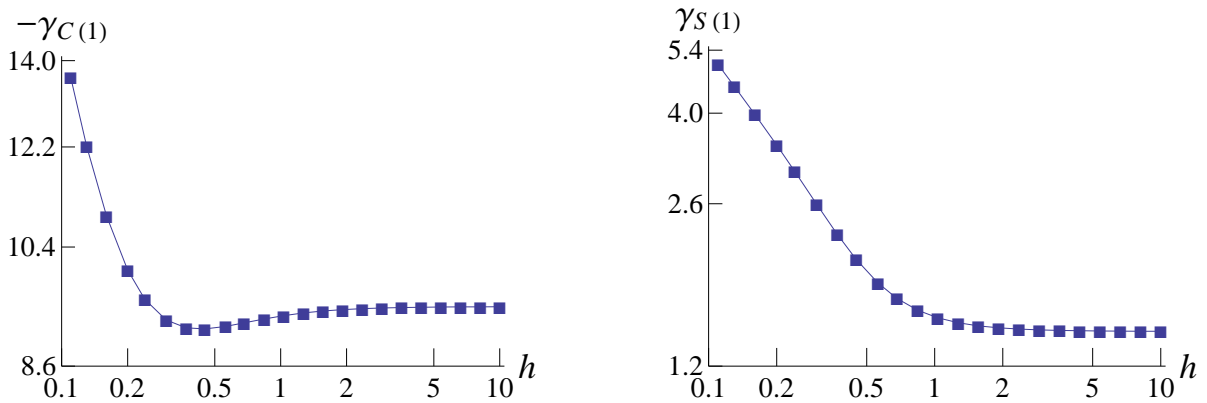


Figure 3.12: Travelling wavy surface with panel code: vorticity at the trailing edge for different values of the semi-channel width h (double-logarithmic plot, solution points connected by lines).

The behaviour is qualitatively equivalent to that in the flapping foil motion. While $\gamma_C(1)$ has switched sign, there is again a minimum at intermediate semi-channel width h , while the minimum occurs at a lower value of h . From the double-logarithmic plot that includes also very small values of the semi-channel width, the h^{-1} behaviour at $h \ll 1$ is evident.

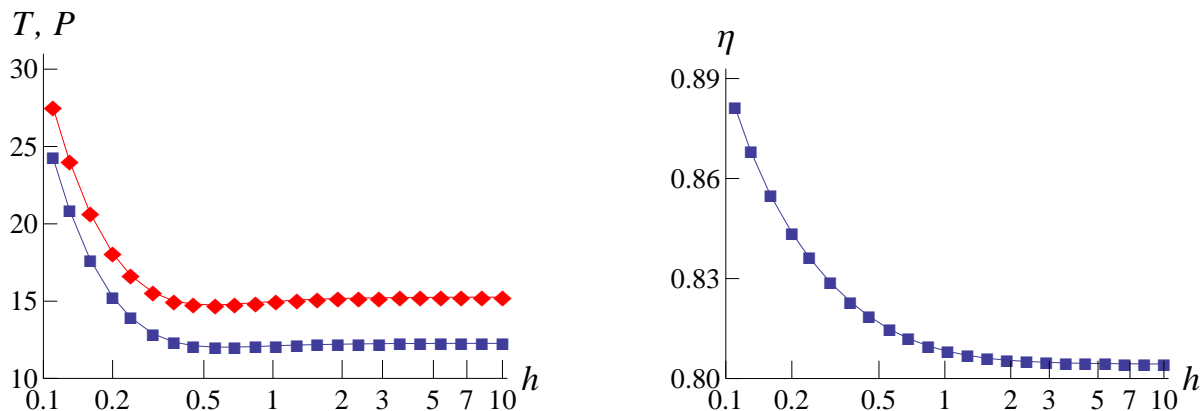


Figure 3.13: Travelling wavy surface with panel code: Thrust, power and efficiency for different values of the semi-channel width h ; left: Thrust T (blue points \blacksquare) and power P (red points \blacklozenge), right: efficiency η (logarithmic plot, solution points connected by lines).

The results for unbounded domain in Appendix A.3 are attained at large values of h . It is interesting that a minimum of thrust and power occurs at $h \approx 0.5$, corresponding to that in $\gamma_C(1)$. As for the flapping foil, thrust and power strongly increase at small h . However, in the flapping foil motion, power and thrust are significantly increased already at $h = 0.5$ (compare to Fig. 3.9). In a very narrow channel, the efficiency increases by less than 10 percent.

3.4 Limit of large wave numbers

We will now exclude the fluid structure interaction and the presence of the channel walls and consider the simple downstream travelling wave with small deflections in the limit of large wave number and large dimensionless flapping frequency (with respect to chord). The potential flow model may still be applicable at high frequencies (up to $\sigma \approx 8$) when the deflection remains sufficiently small, see the discussion in Sec. 3.1.6. We will focus the discussion on the contribution of chordwise elements to the thrust force. The surface pressure is considered in the mid-chord limit. It turns out that its leading-order term is independent of effects from the body edges and the wake. This results motivates us to extend the surface to infinity in streamwise direction and to apply periodic boundary conditions. Viscous flow over a wavy surface of infinite extension has been studied in the literature and a total thrust force has been reported under certain conditions. The laminar case is revisited in Sec. 3.5.

3.4.1 Body of finite length

We consider the potential flow solution in the limit of infinite wave number k at a fixed dimensionless phase velocity $c > 0$. Thus, from the definitions of σ , c and k in Eqs. (1.20), (1.21), it follows that $\sigma \rightarrow \infty$. From the closed-form solutions for the travelling wavy in Sec. 3.3.2, the expressions in the limit can be readily obtained. In addition, it may be of interest how the generation of the time-averaged pressure thrust T_p is distributed along the chord. The real- and

imaginary part of the Theodorsen function Eq. (2.33) read in the limit $\sigma \rightarrow \infty$

$$F \sim \frac{1}{2}, \quad G \sim -\frac{1}{8\sigma} \quad (3.59)$$

and the Bessel functions are in the limit $k \rightarrow \infty$ (cf. [2], 9.2.1)

$$J_0(k) \sim \sqrt{\frac{2}{\pi k}} \cos\left(k - \frac{\pi}{4}\right), \quad J_1(k) \sim \sqrt{\frac{2}{\pi k}} \cos\left(k - \frac{3\pi}{4}\right). \quad (3.60)$$

Inserting the expansions for F , G , $J_0(k)$ and $J_1(k)$ into Eqs. (3.55)–(3.58) and replacing $\sigma = ck$, yields in the leading order with respect to k the following time-averaged quantities

$$E \sim \frac{8k}{\pi}(c-1)^2, \quad T \sim \frac{8k}{\pi}(c^2-1), \quad P \sim \frac{16k}{\pi}c(c-1), \quad \eta \sim \frac{1}{2} + \frac{1}{2c}.$$

Thus, the phase speed must exceed the freestream speed $c > 1$ to attain thrust. At $c = 1$ the thrust vanishes and the efficiency reaches $\eta = 1$. Both results hold also for any value of k (compare to Sec. 3.3.2). Efficient propulsive motion is attained when c is not too large. The produced thrust and required power scale linearly with the wave number. Thus, when a certain thrust force is demanded from a motion with constraint amplitude, one can always increase k (and thus the wriggling of the profile) and accordingly bring c closer to 1 in the attempt to increase the efficiency η . This finding is in accord to the statement by Sparenberg et. al. [96] that (in the realm of linear theory) no optimum thrust producing motion exists when only a constraint is put on the amplitude of motion.

It may be of interest how T splits into its parts T_s and T_p and how each chordwise elements contributes to the generation of T_p . The Fourier coefficient given in Eq. (3.44) reads in the limit $k \rightarrow \infty$

$$a_0 \sim -\frac{2(1+i)(c-1)e^{ik}}{\sqrt{\pi}}\sqrt{k} \quad (3.61)$$

and with Eq. (2.39) the real- and imaginary parts from Eq. (3.49) are

$$a'_0 \sim -\frac{2(c-1)\sqrt{k}(\cos k - \sin k)}{\sqrt{\pi}}, \quad a''_0 \sim -\frac{2(c-1)\sqrt{k}(\cos k + \sin k)}{\sqrt{\pi}}. \quad (3.62)$$

Then the dimensionless, time-averaged leading edge thrust Eq. (2.46) is

$$T_s \sim \frac{8k}{\pi}(c-1)^2.$$

Regarding the generation of thrust by surface pressure, it is shown in Sec. 3.3.2 (for any value of k) that only the a_0 -term in the pressure distribution contributes to time-averaged pressure thrust. On the other hand, the results in the next section Sec. 3.4.2 for the pressure at the mid-chord position unveil that the portion of pressure that does not contribute to thrust becomes the leading pressure term with respect to large k . The chordwise contribution to the thrust from pressure is obtained from the differential of Eq. (3.51) with Eqs. (3.52, 3.62) inserted

$$-\frac{4}{\pi}\overline{\Delta p_1 \frac{\partial w_1}{\partial x}} = \frac{2}{\pi} \frac{\sqrt{1-x^2}}{1+x} (a'_0 w_{x,c} - a''_0 w_{x,s}) \sim \frac{16}{\pi}(c-1) \frac{k^{3/2}}{\sqrt{2\pi}} \frac{\sqrt{1-x^2}}{1+x} \sin\left(kx + k + \frac{\pi}{4}\right). \quad (3.63)$$

Integration along the chord from $x = -1$ to $x = 1$ then yields

$$T_p = -\frac{4}{\pi} \int_{-1}^1 \Delta p_1 \frac{\partial w_1}{\partial x} dx \sim \frac{16k}{\pi} (c - 1). \quad (3.64)$$

This result can be obtained directly when we insert the expansions for F , G , $J_0(k)$ and $J_1(k)$, Eqs. (3.59, 3.60), into Eq. (3.54). One may check that $T = T_s + T_p$. Also, $P = c T_p$ holds for the travelling wave at any phase speed, see Sec. 3.3.2. It can be seen from the examples depicted in Fig. 3.15 that some sections along the chord generate favourable thrust, while others produce drag. At phase speeds slightly above one, say $c = 1.2$, the efficiency is quite high $\eta \approx 0.9$ and the leading-edge suction is rather small compared to the pressure thrust $T_s/T_p \approx 0.1$.

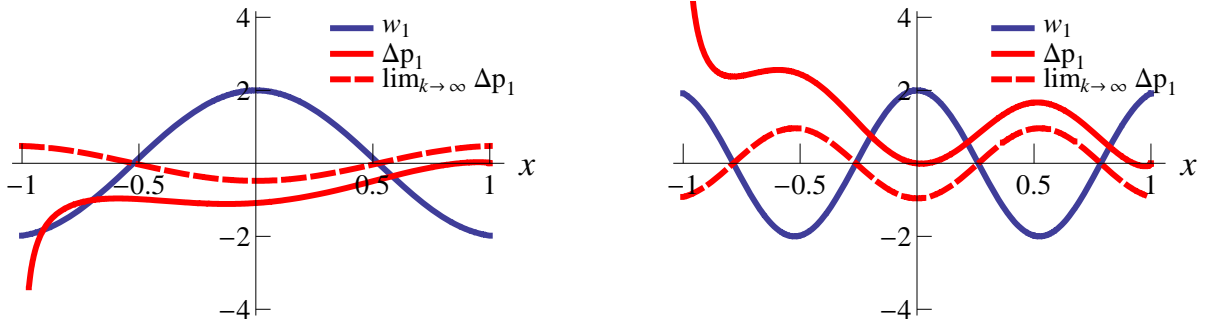


Figure 3.14: Deflection w_1 and pressure difference Δp along the chord (at $t = 0$) for a phase speed of $c = 1.2$ at different wave numbers; Left: $k = 3$, Right: $k = 6$.

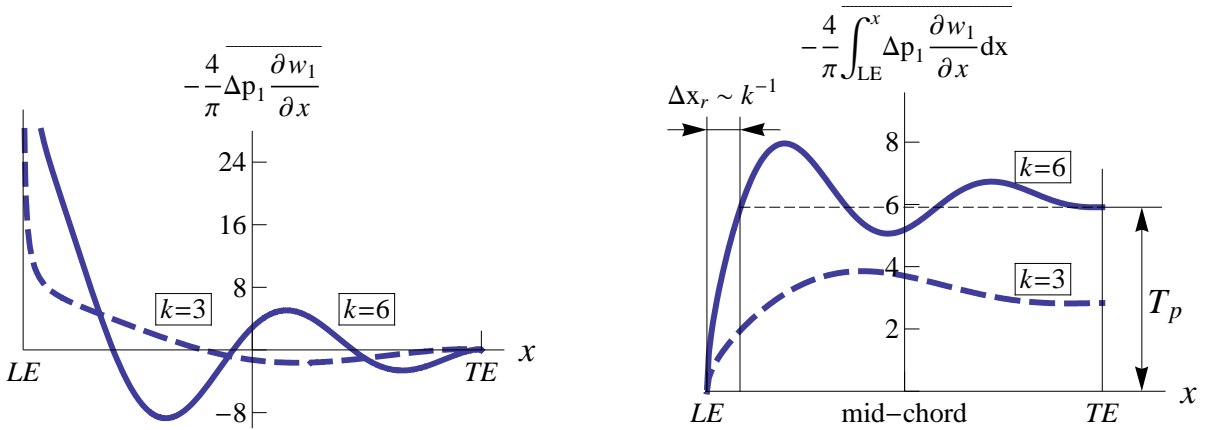


Figure 3.15: Chordwise contribution to time-averaged thrust force due to pressure, T_p . Left: Distribution along the chord, Right: Accumulated value, starting at the leading edge. The value T_p is generated in the LE -region $\Delta x_r \sim k^{-1}$ and at the trailing edge (sketched for the wavenumber $k = 6$).

When k is large, the main portion of the thrust force due to surface pressure is produced in a region in immediate vicinity to the leading edge, as illustrated in Fig. 3.15. Let the extension Δx_r of the leading-edge region be determined from the position where the accumulated pressure thrust is equal to the overall pressure thrust T_p (see Fig. 3.15, right). We expect the length of this region to be small when k is large. Thus, we can take the solution from Eq. (3.63) and expand it in x about the leading edge. Integration in the interval of length Δx_r then yields

$$-\frac{4}{\pi} \int_{-1}^{-1+\Delta x_r} \lim_{x \rightarrow -1} \overline{\Delta p_1 \frac{\partial w_1}{\partial x}} dx \sim \frac{8k}{\pi} (c-1) \frac{1}{\sqrt{2\pi}} \sqrt{k \Delta x_r} (4 + k \Delta x_r). \quad (3.65)$$

The expression represents the contribution to the time-averaged pressure thrust from a small region of length Δx_r in the vicinity of the *LE* at large k . The size of the *LE*-region in the limit of large k is then determined by equating the expressions in Eq. (3.65) and Eq. (3.64) as

$$\Delta x_r \sim \frac{4}{3} \left(-2 + g^{1/3} + g^{-1/3} \right) k^{-1}, \quad \text{with} \quad g = \frac{16 + 27\pi + 3\sqrt{3\pi(32 + 27\pi)}}{16}.$$

Consequently, the size of the *LE*-region where the net amount of pressure thrust T_p is produced becomes small when k is increased. We note that the linear relation between T_p and k in Eq. (3.64) that holds for large k is a good approximation even at not so large values for k of 3 and 6 (see Fig. 3.15, right).

3.4.2 Travelling pressure wave in the mid-chord limit

It has been shown in Sec. 3.3.2 that for a body of *finite* length, moving in prescribed cosine-shape motion, only the first term in the Fourier series of the pressure (with factor a_0) contributes to T_p , see Eq. (3.53). From this result it may be concluded that the higher order terms in the pressure are of less importance. However, evaluating the pressure at various positions x along the chord for growing values of k , the a_0 -term seems to be *not* the leading term in the expansion of the pressure difference. Indeed, in Eq. (3.46) the integral expression contributes largely to Δp_1 when $k \rightarrow \infty$. As the surface waves are short compared to the chord when k is large, it can be expected that far away from the *LE* and *TE* (in terms of number of waves) the effects due to the edges will be small and the flow field will approach periodic conditions in streamwise direction. The integral for the pressure difference across the wall in Eq. (3.46) is written in a slightly different form with $\sigma = ck$ as

$$\Delta p_1(x, \tau) = -\Re \left\{ \left[a_0 \frac{\sqrt{1-x^2}}{1+x} - 8k(c-1)^2 i \frac{\sqrt{1-x^2}}{2\pi} e^{-ikx} \int_{-1}^1 \frac{e^{ik(\xi+x)}}{\xi+x} \frac{d\xi}{\sqrt{1-\xi^2}} \right] e^{i\tau} \right\}.$$

Let us consider the pressure difference in the vicinity of the mid-chord $x = 0$, i. e. at equal distance from the *LE* and *TE*. We scale the streamwise coordinate component with the wavelength, $\hat{x} = kx/(2\pi)$, cf. scaling III in Eq. (1.23). When k is assumed large and $c = \mathcal{O}(1)$, we have $a_0 \sim \sqrt{k}$ from Eq. (3.61) and we obtain for the pressure difference in the vicinity of the mid-chord

$$\Delta p_1(\hat{x}, \tau) \sim -\Re \left\{ \left[a_0 - 8k(c-1)^2 \frac{i}{2\pi} e^{-i2\pi\hat{x}} \int_{-1}^1 \frac{e^{ik\xi}}{\xi} \frac{d\xi}{\sqrt{1-\xi^2}} \right] e^{i\tau} + \mathcal{O}(1) \right\}.$$

With the help of *Mathematica*, the integral can be evaluated and expanded in the limit $k \rightarrow \infty$ as

$$\frac{1}{i\pi} \int_{-1}^1 \frac{e^{ik\xi}}{\xi} \frac{d\xi}{\sqrt{1-\xi^2}} = k {}_1F_2\left(\frac{1}{2}; 1, \frac{3}{2}; -\frac{k^2}{4}\right) \sim 1 + \sqrt{\frac{2}{\pi}} \sin\left(k - \frac{\pi}{4}\right) \frac{1}{\sqrt{k}} + \mathcal{O}(k^{-1}),$$

where ${}_1F_2$ denotes the generalized hypergeometric function. Thus, we obtain for the pressure difference in the mid-chord limit

$$\Delta p_1(\hat{x}, \tau) \sim -4k(c-1)^2 \cos(2\pi\hat{x} - \tau) + \mathcal{O}(\sqrt{k}), \quad (3.66)$$

where a_0 scales with \sqrt{k} and is thus smaller than the contribution from the integral that scales linearly with k . In the leading order with respect to k , the mid-chord pressure performs a downstream travelling harmonic wave $\Delta p_1 \sim -2k(c-1)^2 w_1$ that is in counter-phase with the deflection $w_1(\hat{x}, \tau) = 2 \cos(2\pi\hat{x} - \tau)$. It will be shown below that this result is in accord with the result for an infinite travelling wave. A comparison of the exact result for the pressure difference and the leading term of Δp_1 with respect to large k is shown in Fig. 3.14.

Contribution to pressure thrust

The expression for the pressure difference may be summarized as follows:

$$\Delta p_1(x, \tau) \sim k \Delta p_{1,1} + \sqrt{k} \left(\Delta p_{1,2}^{(a_0)} + \Delta p_{1,2}^{(\Sigma)} \right).$$

Note that the first index denotes the leading term of the expansion at $\epsilon \ll 1$, while the second index indicates the terms in orders of the expansion at large dimensionless wavenumber k . $\Delta p_{1,2}^{(a_0)}$ denotes the contribution from the a_0 -term. There may also be a contribution $\Delta p_{1,2}^{(\Sigma)}$ resulting from the sum $S.T.$ in Eq. (3.48). However, according to Eq. (3.53) only the a_0 -term contributes to the time-averaged pressure thrust. Thus, neither $\Delta p_{1,1}$ nor $\Delta p_{1,2}^{(\Sigma)}$ contribute to T_p . Tab. 3.1 depicts the solution path to derive the time-averaged pressure thrust $T_p = -\frac{4}{\pi} \int_{LE}^{TE} \Delta p_1 \frac{\partial w_1}{\partial x} dx$, and lists the magnitude of the corresponding expressions in powers of k .

Component	Δp_1	$\frac{\partial w_1}{\partial x}$	$\Delta p_1 \frac{\partial w_1}{\partial x}$	$\int_{LE}^{TE} \Delta p_1 \frac{\partial w_1}{\partial x} dx$	T_p
$k \Delta p_{1,1}$	k	k	k^2	k	-
$\sqrt{k} \Delta p_{1,2}^{(a_0)}$	\sqrt{k}	k	$k^{3/2}$	$k^{3/2}$	k

Table 3.1: Contribution of pressure components (at large wavenumbers k) to the relevant expressions of the time-averaged thrust T_p : Magnitude of each expression in powers of k .

While in the difference pressure Δp_1 and in $\Delta p_1 \frac{\partial w_1}{\partial x}$ the leading order term is due to $\Delta p_{1,1}$, the chord-integrated expression $\int_{LE}^{TE} \Delta p_1 \frac{\partial w_1}{\partial x} dx$ for the instantaneous thrust is dominated by $\Delta p_{1,2}^{(a_0)}$ and the time-averaged thrust T_p comes solely from $\Delta p_{1,2}^{(a_0)}$. The leading-order pressure term $\Delta p_{1,1}$ is in counter-phase to the deflection w_1 and does *not* contribute to T_p .

3.4.3 Periodic travelling wave as limit of the mid-chord problem

We consider a periodic travelling wave over an infinite surface. It is shown in this section that the solution in the mid-chord limit, as given in Sec. 3.4.2, coincides with the solution of the periodic setting. For an infinitely extended wavy surface Miles [62, 63] observed that the pressure is in counter-phase to the deflection. Lerner [50] gave a representation of p in Fourier space and in integral form. Indeed, it is shown in the following that the wavy surface becomes steady in a frame of reference moving with the phase speed and the result in the moving frame is identical to the classical asymptotic solution by Ackeret [3] for the inviscid flow over a *stationary* wavy surface of small amplitude.

In a frame of reference moving downstream with the dimensionless phase speed c , periodic boundary conditions can be assumed. The situation is sketched in Fig. 3.16.

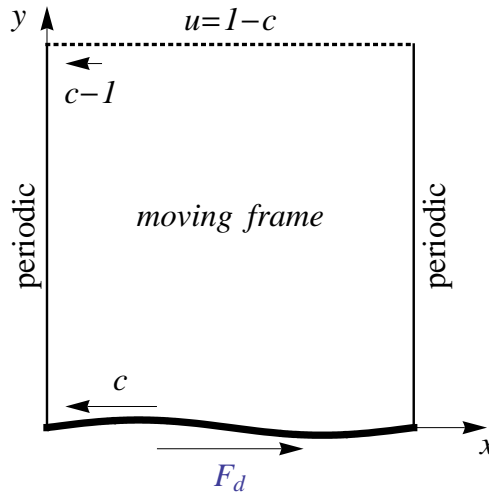


Figure 3.16: Wavy surface with infinite streamwise extension: periodic problem in the moving frame of reference. The frame moves with the dimensionless phase speed c of the wall motion in streamwise direction. Far-field boundary condition $u = 1 - c$ and periodic boundary conditions in streamwise direction are assumed. The no-slip boundary condition at the wall and the total wall force F_d are used only in the viscous flow case.

The no-slip condition at the wall and the total wall force F_d are used only in the viscous flow case discussed in Sec. 3.5. For inviscid flow, the solution for the velocity and pressure distribution at the wall is readily obtained when a distribution of vortices is employed and extended to infinity. Using scaling III from Eq. (1.23) with the wavelength $\tilde{\lambda}$ as the reference length, we obtain in equivalence to Eqs. (2.3, 2.11) the problem in the moving frame of reference

$$u_1(x, 0+) - 1 = -\frac{\gamma(x)}{2}, \quad (3.67)$$

$$\frac{1}{2\pi} \int_{-\infty}^{\infty} \frac{\gamma(\xi)}{x - \xi} d\xi = v_1 = -(c - 1)w_{1,x}, \quad (3.68)$$

where x denotes the streamwise coordinate in the moving frame and v_1 is the vertical component of the fluid velocity at the wall. For the given wall deflection

$$w_1(x) = A_\lambda \sin(2\pi x) \quad (3.69)$$

the ansatz $\gamma(x) = \gamma_S \sin(2\pi x)$ yields

$$v_1 = -2\pi(c-1)A_\lambda \cos(2\pi x), \quad (3.70)$$

$$\frac{\gamma_S}{2\pi} \left[-\cos(2\pi x) \underbrace{\int_{-\infty}^{\infty} \frac{\sin(2\pi \bar{x})}{\bar{x}} d\bar{x}}_{\pi} + \sin(2\pi x) \underbrace{\int_{-\infty}^{\infty} \frac{\cos(2\pi \bar{x})}{\bar{x}} d\bar{x}}_0 \right] = v_1$$

(note that $\cos(2\pi \bar{x})/\bar{x}$ is an odd function) and consequently

$$\gamma_S = 4\pi(c-1)A_\lambda.$$

The perturbation of the velocity component in streamwise direction is then obtained as

$$u_1(x, 0+) - 1 = -\frac{\gamma(x)}{2} = -2\pi(c-1)A_\lambda \sin(2\pi x). \quad (3.71)$$

The dimensionless perturbation pressure on the wall can then be obtained analogous to Eq. (2.4) as

$$p_1(x, 0+) = -2\pi(c-1)^2 A_\lambda \sin(2\pi x). \quad (3.72)$$

p_1 denotes the difference to the freestream pressure. The same result is obtained when the (steady) Bernoulli equation is applied in the moving frame of reference. Then, from symmetry considerations of the pressure along the upper and lower surface $\Delta p_1 = -4\pi(c-1)^2 w_1$. The pressure is minimal at the wave crest and maximal at the trough. The result for the infinitely extended surface is equal to the leading-order difference pressure in the vicinity of the mid-chord in Sec. 3.4.2. Thus, when periodicity is prescribed in streamwise direction, the effects that arise from the edges (suction at the *LE*, vortex-shedding from the *TE*) are suppressed. Accordingly, in the space-periodic setting, there is no force acting on the wall

$$T_p^{Periodic} = 0$$

at any phase speed c . The result is equivalent to the drag-free solution over a stationary wavy surface by Ackeret [3]. The results Eqs. (3.69)-(3.72) may be summarized as follows:

$$\begin{aligned} w_1 &= A_\lambda \sin(2\pi x), \\ u_1 &= 1 - 2\pi(c-1)A_\lambda \sin(2\pi x), \\ v_1 &= -2\pi(c-1)A_\lambda \cos(2\pi x), \\ p_1 &= -2\pi(c-1)^2 A_\lambda \sin(2\pi x). \end{aligned}$$

Nonlinear effect of deflection

We want to study the difference in the results between prescribing the kinematic boundary condition at the undisturbed position of the wavy wall (linearized boundary condition) and at the disturbed wall position. In the notation we drop the index 1 that indicates small perturbations. The Laplace equation for the streamfunction is employed to solve the irrotational flow over a wavy wall to investigate the effect of wave steepness on the solution. The problem is approximated with the finite-volume method (FVM). An overview of commonly used discretization approaches in fluid dynamics is given in Appendix D. In the FVM the equation in each cell is formulated by means of a flux over each cell face (in 2-dim, cells are areas and faces are lines). A co-located variable arrangement is chosen (the unknown streamfunction is assigned to each cell), requiring the flux to be interpolated from the unknowns. The flux at a face is proportional to the derivative of the streamfunction in direction normal to the face. Making use of the definition of the streamfunction, this derivative is equal to the velocity component along the face's path vector. Thus, regarding the boundary conditions of the problem, the condition of a moving wall (applied here at the top boundary) can be implemented easily in that the tangential speed of the wall can be used directly to prescribe the flux. The situation is more delicate, however, if a Dirichlet condition is required at the boundary, since for a diffusion equation, solved with the FVM, the value of the unknown does not appear at the boundary. This situation occurs – for instance – on the wavy wall at the bottom boundary, where the streamfunction needs to be prescribed to ensure that the boundary resembles a streamline in the moving frame of reference. On a Dirichlet boundary, the interpolation to determine the flux is modified insofar as the value of the streamfunction at the boundary is affiliated to the unknowns (substituting the streamfunction in the cell farthest from the boundary) in such a way that the flux fulfills the b. c. to prescribed order of accuracy.

In particular, the diffusive flux with non-symmetric stencil (needed at or close to boundaries) needs extrapolation from a chain of 5 cells to be 4th order accurate in grid spacing on orthogonal grid and 9 cells to be 3rd order on arbitrary grid. The average over the Dirichlet value substitutes the cell-average value from the cell in the chain being farthest from the boundary.

In Fig. 3.17, the numerical results are compared to the asymptotic solution from this section.

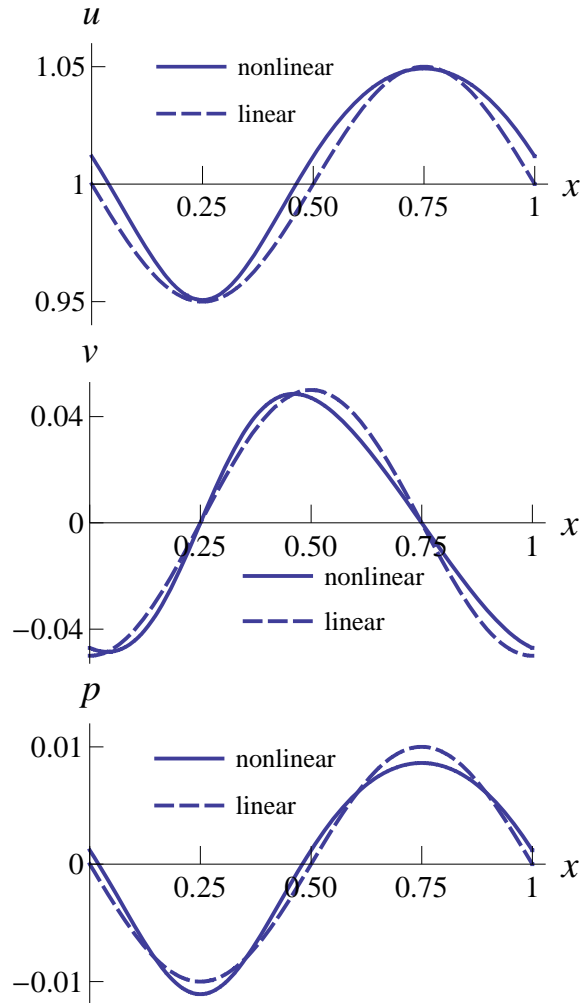


Figure 3.17: Potential flow over infinitely extended wavy wall. Effect of prescribing the boundary condition at the undisturbed (linear) and deflected (nonlinear) wall position. Solution of horizontal and vertical velocity components u (in the stationary frame) and v , and pressure p along the wavy wall; $c = 1.2$, $A_\lambda = 1/(8\pi)$.

Isoline plots of the numerical inviscid solution in the domain are presented in Sec. 3.5.

3.5 Viscous effects (periodic case)

The results from Sec. 3.4 for potential flow over a downstream travelling wave at large wave number show that the thrust force increases with the wave number and with the phase speed, but the main portion of thrust is produced in a region close to the leading edge. The leading-order pressure at mid-chord resembles the thrust-free downstream travelling pressure wave over an undulating surface with infinite streamwise extension, cf. Sec. 3.4.3. Thus, with the inviscid theory there is no thrust in the space-periodic case. In this section, the streamwise periodic

travelling wave is considered as in Sec. 3.4.3, but now viscous effects are taken into account. The Navier–Stokes equations Eq. (1.11) are solved together with the conservation of mass Eq. (1.3). As in Sec. 3.4.3, the dimensionless formulation from Eq. (1.23) is used, where $\tilde{\lambda}$ is the wavelength and \tilde{A} is the amplitude of the travelling wave. $\tilde{\rho} \tilde{U}^2$ is used as reference pressure.

3.5.1 Results in the literature

The case of viscous flow over a wavy surface with infinite streamwise extension has been considered in the literature. When viscosity of the fluid is taken into account, a dimensionless viscous drag force

$$F_f = -\frac{1}{\text{Re}_\lambda} \int_0^1 \left(2 \frac{\partial u}{\partial x} \frac{\partial w}{\partial x} - \frac{\partial u}{\partial y} - \frac{\partial v}{\partial x} \right) dx \quad (3.73)$$

(with $F_f > 0$) acts on the wall (F_f positive in x -direction). u and v are the velocity components at the wavy wall and Re_λ is the Reynolds number defined in Eq. (1.23). Then, the surface pressure may alter such that it gives rise to a thrust force ($-F_p$), given as

$$F_p = \int_0^1 p \frac{\partial w}{\partial x} dx, \quad (3.74)$$

where p is the fluid pressure along the upper surface of the wall. The *total* force is

$$F_d = F_p + F_f. \quad (3.75)$$

In the literature, the total wall force has been reported to become a thrust ($F_d < 0$) for both turbulent [91] and laminar [57] flow when c is sufficiently large. These results are reproduced in Fig. 3.18.

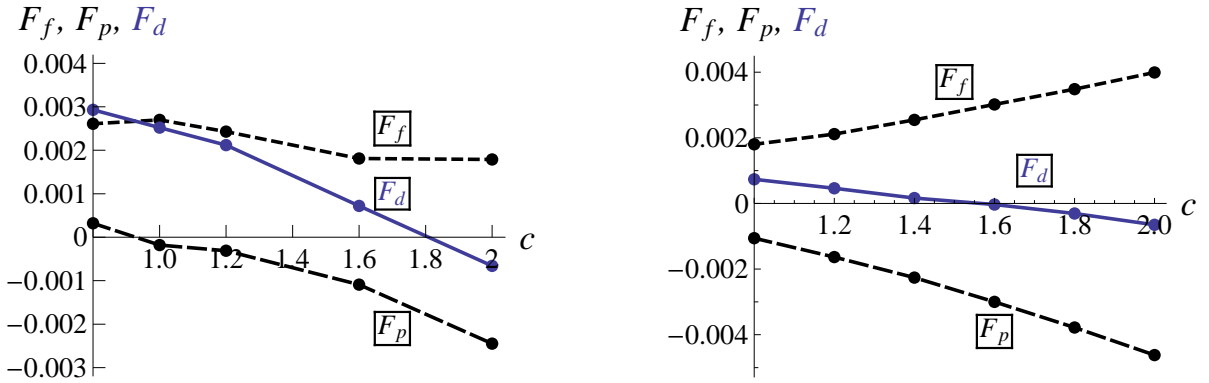


Figure 3.18: Dimensionless forces at the wall of an infinitely extended surface as a function of the phase speed c at a wave amplitude $A_\lambda = 1/(8\pi)$. Viscous force F_f , pressure force F_p , and total force $F_d = F_p + F_f$; Left: DNS results for turbulent flow at $\text{Re}_\lambda = 10170$, reproduced from Shen et. al. [91]; Right: laminar flow at $\text{Re}_\lambda = 2000$, reproduced from Lu & Yin [57].

The pressure force is thrust $F_p < 0$ at phase speeds $c \gtrsim 1$ and increases in size with increasing c . The result is similar to inviscid travelling-wave swimming, where at large wave numbers the

pressure thrust T_p scales with $(c - 1)$, see Eq. (3.64). Indeed, in the aforementioned literature [57], [91] the viscous flow over the surface of infinite extension has been related to the propulsive performance of fish swimming. However, the cause of thrust production is fundamentally different: In inviscid swimming of a body of finite length the vortex-shedding mechanism is crucial to generate thrust; On the infinitely extended surface the incorporation of viscosity is the cause for pressure thrust. Thus, in the inviscid limit the thrust vanishes, Sec. 3.4.3. In the viscous case, one would expect that the total force is always drag. In the attempt to understand the reported phenomenon of the total force being thrust $F_d < 0$ at large c , the laminar case from [57] is reconsidered and the results are questioned. As in [57] the problem is considered in the moving frame of reference, Fig. 3.16.

3.5.2 Discretization method

Discretization schemes for fluid flow can be distinguished in several ways. In this section, the discretization method used for the self-developed solver of the Navier–Stokes equations is briefly outlined. The references in this section point to literature where the used terms are explained in detail and where similar approaches have been pursued. Differences of commonly used approaches are discussed in detail in Appendix D. A verification of the present solver is given in Appendix E.

The finite volume method (cf. [21]) is used to discretize the continuity and Navier–Stokes equations Eqs. (1.3), (1.11). In the discretization and solution method, incompressibility is enforced to machine precision. The domain is partitioned into a structured, nonuniform grid with control volumes (or cells) of quadrilateral shape. The primitive variables (velocity components and pressure) are used as unknowns. A colocated variable arrangement is chosen. This means that the unknowns adhere to a certain cell, see [116], [75]. Cell average values are used for the set of unknowns (cf. [43]). The spatial interpolation of the variables is performed in physical space (cf. [46]). A polynomial ansatz is used for the interpolation (cf. [18]). The interpolation is performed as so-called k -exact reconstruction (cf. [10], [73]) from a central discretization scheme (cf. [55]). Eight cell-average values are employed in the reconstruction and the grid-dependent coefficients are solved numerically at each face-center point. From this, the fluxes at each cell boundary are expressed explicitly by the unknowns (cf. [24]). The non-linear expressions that originate from the convection terms are treated with the method sketched in [75]. The overall scheme is third-order accurate in space on arbitrary grid. The accuracy is of fourth-order on any Cartesian (possibly non-orthogonal and non-uniform) grid.

On inlet boundaries, the flux is imposed, while on outlet boundaries the flux is extrapolated by a third-order upwind reconstruction, (cf. [43], [58]). The numerical boundary conditions have to be chosen with great care to avoid a singular system matrix. It is well known that for non-penetrating boundary conditions (in a closed domain, or with periodic b. c. in one direction and walls in the other direction), the conservation and telescopic properties that are inherent to the finite volume method (due to unique fluxes between adjacent cells) result in a set of discrete continuity equations that already fulfill the boundary conditions, giving rise to a singular discrete divergence operator. This issue is circumvented (as usually) in that the continuity equation in one control volume is replaced with a condition that sets the absolute value of the pressure. Another challenge is the proper choice of pressure boundary conditions

to avoid a singular discrete gradient operator in Eq. (1.11). Somewhat surprisingly, tests with periodic pressure boundary conditions (on equidistant grid) unveil that the discrete gradient operator has full rank only when the number of control volumes in direction of the periodicity is odd.

The resulting algebraic system is arranged as linear system of equations. The matrix has sparse fill-in and its elements partly depend on the solution. The linear system is solved with a direct solver and the nonlinearity is iterated with a Newton–Raphson procedure. To display the results, a so-called deconvolution (cf. [75]) is used that returns the point value in each node from a fourth-order accurate interpolation of the average values from twelve surrounding cells.

3.5.3 Results

The present results for inviscid flow from Sec. 3.4.3 are compared to the DNS results by Shen et. al. [91] for turbulent flow at $\text{Re}_\lambda = 10170$, and to the present results for laminar flow at $\text{Re}_\lambda = 2000$. In all plots the phase speed is $c = 1.2$. The shape of the wave is given by $w = A_\lambda \sin(2\pi x)$ with a wave amplitude of $A_\lambda = 1/(8\pi)$. Fig. 3.19 shows an isoline plot for the distribution of the pressure in the domain close to the wavy wall.

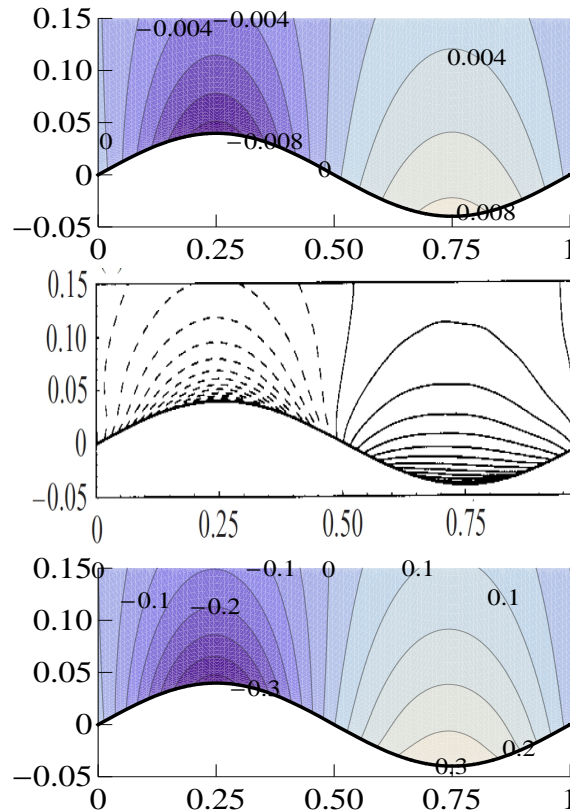


Figure 3.19: Isolines of the pressure. Comparison of inviscid (top), turbulent $\text{Re}_\lambda = 10170$ (mid) and laminar $\text{Re}_\lambda = 2000$ (bottom) solution for $c = 1.2$, $A_\lambda = 1/(8\pi)$. The turbulent case is copied from [91], dashed lines represent negative values and the isoline intervals is 0.005.

The distribution of the pressure looks qualitatively very similar in the inviscid, turbulent and laminar case, respectively. The pressure is minimum at the wave crest and maximum at the trough in all cases. At decreasing Reynolds number, the pressure perturbations increase. This result appears to be of importance when the fluid-structure interaction problem discussed above is considered at a lower Reynolds number. A plot of the vertical velocity component v is given in Fig. 3.20.

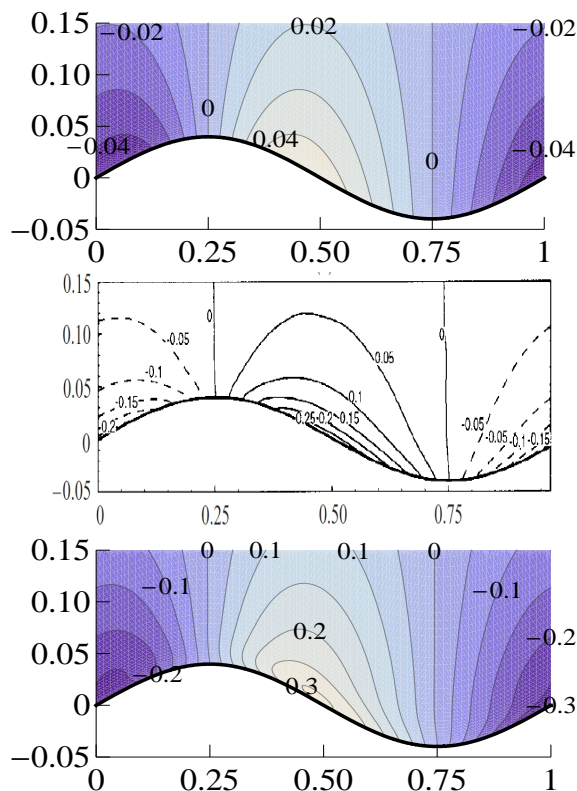


Figure 3.20: Isolines of the flow velocity component in vertical direction. Comparison of inviscid (top), turbulent (mid) and laminar (bottom) solution for $c = 1.2$, $A_\lambda = 1/(8\pi)$. Reynolds numbers Re_λ as in Fig. 3.19. The turbulent case is copied from [91].

In all cases, the maximum of the vertical velocity component along the wall occur at a position shifted slightly upstream from the point of steepest slope at $x = 0.5$, as can be seen from the distribution of velocity along the wall in the inviscid case Fig. 3.17. The perturbation of the vertical velocity component increases strongly from the inviscid to the turbulent case, but the increase is significantly slowed when the Reynolds number is further decreased to the laminar case. The streamlines in the moving frame of reference are shown in Fig. 3.21.

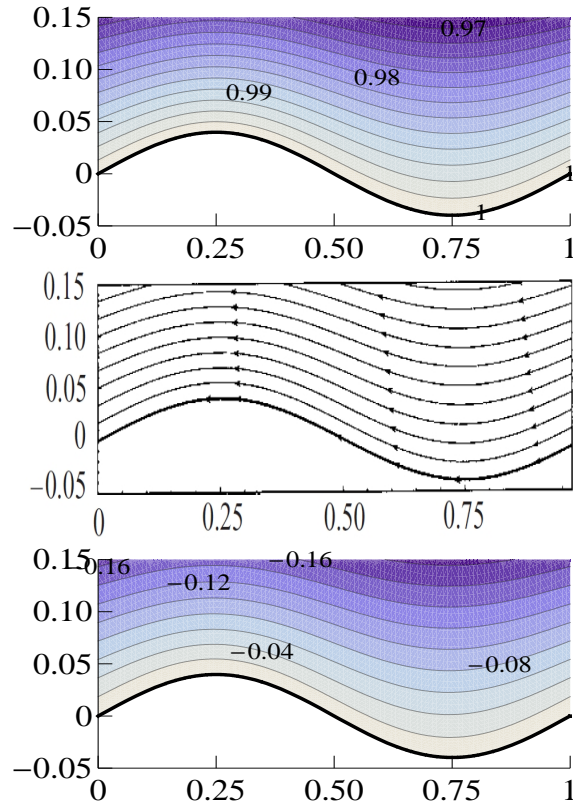


Figure 3.21: Isolines of the streamfunction in the frame moving with the phase speed c . Comparison of inviscid (top), turbulent (mid) and laminar (bottom) solution for $c = 1.2$, $A_\lambda = 1/(8\pi)$. Reynolds numbers Re_λ as in Fig. 3.19. The turbulent case is copied from [91].

The streamlines look rather unspectacular. However, they indicate that for the downstream travelling wave at a phase speed of $c = 1.2$ the flow is attached to the wavy wall at all considered Reynolds numbers. An important implication of the result is that in the potential flow theory for the downstream travelling wave in Sec. 3.4 the assumption of attached flow is applicable. The elimination of flow separation at $c = 1.2$ is the reason why the pressure distribution in Fig. 3.19 is almost completely symmetric. The solution of the streamlines, vertical velocity component, and pressure look qualitatively very similar for inviscid and viscous flow. However, the horizontal velocity component u is significantly different, see the comparison in Fig. 3.22.

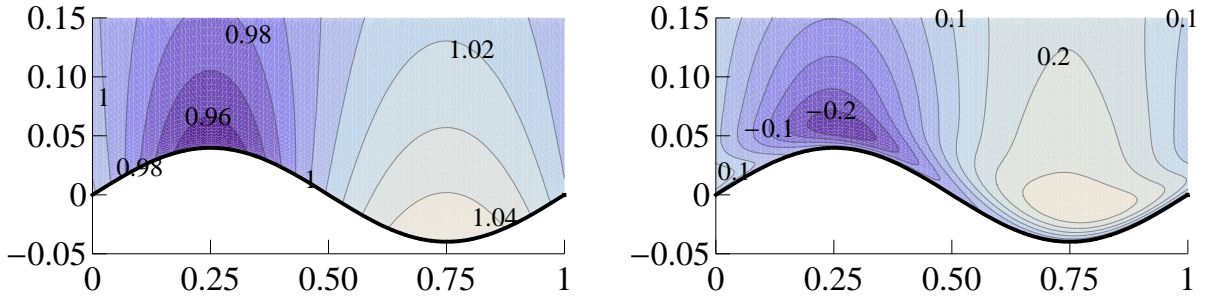


Figure 3.22: u in the stationary frame. Comparison of inviscid (left) and laminar (right) solution at $c = 1.2$, $A_\lambda = 1/(8\pi)$.

In the inviscid case, the fluid slips along the wavy wall, while in case of viscous flow $u = 0$ holds at the wall due to the no-slip condition Eq. (1.12). In the inviscid potential flow solution, the vorticity is zero everywhere by definition Eq. (1.1). Isolines of the vorticity for the laminar case in the vicinity of the wavy wall are shown in Fig. 3.23.

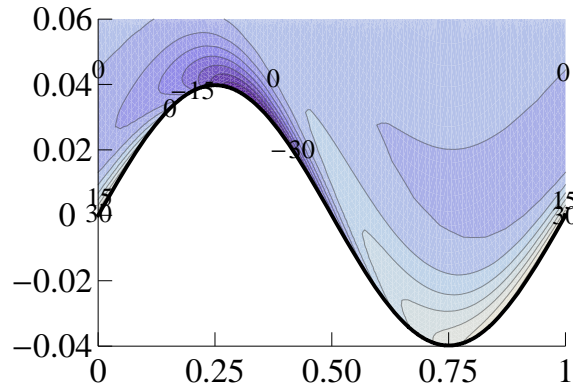


Figure 3.23: Vorticity $\omega = \partial u/\partial y - \partial v/\partial x$ for the laminar solution at $c = 1.2$, $A_\lambda = 1/(8\pi)$.

The vorticity is very high directly at the wall and reaches the maximum value in the wave trough. The flow is almost irrotational at a small distance above the wall (isolines with $\omega = 0$).

3.5.4 Comparison to literature for different phase speeds

From the above results for pressure and velocity field the viscous, pressure, and total force on the wall can be obtained from Eqs. (3.73)-(3.75). For the laminar flow with Reynolds number $Re_\lambda = 2000$ over the wavy wall with amplitude $A_\lambda = 1/(8\pi)$, the phase speed is varied in the interval $c = [1, 2]$ and the forces are evaluated in each case. The present results for the wall forces in comparison to the results in the literature are shown in Fig. 3.24.

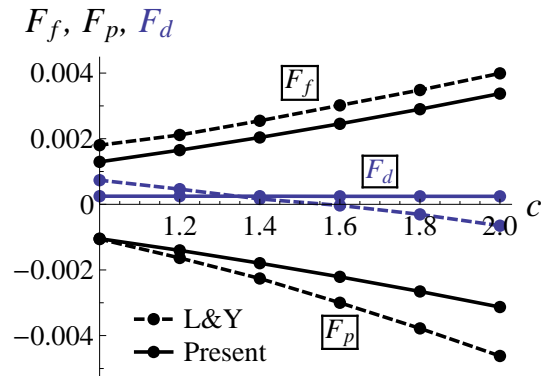


Figure 3.24: Infinite wavy surface: Viscous force F_f , pressure force F_p , and total drag force F_d for laminar flow as a function of the phase speed c ; $\text{Re}_\lambda = 2000$, $A_\lambda = 1/(8\pi)$. Dashed lines: Results reproduced from [57], Fig. 6a. Solid lines: Present results.

The present results confirm that the surface pressure gives rise to a thrust that counteracts the viscous force. Furthermore, both viscous drag and pressure thrust increase in size with increasing phase speed c . However, the present results reveal – in contrast to the results by Lu & Yin [57] – that for laminar flow over a surface of infinite extension the total force at the wall is always drag.

Chapter 4

Fluid Structure Interaction

4.1 Membrane in unbounded flow

In this section the interaction of the membrane equation with the unbounded potential flow is considered. The focus is on the optimum motion with regard to the efficiency-thrust trade-off. The result from above for prescribed optimum propulsion of a flapping foil Sec. 3.2.2, and a travelling wavy surface Sec. 3.3.2, are used for comparison to the membrane solutions. The unsteady potential flow theory from Sec. 2.1 in the representation by Chebyshev polynomials is used to describe the flow. Unsteady potential flow theory has been successfully employed in the literature: [61] and [5] discussed the instability of a flapping flag clamped at the leading edge; The propulsive performance of a flapping appendage has been studied by Alben [4] for small-amplitude pitching motion at the leading edge and by Michelin & Smith [60] for heaving motion at the leading edge. [4] reports that the optimal efficiency approaches 1 as rigidity becomes small and decreases to 30–50% (depending on pitch frequency) as rigidity becomes large.

In the present work we use a monolithic approach to solve the interaction problem, see the discussion in Sec. 4.2.3. A time-harmonic transverse motion is prescribed to the leading-edge point. Results with and without membrane inertia and for a different boundary condition at the trailing edge are presented.

4.1.1 Forced oscillation of the leading-edge point

The membrane equation

$$-\mu_M w_{1,\tau\tau} + \alpha_M w_{1,xx} - \beta_M w_1 = \Delta p_1 \quad \text{for } x_{LE} \leq x \leq x_{TE} \quad (1.27 \text{ revisited})$$

is used, with the leading and trailing edge placed at $x_{LE} = -1$ and $x_{TE} = 1$, respectively. $w_1(x, t)$ is the deflection of the membrane in first order. The boundary conditions Eq. (1.18) are written in dimensionless form as

$$w_1(-1, \tau) = A_{LE} \sin \tau, \quad (4.1)$$

$$w_{1,x}(1, \tau) = 0. \quad (4.2)$$

4.1.2 Formulation of the coupled problem

From the transformation $x = \cos \theta$ (see Sec. 2.1.7)

$$\frac{\partial}{\partial x} = \frac{\partial \theta}{\partial x} \frac{\partial}{\partial \theta} = -\frac{1}{\sin \theta} \frac{\partial}{\partial \theta},$$

$$\frac{\partial^2}{\partial x^2} = \frac{\partial \theta}{\partial x} \frac{\partial}{\partial \theta} \left(\frac{\partial \theta}{\partial x} \frac{\partial}{\partial \theta} \right) = -\frac{\cos \theta}{\sin^3 \theta} \frac{\partial}{\partial \theta} + \frac{1}{\sin^2 \theta} \frac{\partial^2}{\partial \theta^2}.$$

Then, with Eq. (2.18) one finds

$$w_{1,x} = -\frac{1}{\sin \theta} \sum_{n=1}^{\infty} n \beta_n [-\sin(n\theta)] \exp(i\tau), \quad (4.3)$$

$$w_{1,xx} = -\frac{\cos \theta}{\sin^3 \theta} \sum_{n=1}^{\infty} n \beta_n [-\sin(n\theta)] \exp(i\tau) + \frac{1}{\sin^2 \theta} \sum_{n=1}^{\infty} n^2 \beta_n [-\cos(n\theta)] \exp(i\tau). \quad (4.4)$$

Since time-harmonic motion is assumed, lateral pre-strain and inertia of the membrane can be grouped in the term $(\beta_M - \mu_M)$. Eq. (1.27) becomes with Eq. (2.21)

$$\alpha_M \left[\frac{\cos \theta}{\sin^3 \theta} \sum_{n=1}^{\infty} n \beta_n \sin(n\theta) - \frac{1}{\sin^2 \theta} \sum_{n=1}^{\infty} n^2 \beta_n \cos(n\theta) \right] -$$

$$(\beta_M - \mu_M) \left[\frac{1}{2} \beta_0 + \sum_{n=1}^{\infty} \beta_n \cos(n\theta) \right] = -a_0 \tan(\theta/2) + 2 \sum_{n=1}^{\infty} a_n \sin(n\theta). \quad (4.5)$$

Observing $\tan(\theta/2) = \frac{\sin \theta}{1 + \cos \theta}$, we multiply the equation by the factor $(1 + \cos \theta) \sin^3 \theta$

$$\alpha_M (1 + \cos \theta) \cos \theta \sum_{n=1}^{\infty} n \beta_n \sin(n\theta) - \tilde{\alpha} \sin \theta (1 + \cos \theta) \sum_{n=1}^{\infty} n^2 \beta_n \cos(n\theta) -$$

$$(\beta_M - \mu_M) \sin^3 \theta (1 + \cos \theta) \left[\frac{\beta_0}{2} + \sum_{n=1}^{\infty} \beta_n \cos(n\theta) \right] =$$

$$-a_0 \sin^4 \theta + 2 \sin^3 \theta (1 + \cos \theta) \sum_{n=1}^{\infty} a_n \sin(n\theta). \quad (4.6)$$

Before the relation between coefficients of deflection and pressure can be applied, the membrane equation requires some manipulation. In particular, Fourier half-range series are used to allow a comparison of coefficients. Using well-known relations for trigonometric functions, the left-hand side of the equation can be expressed solely by shifted sine terms, while the right-hand side can be expression solely by shifted cosine terms. One obtains for the lhs

$$(1 + \cos \theta) \cos \theta \sin(n\theta) = \frac{\sin(n\theta)}{2} - \frac{\sin(\theta - n\theta)}{2} - \frac{\sin(2\theta - n\theta)}{4} + \frac{\sin(\theta + n\theta)}{2} + \frac{\sin(2\theta + n\theta)}{4},$$

$$\sin \theta (1 + \cos \theta) \cos(n\theta) = \frac{\sin(\theta - n\theta)}{2} + \frac{\sin(2\theta - n\theta)}{4} + \frac{\sin(\theta + n\theta)}{2} + \frac{\sin(2\theta + n\theta)}{4},$$

$$\sin^3 \theta (1 + \cos \theta) = 3 \frac{\sin \theta}{4} + \frac{\sin(2\theta)}{4} - \frac{\sin(3\theta)}{4} - \frac{\sin(4\theta)}{8},$$

$$\begin{aligned} \sin^3 \theta (1 + \cos \theta) \cos(n\theta) &= 3 \frac{\sin(\theta - n\theta)}{8} + \frac{\sin(2\theta - n\theta)}{8} - \frac{\sin(3\theta - n\theta)}{8} - \frac{\sin(4\theta - n\theta)}{16} + \\ & 3 \frac{\sin(\theta + n\theta)}{8} + \frac{\sin(2\theta + n\theta)}{8} - \frac{\sin(3\theta + n\theta)}{8} - \frac{\sin(4\theta + n\theta)}{16}, \end{aligned}$$

and for the rhs

$$\sin^4 \theta = \frac{3}{8} - \frac{\cos(2\theta)}{2} + \frac{\cos(4\theta)}{8},$$

$$\begin{aligned} \sin^3 \theta (1 + \cos \theta) \sin(n\theta) &= 3 \frac{\cos(\theta - n\theta)}{8} + \frac{\cos(2\theta - n\theta)}{8} - \frac{\cos(3\theta - n\theta)}{8} - \frac{\cos(4\theta - n\theta)}{16} - \\ & 3 \frac{\cos(\theta + n\theta)}{8} - \frac{\cos(2\theta + n\theta)}{8} + \frac{\cos(3\theta + n\theta)}{8} + \frac{\cos(4\theta + n\theta)}{16}. \end{aligned}$$

The coupled equation Eq. (4.6) thus reads

$$\begin{aligned}
& \left[-(\beta_M - \mu_M) \left(\frac{3\beta_0}{8} + \frac{\beta_1}{8} - \frac{\beta_2}{2} - \frac{3\beta_3}{16} + \frac{\beta_4}{8} + \frac{\beta_5}{16} \right) + \tilde{\alpha} (3\beta_2 + 3\beta_3) \right] \sin \theta + \\
& \left[-(\beta_M - \mu_M) \left(\frac{\beta_0}{8} + \frac{\beta_1}{4} - \frac{\beta_2}{16} - \frac{3\beta_3}{8} - \frac{\beta_4}{8} + \frac{\beta_5}{8} + \frac{\beta_6}{16} \right) + \tilde{\alpha} (\beta_2 + 6\beta_3 + 5\beta_4) \right] \sin(2\theta) + \\
& \left[-(\beta_M - \mu_M) \left(-\frac{\beta_0}{8} + \frac{\beta_1}{16} + \frac{3\beta_2}{8} - \frac{3\beta_4}{8} - \frac{\beta_5}{8} + \frac{\beta_6}{8} + \frac{\beta_7}{16} \right) + \right. \\
& \quad \left. \alpha_M \left(-\beta_2 + \frac{3\beta_3}{2} + 10\beta_4 + \frac{15\beta_5}{2} \right) \right] \sin(3\theta) + \\
& \left[-(\beta_M - \mu_M) \left(-\frac{\beta_0}{16} - \frac{\beta_1}{8} + \frac{\beta_2}{8} + \frac{3\beta_3}{8} - \frac{3\beta_5}{8} - \frac{\beta_6}{8} + \frac{\beta_7}{8} + \frac{\beta_8}{16} \right) + \right. \\
& \quad \left. \alpha_M \left(-\frac{\beta_2}{2} - 3\beta_3 + 2\beta_4 + 15\beta_5 + \frac{21\beta_6}{2} \right) \right] \sin(4\theta) + \\
& \sum_{n=5}^{\infty} \left\{ -(\beta_M - \mu_M) \left[-\frac{\beta_{n-4}}{16} - \frac{\beta_{n-3}}{8} + \frac{\beta_{n-2}}{8} + \frac{3\beta_{n-1}}{8} - \frac{3\beta_{n+1}}{8} - \frac{\beta_{n+2}}{8} + \frac{\beta_{n+3}}{8} + \frac{\beta_{n+4}}{16} \right] + \right. \\
& \quad \alpha_M \left[\left(\frac{n-2}{4} - \frac{(n-2)^2}{4} \right) \beta_{n-2} + \left(\frac{n-1}{2} - \frac{(n-1)^2}{2} \right) \beta_{n-1} + \frac{n}{2} \beta_n + \right. \\
& \quad \left. \left(\frac{n+1}{2} + \frac{(n+1)^2}{2} \right) \beta_{n+1} + \left(\frac{n+2}{4} + \frac{(n+2)^2}{4} \right) \beta_{n+2} \right] \left. \right\} \sin(n\theta) = \\
& - \left\{ \left(\frac{3a_0}{8} + \frac{3a_1}{4} + \frac{a_2}{4} - \frac{a_3}{4} - \frac{a_4}{8} \right) + \left(\frac{3a_2}{4} + \frac{a_1+a_3}{4} - \frac{a_2+a_4}{4} - \frac{a_3+a_5}{8} \right) \cos \theta + \right. \\
& \quad \left(-\frac{a_0}{2} + \frac{3a_3}{4} + \frac{a_4}{4} - \frac{a_1+a_5}{4} - \frac{a_2+a_6}{8} - \frac{3a_1}{4} \right) \cos(2\theta) + \\
& \quad \left(\frac{3a_4}{4} + \frac{a_5}{4} - \frac{a_6}{4} - \frac{a_1+a_7}{8} - \frac{3a_2}{4} - \frac{a_1}{4} \right) \cos(3\theta) + \\
& \quad \left(\frac{a_0}{8} + \frac{3a_5}{4} + \frac{a_6}{4} - \frac{a_7}{4} - \frac{a_8}{8} - \frac{3a_3}{4} - \frac{a_2}{4} + \frac{a_1}{4} \right) \cos(4\theta) + \\
& \quad \left. \sum_{k=5}^{\infty} \left(\frac{a_{k-4}}{8} + \frac{a_{k-3}}{4} - \frac{a_{k-2}}{4} - \frac{3a_{k-1}}{4} + \frac{3a_{k+1}}{4} + \frac{a_{k+2}}{4} - \frac{a_{k+3}}{4} - \frac{a_{k+4}}{8} \right) \cos(k\theta) \right\} \quad (4.7)
\end{aligned}$$

The lhs is expressed solely in terms of sine functions, while the rhs consists solely of cosine functions. To compare coefficients, odd and even trigonometric functions need to be matched. Thus, we apply Fourier *half-range* series. There are two possibilities. In the first approach

$\sin(nx)$ on $x \in [0, \pi]$ is expressed in terms of Fourier half-range cosine series

$$\sin(nx) = \begin{cases} \frac{4}{\pi} \sum_{k=1}^{\infty} \frac{n}{n^2 - (2k-1)^2} \cos[(2k-1)x] & \text{when } n \text{ is even} \\ \frac{2}{\pi n} + \frac{4}{\pi} \sum_{k=1}^{\infty} \frac{n}{n^2 - 4k^2} \cos(2kx) & \text{when } n \text{ is odd} \end{cases} \quad (4.8)$$

In this case, $\sin(nx)$ has a jump-free periodic extension. The second choice, replacing cosine terms by sine terms, is not pursued to avoid the Gibbs phenomenon at the jumps that arise from periodic continuation. We replace the sum in the lhs of Eq. (4.7) with Eq. (4.8)

$$\begin{aligned} \sum_{n=5}^{\infty} a_n \sin(n\theta) &= \sum_{n=3}^{\infty} a_{2n-1} \sin[(2n-1)\theta] + \sum_{n=3}^{\infty} a_{2n} \sin(2n\theta) = \\ &= \sum_{n=3}^{\infty} a_{2n-1} \left[\frac{2}{\pi(2n-1)} + \frac{4}{\pi} \sum_{k=1}^{\infty} \frac{2n-1}{(2n-1)^2 - 4k^2} \cos(2k\theta) \right] + \\ &= \sum_{n=3}^{\infty} a_{2n} \frac{4}{\pi} \sum_{k=1}^{\infty} \frac{2n}{(2n)^2 - (2k-1)^2} \cos[(2k-1)\theta] \end{aligned}$$

such that a comparison of coefficients for the terms $\cos(m\theta)$ with $m = 0, 1, 2, \dots$ can be conducted. Then, by using Eqs. (2.29), (2.31), written in full form

$$\begin{aligned} a_0 &= -i\sigma C(\sigma)\beta_0 + [(1 - C(\sigma))i\sigma - 2C(\sigma)]\beta_1 + \\ &= 2(1 - C(\sigma)) \sum_{k=1}^{\infty} 2k\beta_{2k} - 2C(\sigma) \sum_{k=2}^{\infty} (2k-1)\beta_{2k-1} \end{aligned} \quad (4.9)$$

$$a_n = \begin{cases} \frac{\sigma^2}{2n}\beta_{n-1} - i2\sigma\beta_n - \left[\frac{\sigma^2}{2n} + 2(n+1) \right] \beta_{n+1} - 2 \sum_{k=\frac{n+3}{2}}^{\infty} 2k\beta_{2k} & \text{when } n \text{ is odd} \\ \frac{\sigma^2}{2n}\beta_{n-1} - i2\sigma\beta_n - \left[\frac{\sigma^2}{2n} + 2(n+1) \right] \beta_{n+1} - 2 \sum_{k=\frac{n+4}{2}}^{\infty} (2k-1)\beta_{2k-1} & \text{when } n \text{ is even} \end{cases} \quad (4.10)$$

the membrane equation is expressed solely by coefficients of motion β_n for each "half-range mode" m .

4.1.3 Boundary conditions

Using Eq. (2.18) and Eq. (4.3), the boundary conditions Eq. (4.1) at the leading edge $\theta = -\pi$ and Eq. (4.2) at the trailing edge $\theta = 0$ become

$$\Re \left[\left(\frac{\beta_0}{2} + \sum_{n=1}^{\infty} (-1)^n \beta_n \right) (\cos \tau + i \sin \tau) \right] = A_{LE} \sin \tau, \quad (4.11)$$

$$\Re \left[\sum_{n=1}^{\infty} n\beta_n \underbrace{\lim_{\theta \rightarrow 0} \frac{\sin(n\theta)}{\sin \theta}}_n (\cos \tau + i \sin \tau) \right] = 0, \quad (4.12)$$

which can be grouped into

$$\frac{\beta_0}{2} + \sum_{k=1}^{\infty} (-1)^k \beta_k = -iA_{LE}, \quad (4.13)$$

$$\sum_{k=1}^{\infty} k^2 \beta_k = 0. \quad (4.14)$$

4.1.4 Solution procedure

The above system is truncated at a certain wave number. The modes n in Eq. (4.7) are resolved up to a maximum value n_{Max} . The maximum number of half-range modes m is limited to $m_{Max} = n_{Max} - 2$ and yields coefficient matrices for the lhs and for the rhs. Inclusion of the two boundary conditions Eq. (4.13) gives a linear system with square matrices A_{mn} and B_{mn}

$$A_{mn}\beta + B_{mn}\beta = b \quad (4.15)$$

that is solved for the solution vector β .

4.1.5 Postprocessing

From the solution β_n , the pressure coefficients Eqs. (4.9, 4.10) and thus the thrust force T and the efficiency η can be determined as in Sec. 2.1.9. In the postprocessing, the maximum deflection of the membrane along the chord $w_{1,max}$ is determined. To allow a fair comparison of the generated thrust between membrane motions with small and large deflection, the amplitude of motion (the dimensionless leading-edge amplitude $A_{LE} = \dot{A}_{LE}/\dot{L}$) is rescaled in all the calculated results such that $w_{1,max} = 2$.

4.1.6 Results

The flapping frequency is limited to $\sigma = 5$. In the plots the efficiency η vs. the thrust force T is shown. The results are compared to the optimum propulsion of a rigid foil shown in Fig. 3.6 and to the prescribed TWS motion moving at a frequency $\sigma = 5$ (and varying wavenumber k) depicted in the right bottom plot of Fig. 3.11. The number of resolved modes is chosen $n_{Max} = 100$ in all examples. An example in Appendix A.4 shows that results with the present method using only $n_{Max} = 20$ modes agree very well with the results from the panel method.

Membrane without inertia terms

In the following the mass of the membrane is assumed to be negligible, i. e. $\mu_M = 0$ in Eq. (1.27). The results from all runs that generate positive thrust and have efficiency between 0.5 and 1 are depicted in Fig. 4.1.

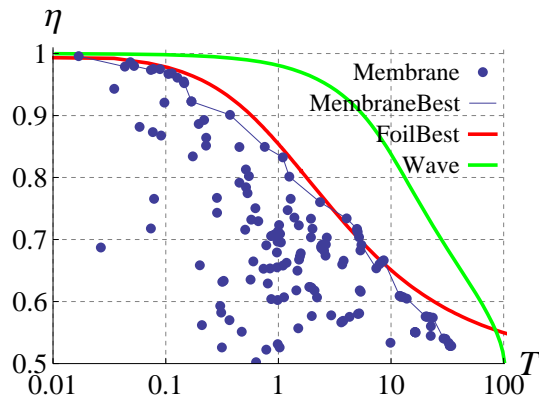


Figure 4.1: Results of propulsive efficiency η vs. dimensionless thrust force T : Membrane model without inertia term (blue points \bullet , maxima connected by blue line); Pareto curves for optimum foil motion (red line) and travelling wavy surface (green line).

When the membrane parameters are tuned appropriately, the resulting thrust and efficiency values reach the Pareto curve of the best foil motions. However, the massless membrane model cannot outperform the rigid foil and does not arrive at the efficiency of a travelling wavy surface. The input parameters and results for the combinations that give the best results are given in Tab. 4.1.

α_M	β_M	σ	A_{LE}	T	η
0.02	0.	0.5	1.98	0.0169	0.996
0.02	0.	1.	1.97	0.0433	0.979
0.05	0.	0.5	1.98	0.0485	0.986
0.07	0.	0.5	1.96	0.0523	0.98
0.09	0.	0.5	1.96	0.0738	0.974
0.08	0.	0.5	1.97	0.089	0.975
0.18	1.05	1.15	1.07	0.127	0.961
0.18	1.04	1.15	1.09	0.146	0.952
0.18	1.03	1.15	1.12	0.169	0.923
0.1	0.	1.	1.93	0.372	0.901
0.185	0.	1.5	1.7	0.757	0.85
0.187	0.	1.5	1.89	1.09	0.833
0.19	0.	1.5	1.98	1.25	0.801
0.1	0.	3.	2.	2.34	0.76
0.1	0.	4.	2.	4.04	0.734
0.1	0.	5.	2.	4.98	0.717
0.1	0.1	5.	2.	5.02	0.714
0.1	0.2	5.	2.	5.06	0.712
0.1	0.5	5.	2.	5.2	0.704
0.1	1.	5.	2.	5.46	0.691
0.2	1.	5.	2.	7.4	0.654
0.2	0.5	5.	2.	7.9	0.66
0.2	0.2	5.	2.	8.3	0.664
0.2	0.1	5.	2.	8.45	0.665
0.2	0.	5.	2.	8.6	0.666
0.5	0.	5.	2.	11.9	0.609
0.5	0.1	5.	2.	12.1	0.609
0.5	0.2	5.	2.	12.3	0.608
0.5	0.5	5.	2.	12.8	0.607
0.5	1.	5.	2.	13.8	0.605
1.	0.	5.	2.	20.3	0.576
1.	0.1	5.	2.	20.6	0.576
1.	0.2	5.	2.	20.9	0.576
1.	0.5	5.	2.	21.9	0.575
1.	1.	5.	2.	23.5	0.574
3.	0.	5.	1.7	29.2	0.54
5.	0.	5.	1.31	33.2	0.529
5.	0.1	5.	1.32	33.3	0.529
5.	0.2	5.	1.33	33.4	0.529
5.	0.5	5.	1.37	33.7	0.529
5.	1.	5.	1.44	34.3	0.528

Table 4.1: Best results for the membrane model that excludes inertia ($\mu_M = 0$): Input parameters and output.

Membrane with inertia terms

In the following the mass of the membrane is taken into account, i. e. $\mu_M > 0$. The results are shown in Fig. 4.2.

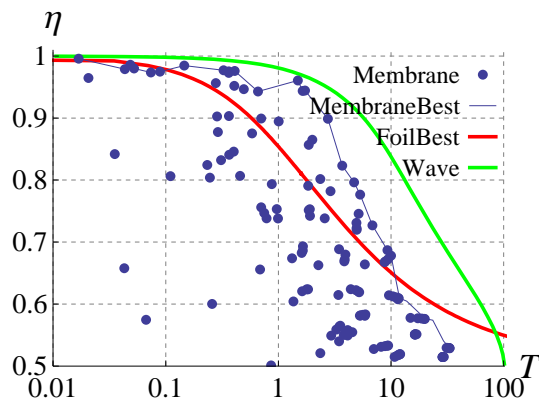


Figure 4.2: Results of efficiency η vs. thrust force T : Membrane model with inertia term (points ●); Pareto curves as indicated.

When inertia of the membrane is taken into account, combinations of parameters exist that admit $\beta_M - \mu_M < 0$, i. e. that the inertia term of the membrane becomes larger in size than the term for lateral pre-strain. Then, the membrane device can significantly outperform the best foil motions. At low levels of thrust, the membrane device allows efficiencies that approach the travelling wavy surface. The input parameters and results for the combinations that give the best results are given in Tab. 4.2.

α_M	$\beta_M - \mu_M$	σ	A_{LE}	T	η
0.02	0.	0.5	1.98	0.0169	0.996
0.02	0.	1.	1.97	0.0433	0.979
0.05	0.	0.5	1.98	0.0485	0.986
0.07	0.	0.5	1.96	0.0523	0.98
0.09	0.	0.5	1.96	0.0738	0.974
0.08	0.	0.5	1.97	0.089	0.975
0.02	-0.1	2.	1.9	0.146	0.985
0.05	-0.2	2.	1.85	0.326	0.977
0.005	-0.1	5.	1.58	0.363	0.975
0.025	-0.1	2.	1.97	0.41	0.976
0.0125	-0.1	2.	2.	0.659	0.943
0.02	-0.5	5.	1.63	1.49	0.961
0.04	-1.	5.	1.54	1.64	0.944
0.01	-0.1	5.	2.	1.72	0.944
0.05	-1.	5.	1.79	2.75	0.899
0.08	-2.	5.	1.78	3.69	0.823
0.09	-2.	5.	1.93	4.7	0.796
0.1	-2.	5.	1.84	5.32	0.776
0.14	-2.	5.	1.94	6.83	0.727
0.2	-2.	5.	1.97	9.3	0.687
0.2	-0.5	5.	2.	9.41	0.672
0.2	-1.	5.	1.99	9.99	0.678
0.5	0.	5.	2.	11.9	0.609
0.5	0.1	5.	2.	12.1	0.609
0.5	0.2	5.	2.	12.3	0.608
0.5	0.5	5.	2.	12.8	0.607
0.5	1.	5.	2.	13.8	0.605
1.	0.	5.	2.	20.3	0.576
1.	0.1	5.	2.	20.6	0.576
1.	0.2	5.	2.	20.9	0.576
1.	0.5	5.	2.	21.9	0.575
1.	1.	5.	2.	23.5	0.574
3.	0.	5.	1.7	29.2	0.54
5.	0.	5.	1.31	33.2	0.529
5.	0.1	5.	1.32	33.3	0.529
5.	0.2	5.	1.33	33.4	0.529
5.	0.5	5.	1.37	33.7	0.529
5.	1.	5.	1.44	34.3	0.528

Table 4.2: Best results for the membrane model that includes inertia: Input parameters and output.

The theoretical results in Tab. 4.2 show that inertia (i. e. $\beta_M - \mu_M < 0$) has a positive effect

on the propulsive properties in the medium range of thrust $T = 0.15, \dots, 10$. The positive effect is similar to the efficiency-enhancement observed in a foil with passive chordwise flexibility (see Sec. 3.3.1).

Membrane with inertia and different B. C. at the trailing edge

The results in Fig. 4.2 show that the efficiency cannot be enhanced up to the efficiency of the travelling wavy surface at higher levels of thrust by taking into account the mass of the membrane ($\mu_M > 0$). The boundary condition of zero inclination at the trailing edge that does not allow a travelling wave solution Eq. (4.2). In order to study if higher efficiency is prohibited by this boundary condition, the boundary condition at the TE is altered to allow an “outgoing kinematic wave“ such that it follows from the linearized kinematic boundary condition on the membrane Eq. (2.15) that

$$v(1, 0, \tau) = \Omega \frac{\partial w(1, \tau)}{\partial \tau} + \frac{\partial w(1, \tau)}{\partial x} = 0.$$

This boundary condition appears to be rather artificial. However, we show in the following that it permits a membrane deflection of cosine shape at a certain choice of parameters.

It can be readily seen that the membrane equation Eq. (1.27) obeys the solution of a single travelling wave (as discussed in Sec. 3.3.2) at a phase speed equal to the speed of oncoming flow ($c = 1$, or $\sigma = k$) if the parameters are chosen such that

$$\beta_M - \mu_M = -\alpha_M \sigma^2, \quad (4.16)$$

provided that we can set $\Delta p = 0$ in Eq. (1.27). Indeed, the latter condition is fulfilled by a single travelling wave motion when $\sigma = k$ (see Eq. (3.46) with a_0 from Eq. (3.44)). Thus, we can conclude that the deflection of the membrane performs a single travelling wave with phase speed $c = 1$ when the ratio of parameters is set to $(\beta_M - \mu_M)/(-\alpha_M \sigma^2) = 1$. In this case, $T = 0$ and $\eta = 1$ (see Sec. 3.3.2). Thrust is generated when $\beta_M - \mu_M > -\alpha_M \sigma^2$. Thus, either $(\beta_M - \mu_M)$, α_M , or σ need to be increased with respect to Eq. (4.16). The following parameter values are considered:

Parameter	Range of values
σ	0.5, 1, 2, 5
$\beta_M - \mu_M$	-10, \dots , 0
α_M	$-(\beta_M - \mu_M) / \sigma^2, \dots, 10$

Table 4.3: Range for the input parameters.

The results are displayed in Fig. 4.3.

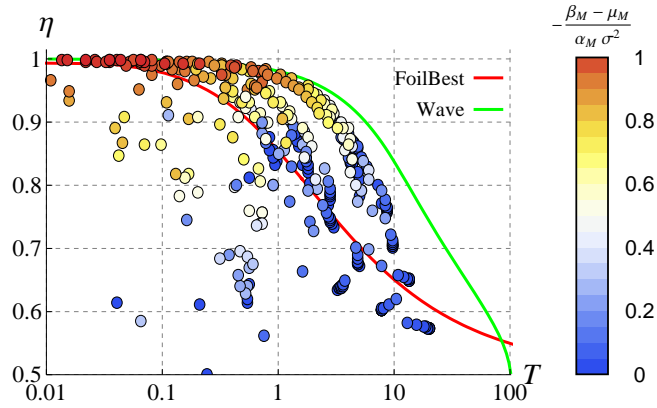


Figure 4.3: Results of efficiency η vs. thrust force T : Membrane model with inertia term and travelling wave B. C. at the TE (colored points); Pareto curves as indicated. The color given to each point indicates the value of the ratio $(\beta_M - \mu_M)/(-\alpha_M \sigma^2)$.

An analysis of the data points shows that optimum efficiency is achieved when the frequency reaches the maximum value, i. e. $\sigma = 5$ (see Tab. 4.4), as it is the case for the Pareto front of the travelling wave. The best solutions obtained for the coupled problem closely stick to the Pareto curve of the cosine wave. The color given to each of the solution points in Fig. 4.3 indicates the value of the ratio $(\beta_M - \mu_M)/(-\alpha_M \sigma^2)$. The highest efficiency is attained when the ratio is chosen slightly below one, i. e. for solutions that evolve from the point where $T = 0$ and $\eta = 1$. It may be of interest if there exists a correlation between the efficiency and the value of the ratio $(\beta_M - \mu_M)/(-\alpha_M \sigma^2)$. In order to find out if the ratio is a crucial parameter for good efficiency, the ratio is plotted in Fig. 4.4 with the efficiency given as color to each of the points.

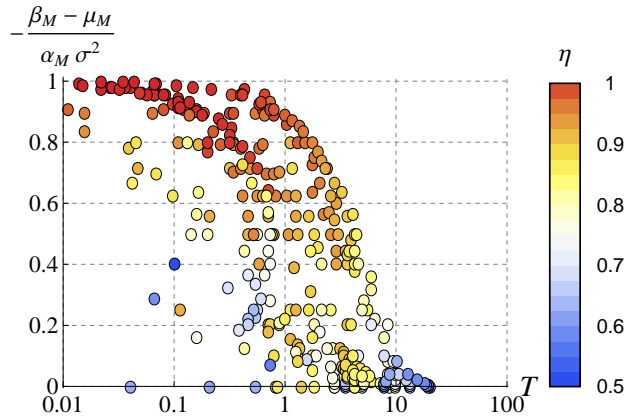


Figure 4.4: Ratio of membrane parameters vs. thrust force T for the solutions in Fig. 4.3. The color given to each point indicates the value of the efficiency η .

The Pareto optimum of the ratio stays very close to one (a value of one obeys Eq. (4.16) with the thrust-free solution $T = 0$) in the range of small and intermediate thrust, and falls to zero at high thrust. The color of the points indicates the propulsive efficiency of the motion. The plot

confirms that high efficiency is obtained only when the ratio $(\beta_M - \mu_M) / (-\alpha_M \sigma^2)$ is chosen at a value below one. From the results, a recommendation for the optimum design and operating parameters can be derived. Dependent on the required thrust T , the ratio $(\beta_M - \mu_M) / (-\alpha_M \sigma^2)$ can be depicted from Fig. 4.4. Then, α_M , β_M , μ_M , and σ can be tuned for an optimal setting. The input parameters and results for the combinations that give the best results are depicted in Tab. 4.4.

α_M	$\beta_M - \mu_M$	σ	A_{LE}	T	η
0.0201	-0.5	5.	2.	0.0353	0.998
0.0045	-0.11	5.	1.99	0.0356	0.999
0.0043	-0.105	5.	2.	0.0398	0.998
0.402	-10.	5.	2.	0.0436	0.999
0.0046	-0.11	5.	1.98	0.0568	0.998
0.0033	-0.08	5.	1.99	0.065	0.998
0.0202	-0.5	5.	2.	0.0689	0.996
0.0044	-0.105	5.	1.99	0.0801	0.997
0.0203	-0.5	5.	2.	0.106	0.994
0.0045	-0.105	5.	1.98	0.107	0.996
0.0056	-0.13	5.	1.97	0.138	0.995
0.0031	-0.07	5.	1.91	0.162	0.997
0.0045	-0.1	5.	1.97	0.178	0.994
0.05	-1.	5.	1.98	0.201	0.994
0.41	-10.	5.	2.	0.213	0.993
0.0032	-0.07	5.	1.93	0.25	0.995
0.0056	-0.12	5.	1.95	0.277	0.991
0.0034	-0.07	5.	2.	0.319	0.988
0.0045	-0.09	5.	1.95	0.321	0.99
0.0033	-0.07	5.	1.98	0.327	0.992
0.21	-5.	5.	2.	0.392	0.989
0.42	-10.	5.	2.	0.417	0.986
0.0056	-0.11	5.	1.93	0.417	0.986
0.041	-1	5.	1.99	0.438	0.989
0.0056	-0.1	5.	1.92	0.558	0.982
0.13	-3.	5.	2.	0.593	0.986
0.042	-1	5.	2.	0.663	0.982
0.09	-2.	5.	2.	0.777	0.982
0.1	-2.	5.	2.	1.29	0.968
0.11	-2.	5.	2.	1.78	0.956
0.12	-2.	5.	2.	2.04	0.946
0.071	-1.	5.	2.	2.19	0.943
0.08	-1.	5.	2.	2.53	0.934

Table 4.4: Best results for the membrane model with inertia and adjusted trailing-edge boundary condition: Input parameters and output (continued on next page).

α_M	$\beta_M - \mu_M$	σ	A_{LE}	T	η
0.09	-1.	5.	2.	2.84	0.924
0.1	-1.	5.	2.	2.91	0.916
0.2	-3.	5.	2.	2.91	0.921
0.16	-2.	5.	2.	2.98	0.912
0.063	-0.2	5.	2.	3.08	0.901
0.071	-0.2	5.	2.	3.31	0.898
0.18	-2.	5.	2.	3.54	0.9
0.1	-0.5	5.	2.	3.6	0.894
0.09	-0.2	5.	2.	3.71	0.887
0.09	-0.1	5.	2.	3.77	0.883
0.1	-0.2	5.	2.	3.98	0.881
0.25	-3.	5.	2.	3.98	0.891
0.1	-0.1	5.	2.	4.1	0.877
0.4	-5.	5.	1.97	4.2	0.874
0.1	0.	5.	2.	4.21	0.873
0.12	-0.2	5.	2.	4.38	0.871
0.12	-0.1	5.	2.	4.43	0.867
0.14	-0.2	5.	2.	4.77	0.861
0.14	-0.1	5.	2.	4.87	0.858
0.18	-0.2	5.	2.	5.27	0.845
0.18	-0.1	5.	2.	5.28	0.842
0.32	-2.	5.	2.	5.5	0.838
0.22	-0.2	5.	2.	5.79	0.83
0.22	-0.1	5.	2.	5.91	0.828
0.56	-5.	5.	1.96	5.99	0.825
0.32	-0.1	5.	2.	7.35	0.8
0.5	-2.	5.	2.	7.74	0.791
0.5	-1.	5.	1.93	8.31	0.777
0.5	-0.5	5.	1.93	8.51	0.77
0.5	-0.2	5.	1.93	8.6	0.765
0.5	-0.1	5.	1.94	8.62	0.764
0.5	0.	5.	1.94	8.64	0.763
0.5	0.1	5.	1.95	8.65	0.761
0.5	0.2	5.	1.95	8.66	0.76
0.5	0.5	5.	1.97	8.66	0.756
1.	-2.	5.	1.72	9.47	0.721
1.	-1.	5.	1.77	9.66	0.713
1.	-0.5	5.	1.81	9.69	0.709
2.	-2.	5.	2.	10.7	0.658
2.	-1.	5.	2.	12.3	0.654

Table 4.4: Best results for the membrane model with inertia and adjusted trailing-edge boundary condition: Input parameters and output (continued on next page).

α_M	$\beta_M - \mu_M$	σ	A_{LE}	T	η
2.	-0.5	5.	2.	13.2	0.652
2.	-0.2	5.	1.97	13.4	0.651
2.	-0.1	5.	1.96	13.5	0.651
2.	0.	5.	1.95	13.5	0.65
2.	0.1	5.	1.94	13.6	0.65
2.	0.2	5.	1.93	13.6	0.65
2.	0.5	5.	1.89	13.7	0.648
10.	-5.	5.	2.	15.6	0.579
10.	-2.	5.	2.	17.9	0.576
10.	-1.	5.	2.	18.9	0.575
10.	-0.5	5.	2.	19.4	0.575
10.	-0.1	5.	2.	19.8	0.574
10.	-0.2	5.	2.	19.7	0.574
10.	0.	5.	2.	19.9	0.574
10.	0.1	5.	2.	20.	0.574
10.	0.2	5.	2.	20.2	0.574
10.	0.5	5.	2.	20.5	0.574

Table 4.4: Best results for the membrane model with inertia and adjusted trailing-edge boundary condition: Input parameters and output.

A further increase in efficiency may be attained from an improved design at the trailing edge (for instance, if the free end is replaced by prescribed motion). However, comparing Fig. 4.3 to Fig. 4.2 and Fig. 4.1, the present results show that proper tuning of membrane inertia is of more importance.

4.2 Double channel membrane pump

4.2.1 Potential flow theory with the panel method

Solutions for the dependence of the trailing edge vorticity on the channel width have been discussed for pure heaving foil motion in Sec. 2.2. The propulsive efficiency for the channel flow of a flapping foil and of a prescribed travelling wave motion have been given in Sec. 3.2.3 and Sec. 3.3.4, respectively. In this section, the results with the panel code for a flapping membrane in channel flow from Sec. 2.3 are compared with the CFD results in Sec. 4.2.3.

4.2.2 CFD results

In this chapter the start-up phase of the pump, the obtained flow velocity and Reynolds number from prescribed plate motion, and the coupling strategies for fluid-structure interaction are discussed by employed the commercial CFD package Fluent[®]. The results, although potentially inaccurate due to coarse grid resolution, elucidate the principle features of the membrane pump. Conclusions are drawn for the procedure in the subsequent chapters.

Regarding the start-up phase of the pump it is outlined in Sec. 1.2.1 that the asymmetric excitation of a motion (at one end of the channel) results in a mean flow through the channel. However, in [110] it is shown that symmetric flapping in otherwise quiescent fluid can also result in a mean motion in one direction due to instability. In the following, asymmetric excitation is considered.

Pitching plate pump

T. Müllner¹ employed Fluent[®] to investigate pumping of incompressible fluid through a channel via a flat plate (with initial position at the centerline of the channel) that is pitching about one of its endpoints in prescribed periodic motion. The model can be illustrated by replacing the membrane in Fig. 1.1 by the flat plate, pitching about the *LE* with ($\tilde{A}_{LE} = 0$) with *TE* amplitude \tilde{A}_{TE} . The problem has been treated as two-dimensional in the \tilde{x} - \tilde{y} -plane. The user-defined function (UDF) DEFINE_GRID_MOTION has been used to move the mesh congruently with the plate. A so-called PRESSURE_OUTLET boundary condition at both ends of the channel, combined with the initial condition of quiescent fluid, guarantee that the occurrence of mean flow is a direct consequence of the asymmetry arising from pitching motion. In the long-term, a time-periodic mean channel flow evolves that is directed from the plate's pitching point downstream, i. e. the pitching plate acts as a pump. Two values for the deflection of the pitching motion \tilde{A}_{TE} are used. The results for the mean flow velocity \tilde{U}_m are given in Tab. 4.5.

Amplitude	Inviscid	Laminar	Turbulent ($k - \epsilon$)
$\tilde{A}_{TE} = 0.010$ m	0.374 m/s	0.378 m/s	0.418 m/s
$\tilde{A}_{TE} = 0.025$ m	0.830 m/s	0.793 m/s	0.956 m/s

Table 4.5: Channel flow of incompressible fluid due to pitching motion of a flat plate: Results for the mean channel velocity \tilde{U}_m for different pitching amplitudes \tilde{A}_{TE} and different models for fluid viscosity; fluid: water ($\tilde{\rho} = 1000$ kg/m³, $\tilde{\nu} = 10^{-6}$ m²/s), plate chord $\tilde{L} = 0.1$ m, channel semi-height $\tilde{h} = 0.05$ m, Angular frequency $\tilde{\omega} = 20 \pi$ rad/s (courtesy of T. Müllner¹).

Two important statements follow from the results. Firstly, the mean flow velocity \tilde{U}_m increases almost linearly (exponent ≈ 0.87) with the endpoint deflection \tilde{A}_{TE} . The result illustrates that the linear relation $\tilde{U}_m \sim \tilde{A}_{TE}$ (valid for small \tilde{A}_{TE}/\tilde{h}) adequately describes the behaviour at amplitudes that are not small (here $\tilde{A}_{TE}/\tilde{h} = 0.5$). Secondly, the inclusion of fluid viscosity – whether laminar or turbulent – affects the flow velocity only to a limited extent (≤ 15 percent). These results support the present assumption that the effect of viscosity can be neglected in a first approach.

It may be noted that the obtained Reynolds number is in good agreement with the measurements for the membrane pump. When the solution for $\tilde{A}_{TE} = 0.010$ m with laminar flow is considered, the Reynolds number in Eq. (1.22), built with the hydraulic diameter $\tilde{d}_h = 2\tilde{h}$, amounts to $\text{Re}_h = 37800$. This value is in good agreement to the measurements for the membrane pump Tab. 1.2.

¹Project “plate pump“, Vienna University of Technology, 2006, T. Müllner (personal communication)

Flexible membrane: explicit coupling

In the present work, a more elaborate version of the above example is performed by replacing the pitching plate by a prestrained membrane, with the motion being coupled to the pressure difference across the membrane Eq. (1.17). The pressure inlet at the left boundary is replaced by a VELOCITY_INLET with prescribed velocity \tilde{U} in order to make the mean flow through the pump independent from the solution, cf. Fig. 1.1. A PRESSURE_OUTLET condition is chosen at the channel outlet. The membrane has a forced oscillation of the LE point and a zero-slope trailing edge deflection Eq. (1.18). The parameters are:

$$\begin{aligned} \tilde{L} &= 0.1 \text{ m}, & \tilde{h} &= 0.05 \text{ m}, & \tilde{U} &= 1 \text{ m/s}, & \tilde{\rho} &= 1000 \text{ kg/m}^3, \\ & & & & \tilde{\omega} &= 20 \pi \text{ rad/s}, & \tilde{A}_{LE} &= 0.001 \text{ m}, \\ \tilde{\alpha}_M &= 28.735 \text{ N/m}, & \tilde{\beta}_M &= 114938 \text{ N/m}^3, & \tilde{D}_M &= 0 \text{ m}. \end{aligned} \quad (4.17)$$

Regarding the time discretization, *explicit coupling* of the motion has been employed. In doing so, the fluid pressure from the last time step is plugged into the membrane equation to determine the deflections of the membrane. The membrane positions are prescribed in the next time step, where again the flow field is solved. The present method is classified in the literature as *partitioned* approach, as the problem is split into the parts fluid and solid. Within this class, the present strategy is usually described as *weak* coupling, as the exchange of information between fluid and solid is done only *once* a time-step. It has been shown by Le Tallec & Mouro [48] that this coupling strategy exhibits a severe limitation: to guarantee numerical stability of the method, the size of the timestep needs to be *larger* than a certain threshold. The limit is associated with the so-called "artificial added mass" effect (cf. [64]). Usually, the limitation is crucial for problems that have the following properties:

- incompressible fluid,
- the wall is very compliant, and
- the ratio of the specific weights of fluid and solid is close to one.

For example, the instability of explicitly coupled schemes is typically *not* observed in aerodynamics, where the fluid density is well below the density of the solid body. For the present problem, however, it seems that all the criteria are fulfilled. Membrane-water interaction, in particular, is expected to yield an unstable explicit scheme.

To obtain an estimate for the stability limit of the explicit coupling procedure, convection is neglected, and the membrane equation Eq. (1.17) is replaced by a simple spring model $\Delta \tilde{p} = -\tilde{\beta}_M \tilde{w}$. Then, the dimensionless ratio $\tilde{\rho} \tilde{h} / (\tilde{\beta}_M \Delta t^2)$ is identified to be characteristic for the stability of the method, where $\tilde{\rho}$ is the density of the fluid and Δt is the time step size.

In the numerical investigation, performed with Fluent[®] (taking the full model for flow and membrane), the fluid density is varied for a given time step size to detect the stability limit. If the density is chosen too high, pressure and deflection start to show strong oscillations in time after several timesteps, revealing the numerical instability, Tab. 4.6.

Δt	no oscillations	oscillations	$\tilde{\rho}\tilde{h}/(\tilde{\beta}_M\Delta t^2)$
0.005	$\tilde{\rho} = 11.5$	$\tilde{\rho} = 11.6$	0.201
0.010	$\tilde{\rho} = 44.5$	$\tilde{\rho} = 45.0$	0.195
0.020	$\tilde{\rho} = 173$	$\tilde{\rho} = 174$	0.189

Table 4.6: Numerical test for the stability limit of an explicit coupling strategy: Timestep size Δt , fluid density $\tilde{\rho}$, semi-channel width \tilde{h} , membrane stiffness β_M , and characteristic dimensionless stability parameter $\tilde{\rho}\tilde{h}/(\tilde{\beta}_M\Delta t^2)$.

The result pinpoints that the method becomes unstable if the ratio $\tilde{\rho}\tilde{h}/(\tilde{\beta}_M\Delta t^2)$ exceeds a certain level, in accord with the result in [48]. From the result, it may be concluded that stability is ensured when the time-step is chosen sufficiently large. While this is true regarding initial stability, though, Mok [64] has shown that the approach of weak coupling also encounters a stability problem (under the conditions listed above) in the long term. Indeed, it has been proven by Förster [23] that (for fully recursive temporal discretization) the proposed method is *necessarily unstable*, i. e. there exists no time-step that allows a stable scheme.

Flexible membrane: partitioned strong coupling

The setting is equal to Eq. (4.17), except that $\tilde{A}_{LE} = 0.01$ m. The flow chart of the solution procedure is represented in Fig. 4.5. The main feature of the partitioned approach with strong coupling is that data between the membrane and the fluid is exchanged within a timestep. In the present approach the deflection of the membrane at each chordwise position is split into two parts: The first part $w(t_i)$ is a guess of the membrane deflection that is prescribed at the beginning of the timestep (index i) via the grid motion; The second part serves as a correction term that is obtained from the solution w_j of the membrane equation and is prescribed as velocity boundary condition v_j to the fluid problem. For this purpose the DEFINE_PROFILE-UDF is used in Fluent[®]. A very small value has to be given to the relaxation factor $\delta = 1.6 \times 10^{-3}$ in order to obtain a stable scheme. In the “fluid”-loop it suffices to perform only one PISO step. The surface pressure is read out and fed back into the iteration loop (index j). Despite of the strong coupling, the residuals of the membrane equation decrease slowly ($jMax = 3000$). The deflections are calculated at the end of the timestep and are used for the grid positions in the subsequent timestep.

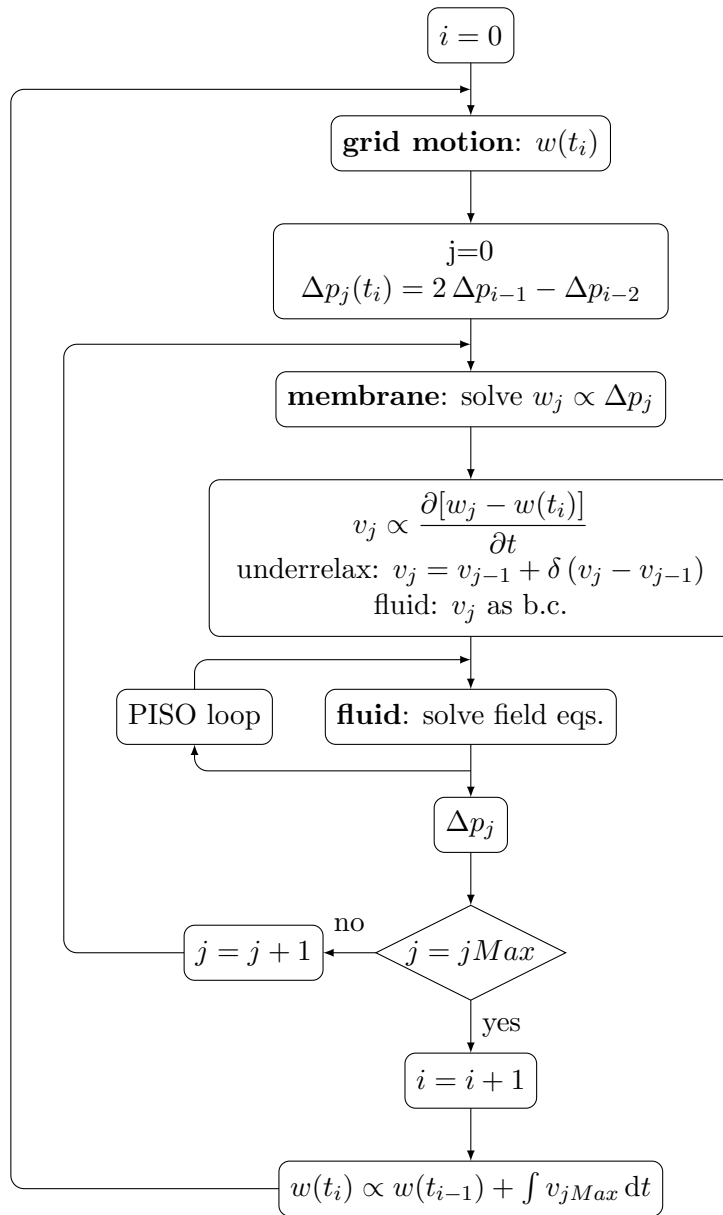
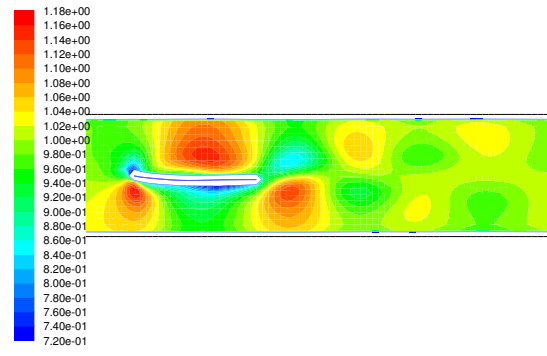
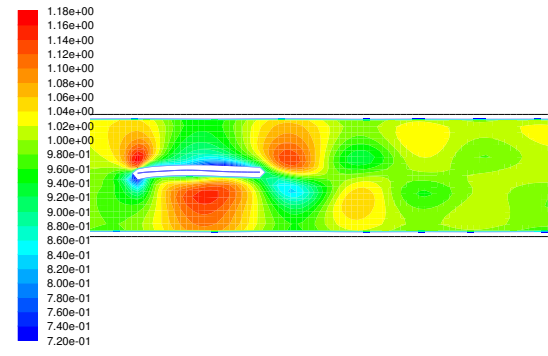


Figure 4.5: Flow chart of the solution procedure with strong coupling: timestep index i , iteration index j , relaxation factor δ .

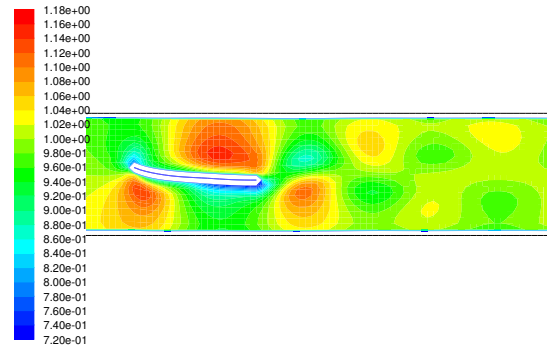
The solution of the horizontal flow component is depicted in Fig. 4.6.



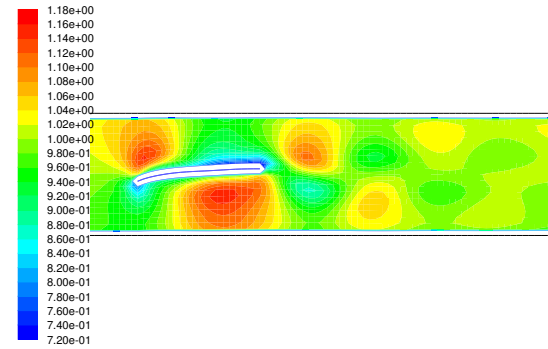
Contours of X Velocity (m/s) (Time=3.0000e-01) Feb 27, 2014
 FLUENT 6.3 (2d, dp, pbns, dynamesh, lam, unsteady)
 (a) $t/T = 0/8$



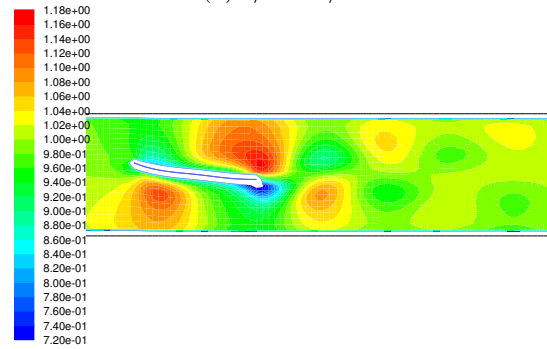
Contours of X Velocity (m/s) (Time=3.4750e-01) Feb 27, 2014
 FLUENT 6.3 (2d, dp, pbns, dynamesh, lam, unsteady)
 (e) $t/T = 4/8$



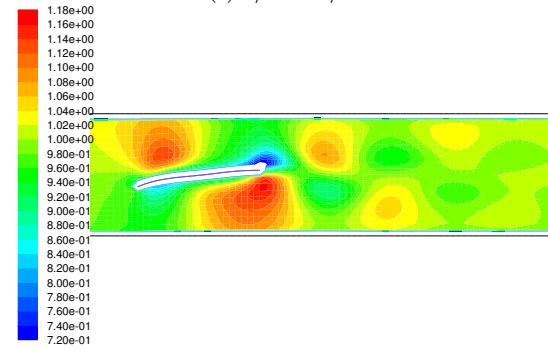
Contours of X Velocity (m/s) (Time=3.1000e-01) Feb 27, 2014
 FLUENT 6.3 (2d, dp, pbns, dynamesh, lam, unsteady)
 (b) $t/T = 1/8$



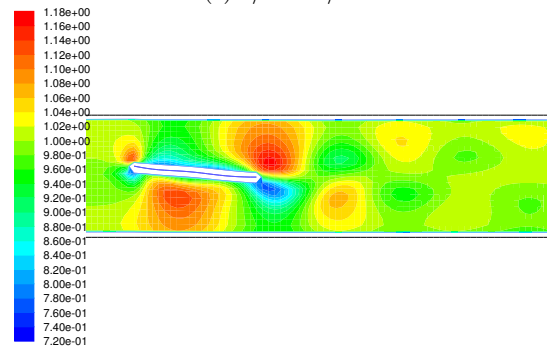
Contours of X Velocity (m/s) (Time=3.6000e-01) Feb 27, 2014
 FLUENT 6.3 (2d, dp, pbns, dynamesh, lam, unsteady)
 (f) $t/T = 5/8$



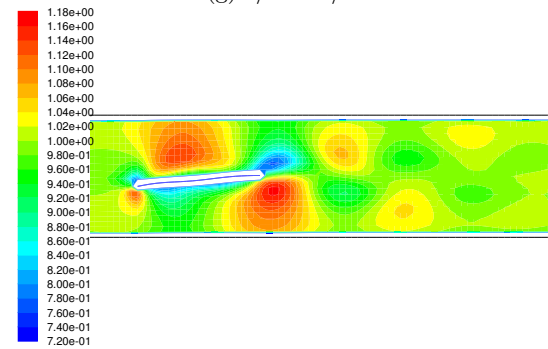
Contours of X Velocity (m/s) (Time=3.2250e-01) Feb 27, 2014
 FLUENT 6.3 (2d, dp, pbns, dynamesh, lam, unsteady)
 (c) $t/T = 2/8$



Contours of X Velocity (m/s) (Time=3.7250e-01) Feb 27, 2014
 FLUENT 6.3 (2d, dp, pbns, dynamesh, lam, unsteady)
 (g) $t/T = 6/8$



Contours of X Velocity (m/s) (Time=3.3500e-01) Feb 27, 2014
 FLUENT 6.3 (2d, dp, pbns, dynamesh, lam, unsteady)
 (d) $t/T = 3/8$



Contours of X Velocity (m/s) (Time=3.8500e-01) Feb 27, 2014
 FLUENT 6.3 (2d, dp, pbns, dynamesh, lam, unsteady)
 (h) $t/T = 7/8$

Figure 4.6: Fluent[®] simulation of a flexible membrane with flapping *LE*-point in a water-filled channel: Streamwise velocity component for selected time instances t within one period T (details are given in the text).

The evolution of the membrane's deflection over time is very similar to that of a flapping foil. The flow pattern downstream of the moving membrane is an indication of the formation of a vortex wake. As the motion is periodic in time, advancing in time by a half-period yields results that are reflected about the channel's centerline (compare in Fig. 4.6 for instance (a) and (e)). The deflection of the membrane is shown in detail in Fig. 4.7.

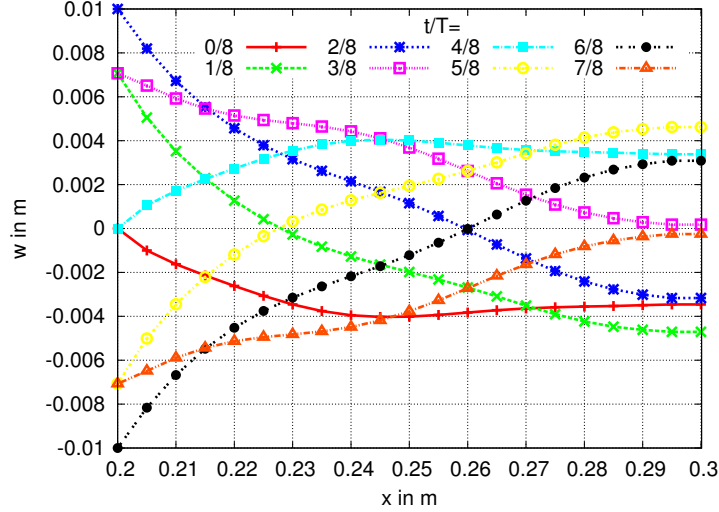


Figure 4.7: Fluent[®] simulation of a flexible membrane with flapping *LE*-point in a water-filled channel: Membrane deflection along the chord at different time instants t within one period T .

It should be mentioned that the grid has only twenty points along the chord. Thus, the *LE* and *TE* region may not be sufficiently resolved and the quality of the results may need to be improved. The reason for the coarse grid is the expensive coupling strategy. Nevertheless, the deflection of the membrane performs a travelling wave pattern in direction of the mean channel flow. To estimate the phase speed of the wave, one may consider the temporal travel of the deflections' zero-crossing chordwise position. The chord ($\tilde{L} = 0.1$ m) is travelled through in a time of $3/8 \times T \approx 0.0375$ s. The phase speed is thus $\tilde{c} \approx 2.67$ m/s.

4.2.3 Comparison of the CFD results to potential flow theory

For the membrane in the channel, the results from the panel code are compared to the CFD results in Sec. 4.2.2. The CFD results from the fully coupled problem in Sec. 4.2.2 are compared to the potential flow solution with the panel code. The membrane is excited at the leading edge with dimensionless amplitude A_{LE} . The following parameters are adopted from Sec. 4.2.2:

$$h = 0.5, \quad A_{LE} = 0.1, \quad \sigma = 3.14, \quad \alpha_M = 0.575, \quad \beta_M = 5.75, \quad \mu_M = 0. \quad (4.18)$$

For additional comparison, the results in unbounded domain from the Chebyshev code in Sec. 4.1 are also provided. The panel-code uses 30 panels and the Chebyshev code resolves 20 modes.

The results from Fluent[®], the Panel code, and the Chebyshev code (denoted as $h \rightarrow \infty$) for the chordwise distribution of deflection and pressure difference across the membrane are shown in Fig. 4.8.

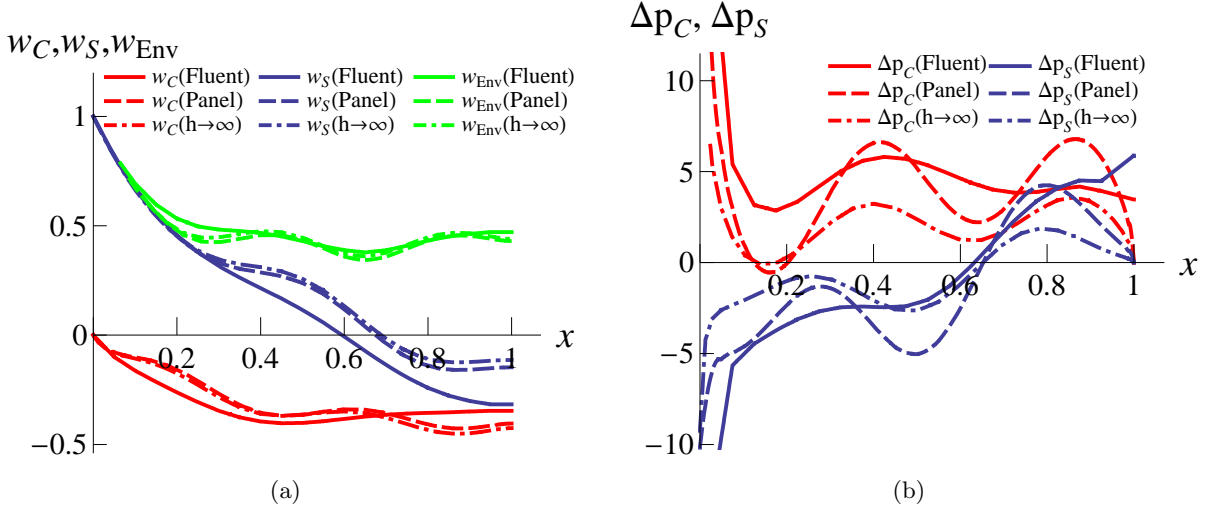


Figure 4.8: Deflection of membrane (a) and pressure difference across the membrane (b), along the chord: Cosine- (in red) and sine- (in blue) component, respectively, envelope (in green); Solid lines: Fluent[®] result in the channel (for dimensionless semi-channel width $h = 0.5$), dashed lines: potential flow theory in the channel ($h = 0.5$), dashed-dotted lines: potential flow theory in infinite domain.

The Fluent[®] results for the deflection are taken from Fig. 4.7: The cosine component w_C corresponds to $t/T = 0/8$ (in red) and the sine component w_S corresponds to $t/T = 2/8$ (in blue), respectively. Higher harmonics in the signal can be neglected (the form factor of the TE -deflection is 1.112). As mentioned already in Sec. 4.2.2, the solution in Fluent[®] is obtained on a quite coarse grid of 20 equi-distant cells along the chord. Nevertheless, the results for the deflection agree fairly well to each other. Each of the three solutions shows the pattern of a downstream travelling wave, see Fig. 4.7. The sine and cosine component start at the prescribed leading-edge values $w_S = 1$ and $w_C = 0$, respectively, and both components decrease to negative values towards the trailing edge. The envelope decreases rapidly off the leading edge up to $x \approx 0.2$ and remains roughly at a constant value of $w_{Env} \approx 0.5$ downstream from that point. Regarding the sine and cosine components of the membrane deflection at the trailing edge $x = 1$, the results from the panel code lie between those from CFD and those in unbounded domain. From the results of the pressure it becomes apparent that the CFD solution does not obey the Kutta condition of vanishing pressure difference at the TE (compare to [98]). Nonetheless, the chordwise distribution of the pressure from Fluent[®] and the panel code are substantially similar, even in the downstream fifth of the chord. Each of the three solutions feature a cosine pressure component Δp_C that is positive along the entire chord and a sine component Δp_S that is negative at the leading edge and becomes positive in the downstream third of the chord. In

both pressure components approximately two full chordwise waves are present. However, the CFD solution is less “wavy” than the panel solution. Compared to the solution in unbounded domain, both solutions in the channel exhibit a larger pressure difference.

Interpretation of the results

The following statements can be made for the results in this section. The Reynolds number obtained with the flat plate in pitching motion agrees well with the measurements for the membrane pump. The mean flow rate does not change significantly when the simulation is performed with an inviscid fluid. The fluid viscosity is not crucial for the propulsive mechanism. Accordingly, the unsteady potential flow theory gives good results. The CFD results in Fig. 4.6 indicate the occurrence of a vortex wake. Equivalently, the circulatory part of the flow has been taken into account within the potential flow model. From the computational viewpoint, the explicit coupling strategy is inapplicable to the problem of channel flow of incompressible fluid over a compliant membrane. A strong coupling approach is necessary. Alternatively, in the potential flow model a monolithic coupling strategy has been pursued.

Chapter 5

Summary and Conclusions

5.1 Discussion of the inviscid model

A new valveless pump design that uses travelling waves passing along an excited prestrained membrane as working principle has been studied with theoretical models. In contrast to other membrane pumps, the present pump operates in the regime of high Reynolds numbers. Thus peristalsis drops out as pumping principle, despite the similarity by the observed travelling waves. In the contrary, two-dimensional CFD simulations for a channel pump with prescribed pitching motion of a plate in inviscid, laminar, and turbulent flow show by comparison that the mean flow differs by only 15%. Thus, it is supposed that the exclusion of fluid viscosity provides a sufficiently accurate basis for a first theoretical approach. The problem is then stated such to have prescribed mean flow through the pump and solutions are discussed with the aim to optimize the Pareto of propulsive efficiency and propulsive force. The solution for the membrane is compared to the optimum motion of a rigid foil in combined plunging and pitching motion. The theoretical model confirms the appearance of a downstream travelling wavy surface (TWS) of the membrane's deflection intended by the inventor Wilhelm Zackl that is also observed in the experiment. The TWS motion occurs frequently in nature and is strongly related to propulsion of slender fish.

5.2 Flapping foil motion, chordwise flexibility and TWS

It is well-known that living fish use a vortex shedding mechanism as means of thrust production. The thrust production is retained when the inviscid limit is approached. However, an appropriate trailing edge condition is required to determine the amount of circulation. The unsteady Kutta condition is used, as usual. The limits of the Kutta condition have been discussed.

Theodorsen's linear model for amplitude-constraint flapping motion of a slender rigid foil is used as basis for an optimization problem. Optimum flapping motions are determined. In accordance to the literature, a combined plunging and pitching motion turns out to be superior to that of a foil in pure plunging motion. The obtained optimum motion of the rigid flapping foil resembles a downstream travelling wave. The relation between plunging and pitching changes subject to the required thrust level. Surprisingly, the reduced frequency needs to be of order

one when the thrust is very low. A simple analytical relation between the dimensionless thrust T and the propulsive efficiency η is given for the first time.

It has been proposed for some time that chordwise flexibility can enhance efficiency. Theoretical results for the prescribed motion of a waving plate by Wu emphasize the high propulsive efficiency of such fish-like motions. However, the theoretical findings of increased efficiency by chordwise flexibility, compared to a rigid foil that operates at the same level of thrust, have been confirmed experimentally only recently by Prempraneerach et. al. Clearly, from theory and the observation in nature, it appears desirable to have a technical device that is capable to propagate a downstream travelling wave along a slender profile. Nevertheless, it appears to be difficult to design such a mechanism. The prestrained-membrane pump is a valuable candidate, as it shows theoretically and experimentally how such a TWS mode can be realized.

5.3 FSI, TWS with prestrained membrane

The two-way FSI of the membrane equation with the oncoming inviscid flow is solved with a monolithic approach by expansion in Chebyshev polynomials. For simplicity, only the leading edge point is moved in transverse motion. Parameter combinations of frequency, prestrain, and inertia are investigated in order to identify which combination leads to the optimum η - T envelope.

When the inertia of the membrane is excluded, the best results are on the level with the optimum flapping foil motions. As membrane inertia is taken into account, the results improve significantly. An additional marginal improvement is achieved when the trailing edge condition is altered to allow a downstream propagating wave. Although this model is rather theoretical, it is of particular interest as it contains the solution where the membrane deflection performs a single uniform downstream propagating wave at a phase speed equal to the speed of the oncoming flow. In this case, the oncoming flow is not perturbed by the membrane's motion, adding up to a vanishing thrust force $T = 0$ and an efficiency of $\eta = 1$. The set of design- and operating parameters that can perform this motion is easily determined.

Among the thrust-producing solutions, it turns out that the optimum η - T envelope is formed by those sets of design- and operating parameters that lie in the vicinity of the set that passes through the point $(T, \eta) = (0, 1)$. For future work, it would be of interest if these sets can be verified by experiments. Certainly, an improved theoretical model for the fluid flow and the membrane equation would be desirable.

5.4 The effect of channel width to chord ratio

The effect of bounding the flow by channel walls is treated both analytically and with the unsteady panel method, within the assumption of inviscid flow and small deflections. By making use of the complex function theory, a novel closed-form solution is presented for the circulation produced by a thin wall sheet executing small-amplitude motions in oncoming flow that is confined by parallel channel walls being apart an arbitrary distance. The expansion of the result for large channel width reproduces a wall correction formula used for instance for wind tunnel measurements. For comparison of the results of any channel width, a panel code is developed

with panels that account for the presence of the channel walls and feature second order accuracy advisable for interaction problems. The results are in good agreement. The largest source of error stems from the accurate prediction of the leading edge singularity. When the dimensionless channel width is reduced to small values, thrust and power increase significantly, while the efficiency increases slightly. The effect is similar to the well-known increase in the lift force of a wing in extreme ground effect. However, the dependence on the channel width turns out to be not necessarily monotonic. For instance, the extremum of the trailing edge vorticity is reached at lower channel width when the flapping frequency is higher.

5.5 Relation to viscous flow over TWS of infinite extension

In the literature, the travelling wave mode has been associated with drag reduction. Barrett et. al. have shown that in a self-propelled robotic fish that exhibits a TWS mode the viscous drag can be reduced in comparison to the rigid hull towed through the water. To study the mechanism in fish swimming, a simple configuration with viscous flow over a travelling wavy wall with streamwise periodic boundary conditions has been proposed in the literature. Shen et. al. have shown with direct numerical simulation that the viscous drag force is reduced by restraining the separation with increasing phase speed of the downstream propagating wave. Lu & Yin discussed the same configuration for laminar flow and came to the conclusion that the total force acting on the wall can be thrust when the phase speed is large enough.

In the present work, a relation between the case of inviscid flow over a TWS of finite length and viscous flow over a TWS of infinite streamwise extension is established. In order to interlink the problems, the TWS over a surface of finite length is treated in the limit of large wave number, with the phase speed kept at the same magnitude as the speed of the oncoming flow. The thrust increases with the wave number, but it turns out that the main portion of thrust is produced in the region close to the leading edge. On the other hand, the leading term of the pressure (with respect to the wave number) in the mid-chord limit equals that of a wavy surface of infinite streamwise extension, and does not contribute to the thrust. The simultaneously increasing and vanishing thrust looks like a paradox. However, the vortex shedding mechanism on which the thrust production of the waving surface of finite length is based on, is completely absorbed in the perturbation term of the pressure. By enforcing periodic conditions to the pressure, vortex shedding and thrust generation are prohibited as the contributions from the streamwise harmonic wall pressure cancel each other out. At larger wave steepness, the inviscid solution is no longer harmonic in streamwise direction, but still there is no thrust.

A finite volume solver for the Navier–Stokes equations is developed in order to study the viscous flow over the downstream travelling wavy wall. When viscosity is taken into account, the viscous force is always drag, and the wall pressure brings about thrust that balances the viscous drag. The present results contradict the conclusion by Lu & Yin that the total force can be thrust. Generally, the oscillations in velocity and pressure become stronger when the Reynolds number is decreased.

Appendix A

Verification of The Panel Code

In order to verify the implementation of the panel code described in Sec. 2.3 a steady channel flow problem, a prescribed flapping foil motion in unbounded domain, a prescribed travelling wavy surface, and coupling to a membrane equation are considered.

A.1 Steady channel flow

In this section a steady example with a prescribed velocity profile is considered (no coupling to a membrane equation). The solution of the vorticity distribution is determined in closed form and used as a reference. We prescribe the following profile for the vertical velocity component along the body

$$v(x, 0) = \frac{2h}{\pi} \sqrt{\sinh\left(\frac{\pi}{2h}x\right) \sinh\left[\frac{\pi}{2h}(1-x)\right]} \quad \text{for } 0 \leq x \leq 1.$$

Note that in the steady case $v(x, 0)$ is equal to the slope of the shape of the body. From the stationary version of the Kutta condition Eq. (2.7) and the transport equation Eq. (2.10) follows $\gamma(x) = 0$ at the trailing edge and in the wake $x \geq 1$. Then, with Eq. (2.73) the vorticity distribution is expressed in closed-form

$$\gamma(x) = \frac{2}{\pi} \sqrt{\frac{\sinh\left[\frac{\pi}{2h}(1-x)\right]}{\sinh\left(\frac{\pi}{2h}x\right)}} \left(\cosh\left(\frac{\pi}{2h}x\right) + \frac{2h}{\pi} \sinh\left(\frac{\pi}{2h}x\right) \ln \frac{\sinh\left[\frac{\pi}{2h}(1-x)\right]}{\sinh\left(\frac{\pi}{2h}x\right)} \right) \quad (0 \leq x \leq 1).$$

In the panel code a stationary version of the discretized equations Eqs. (2.88, 2.89) is solved using Eqs. (2.108, 2.109) on non-uniformly distributed panels Eq. (2.98). The kinematic boundary condition $w_x = v(x, 0)$ is prescribed in Eq. (2.88). The membrane equation Eq. (2.90b) is omitted. The result of the vorticity distribution $\gamma(x)$ for a semi-channel width of $h = 1$ is shown in Fig. A.1.

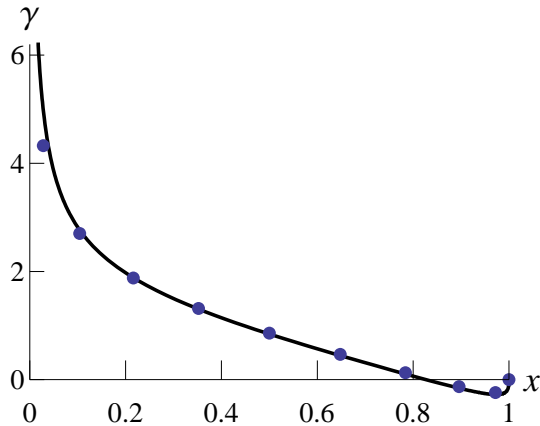


Figure A.1: Test example for the panel code: Result of the distribution of vorticity for a steady case with semi-channel width $h = 1$; Blue points \bullet : panel-code results with $n = 10$ panels; Black line: analytical solution.

With the nonuniform distribution of the panel nodes a very good agreement is attained with only $n = 10$ panels.

A.2 Flapping foil in unbounded domain

The propulsive performance of a prescribed flapping foil motion in unbounded domain is investigated. The panel weights for unbounded domain from Eqs. (2.110, (2.111) are used (without the h^{-2} -correction). The parameters of motion (see Fig. 3.1) are chosen as:

$$H = 1.9343, \quad A = 0.338824, \quad B = 0.50054, \quad \sigma = 1.$$

In the panel code, 30 panels with the distribution from Eq. (2.98) are used. The results are calculated from Eqs. (2.112–2.114). The forces in the exact flapping foil solution are given in Sec. 3.1.2. The results are shown in Tab. A.1.

Output	Panel code	Exact
T_s	2.79267	2.96339
T_p	1.05095	1.05154
P	6.43895	6.44226
η	0.596934	0.623218

Table A.1: Comparison of the output from the panel code ($n = 30$ panels) to exact solution.

The results for T_p and P are very accurate. The leading edge force predicted by the panel method is somewhat inaccurate (about 5 percent) although the grid is refined at the leading edge and trailing edge. This error is propagated to the efficiency η .

A.3 Travelling wavy surface in unbounded domain

The travelling wavy surface $w(x, \tau) = 2 \cos(kx - \tau)$ in unbounded domain as discussed in Sec. 3.3.2 is considered for a frequency $\sigma = 5$ and a wavenumber $k = 3$. The panel weights for unbounded domain Eqs. (2.110, 2.111) are used (the first two terms without the h^{-2} -correction). The result of the panel code is compared to the representation by Chebyshev polynomials outlined in Sec. 2.1.7. The representation by Chebyshev polynomials gives exact solutions (results see Fig. 3.11). In the panel code, only 15 panels are used. The results for the particular case are shown in Tab. A.2.

Output	Panel code	Exact
T_s	3.10981	3.19891
T_p	9.16391	9.16977
P	15.2597	15.2829
η	0.804322	0.809312

Table A.2: Comparison of the output from the panel code ($n = 15$ panels) to exact solution.

The exact results are obtained from Eqs. (3.56)-(3.58). In comparison, the results from the panel code are very accurate.

A.4 Membrane without inertia in unbounded domain

We consider the problem from Sec. 4.1.6. The membrane equation Eq. (2.90b) is solved for the following membrane parameters: $\sigma = 1.5$, $\alpha_M = 0.19$, $\beta_M = \mu_M = 0$. A forced motion is given only to the leading edge point, i. e. the panel code is used without baffle and flap, $x_A = 0$ (see Fig. 2.8). The number of panels is $n = 200$. The results are compared to the representation by Chebyshev polynomials presented in Sec. 4.1.2. The Chebyshev version is resolved up to $n_{Max} = 20$ modes. In postprocessing the leading-edge amplitude is rescaled as in Sec. 4.1 for comparison reasons. The results are given in Tab. A.3.

Output	Panel code	Chebyshev
T_s	0.11548	0.11219
T_p	1.15457	1.15600
P	1.58112	1.58188
η	0.803256	0.801687

Table A.3: Comparison of the output from the panel code ($n = 200$ panels) to Chebyshev version ($n_{Max} = 20$).

The solution point is displayed in Fig. 4.1 and lies on the curve of best attained membrane solutions (blue line). The results from the panel code and the Chebyshev method are practically identical. In comparison to the simple forced TWS motion in Sec. A.3 a considerably higher number of panels needs to be utilized in the coupled problem ($n = 200$ versus $n = 15$), while the

Chebyshev version provides the same accuracy with only 20 modes being resolved. Nevertheless, the Chebyshev version is not suitable to study the channel flow.

Appendix B

Conversion to The Notation by Katz & Weihs For Large Deflection Motion

In Sec. 3.1.5 the linearized model for small-amplitude motion of a rigid foil (method discussed by Wu [118]) is employed for large amplitudes and is compared to the potential flow results reported by Katz & Weihs [38] that account for the geometrical nonlinearity of large-deflection motion and free motion of the vortex wake. The aim is to study the limit of validity of the linear model. In the following the conversion among the two different notations is given.

With the notation given in [38], the relation for the path angle with linearization $\tan \theta \approx \theta$ is

$$\theta(t) = -2\frac{H}{c}\sigma \cos(\tilde{\Omega}t).$$

The *effective* angle of attack (inclination of foil with respect to the patch drawn by the foil) is chosen as

$$\alpha(t) = \alpha_1 + \alpha_0 \sin(\tilde{\Omega}t - \varphi)$$

with $\alpha_1 = 0$ for the considered examples. Then the instantaneous pitch angle is

$$\text{Pitchangle}(t) = \theta(t) - \alpha(t).$$

Ideally, θ and α are negative at $t = 0$. The motion consists of heaving and pitching such that

$$w(x, t) = H \sin(\tilde{\Omega}t) + (x - x_p) \left[-2H\sigma \cos(\tilde{\Omega}t) - \alpha_0 \sin(\tilde{\Omega}t - \varphi) \right] \quad \text{for } 0 \leq x \leq 1$$

with the location of the pitching axis at x_p . Inserting the phase difference $\varphi = \frac{1}{2}\pi$

$$w^{Katz} = H^{Katz} \sin(\tilde{\Omega}t) - (x^{Katz} - x_p^{Katz}) [2H^{Katz}\sigma - \alpha_0] \cos(\tilde{\Omega}t).$$

In contrast, the motion in the work of Wu [118] is given by

$$h^{Wu} = H^{Wu} \cos(\tilde{\omega}t) + A^{Wu}(x^{Wu} - B) \sin(\tilde{\omega}t) \quad \text{for } -1 \leq x^{Wu} \leq 1.$$

To compare with [118], the motion in Katz is shifted in time angle by $\pi/2$. Then, the transformation $\tilde{\Omega}t + \frac{\pi}{2} = \tilde{\omega}t$, $x^{Katz} = \frac{1+x^{Wu}}{2}$ yields

$$w^{Katz} = H^{Katz} \cos(\tilde{\omega}t) + \frac{2H^{Katz}\sigma - \alpha_0}{2} (x^{Wu} - B) \sin(\tilde{\omega}t)$$

and by comparison $h^{Wu} = 2w^{Katz}$ (factor 2 because h^{Wu} is non-dimensionalized with the half-chord)

$$H^{Wu} = 2H^{Katz}, \quad A^{Wu} = 2H^{Katz}\sigma - \alpha_0, \quad B = 2x_p - 1.$$

[38], Fig. 3 consider the case of $\alpha_0 = 5^\circ$ (small value to avoid flow separation), phase angle $\varphi = \frac{1}{2}\pi$, and pitch axis placed at the leading edge $x_p = 0$. The heaving amplitude is continuously varied for three different flapping frequencies. Thus, in the present notation, the input parameters for these cases are given as (taking $\epsilon = 1$)

$$\sigma = \left\{ \frac{\pi}{40}, \frac{2\pi}{40}, \frac{3\pi}{40} \right\}, \quad H = 2 \frac{\tilde{H}}{\tilde{L}}, \quad A = 2\sigma \frac{\tilde{H}}{\tilde{L}} - 5^\circ, \quad B = -1. \quad (\text{B.1})$$

The results are shown in Fig. 3.3.

Appendix C

Optimal foil motion

In this appendix the calculations for the optimization under constraints from Sec. 3.2.1 are described in detail.

C.1 Solution via Lagrange function

From the Lagrange multiplier method in Sec. 3.2.1, the 6 equations Eq. (3.11) for the 6 unknowns A , B , H , σ , μ and λ are given in full form as:

$$\begin{aligned} & \lambda 2A(1+B)^2 + (8A - 8H\sigma + 2A(1-2B)^2\sigma^2)(F - F^2 - G^2) + \\ & \mu [2A(1-2B)\sigma^2 - (8A - 4H\sigma + 4A(1-2B)\sigma^2)F + (-4A(1+2B)\sigma + 4H\sigma^2)G + \\ & \quad (8A - 8H\sigma + 2A(1-2B)^2\sigma^2)(F^2 + G^2)] = 0, \end{aligned} \quad (\text{C.1})$$

$$\begin{aligned} & \lambda 2A^2(1+B) - 4A^2(1-2B)\sigma^2(F - F^2 - G^2) + \\ & \mu [-2A^2\sigma^2 + 4A^2\sigma^2F - 4A^2\sigma G - 4A^2(1-2B)\sigma^2(F^2 + G^2)] = 0, \end{aligned} \quad (\text{C.2})$$

$$\begin{aligned} & \lambda 2H + (-8A\sigma + 8H\sigma^2)(F - F^2 - G^2) + \\ & \mu [4A\sigma F + 4A\sigma^2 G + (-8A\sigma + 8H\sigma^2)(F^2 + G^2)] = 0, \end{aligned} \quad (\text{C.3})$$

with $()' = \frac{d}{d\sigma}()$

$$\begin{aligned} & [-8AH + 2(A^2(1-2B)^2 + 4H^2)\sigma] (F - F^2 - G^2) + \\ & [4A^2 - 8AH\sigma + (A^2(1-2B)^2 + 4H^2)\sigma^2] (F' - 2FF' - 2GG') + \\ & \mu \{ 2A^2(1-2B)\sigma - (-4AH + 4A^2(1-2B)\sigma)F + (-2A^2(1+2B) + 8AH\sigma)G + \\ & \quad [-8AH + 2(A^2(1-2B)^2 + 4H^2)\sigma] (F^2 + G^2) + \\ & \quad [4A^2 - 8AH\sigma + (A^2(1-2B)^2 + 4H^2)\sigma^2] (2FF' + 2GG') - \\ & \quad (4A^2 - 4AH\sigma + 2A^2(1-2B)\sigma^2)F' + (-2A^2(1+2B)\sigma + 4AH\sigma^2)G' \} = 0, \end{aligned} \quad (\text{C.4})$$

$$(1+B)^2 A^2 + H^2 = w_{1,max}^2, \quad (\text{C.5})$$

$$\begin{aligned}
T = & A^2(1 - 2B)\sigma^2 - (4A^2 - 4AH\sigma + 2A^2(1 - 2B)\sigma^2) F - \\
& (2A^2(1 + 2B)\sigma - 4AH\sigma^2) G + \\
& [4A^2 - 8AH\sigma + (A^2(1 - 2B)^2 + 4H^2)\sigma^2] (F^2 + G^2). \tag{C.6}
\end{aligned}$$

μ and λ denote the Lagrange multipliers. F and G are the respective real- and imaginary part of the Theodorsen function Eq. (2.33) and depend on the reduced frequency σ . The system is solved in the following way: Eqs. (C.1, C.2) are solved for the Lagrange multipliers and these are inserted into Eqs. (C.3, C.4). The resulting two equations are sufficient to determine both the pitching motion reference point B and the ratio of pitching and plunging amplitudes A/H as functions of σ . First, Eqs. (C.1, C.2) are considered as linear system for the Lagrange multipliers. Its solution is

$$\mu = \frac{N_\mu}{D_\mu}, \tag{C.7}$$

$$\lambda = \frac{N_\lambda}{D_\lambda}, \tag{C.8}$$

with the auxiliary expressions

$$N_\mu = - [4H\sigma + A(-4 + (-3 + 6B)\sigma^2)] (F - F^2 - G^2), \tag{C.9}$$

$$\begin{aligned}
D_\mu = & A(-2 + B)\sigma^2 - 2 [H\sigma + A(-2 + (-2 + B)\sigma^2)] F + \\
& 2\sigma(AB - H\sigma)G + [4H\sigma + A(-4 + (-3 + 6B)\sigma^2)] (F^2 + G^2), \tag{C.10}
\end{aligned}$$

$$\begin{aligned}
N_\lambda = & \sigma \{ -\sigma [4H\sigma + A(-4 + \sigma^2(1 - 2B)^2)] + \\
& 2\sigma [2(1 + 2B)H\sigma + A(-8B + \sigma^2(1 - 2B)^2)] F + \\
& [4H\sigma(-2 + (-1 + 2B)\sigma^2) + A(8 + (6 - 8B(1 + B))\sigma^2)] G \} (F - F^2 - G^2), \tag{C.11}
\end{aligned}$$

$$D_\lambda = (1 + B)D_\mu. \tag{C.12}$$

Then, inserting Eqs. (C.7, C.8) into Eqs. (C.3, C.4) yields

$$\begin{aligned}
& \sigma(4A^2(-2 + B)(1 + B)\sigma + 4H^2\sigma + AH(-4 + 9\sigma^2)) + \\
& 2 [2H^2\sigma^2 - AH\sigma(8 + 9\sigma^2) + A^2(1 + B)(4 + (5 + 2B)\sigma^2)] F + \\
& 2 [2H^2\sigma(2 + 3\sigma^2) - AH(4 + 3\sigma^2) + A^2(1 + B)\sigma(-4 - 3\sigma^2 + B(4 + 6\sigma^2))] G = 0 \tag{C.13}
\end{aligned}$$

$$\begin{aligned}
& \{ A(-2 + B)\sigma^2 - 2 [H\sigma + A(-2 + (-2 + B)\sigma^2)] F + 2\sigma(AB - H\sigma)G \} \\
& \{ 2(-4AH + A^2(1 - 2B)^2\sigma + 4H^2\sigma)(F - F^2 - G^2) + \\
& [-8AH\sigma + 4H^2\sigma^2 + A^2(4 + \sigma^2(1 - 2B)^2)] (F' - 2FF' - 2GG') \} + \\
& [4H\sigma + A(-4 + (-3 + 6B)\sigma^2)] \\
& [-8AH\sigma + 4H^2\sigma^2 + A^2(4 + \sigma^2(1 - 2B)^2)] ((-F^2 + G^2)F' - 2FGG') + \\
& 2 \{ A^2(1 - 2B)\sigma + 2A(H + A(-1 + 2B)\sigma)F - A(A + 2AB - 4H\sigma)G + \\
& A [2H\sigma + A(-2 + (-1 + 2B)\sigma^2)] F' - A\sigma(A + 2AB - 2H\sigma)G' \} \\
& [-4H\sigma + A(4 + 3(1 - 2B)\sigma^2)] (F - F^2 - G^2) = 0. \tag{C.14}
\end{aligned}$$

Together with the (unchanged) side conditions Eqs. (C.5, C.6) a system of 4 equations is obtained that can be sorted in powers of A and H and may be sketched as

$$()A^2 + ()AH + ()H^2 = 0, \quad (\text{C.15})$$

$$()A^3 + ()A^2H + ()AH^2 + ()H^3 = 0, \quad (\text{C.16})$$

$$()A^2 + H^2 = w_{1,max}^2, \quad (\text{C.5 revisited})$$

$$T = \dots, \quad (\text{C.6 revisited})$$

where the braces $()$ represent different (distinct) given functions of B and σ . For a given thrust T , these 4 equations can be solved for the unknowns A , H , B and σ . Since F and G are related to Bessel functions of the parameter σ , the problem is nonlinear and appears to call for a numeric solution. However, in the attempt to circumvent this problem and to find an analytic solution, the following trick is used: Instead of assuming T as given we assume the frequency σ as given. This approach is motivated by the fact that we have an explicit expression for T . In case that we can manage to solve Eqs. (C.15, C.16, C.5) for A , H and B (for various values of σ), the thrust T can be easily determined in postprocessing from Eq. (C.6). Indeed, the various expressions in braces $()$ are polynomials in B and thus we have a system of polynomial equations for A , H and B . In particular, Eqs. (C.15, C.16) are sufficient to obtain a polynomial equation for B as a function of σ . This equation can be derived in 3 steps that may be delineated as follows (assuming $H, A \neq 0$):

Step 1: Multiply the first equation appropriately to eliminate A^3 from the second equation:

$$\frac{\text{Eq. (C.16)} - A \cdot \text{Eq. (C.15)}}{H} \Rightarrow ()A^2 + ()AH + ()H^2 = 0. \quad (\text{C.17})$$

Step 2: Subtract the first equation appropriately to eliminate H^2 from the result of Step 1:

$$\frac{\text{Eq. (C.17)} - \text{Eq. (C.15)}}{4\sigma A} \Rightarrow A/H = f(B, \sigma). \quad (\text{C.18})$$

The results is an expression for the pitching-to-plunging ratio A/H . $f(B, \sigma)$ is a given function of B and σ and is polynomial in B .

Step 3: Factor out H^2 from Eq. (C.15) and insert A/H from Eq. (C.18). This simplification paves the way to a (rather tedious) equation for B only:

$$()f^2 + ()f + () = 0. \quad (\text{C.19})$$

The result is a polynomial equation of order 6 in B (the coefficient for B^7 is zero) and the coefficients are nonlinear functions of σ . The roots of Eq. (C.19) are solved in closed form:

- $B_1 = \left(\frac{1}{4} \frac{C_1}{C_0} - 1\right)^{-1}$ solution that gives the optimum η - T -envelope,

- $B_{2,3}$ not optimal,
- $B_{4,5} = \frac{1}{2}$ gives $T = 0$,
- $B_6 = -1$ violates the assumption $B \geq 0$.

C_1 and C_0 are functions of σ . The solution B_1 is equal to $B(\sigma)$ in Appendix C.2, Eq. (C.57).

C.2 Direct approach with the elimination method

The idea of the elimination method in Sec. 3.2.1 is to eliminate two variables (H and A , steps 1 and 2) and in this way incorporate the two side conditions Eqs. (3.13, 3.14). This gives an implicit expression Eq. (3.15) for the objective function E from which the conditions for the optimum motion Eq. (3.16) are derived. The resulting equations are solved one after the other (steps 3 and 4) to simplify the procedure.

Step 1

The side conditions are used to eliminate H . First, Eq. (3.5) is recast into

$$8A\sigma H = 4A^2 + (A^2(1 - 2B)^2 + 4H^2) \sigma^2 - \frac{E}{F - F^2 - G^2}. \quad (\text{C.20})$$

Eq. (C.20) is squared and H^2 is eliminated using Eq. (C.5). This gives

$$\begin{aligned} & (w_{1,max}^2 - A^2(1 + B)^2) (8A\sigma)^2 = \\ & \left[4A^2 + (A^2(1 - 2B)^2 + 4(w_{1,max}^2 - A^2(1 + B)^2)) \sigma^2 - \frac{E}{F - F^2 - G^2} \right]^2 \end{aligned} \quad (\text{C.21})$$

Secondly, the equation for the thrust Eq. (3.6) is recast into

$$\begin{aligned} H = \{ & A^2(1 - 2B)\sigma^2 - (4A^2 + 2A^2(1 - 2B)\sigma^2) F - 2A^2(1 + 2B)\sigma G + \\ & [4A^2 + (A^2(1 - 2B)^2 + 4H^2) \sigma^2] (F^2 + G^2) - T \} / \\ & [4A\sigma(-F - \sigma G + 2F^2 + 2G^2)]. \end{aligned} \quad (\text{C.22})$$

Inserting Eq. (C.22) into H on the lhs of Eq. (C.20) and thereafter eliminating all H^2 with Eq. (C.5) yields

$$\begin{aligned} & \left(-\frac{F}{2} - \sigma \frac{G}{2} + F^2 + G^2 \right) \cdot \\ & \left\{ 4A^2 + [A^2(1 - 2B)^2 + 4(w_{1,max}^2 - A^2(1 + B)^2)] \sigma^2 - \frac{E}{F - F^2 - G^2} \right\} = \\ & A^2(1 - 2B)\sigma^2 - (4A^2 + 2A^2(1 - 2B)\sigma^2) F - 2A^2(1 + 2B)\sigma G + \\ & \{ 4A^2 + [A^2(1 - 2B)^2 + 4(w_{1,max}^2 - A^2(1 + B)^2)] \sigma^2 \} (F^2 + G^2) - T \end{aligned} \quad (\text{C.23})$$

The thrust T and the maximum deflection $w_{1,max}$ are considered as given parameters. We can now introduce the abbreviations

$$S = S(\sigma, E; w_{1,max}) = w_{1,max}^2 4\sigma^2 - E / (F - F^2 - G^2) , \quad (C.24)$$

$$R = R(\sigma, E; T, w_{1,max}) = w_{1,max}^2 4\sigma^2 (F^2 + G^2) - T + \left(\frac{F}{2} + \sigma \frac{G}{2} - F^2 - G^2 \right) S , \quad (C.25)$$

$$D_0 = D_0(\sigma) = \left(2 + \frac{7}{2}\sigma^2 \right) F - \sigma^2 \left(1 - \frac{3}{2}\sigma G \right) , \quad (C.26)$$

$$D_1 = D_1(\sigma) = 2\sigma^2(1 + F) + 2(2 + 3\sigma^2)\sigma G \quad (C.27)$$

to write Eq. (C.21) and Eq. (C.23) as

$$A^4 (4 + 9\sigma^2) (4 + (1 + 4B)^2 \sigma^2) - A^2 [(w_{1,max} 8\sigma)^2 - 2(4 - 3(1 + 4B)\sigma^2) S] + S^2 = 0 , \quad (C.28)$$

$$(D_0 + D_1 B) A^2 = R . \quad (C.29)$$

Step 2

A is eliminated by inserting Eq. (C.29) into Eq. (C.28). This results in a quadratic equation for B

$$f = f(B, \sigma, E; T, w_{1,max}) = NB^2 + PB + Q = 0 \quad (C.30)$$

with the abbreviations (sorted in powers of R)

$$N = N_0 + N_1 R + N_2 R^2 , \quad (C.31)$$

$$P = P_0 + P_1 R + P_2 R^2 , \quad (C.32)$$

$$Q = Q_0 + Q_1 R + Q_2 R^2 , \quad (C.33)$$

and

$$N_0 = S^2 D_1^2, \quad N_1 = -24\sigma^2 S D_1, \quad N_2 = (4 + 9\sigma^2) (4\sigma)^2 , \quad (C.34)$$

$$P_0 = 2S^2 D_0 D_1, \quad P_1 = -24\sigma^2 S D_0 - D_1 [(w_{1,max} 8\sigma)^2 - 2S(4 - 3\sigma^2)] , \quad P_2 = (4 + 9\sigma^2) 8\sigma^2 , \quad (C.35)$$

$$Q_0 = S^2 D_0^2, \quad Q_1 = -D_0 [(w_{1,max} 8\sigma)^2 - 2S(4 - 3\sigma^2)] , \quad Q_2 = (4 + 9\sigma^2) (4 + \sigma^2) . \quad (C.36)$$

Step 3

The optimization problem can now be stated. Eq. (C.30) forms an implicit representation for the energy E that depends on the variables B and σ and the given parameters T and $w_{1,max}$. Optimal motion is attained (cf. [41]) when

$$\frac{\partial f}{\partial B} = 0, \quad \frac{\partial f}{\partial \sigma} = 0 . \quad (C.37)$$

The first condition suffices to decouple B . As a result, a simpler optimization problem can be stated. The first condition yields

$$B = B(\sigma, E; T, w_{1,max}) = -\frac{P}{2N} \quad (\text{C.38})$$

and together with Eq. (C.30) $P^2 = 4QN$. From that it can be readily seen that

$$P_0^2 - 4Q_0N_0 = 0, \quad 2P_0P_1 - 4(Q_0N_1 + Q_1N_0) = 0. \quad (\text{C.39})$$

and consequently Eq. (C.30) can be reduced to a quadratic equation in R

$$P_1^2 + 2P_0P_2 - 4(Q_0N_2 + Q_1N_1 + Q_2N_0) + [2P_1P_2 - 4(Q_1N_2 + Q_2N_1)]R + (P_2^2 - 4Q_2N_2)R^2 = 0. \quad (\text{C.40})$$

Furthermore, inserting S and R from Eqs. (C.24,C.25) results in a quadratic equation in E

$$K^2 \left(\frac{E}{T(F - F^2 - G^2)(4 + 9\sigma^2)} \right)^2 - 2 \left(2\frac{L}{T} + K \right) \frac{E}{T(F - F^2 - G^2)(4 + 9\sigma^2)} + 1 = 0 \quad (\text{C.41})$$

with the σ -dependent functions

$$K = K(\sigma) = 2G\sigma + 3\sigma^2 - 2F(2 + 3\sigma^2) + (F^2 + G^2)(4 + 9\sigma^2), \quad (\text{C.42})$$

$$L = L(\sigma; w_{1,max}) = w_{1,max}^2 4\sigma^2 [\sigma^2/4 + F + \sigma G - (1 + \sigma^2)(F - F^2 - G^2)], \quad (\text{C.43})$$

$$Q = Q(\sigma) = \frac{(4 + 9\sigma^2)(F - F^2 - G^2)}{K}, \quad (\text{C.44})$$

$$M = M(\sigma) = \frac{Q}{K}. \quad (\text{C.45})$$

Note that Q is *different* to the expression in Eq. (C.30). The solution of the quadratic equation is

$$E = E(\sigma; T, w_{1,max}) = \frac{Q}{K} \left(\sqrt{L + KT} \binom{-}{+} \sqrt{L} \right)^2. \quad (\text{C.46})$$

where only the minus sign is used in what follows. Note that $E = 0$ at $T = 0$.

Step 4

Finally, the simplified optimization problem is solved. The energy in Eq. (C.46) has a minimum when

$$\frac{dE}{d\sigma} = 0. \quad (\text{C.47})$$

With $(\prime) = \frac{d}{d\sigma}(\prime)$ this results in

$$M'(\sqrt{L + KT} - \sqrt{L}) + 2M(\sqrt{L + KT} - \sqrt{L})' = 0. \quad (\text{C.48})$$

Performing the differentiation of the $\sqrt{\quad}$ terms, multiplication with $\sqrt{L + KT}$, and sorting for $\sqrt{L + KT}$ gives

$$(M'L + ML') + (M'K + MK')T = (M'\sqrt{L} + ML'/\sqrt{L})\sqrt{L + KT}. \quad (\text{C.49})$$

The solution is

$$T = T(\sigma; w_{1,max}) = \frac{(ML)' (ML)'K/L - 2(MK)'}{(MK)'} \quad (\text{C.50})$$

The result can now be used to rewind the procedure. From Eq. (C.45) follows

$$(MK)' = Q', \quad (\text{C.51})$$

$$(ML)' = \frac{L}{K} \left[Q' - Q \left(\frac{K'}{K} - \frac{L'}{L} \right) \right], \quad (\text{C.52})$$

$$(ML)' \frac{K}{L} - 2(MK)' = - \left[Q' + Q \left(\frac{K'}{K} - \frac{L'}{L} \right) \right]. \quad (\text{C.53})$$

Thus

$$T = T(\sigma; w_{1,max}) = -\frac{L}{K} \left[1 - \left(\frac{Q}{Q'} \left(\frac{K'}{K} - \frac{L'}{L} \right) \right)^2 \right] \quad (\text{C.54})$$

and

$$\sqrt{L}\sqrt{L + KT} = (\pm) \frac{KQ(L/K)'}{Q'}, \quad (\text{C.55})$$

where only the plus sign is used. Inserting the result into Eq. (C.46) eliminates T

$$E = E(\sigma; w_{1,max}) = 4 \left[\frac{\sqrt{L/(KQ)'}}{(1/Q)'} \right]^2 \quad (\text{C.56})$$

with K , L and Q defined in Eqs. (C.42–C.44). With the results, the motion variables can be expressed solely as functions of σ . Eq. (C.54) and Eq. (C.56) are plugged into Eq. (C.24) and Eq. (C.25) to achieve that S and R , respectively, depend only on σ . With D_0 and D_1 from Eq. (C.26) and Eq. (C.27), respectively, N and P in Eq. (C.31) and Eq. (C.32), respectively, are pure functions in σ as well. Then, the location of the pitching axis is obtained from Eq. (C.38)

$$B = B(\sigma) = -P/(2N). \quad (\text{C.57})$$

Employing *Mathematica*, it has been proven (by *symbolic* comparison) that the solution is identical to the solution for B from the Lagrange multiplier method in Appendix C.1. The pitching and plunging amplitude A and H , respectively, follow from Eq. (C.29) and Eq. (C.5).

C.3 Limit $\sigma \rightarrow \infty$

The following results are obtained for $w_{1,max} = 2$ for an expansion in the limit $\sigma \rightarrow \infty$. The real and imaginary part of the Theodorsen function in Sec. 2.1.7 are

$$F(\sigma) = \frac{1}{2} + \frac{1}{16\sigma^2} - \frac{19}{256\sigma^4} + \dots \quad (\text{C.58})$$

$$G(\sigma) = -\frac{1}{8\sigma} + \frac{7}{128\sigma^3} + \dots \quad (\text{C.59})$$

[note that there is a minor error in the second term of G in [119], Eq. (22)]
From Sec. 3.2.1, Eq. (3.19), Eq. (3.20) and Eq. (3.21)

$$K = \frac{9}{4}\sigma^2 - \frac{59}{64} + \dots \quad (\text{C.60})$$

$$L = \frac{9}{4}\sigma^2 + \frac{63}{32} + \dots \quad (\text{C.61})$$

$$Q = 1 + \frac{19}{24\sigma^2} + \dots \quad (\text{C.62})$$

Then with Eq. (3.17) and Eq. (3.18)

$$T = \frac{21229}{12996} - \frac{438544535}{35557056\sigma^2} + \dots$$

$$E = \frac{5041}{12996} - \frac{168306281}{35557056\sigma^2} + \dots$$

From this result, one can see that the optimization limits the thrust to $T^{opt} = \frac{21229}{12996}$. The propulsive efficiency is

$$\eta = \frac{1}{1 + E/T} = \frac{299}{370} + \frac{2370511}{3285600\sigma^2} + \dots$$

From that with Eq. (C.24) and Eq. (C.25)

$$S = 16\sigma^2 - \frac{5041}{3249} + \dots$$

$$R = \frac{3}{4}\sigma^2 - \frac{865}{1444} + \dots$$

as well as Eq. (C.26) and Eq. (C.27)

$$D_0 = \frac{9}{16}\sigma^2 + \frac{333}{256} + \dots$$

$$D_1 = \frac{9}{4}\sigma^2 - \frac{3}{64} + \dots$$

follows from Eq. (C.31) and Eq. (C.32)

$$N = 144\sigma^6 - \frac{19976}{361}\sigma^4 + \frac{2478076393}{3127704}\sigma^2 + \dots$$

$$P = -144\sigma^6 + \frac{10817}{361}\sigma^4 - \frac{5242568801}{6255408}\sigma^2 + \dots$$

the solution of Eq. (C.38)

$$B = \frac{1}{2} + \frac{3053}{34656\sigma^2} + \frac{347402743}{1801557504\sigma^4} + \dots \quad (\text{C.63})$$

Once B is known, one obtains from Eq. (C.29)

$$A = \frac{4}{3} - \frac{55835}{77976\sigma^2} + \frac{43086749903}{16214017536\sigma^4} + \dots \quad (\text{C.64})$$

and finally from Eq. (C.5)

$$H = \frac{223}{114\sigma} - \frac{53427229}{11852352\sigma^3} + \dots \quad (\text{C.65})$$

We note that the same result is obtained for B if the Lagrange multiplier method in Sec. 3.2.1 is used. In the limit $\sigma \rightarrow \infty$, one obtains

$$C_0 = -\frac{263169}{32768}\sigma^4 - \frac{727461}{262144}\sigma^2 + \frac{105066315}{8388608} + \dots$$

$$C_1 = -\frac{789507}{8192}\sigma^4 - \frac{180063}{8192}\sigma^2 + \frac{371185173}{2097152} + \dots$$

and with $B = \left(\frac{1}{4}\frac{C_1}{C_0} - 1\right)^{-1}$ one obtains the same result as Eq. (C.63). The feathering parameter in Eq. (3.2) is To complete the results

$$\lambda = \frac{5041}{84360} - \frac{1341396823}{2372203200\sigma^2} + \dots$$

$$\mu = -\frac{71}{185} + \frac{189561}{136900\sigma^2} + \dots$$

C.4 Boundary optimum

We attempt to find an optimum motion for the case $T > T^{opt}$. The ansatz

$$B = \frac{1}{2} + \frac{B_2(T)}{\sigma^2} + \dots$$

$$A = \frac{4}{3} + \frac{A_2(T)}{\sigma^2} + \dots$$

$$H = \frac{H_1(T)}{\sigma} + \frac{H_3(T)}{\sigma^3} + \dots$$

allows to match to the solution Eqs. (3.32)–(3.34) at $T = T^{opt}$. Note that $H_2(T) = 0$ is a consequence of the matching. Considering this composition of B , A and H in terms of σ and

Eqs. (C.58), (C.59) (only 2 terms in F and one term in G is needed), Eqs. (C.1)–(C.3), (C.5)–(C.6) are expanded at $\sigma \rightarrow \infty$ and all terms that are not of leading order in σ are skipped. Then, the 5 equations Eq. (3.37) read

$$\begin{aligned} & \frac{1}{2}A(1-2B)^2(1+\mu)\sigma^2 + \frac{A(63+4B-4B^2)-64H\sigma}{32} + \\ & 2A(1+B)^2\lambda + \frac{A(-51+28B+20B^2)-16H\sigma}{32}\mu = 0, \end{aligned} \quad (\text{C.66})$$

$$A^2(-1+2B)(1+\mu)\sigma^2 + \frac{A^2(1-2B)}{16} + 2A^2(1+B)\lambda + \frac{A^2(7+10B)}{16}\mu = 0, \quad (\text{C.67})$$

$$-2(A-H\sigma) + \left(-\frac{A}{2} + 2H\sigma\right)\mu + \frac{A-H\sigma}{8\sigma^2} + \frac{2H\sigma}{\sigma^2}\lambda + \frac{-3A+5H\sigma}{8\sigma^2}\mu = 0, \quad (\text{C.68})$$

$$(1+B)^2A^2 + H^2 = w_{1,max}^2, \quad (\text{C.69})$$

$$T = \frac{A^2(1-2B)\sigma^2}{4} + \frac{A^2(-51+28B+20B^2) - 32AH\sigma + 64(H\sigma)^2}{64}. \quad (\text{C.70})$$

From Eqs. (C.66, C.67), in leading terms of σ

$$\mu = \frac{A(61+6B) - 48A(-1+2B)\sigma^2 - 64H\sigma}{16H\sigma + A(65+6B) + 48A(-1+2B)\sigma^2}, \quad (\text{C.71})$$

$$\lambda = \frac{24[-A + H\sigma + (-1+2B)(-2A + H\sigma)\sigma^2]}{(1+B)[16H\sigma + A(65+6B) + 48A(-1+2B)\sigma^2]}. \quad (\text{C.72})$$

Plug λ and μ into Eq. (C.68)

$$\begin{aligned} & 24(H\sigma)^2(1-24\sigma^2) + 32A(H\sigma + 48H\sigma\sigma^2) + A^2(-59 + 738\sigma^2 + 288\sigma^4) - \\ & [168(H\sigma)^2 - 4AH\sigma(59 + 48\sigma^2) + A^2(65 + 606\sigma^2 + 288\sigma^4)]B - \\ & 6A(-1 + 16\sigma^2)[2H\sigma + A(-1 + 6\sigma^2)]B^2 = 0. \end{aligned} \quad (\text{C.73})$$

Inserting $A = (\pm)\sqrt{w_{1,max}^2 - H^2}/(1+B)$ from Eq. (C.69) into Eqs. (C.73, C.70) gives 2 equations for B and $H_1(T)$. Taking $w_{1,max} = 2$, each equation solved for B yields

$$\begin{aligned} B &= \frac{1}{2} + \frac{-28 + 33H_1(T) - 9H_1(T)^2}{24} \frac{1}{\sigma^2} + \dots, \\ B &= \frac{1}{2} \pm \frac{\sqrt{8 + 6H_1(T) - 9H_1(T)^2 + 9T}}{4} \frac{1}{\sigma} + \frac{-3 + H_1(T) - 3H_1(T)^2 + 3T}{8} \frac{1}{\sigma^2} + \dots. \end{aligned}$$

A comparison of coefficients in terms of σ yields

$$H_1(T) = \frac{1(\pm)3\sqrt{1+T}}{3}.$$

Only the solution with the plus sign matches Eq. (3.34) at $T = T^{opt}$. Thus the results are

$$H = \frac{1 + 3\sqrt{1+T}}{3} \frac{1}{\sigma} + \mathcal{O}(\sigma^{-3}) ,$$

$$B = \frac{1}{2} + \frac{3(-3 - T + 3\sqrt{1+T})}{8} \frac{1}{\sigma^2} + \mathcal{O}(\sigma^{-3}) ,$$

$$A = \frac{4}{3} - \frac{-44 - 9T + 60\sqrt{1+T}}{54} \frac{1}{\sigma^2} + \mathcal{O}(\sigma^{-3}) .$$

To complete, from Eq. (C.71) and Eq. (C.72)

$$\mu = \frac{13 + 3T - 13\sqrt{1+T}}{-3 - 3T + 10\sqrt{1+T}} + \dots ,$$

$$\lambda = \frac{26 + 16T - (26 + 3T)\sqrt{1+T}}{4(-3 - 3T + 10\sqrt{1+T})} + \dots .$$

From Eq. (3.5)

$$E = \left(\sqrt{1+T} - 1\right)^2 + \dots .$$

This result is also obtained from Eq. (C.56) with Eqs. (C.60)–(C.62). From Eq. (2.47)

$$\eta = \frac{1}{2} + \frac{1}{2\sqrt{1+T}} + \dots .$$

Appendix D

Comparison of Common Discretization Schemes in Fluid Dynamics

An overview of discretization schemes that are commonly used in fluid dynamics is given here with the aim to classify the method described in Sec. 3.5.2 for the self-developed Navier–Stokes solver.

D.1 FD-, FV- and FE-method

Finite difference (FD) methods approximate the derivatives in the differential equation by finite differences. The unknowns are usually point-values, sometimes face-averages. In finite volume (FV) methods the domain is subdivided into control volumes (CV) that are connected to each other. Often simplices are used for the shape of the volumes. The differential equation is integrated over the cell and applying Gauß theorem the quantities can be expressed by fluxes at the cell bound, where each flux is at that part of the cell bound that is connected to the other cell. Similar methods are the finite integral method and FDTD used to solve the electromagnetic (Maxwell) equations. A special property of the FV-method is the requirement that each of this fluxes is unique, id est it is a property only of this part of the cell bound. This guarantees full-conservation of the states in a conservation equation (cf. [21], Sec. 7.1.3) due to the telescopic sum property. The fluxes are then interpolated from the unknowns (in the unsteady case, this is called the semi-discrete system of equations). In contrast, in Finite Element (FE) Methods, an ansatz function for the spatial distribution of the unknowns is assumed for each control-volume and it is therefore denoted as element. For the unknowns usually the cell node values are used. Some of the quantities (like stresses in a solid) often have a discontinuity at the cell bounds. The FE-method is a special case of the method of (mean) weighted residuals, where the differential equation that contains the solution function is multiplied with a test-function (or weight-function) and then integrated over the element. Integration by parts then allows to state the problem in a weak formulation. The integrals are usually evaluated approximately by quadrature. In Galerkin methods, for the test function the same ansatz is used as for the

unknowns. The Petrov–Galerkin method can be used if the differential equation contains also a first derivative (like a diffusion term). It is not possible to obtain a weak formulation when the test function and the solution function lie in the same function space. In fluid dynamics, for instance, an upwind formulation is used for the test function. The ansatz of the solution function is different and thus the matrix of the resulting linear system is asymmetric. Discontinuous Galerkin methods (cf. [76]) combine the features of the FE- and FV-method. Unlike classical (continuous) Galerkin methods, the trial function space is piecewise discontinuous. Other methods that use the advantages of both FE and FV are the spectral element method by Patera (high-order elements) and the spectral finite volume method by Wang. A mesh-free FE method is the finite cell method by Düster. In the following, the focus is on the finite volume method, but other methods are also discussed.

D.2 Incompressible versus compressible flow

Incompressible flow problems can be solved by numerical methods designed for compressible flow that fulfill the incompressibility condition only approximately. An asymptotic analysis that addresses the singular limit problem at low Mach number is described in [42]. The main issue is the treatment of the acoustic system. When it is solved explicitly, the CFL-condition contains the speed of sound and the time step would be impractically small. An implicit scheme would be expensive too. However, as the acoustic system contains only the long-wave dynamics, it is sufficient to solve it on coarser grid and then the explicit method can be used with low computational effort. In the present work the continuity equation for a fluid with constant density is considered and within the discretized system the incompressibility condition is thus exactly fulfilled.

D.3 Uniform versus nonuniform grid

Employing schemes that are derived and optimized for uniform (e. g. rectangular, equi-distant) grids [24] on nonuniform grid can lead to several problems. One problem is the poorer accuracy due to loss of order of the scheme. More severe problems are a non-converging (iterative) solution procedure or a solution that shows oscillations. There are different attempts to overcome these problems. To preserve accuracy on nonuniform grid, the positions of the cell bounds need to enter the discretization scheme in a particular way. Naturally, this leads to an interpolation of the cell boundary quantities where the coefficients (factors or weights) of the cell-averages differ from those on uniform grid. As an example, the method in [18] can be interpreted as a 1-dim finite volume approach. A 1-dim finite volume method on nonuniform grid (for linear wave equation) using a compact stencil was proposed by [24]. Often so-called compact methods are used, see below in Appendix D.10. A compact finite difference method for the 1-dim case (applied also to multi-dim. problems) is given by [25]. A 2-dim approach that uses a finite volume compact scheme on physical space is given in [46]. A 2-dim finite difference method that uses mapping is used by [113]. For a finite volume method that uses mapping, cf. [27].

D.4 Point versus cell average values

The unknowns to be solved for – in primitive variable notation usually the states – may either be point values (at cell nodes/vertices, cell centers, or face centers) or cell-average values, cf. [43]. Using cell-average values as unknowns gives more accurate solutions [82]. [82] demonstrates that the point value at the center of a cell is a second-order accurate estimate to the value averaged over the cell volume. The same relation holds between the center value on a cell face and the averaged value along the face, cf. [55]. Thus, it is of no consequence for first- or second-order accurate models whether variables represent point values or averages over some volume or area. But it is of crucial importance for third- or higher order numerical methods to properly define the discretized variable as either point values (as in [21]) or cell-center values as computational nodes (in [55], [17]).

D.5 Staggered versus colocated grid

An explanation and comparison of staggered and colocated grids is given in [116]. The staggered variable arrangement was developed by [30]. Applications can be found in [112], [77]. In a staggered arrangement the respective velocity components are usually placed at different locations in the grid. This arrangement has the unfavorable property that the discretization scheme for the spatial derivative changes with the coordinate direction. This is not the case with the colocated variable arrangement, see [75], [46]. A comparison of a C-Grid (staggered grid) with an A-grid (all quantities colocated) is given in [82]. The main advantage of the colocated grid is that there are always as much equations as unknowns, independent of the subdivision of the domain. However, it is well known that the solution in a colocated arrangement is more prone to odd-even decoupling. An effective cure to this problem is given in [90]. A partially staggered arrangement (staggering for the pressure) is discussed in [47]. Similarly, in a classical pressure-correction approach the decoupling is avoided in that the cell-face velocity is corrected with a pressure source term calculated on a staggered control volume [55].

D.6 Physical versus computational space

On distorted but structured grid, there exist two different approaches to derive a discretization scheme: The discretization can be performed either in physical space or in a computational space [25]. In the physical space the metrics of the grid need to be taken into account directly and it appears to be difficult to find a discretization that gives a stable scheme with the desired order [46]. To obtain the coefficients in a higher-order scheme one needs to invert a linear system that contains the so-called image moments. In a more frequently used approach, the equations are mapped into a computational space [17]. The advantage is a simpler choice of the grid in the new space (say rectangular, equi-distant), allowing easier interpolation of the quantities. However, there are also some drawbacks:

- To ensure the overall order of the scheme, the mapping function needs to be either given analytically [113] or approximated very accurately by a large set of points, see [27]. Furthermore, the mapping function must be smooth to achieve good accuracy, see [52].

- The transformed equations include the metric terms [52]. Therefore, the terms become more laborious. The evolution term becomes nonlinear and the couples that arise from the nonlinear terms transform to difficult multi-products.
- The cell-average values used as unknowns in the mapped space have no meaning in physical space. This requires a reconstruction of the solution to point values.
- To obtain the evolution term in unsteady problems, it is required to determine the evolution of the Jacobi determinant (the cell volume) such that it obeys the Geometric Conservation Law (GCL), cf. [113], [105], [51].
- In gas dynamics, using a Godunov-type method, the transformed Riemann problem [106] may not be physically meaningful, see [52].

Although the method that uses mapping (or Jacobian transformation) is often employed with success [113], [77], [69], [17], [27], according to [25] the approach in physical space (Fully Included Metrics, FIM) is more accurate. Nevertheless, it is difficult to derive a scheme in physical space and it seems that it is used by less authors [46], [70], [71], [93], [56].

D.7 PPM versus PPH

Usually a polynomial ansatz (a truncated Taylor series) is used to obtain an interpolation. A fourth-order accurate polynomial is used in the Piecewise Polynomial Method (PPM) by [18]. The coefficients for the explicit scheme are determined on a 1-dim nonuniform grid. The flux at the cell bound (the value at cell border) is expressed by the cell-average values. A hyperbolic linear transport equation is solved. The high-order interpolation is used in regions where the solution is smooth and is corrected near steep gradients, for instance at shocks in a gasdynamics. A different approach, the Piecewise Polynomial Harmonic (PPH), is used in [6] where a harmonic mean of second derivatives is used instead of the polynomial ansatz. The PPH method gives fourth-order accuracy for smooth solutions. However, it is proposed to have better properties where the solution is discontinuous.

D.8 Reconstruction versus ansatz

In the reconstruction approach, a truncated Taylor series (TTS) is employed that relates a set of partial derivatives in a point to unknowns (for instance: cell-averages). When the system is solved, the partial derivatives can be reconstructed. A k -exact least squares reconstruction (using control volume moments) can be found in [72], [73]. For applications of the reconstruction, see [112], [111]. In a unique reconstruction, the system matrix must be regular. In a least-squares reconstruction, more cells than moments are provided [72]. Instead of the reconstruction, [55] use a two-step procedure to obtain the fluxes: The surface integrals representing the fluxes are first approximated by a number of point values of the flux, which are then expressed by the unknowns by means of interpolation. In [43], a simple approach is proposed where an ansatz directly couples the flux (or for a compact scheme, the weighted sum of fluxes) to the

unknowns. This idea is also used in [75]. The idea makes use of the property that on simple meshes (Cartesian grid, for instance) some conditions for the control volume moments (cf. [72]) are fulfilled concurrently. Hence, less coefficients than conditions are required to fulfill the order of accuracy of the discretization scheme.

D.9 Central versus upwind schemes

In [55] several different schemes are reported: Central difference scheme (CDS), upwind scheme (UDS), and a linear extrapolation using two upstream nodal values, the linear upwind scheme (LUDS). It is well-known that central or symmetric schemes have better spectral properties and are less diffusive, see [43], [75]. This property is particularly important in large eddy simulation (LES), see [94]. However, asymmetric schemes (like the upwind-scheme) are often employed in fluid dynamics to suppress oscillations, see [24], [87]. For a comparison of central and upwind schemes, see [14] (compact schemes on nonuniform grid, treated in physical space). Their scheme is generalized for the 1-dim case by [93].

D.10 Explicit versus compact discretization method

In an explicit method (often called Lagrange method, see [24]), the flux is explicitly expressed by the a priori unknowns. In an explicit method, the fill-in of the system matrix is usually sparse. In a compact method (also called Padé, Hermitian, or spline), an implicit relation between the fluxes and the unknowns is established, see [87], [24], [75], [82]. [49] extensively studied 1-dim compact finite difference schemes on nonuniform grid. A 1-dim compact finite volume scheme on nonuniform grid is given in [24]. The compact method is more accurate and has better spectral properties [43], [46]. Therefore, the method is sometimes grouped within the quasi-spectral methods. However, the actual quasi spectral methods (like Chebyshev polynomial, wavelet transformation) are closer related to the classical Fourier spectral method. When the compact method is employed on rectangular grid, a tridiagonal system has to be solved in each direction (x, y, z) with the Thomas algorithm. As a result, the fill-in of the system matrix is dense. To reduce the computational effort, the system is usually solved with a Krylov subspace method, see [75]. Although this step is computationally cheap on simple grids, it is more difficult to employ a compact scheme for more complex (industrial) geometries. The usage on curvilinear coordinates is sketched in [75]. For a discussion of boundary condition and stability issues we refer to [43].

D.11 Nonlinear terms

The convection (or advection) term appearing in fluid dynamics is a nonlinear term, if expressed in terms of primitive variables (in 2-dim the velocity components u, v). For a finite volume method, the integral of the nonlinear flux along each part of a cell bound can be calculated by a method proposed first by [75], consisting of a 2nd-order accurate product of linear fluxes and a 4th-order correction. This idea has been used by several authors: [77], [17], [27]. The

extension of this idea to fluxes over triple-products is sketched by the same authors [75]. These multi-products appear in several different problems:

- Mapping to computational domain: $\int u(x, y)dy$ becomes $\int y_\eta u(\xi, \eta)d\eta$, [113], [17], [27].
- Compressible media: In gas dynamics, the convective flux terms are of the triple-product form $\rho u v$, see [46].
- Mapping for compressible medium: Even quad product terms appear, see [113], [27].

D.12 Boundary conditions

If boundary conditions (BC) of the Dirichlet type exist, in Finite Volume methods the values at the boundaries can be directly prescribed as fluxes, see [75]. In this regard the FV methods are superior compared to Finite Difference methods that often require a downwind discretization at inlet boundaries that tend to destabilize the system, cf. [43]. If the value at the boundary is not known, extrapolation from internal unknowns or ghost cells [122] are used. For the diffusive (or viscous) terms at boundaries on the right sided boundary the extrapolation scheme changes signs compared to the scheme on the left sided boundary [58]. When extrapolation to the boundary is used, usually each term in the equations (linear contributions from continuity, pressure, diffusion; and nonlinear term from convection, etc.) is extrapolated independently from the other terms. However, for a Finite Volume approach with colocated variable arrangement, there exist problems where the driving force of the system does not enter the discretized problem at all (problems like the lid-driven cavity with prescribed wall motion) when these extrapolations are used. In these cases, an extrapolation to the boundary needs to be employed that couples terms that represent different physical effects.

D.13 Avoiding a singular system

If the reconstruction or the ansatz (to directly relate fluxes and unknowns, see [43]) gives symmetric coefficients, there is a danger that the system of equations is singular ($\det A = 0$). The solution of $Ax = 0$ (eigenvector x to the eigenvalue $\lambda = 0$) is called the Kernel (shortly *ker*) or Nullspace, see [42], [75], and per definition the size of the matrix A minus the rank A is equal to the dimension of the Nullspace $\dim \ker A$. For the incompressible ($\tilde{\rho} = \text{const}$) Navier–Stokes equations, using a symmetric ansatz and colocated arrangement of the unknowns, different terms in the equations can be the cause for a singular system matrix A . When the solution in the Nullspace x is of oscillatory type, often odd-even decoupled solutions are observed (often called checkerboards in 2-dim, see [90]) when an iterative equation solver is used. Maintaining a symmetric discretization scheme, a singular matrix A can only be prohibited by a proper choice of boundary conditions:

- The set of discretized continuity equations (i. e., the discrete divergence operator \mathcal{D}) becomes singular if the unknowns are prescribed at all boundaries (Dirichlet BCs) and hence do not depend on the unknowns. For these cases, if a finite volume approach is employed, due to its conservation-preserving and telescopic sum properties [21], it can

be shown easily that the sum of discretized continuity equations over all cells already fulfills the boundary conditions. Therefore, the field equations together with the boundary conditions result in a singular discrete divergent matrix $\dim \ker \mathcal{D} = 1$. Note: A special case of this consideration is the well-known non-penetration problem for closed systems, where the mass-flux is zero at all faces at the boundary. This problem can be circumvented by using extrapolation at at least one boundary.

- A similar behaviour is observed for the pressure terms (the discrete gradient operator \mathcal{G}) in the momentum equations when the pressure is prescribed at all boundaries of the domain. Then, the system is also singular $\dim \ker \mathcal{G} = 1$, see [116], [83]. When used together with singular operator \mathcal{D} for the continuity equations, the overall system even has $\dim \ker A = 2$. Hence, it should be avoided to set the pressure at all boundaries.
- Finally, also the convective (or advective) terms in the momentum equations can decouple if a FV-approach and a symmetric ansatz are used (see the checkerboard example in [116]).

D.14 Solvers

Alternating Direction Implicit (ADI), see [21], [92] is a Fractional Step Approach and Approximate Factorization Technique (cf. [90] [40], [16], [77]) that can be easily used for 2nd-order discretized Pressure Poisson Equation (PPE) on uniform grid. Another method is the Strongly Implicit Procedure (SIP) method from [101], see the explanation in [21], also [55]. The nonlinear coupled system is solved iteratively with a Newton–Raphson algorithm or a Newton-like method. When a compact scheme is used (see D.10) the system is not sparse. Then a Krylov-subspace method, for instance, is usually a better choice [75].

D.15 Deconvolution

Deconvolution is a post-processing procedure. In this context, deconvolution is understood as reconstruction from the solution field, for example the reconstruction of point-values from cell-average values. Examples for the deconvolution of a solution can be found in [75], [33], [122] and for a finite-volume compact scheme on staggered grid in [77]. A different application is filtering of non-physical oscillations [49].

Appendix E

Verification of The Navier–Stokes Solver

The Navier–Stokes solver described in Sec. 3.5.2 is verified with a Kovasznay flow on random grid and a lid-driven cavity flow on uniform and random grid. The quality of the solution, order of accuracy, and deconvolution from cell-average values to node values are examined.

E.1 Kovasznay flow

E.1.1 Analytical solution

The Kovasznay flow presented in [44] is an analytic solution of the steady, 2-dim Navier–Stokes equations given by

$$u = 1 - \exp(\lambda x) \cos(2\pi y)$$

$$v = \frac{\lambda}{2\pi} \exp(\lambda x) \sin(2\pi y)$$

$$p = -\frac{1}{2} \exp(2\lambda x)$$

where $\lambda = \frac{\text{Re}}{2} - \sqrt{\frac{\text{Re}^2}{4} + 4\pi^2}$. It describes the laminar flow behind a two-dimensional grid shown in Fig. E.1.

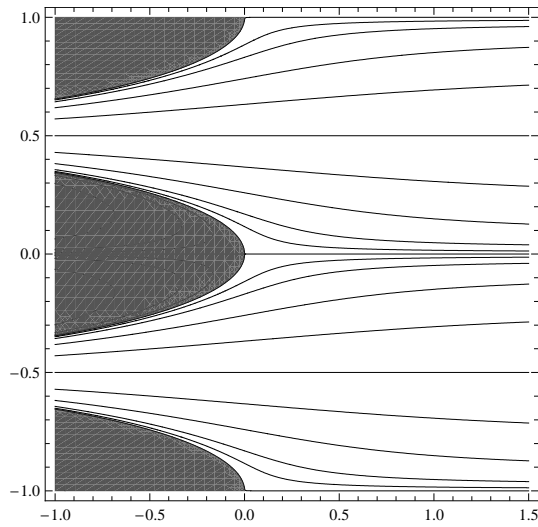


Figure E.1: Streamlines of Kovasznay flow behind a two-dimensional grid; $\text{Re} = 40$.

It is often used to test discretization schemes, [92], [112]. The Reynolds number is built with the undisturbed velocity ($U = 1$) and the vertical grid distance ($L = 1$) that is also used for the size of the domain.

E.1.2 Solution on non-uniform grid

In the test, the domain spans the interval $x = [\frac{1}{2}, \frac{3}{2}]$, $y = [-\frac{1}{2}, \frac{1}{2}]$. At the boundaries

$$u(0.5, y) = 1 - 0.61763 \cos(2\pi y), \quad v(x, \pm 0.5) = 0, \quad p(1.5, y) = -0.027754.$$

n is the number of cells in each direction. A non-uniform grid with random distortion of the node positions is chosen to validate the convergence and accuracy of the numerical scheme. The grid and the results are shown in Fig. E.2.

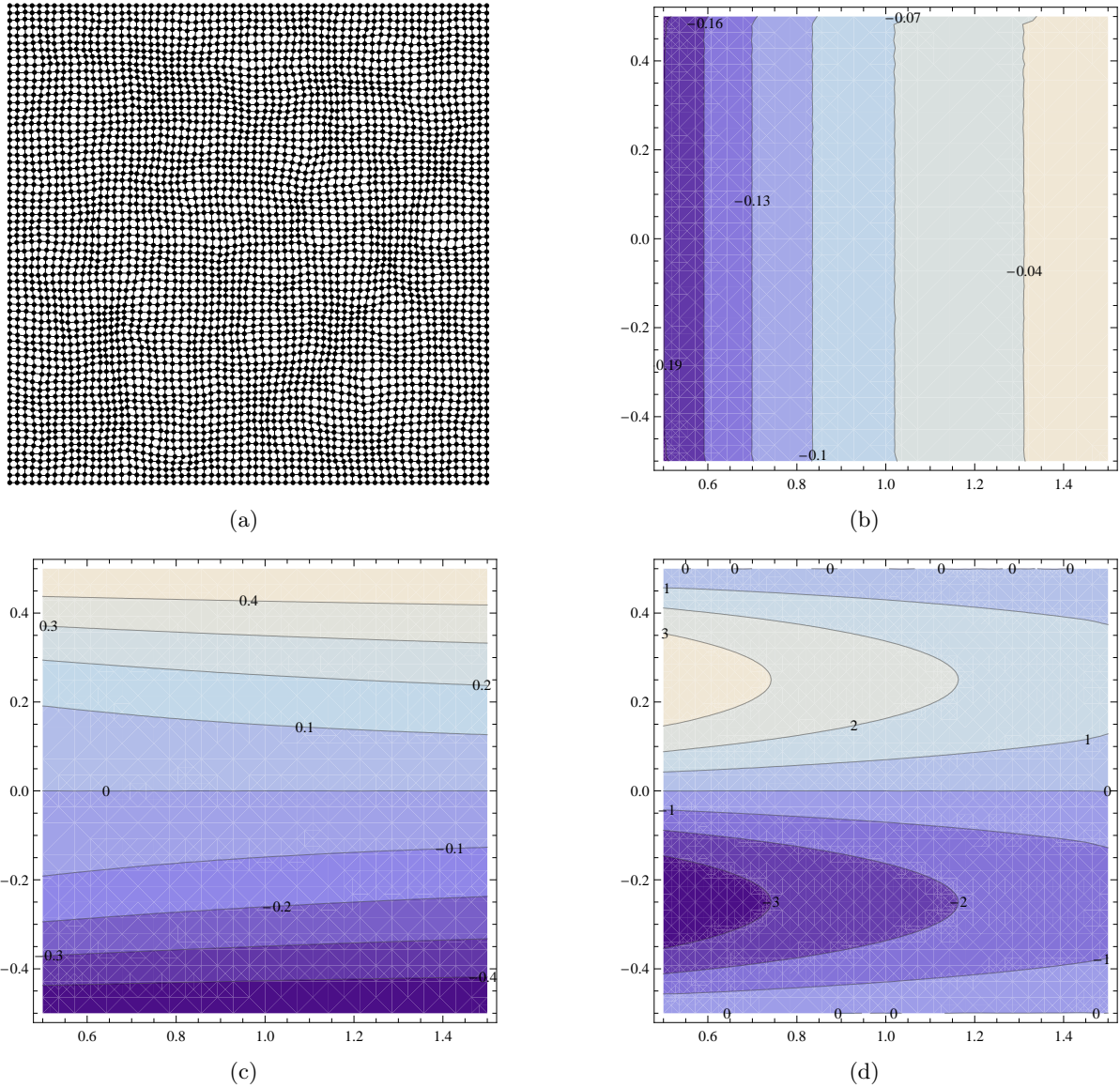


Figure E.2: Kovasznay flow on non-uniform grid: $\text{Re} = 40$, grid with $n = 64$. (a) Random grid; (b) Isolines of the pressure p ; (c) Isolines of the streamfunction ψ ; (d) Isolines of the vorticity ω .

The cell-average values are mapped to point values in the nodes via a deconvolution procedure, before the isolines are plotted. The discrete (finite volume) form of the mass conservation is used to obtain unique values for the streamfunction in the nodes. The streamfunction gives a good impression of the (rather simple) flow field. Pressure and vorticity are more prone to numerical errors than the velocity field. The pressure in a co-located arrangement should be checked for “wiggles”. The accuracy of the vorticity is (at best) one order below the velocity field, as it is derived from its spatial derivatives.

E.2 Lid-driven cavity

The lid-driven cavity has been investigated extensively in the literature, see [28], [20], [12], [81] [42], [83]. The size of the domain is $L = 1$. On the right, bottom and left boundary we prescribe $u = v = 0$ and on the top boundary $u(x, 1) = 1$, $v(x, 1) = 0$.

E.2.1 Solution on uniform grid

A uniform, equi-distant grid is constructed. The results for the pressure and the streamfunction for $Re = 1000$ are shown as isolines in Fig. E.3.

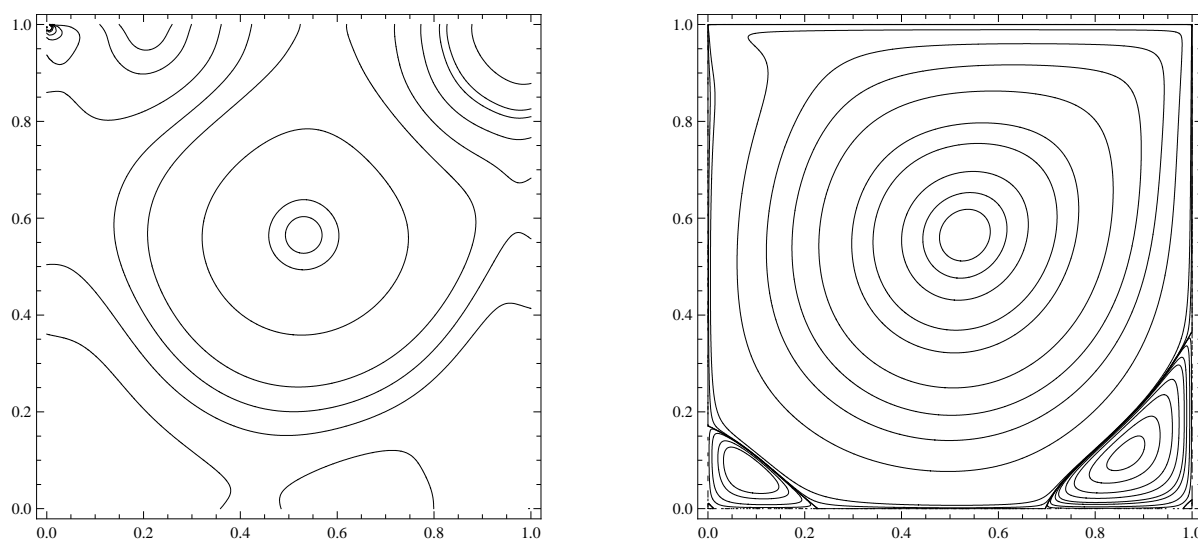


Figure E.3: Lid-driven cavity on uniform grid: $Re = 1000$, grid with $n = 256$. Left: Isolines of pressure p ; Right: Isolines of the streamfunction ψ .

For comparison, the values for the isolines of the streamfunction and pressure are chosen according to [12], Tables 7 and 8, respectively. The results are in very good agreement to those in the literature [20], [12], [81], [42], [83]. Tabs. E.1 and E.2 show a comparison of the results for the primary and secondary vortex, respectively.

Reference	Grid	ψ	ω	x	y
Present	n=128	-0.118894	-2.06795	0.5308	0.5652
Present	n=256	-0.118930	-2.06795	0.5308	0.5652
Ref. [12]	128	-0.118937	-2.06775	0.5308	0.5652
Ref. [12]	160	-0.118937	-2.06775	0.5308	0.5652
Ref. [20]	601	-0.118781	-2.06553	0.5300	0.5650
Ref. [20]	Extrapol.	-0.118942	-2.06721	–	–
Ref. [81]	257	-0.118800	–	0.5325	0.5639
Ref. [28]	129	-0.117929	-2.04968	0.5313	0.5625

Table E.1: Intensity ω of the primary vortex, at $\text{Re} = 1000$; (x,y) refers to the center of the primary vortex, i. e. the location of the maximum value of the streamfunction ψ .

Reference	Grid	ψ	ω	x	y
Present	n=128	0.00172965	1.10902	0.8640	0.1118
Present	n=256	0.00172959	1.10915	0.8640	0.1118
Ref. [12]	128	0.00172972	1.10979	0.8640	0.1118
Ref. [12]	160	0.00172972	1.10979	0.8640	0.1118
Ref. [20]	601	0.0017281	1.11551	0.8633	0.1117
Ref. [20]	Extrapol.	–	–	–	–
Ref. [81]	257	0.00172397	–	0.8658	0.1119
Ref. [28]	129	0.00175102	1.15464	0.8594	0.1094

Table E.2: Intensity ω of the secondary vortex (lower right corner), at $\text{Re} = 1000$; (x,y) refers to the center of the secondary vortex, i. e. the location of the minimum value of the streamfunction ψ .

Since no exact solution exists for this problem, the solution on the finest grid ($n = 256$) is used as a reference solution for the error estimate. We define the error e_n on a grid with fineness n in the L_p norm as

$$e_n = \|\phi - \phi^{ex}\|_{L_p} = \left[\frac{\sum_N (\phi_i - \phi_i^{ex})^p}{N} \right]^{1/p},$$

where ϕ_i and ϕ^{ex} refer to the numerical and exact values of a scalar field ϕ in the nodes and N is the number of nodes. The spatial order of accuracy is then calculated from the error of two contiguous grid sizes as

$$\frac{\ln(e_{n1}/e_{n2})}{\ln(n2/n1)}.$$

The order of accuracy on coarse grids is shown in Tab. E.3.

State	Norm	n								
		8	→	16	→	32	→	64	→	128
u	L_∞	0.00		2.46		0.49		0.61		
	L_2	0.55		2.42		2.82		2.37		
	L_1	0.58		2.39		3.20		3.54		
v	L_∞	0.33		2.36		0.61		0.77		
	L_2	1.06		2.36		2.54		2.48		
	L_1	1.30		2.28		2.80		3.51		
p	L_∞	1.26		1.95		0.52		0.59		
	L_2	1.65		1.93		2.89		3.07		
	L_1	1.79		1.94		3.00		3.79		

Table E.3: Order of accuracy of spatial discretization on uniform grid. Errors from the node values (reconstructed from cell averages); horizontal and vertical velocity components u and v , respectively. Pressure p .

Almost fourth order accuracy is attained on fine grids in the L_1 norm.

E.2.2 Solution on non-uniform grid

Random grids with different grid number are constructed as in Fig. E.2(a). On arbitrarily distorted grids, the scheme is expected to attain order three. Fig. E.4 shows the solution for streamfunction and vorticity for grids with $n = 64$ and $n = 128$, respectively.

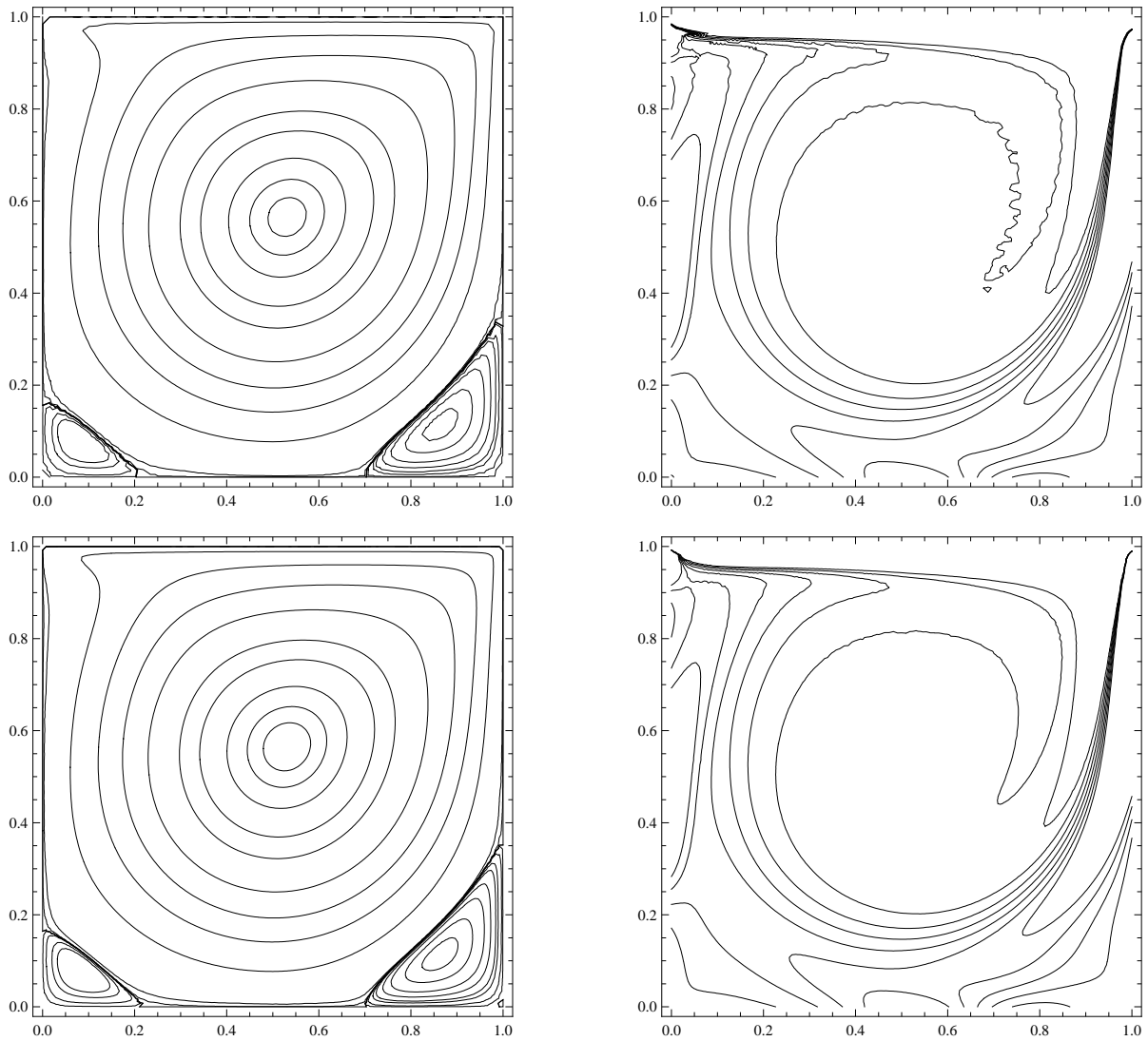


Figure E.4: Lid-driven cavity on non-uniform grid: $Re = 1000$. Left: Isolines of the streamfunction ψ (values as above); Right: Isolines of vorticity ω ; Top row: grid with $n = 64$; Bottom row: grid with $n = 128$.

Only small changes can be observed in the streamfunction (at the center, and the corners) when the grid is refined. The isolines of vorticity become smoother. Again, the solution from the finest *uniform* grid (Fig. E.3) is selected as reference solution for the error estimate. The order of accuracy on coarse grids is shown in Tab. E.4.

State	Norm	n								
		8	→	16	→	32	→	64	→	128
u	L_∞	0.25		2.23		0.36		0.66		
	L_2	0.77		2.21		2.72		2.33		
	L_1	0.81		2.18		3.13		3.16		
v	L_∞	0.54		1.97		0.61		0.69		
	L_2	1.29		2.10		2.52		2.44		
	L_1	1.52		2.08		2.77		3.19		
p	L_∞	1.41		1.87		0.18		0.46		
	L_2	1.72		1.93		2.82		2.50		
	L_1	1.85		1.94		2.96		3.05		

Table E.4: Order of accuracy of spatial discretization on random grid. Errors from the node values (reconstructed from cell averages); horizontal and vertical velocity components u and v , respectively. Pressure p .

On coarse grid, the accuracy of the scheme is pretty much the same as for uniform grid in Tab. E.3. The accuracy in the L_1 norm is slightly above the expected order of three.

Bibliography

- [1] ABOELKASSEM, Y., AND STAPLES, A. E. Flow transport in a microchannel induced by moving wall contractions: a novel micropumping mechanism. *Acta Mech.* 223, 3 (2011), 463–480.
- [2] ABRAMOWITZ, M., AND STEGUN, I. A., Eds. *Handbook of mathematical functions*, tenth printing ed., vol. 55 of *Applied Mathematics Series*. US National Bureau of Standards, 1972.
- [3] ACKERET, J. Über Luftkräfte bei sehr grossen Geschwindigkeiten, insbesondere bei ebenen Strömungen. *Helvetica Physica Acta* 1 (1928), 301–322. (in German).
- [4] ALBEN, S. Optimal flexibility of a flapping appendage in an inviscid fluid. *J. Fluid Mech.* 614 (2008), 355–380.
- [5] ALBEN, S., AND SHELLY, M. J. Flapping states of a flag in an inviscid fluid: Bistability and the transition to chaos. *Phys. Rev. Lett.* 100 (Feb. 2008), 074301.
- [6] AMAT, S., AND LIANDRAT, J. On the stability of the PPH nonlinear multiresolution. *Applied and Computational Harmonic Analysis* 18, 2 (2005), 198–206.
- [7] ANDERSON, J. M., STREITLIEN, K., BARRETT, D., AND TRIANTAFYLLOU, M. Oscillating foils of high propulsive efficiency. *J. Fluid Mech.* 360 (1998), 41–72.
- [8] ASHLEY, H., AND LANDAHL, M. *Aerodynamics of Wings and Bodies*. Addison-Wesley, 1965.
- [9] BARRETT, D. S., TRIANTAFYLLOU, M. S., YUE, D. K. P., GROSENBAUGH, M. A., AND WOLFGANG, M. J. Drag reduction in fishlike locomotion. *J. Fluid Mech.* 392 (1999), 183–212.
- [10] BARTH, T. J., AND FREDERICKSON, P. O. Higher order solution of the Euler equations on unstructured grids using quadratic reconstruction. AIAA paper 90-0013, 28th Aerospace Sciences Meeting, Jan. 1990.
- [11] BISPLINGHOFF, R., ASHLEY, H., AND HALFMAN, R. *Aeroelasticity*. Dover, 1996.
- [12] BOTELLA, O., AND PEYRET, R. Benchmark spectral results on the lid-driven cavity flow. *Comput & Fluids* 27, 4 (1998), 421–433.

- [13] BRESLIN, J. P., AND ANDERSEN, P. *Hydrodynamics of Ship Propellers*. Cambridge University Press, 1996.
- [14] BROECKHOVEN, T., SMIRNOV, S., RAMBOER, J., AND LACOR, C. Finite volume formulation of compact upwind and central schemes with artificial selective damping. *Journal of Scientific Computing* 21, 3 (2004), 341–367.
- [15] CHENG, J.-Y., ZHUANG, L.-X., AND TONG, B.-G. Analysis of swimming three-dimensional waving plates. *J. Fluid Mech.* 232 (1991), 341–355.
- [16] CHOI, H., AND MOIN, P. Effects of the computational time step on numerical solutions of turbulent flow. *J. Comput. Phys.* 113, 1 (1994), 1–4.
- [17] COLELLA, P., DORR, M. R., HITTINGER, J. A. F., AND MARTIN, D. F. High-order, finite-volume methods in mapped coordinates. *J. Comput. Phys.* 230, 8 (2011), 2952–2976.
- [18] COLELLA, P., AND WOODWARD, P. The piecewise parabolic method (PPM) for gas-dynamical simulations. *J. Comput. Phys.* 54 (1984), 174–201.
- [19] COMBES, S. A., AND DANIEL, T. L. Shape, flapping and flexion: Wing and fin design for forward flight. *The Journal of Experimental Biology* 204 (2001), 2073–2085.
- [20] ERTURK, E., CORKE, T. C., AND GÖKÇÖL, C. Numerical solutions of 2-D steady incompressible driven cavity flow at high Reynolds numbers. *Intl. J. Num. Meth. Fluids* 48 (2005), 747–774.
- [21] FERZIGER, J. H., AND PERIĆ, M. *Computational Methods for Fluid Dynamics*, 3rd ed. Springer, 2002.
- [22] FONTANELLA, J. E., FISH, F. E., BARCHI, E. I., CAMPBELL-MALONE, R., NICHOLS, R. H., DINENNO, N. K., AND BENESKI, J. T. Two- and three-dimensional geometries of batoids in relation to locomotor mode. *Journal of Experimental Marine Biology and Ecology* 446 (2013), 273–281.
- [23] FÖRSTER, C., WALL, W. A., AND RAMM, E. Artificial added mass instabilities in sequential staggered coupling of nonlinear structures and incompressible viscous flows. *Computer Methods in Applied Mechanics and Engineering* 196, 7 (2007), 1278–1293.
- [24] GAITONDE, D., AND SHANG, J. S. Optimized compact-difference-based finite-volume schemes for linear wave phenomena. *J. Comput. Phys.* 138, 2 (Dec. 1997), 617–643.
- [25] GAMET, L., DUCROS, F., NICOUD, F., AND POINSOT, T. Compact finite difference schemes on non-uniform meshes. Application to direct numerical simulations of compressible flows. *Intl. J. Num. Meth. Fluids* 29, 2 (1999), 159–191.
- [26] GARRICK, I. E. Propulsion of a flapping and oscillating airfoil. Tech. Rep. 567, N.A.C.A., Washington D. C., 1936.

- [27] GHADIMI, M., AND FARSHCHI, M. Fourth order compact finite volume scheme on nonuniform grids with multi-blocking. *Comput & Fluids* 56 (March 2012), 1–16.
- [28] GHIA, U., GHIA, K. N., AND SHIN, C. T. High-Re solutions for incompressible flow using the Navier–Stokes equations and a multigrid method. *J. Comput. Phys.* 48, 3 (1982), 387–411.
- [29] GREENGARD, L. Potential flow in channels. *SIAM J. Sci. Comput.* 11, 4 (July 1990), 603–620.
- [30] HARLOW, F. H., AND WELCH, J. Numerical calculation of time-dependent viscous incompressible flow of fluid with a free surface. *Phys. Fluids* 8, 12 (1965), 2182–2189.
- [31] HICKERSON, A. I., AND GHARIB, M. On the resonance of a pliant tube as a mechanism for valveless pumping. *J. Fluid Mech.* 555 (2006), 141–148.
- [32] HEPFFNER, J., AND FUKAGATA, K. Pumping or drag reduction? *J. Fluid Mech.* 635 (2009), 171–187.
- [33] IANNELLI, P., DENARO, F. M., AND STEFANO, G. D. An effective fourth order finite volume method for DNS/LES on non-uniform grid. In *Proceedings of the Third AFOSR International Conference on DNS/LES* (Arlington, USA, August 2001), Greyden Press Columbus.
- [34] IOSILEVSKII, G. Asymptotic theory of an oscillating wing section in weak ground effect. *European Journal of Mechanics - B/Fluids* 27, 4 (2008), 477–490.
- [35] JONES, K. D., DOHRING, C. M., AND PLATZER, M. F. Wake structures behind plunging airfoils: A comparison of numerical and experimental results. AIAA paper 96-0078, 34th Aerospace Sciences Meeting and Exhibit, 1996.
- [36] KATZ, J., AND PLOTKIN, A. *Low-Speed Aerodynamics*, 2nd ed. Cambridge University Press, 2001.
- [37] KATZ, J., AND WEIHS, D. Behavior of vortex wakes from oscillating airfoils. *J. Aircraft* 15, 12 (1978), 861–863.
- [38] KATZ, J., AND WEIHS, D. Hydrodynamic propulsion by large amplitude oscillation of an airfoil with chordwise flexibility. *J. Fluid Mech.* 88 (1978), 485–497.
- [39] KELDYSH, M. V., AND LAVRENTIEV, M. On the motion of a wing under the surface of a heavy liquid. In *Proceedings of the Conference on the Theory of Wave Drag* (Moscow, 1937), pp. 31–64. (original in Russian).
- [40] KIM, J., AND MOIN, P. Application of a fractional-step method to incompressible Navier–Stokes equations. *J. Comput. Phys.* 59, 2 (1985), 308–323.
- [41] KIRK, D. E. *Optimal Control Theory: An Introduction*. Dover Publications, 2004.

- [42] KLEIN, R., BOTTA, N., SCHNEIDER, T., MUNZ, C. D., ROLLER, S., MEISTER, A., HOFFMANN, L., AND SONAR, T. Asymptotic adaptive methods for multi-scale problems in fluid mechanics. *Journal of Engineering Mathematics* 39, 1 (2001), 261–343.
- [43] KOBAYASHI, M. H. On a class of Padé finite volume methods. *J. Comput. Phys.* 156, 1 (1999), 137–180.
- [44] KOVASZNAY, L. I. G. Laminar flow behind a two-dimensional grid. *Mathematical Proceedings of the Cambridge Philosophical Society* 44 (1 1948), 58–62.
- [45] KÜSSNER, H. G. Zusammenfassender Bericht über den instationären Auftrieb von Flügeln. *Luftfahrtforschung* 13 (December 1936), 410–424. (in German).
- [46] LACOR, C., SMIRNOV, S., AND BAELMANS, M. A finite volume formulation of compact central schemes on arbitrary structured grids. *J. Comput. Phys.* 198, 2 (2004), 535–566.
- [47] LAIZET, S., AND LAMBALLAIS, E. High-order compact schemes for incompressible flows: A simple and efficient method with quasi-spectral accuracy. *J. Comput. Phys.* 228, 16 (2009), 5989–6015.
- [48] LE TALLEC, P., AND MOURO, J. Fluid structure interaction with large structural displacements. *Computer Methods in Applied Mechanics and Engineering* 190 (2001), 3039–3067.
- [49] LELE, S. K. Compact finite difference schemes with spectral-like resolution. *J. Comput. Phys.* 103, 1 (1992), 16–42.
- [50] LERNER, J. I. *Unsteady Viscous Effects in the Flow Over an Oscillating Surface*. Department of Aeronautics and Astronautics, Stanford University, 1972.
- [51] LESOINNE, M., AND FARHAT, C. Geometric conservation laws for flow problems with moving boundaries and deformable meshes, and their impact on aeroelastic computations. *Computer Methods in Applied Mechanics and Engineering* 134, 1–2 (1996), 71–90.
- [52] LEVEQUE, R. J. *Finite Volume Methods for Hypberbolic Problems*. Cambridge University Press, 2002.
- [53] LIGHTHILL, M. J. Aquatic animal propulsion of high hydromechanical efficiency. *J. Fluid Mech.* 44 (1970), 265–301.
- [54] LIGHTHILL, M. J. *Mathematical Biofluidynamics*. Soc. Industrial and Applied Math, 1975.
- [55] LILEK, Z., AND PERIĆ, M. A fourth-order finite volume method with colocated variable arrangement. *Comput & Fluids* 24, 3 (1995), 239–252.
- [56] LIU, D., KUANG, W., AND TANGBORN, A. High-order compact implicit difference methods for parabolic equations in geodynamo simulation. *Advances in Mathematical Physics* 2009 (2009), 23 pages.

- [57] LU, X., AND YIN, X. Propulsive performance of a fish-like travelling wavy wall. *Acta Mechanica* 175, 1–4 (2005), 197–215.
- [58] MAHESH, K. A family of high order finite difference schemes with good spectral resolution. *J. Comput. Phys.* 145, 1 (1998), 332–358.
- [59] MANOPOULOS, C. G., AND TSANGARIS, S. Modelling of the blood flow circulation in the human foetus by the end of the third week of gestation. *Cardiovascular Engineering* 5, 1 (2005), 29–35.
- [60] MICHELIN, S., AND LLEWELLYN SMITH, S. G. Resonance and propulsion performance of a heaving flexible wing. *Phys. Fluids* 21 (2009), 071902.
- [61] MICHELIN, S., LLEWELLYN SMITH, S. G., AND GLOVER, B. J. Vortex shedding model of a flapping flag. *J. Fluid Mech.* 617 (2008), 1–10.
- [62] MILES, J. On the generation of surface waves by shear flows. *J. Fluid Mech.* 3, 2 (1957), 185–204.
- [63] MILES, J. On the generation of surface waves by shear flows. Part 2. *J. Fluid Mech.* 6, 4 (1959), 568–582.
- [64] MOK, D. P. *Partitionierte Lösungsansätze in der Strukturodynamik und der Fluid-Struktur-Interaktion*. PhD thesis, University of Stuttgart, 2001.
- [65] MOLINA, J., ZHANG, X., AND ANGLAND, D. On the unsteady motion and stability of a heaving airfoil in ground effect. *Acta Mechanica Sinica* 27, 2 (2011), 164–178.
- [66] MÜLLNER, M. Zeitlich harmonisch bewegte Platte im Strom eines idealen Fluids. Untersuchung von Kraft, Leistung und Wirkungsgrad. Master’s thesis, Vienna University of Technology, 2008. (in German).
- [67] MÜLLNER, M., AND SCHNEIDER, W. Laminar mixed convection on a horizontal plate of finite length in a channel of finite width. *Heat and Mass Transfer* 46, 10 (2010), 1097–1110.
- [68] MUSKHELISHVILI, N. I. *Singular integral equations*, 2nd ed. Dover, 1992.
- [69] NIKITIN, N. Finite-difference method for incompressible Navier–Stokes equations in arbitrary orthogonal curvilinear coordinates. *J. Comput. Phys.* 217, 2 (2006), 759–781.
- [70] NYBELEN, L. Temporal DNS of vortex bursting and assessment. Fundamental Research on Aircraft Wake Phenomena, 2005–2008.
- [71] NYBELEN, L. *Etude numérique d’écoulements tourbillonnaires de sillage d’avion*. PhD thesis, University of Toulouse, 2008. (in French).
- [72] OLLIVIER-GOOCH, C., NEJAT, A., AND MICHALAK, K. On obtaining high-order finite-volume solutions to the Euler equations on unstructured meshes. *AIAA Journal* 47 (2009), 2105–2120.

- [73] OLLIVIER-GOOCH, C., AND VAN ALTENA, M. A high-order-accurate unstructured mesh finite-volume scheme for the advection-diffusion equation. *J. Comput. Phys.* 181, 2 (Sept. 2002), 729–752.
- [74] OLVER, F. W. J., LOZIER, D. W., BOISVERT, R. F., AND CLARK, C. W. *NIST Handbook of mathematical functions*. Cambridge University Press, 2010.
- [75] PEREIRA, J. M. C., KOBAYASHI, M. H., AND PEREIRA, J. C. F. A fourth-order-accurate finite volume compact method for the incompressible Navier–Stokes solutions. *J. Comput. Phys.* 167, 1 (Feb. 2001), 217–243.
- [76] PERSSON, P.-O., BONET, J., AND PERAIRE, J. Discontinuous Galerkin solution of the Navier–Stokes equations on deformable domains. *Computer Methods in Applied Mechanics and Engineering* 198, 17–20 (2009), 1585–1595.
- [77] PILLER, M., AND STALIO, E. Finite-volume compact schemes on staggered grids. *J. Comput. Phys.* 197, 1 (June 2004), 299–340.
- [78] PREMPRANEERACH, P., HOVER, F. S., AND TRIANTAFYLLOU, M. S. The effect of chordwise flexibility on the thrust and efficiency of a flapping foil. In *Proc. Int. Symp. Unmanned Untethered Submersible Technology* (2003).
- [79] READ, D. A., HOVER, F. S., AND TRIANTAFYLLOU, M. S. Forces on oscillating foils for propulsion and maneuvering. *J. Fluids Struct.* 17 (2003), 163–183.
- [80] ROZHDESTVENSKY, K. V., AND RYZHOV, V. A. Aerohydrodynamics of flapping-wing propulsors. *Progress in Aerospace Sciences* 39, 8 (2003), 585–633.
- [81] SAHIN, M., AND OWENS, R. G. A novel fully implicit finite volume method applied to the lid-driven cavity problem – Part I: High Reynolds number flow calculations. *Intl. J. Num. Meth. Fluids* 42 (2003), 57–77.
- [82] SANDERSON, B. G., AND BRASSINGTON, G. Accuracy in the context of a control-volume model. *Atmos.-Ocean* 36 (1998), 355–384.
- [83] SCHNEIDER, T., BOTTA, N., GERATZ, K. J., AND KLEIN, R. Extension of finite volume compressible flow solvers to multi-dimensional variable density zero Mach number flows. *J. Comput. Phys.* 155, 2 (1999), 248–286.
- [84] SCHNEIDER, W. *Mathematische Methoden der Strömungsmechanik*. Vieweg, 1978. (in German).
- [85] SCHNEIDER, W. Lift, thrust and heat transfer due to mixed convection flow past a horizontal plate of finite length. *J. Fluid Mech.* 529 (2005), 51–69.
- [86] SCHWARZ, L. Berechnung der Druckverteilung einer harmonisch sich verformenden Tragfläche in ebener Strömung. *Luftfahrtforschung* 17, 11–12 (1940), 379–386. (in German, English translation NACA No. 991).

- [87] SENGUPTA, T. K., GANERIWAL, G., AND DE, S. Analysis of central and upwind compact schemes. *J. Comput. Phys.* 192, 2 (2003), 677–694.
- [88] SETTER, E., AND BUCHER, I. Robotic swimmer/pump based on an optimal wave generating mechanism. *Mechanism and Machine Theory* 70 (2013), 266–277.
- [89] SFAKIOTAKIS, M., LANE, D. M., AND DAVIES, J. B. C. Review of fish swimming modes for aquatic locomotion. *IEEE Journal of Ocean Engineering* 24, 2 (Apr. 1999), 237–252.
- [90] SHASHANK, LARSSON, J., AND IACCARINO, G. Short note: A co-located incompressible Navier–Stokes solver with exact mass, momentum and kinetic energy conservation in the inviscid limit. *J. Comput. Phys.* 229, 12 (June 2010), 4425–4430.
- [91] SHEN, L., ZHANG, X., YUE, D. K. P., AND TRIANTAFYLLOU, M. S. Turbulent flow over a flexible wall undergoing a streamwise travelling wave motion. *J. Fluid Mech.* 484 (2003), 197–221.
- [92] SHEU, T. W. H., AND LIN, R. K. Newton linearization of the incompressible Navier–Stokes equations. *Intl. J. Num. Meth. Fluids* 44, 3 (2004), 297–312.
- [93] SICOT, F. High order schemes on non-uniform structured meshes in a finite-volume formulation. Master’s thesis, Chalmers University of Technology, Göteborg, Sweden, 2006.
- [94] SMIRNOV, S., LACOR, C., AND BAELMANS, M. A finite volume formulation for compact schemes with applications to LES. AIAA paper 2001-2546, 15th AIAA Computational Fluid Dynamics Conference, Anaheim, CA, June 11–14 2001.
- [95] SÖHNGEN, H. Die Lösung der Integralgleichung $g(x) = \frac{1}{2\pi} \oint_{-a}^a \frac{f(\xi)}{x - \xi} d\xi$ und deren Anwendung in der Tragflügeltheorie. *Math. Z.* 45 (1939), 245–264. (in German).
- [96] SPARENBERG, J. A., THOMAS, E. G. F., AND VAN DE VOOREN, A. I. On the existence of small-amplitude optimum hydrofoil propulsion. *Math. Meth. Appl. Sci.* 3 (1981), 424–434.
- [97] STADLER, W. Fundamentals of multicriteria optimization. In *Multicriteria Optimization in Engineering and in the Sciences*, W. Stadler, Ed., vol. 37. Springer, 1988, pp. 1–25.
- [98] STEINRÜCK, H., AND MÜLLNER, M. Simulation of a membrane flow interaction by an iteration based on a panel method. *Proc. Appl. Math. Mech.* 13, 1 (2013), 215–216.
- [99] STEINRÜCK, H., ZACKL, W., MÜLLNER, M., AND NETH, H. A double channel membrane pump. *Proc. Appl. Math. Mech.* 10, 1 (2010), 485–486.
- [100] STEMME, E., AND STEMME, G. A valveless diffuser/nozzle-based fluid pump. *Sensors and Actuators A: Physical* 39, 2 (Nov. 1993), 159–167.
- [101] STONE, H. L. Iterative solution of implicit approximations of multidimensional partial differential equations. *SIAM J. Numer. Anal.* 5, 3 (1968), 530–558.

- [102] STREITLIEN, K., AND TRIANTAFYLLOU, G. S. On thrust estimates for flapping foils. *J. Fluids Struct.* 12 (1998), 47–55.
- [103] TAKAGI, D., AND BALMFORTH, N. J. Peristaltic pumping of viscous fluid in an elastic tube. *J. Fluid Mech.* 672 (2011), 196–218.
- [104] THEODORSEN, T. General theory of aerodynamic instability and the mechanism of flutter. Tech. Rep. 496, N.A.C.A., Washington D. C., 1935.
- [105] THOMAS, P. D., AND LOMBARD, C. K. Geometric conservation law and its application to flow computations on moving grids. *AIAA Journal* 17 (1979), 1030–1037.
- [106] TORO, E. F. *Riemann Solvers and Numerical Methods for Fluid Dynamics, A Practical Introduction*. Springer, 1997.
- [107] TRIANTAFYLLOU, G., TRIANTAFYLLOU, M., AND GROSENBAUGH, M. Optimal thrust development in oscillating foils with application to fish propulsion. *J. Fluids Struct.* 7, 2 (1993), 205–224.
- [108] TUNCER, I., WALZ, R., AND PLATZER, M. A computational study on the dynamic stall of a flapping airfoil. AIAA paper 98-2519, AIAA, 1998.
- [109] TUNCER, I. H., AND KAYA, M. Optimization of flapping airfoils for maximum thrust and propulsive efficiency. *AIAA Journal* 43 (2005).
- [110] VANDENBERGHE, N., ZHANG, J., AND CHILDRESS, S. Symmetry breaking leads to forward flapping flight. *J. Fluid Mech.* 506 (2004), 147–155.
- [111] VIDOVIĆ, D. Polynomial reconstruction of staggered unstructured vector fields. *Theoret. Appl. Mech.* 36 (2009), 85–99.
- [112] VIDOVIĆ, D., SEGAL, A., AND WESSELING, P. A superlinearly convergent finite volume method for the incompressible Navier–Stokes equations on staggered unstructured grids. *J. Comput. Phys.* 198 (2004), 159–177.
- [113] VISBAL, M. R., AND GAITONDE, D. V. On the use of higher-order finite-difference schemes on curvilinear and deforming meshes. *J. Comput. Phys.* 181, 1 (2002), 155–185.
- [114] VOGEL, S. *Life in Moving Fluids. The Physical Biology of Flow*, 2nd ed. Princeton University Press, 1994.
- [115] VON KÁRMÁN, T., AND SEARS, W. R. Airfoil theory for non-uniform motion. *Journal of the Aeronautical Sciences* 5 (1938).
- [116] WESSELING, P. *Principals of Computational Fluid Dynamics*. Springer, 2001.
- [117] WOLFRAM RESEARCH, INC. The Wolfram functions site. <http://functions.wolfram.com/ElementaryFunctions/Csch/06/05/>, visited on August 22nd 2013.

- [118] WU, T. Y.-T. Swimming of a waving plate. *J. Fluid Mech.* 10 (May 1961), 321–344.
- [119] WU, T. Y.-T. Hydromechanics of swimming propulsion. Part 2. Some optimum shape problems. *J. Fluid Mech.* 46 (1971), 521–544.
- [120] ZACKL, W. Experimental investigation of a valveless double channel membrane pump. Master’s thesis, Vienna University of Technology, 2011.
- [121] ZACKL, W., NETH, H., AND STEINRÜCK, H. An experimental investigation of the double channel membrane pump. http://publik.tuwien.ac.at/files/pub-mb_6041.pdf, 2007.
- [122] ZHANG, Q., JOHANSEN, H., AND COLELLA, P. A fourth-order accurate finite-volume method with structured adaptive mesh refinement for solving the advection-diffusion equation. *SIAM J. Sci. Comput.* 34, 2 (2012), B179–B201.

Curriculum Vitae

Personal Data

name: Markus Müllner
born: 1979 in Vienna, Austria
address: Am Stiegl 5, 2120 Wolkersdorf, Austria

Education

2008–2015 doctoral studies at Vienna University of Technology
1999–2008 graduated (Dipl.-Ing.) in Mech. Eng. from Vienna University of Technology
1993–1998 technical school (Ing.) for Vehicle Engineering at TGM, Vienna

Professional Experience

2014 scientific assistant at Vienna University of Technology
2010–2013 scientific assistant at Vienna University of Technology
2008 scientific assistant at Vienna University of Technology

Projects

2012 mathematical model of a wind turbine with self-adjusting blades
2011 CFD simulation of a belt conveyor
2008–2009 CFD simulation of the cylinder head of a reciprocating compressor

Research Interests

Mixed convection flow
Hydraulic free-surface flow
Discretization methods in fluid dynamics